

Essential Climate Variables for the Ice Sheets from Space and Airborne measurements

Fredenslund Levinsen, Joanna; Forsberg, René; Sørensen, Louise Sandberg; Khan, Shfaqat Abbas

Publication date:
2015

Document Version
Publisher's PDF, also known as Version of record

[Link back to DTU Orbit](#)

Citation (APA):

Fredenslund Levinsen, J., Forsberg, R., Sørensen, L. S., & Khan, S. A. (2015). Essential Climate Variables for the Ice Sheets from Space and Airborne measurements. Kgs. Lyngby: Danmarks Tekniske Universitet (DTU).

DTU Library

Technical Information Center of Denmark

General rights

Copyright and moral rights for the publications made accessible in the public portal are retained by the authors and/or other copyright owners and it is a condition of accessing publications that users recognise and abide by the legal requirements associated with these rights.

- Users may download and print one copy of any publication from the public portal for the purpose of private study or research.
- You may not further distribute the material or use it for any profit-making activity or commercial gain
- You may freely distribute the URL identifying the publication in the public portal

If you believe that this document breaches copyright please contact us providing details, and we will remove access to the work immediately and investigate your claim.

Essential Climate Variables for the Ice Sheets from Space and Airborne measurements

Joanna Fredenslund Levinsen
Ph.D. Dissertation
February 28, 2015

Essential Climate Variables for the Ice Sheets from Space and Airborne measurements

Joanna Fredenslund Levinsen

National Space Institute

Ph.D. Dissertation, Kgs. Lyngby, February 28, 2015

Supervised by René Forsberg, National Space Institute, Technical University of Denmark,
Louise Sandberg Sørensen, National Space Institute, Technical University of Denmark,
Shfaqat Abbas Khan, National Space Institute, Technical University of Denmark.

<http://www.space.dtu.dk>

Preface

This Ph.D. dissertation, entitled "*Essential Climate Variables for the Ice Sheets from Space and Airborne measurements*", is the result of the work carried out during my enrollment at the National Space Institute, DTU Space.

The Ph.D. study began on March 1st 2012 with funding from the ESA Ice Sheets CCI project. It was supervised by DTU Space employees René Forsberg, Head of Department; Louise Sandberg Sørensen, Researcher; and Abbas Khan, Senior Researcher.


The Ph.D. study has led to a number of scientific papers, some of which are included in this dissertation:

- * [Levinsen et al. \(2015a\)](#)
- * [Sørensen et al. \(2015\)](#)
- * [Levinsen et al. \(2015b\)](#)
- * [Levinsen et al. \(2015c\)](#)

These publications are enclosed in Appendices A to D. Appendix F contains a complete overview of all written contributions composed during the study.

I have presented my research at various meetings, e.g. through posters in a workshop at the Center for Ice and Climate (CIC), University of Copenhagen, in 2012, at the 2013 and 2014 European Geosciences Union (EGU) meetings, and at the 2014 American Geophysical Union (AGU) Fall meeting. The posters are enclosed in Appendix E. Oral presentations have been given e.g. at the 2013 ESA Living Planet Symposium, the 2013 AGU Fall Meeting, and at the Polar Science Center, Applied Physics Lab, University of Washington (PSC-UW). A number of additional talks and posters have been co-authored.

During the Ph.D. study, I have participated in the "Sea Level Rise and Ice Sheets" and "Space methods for monitoring of the Cryosphere" summer schools organized by the CIC and DTU Space, respectively. I have also spent five months working with Senior Scientist Ben Smith at the PSC-UW. All travels have been funded by DTU, the Oticon Foundation, the Idella Fund, and Selskabet for Arktisk Forskning og Teknologi.



Joanna Fredenslund Levinsen
Kgs. Lyngby, February 2015

Acknowledgements

I am very grateful to all the people who have been involved in making this Ph.D. study successful, both colleagues, friends, and family. I never would have made it without you.

I am deeply thankful to my supervisors, René Forsberg, Louise Sandberg Sørensen, and Abbas Khan, for letting me have this opportunity, and for the many rewarding discussions we have had along the way. I would like to thank Kirill Khvorostovsky for his continuous support throughout this study, and Ben Smith and Ian Joughin for their extraordinary hospitality and support in making my visit at the University of Washington possible.

I acknowledge the Round Robin participants for taking the time to submit elevation change estimates and for reviewing the resulting paper prior to its publication. I also acknowledge ESA for giving me the opportunity to join the Ice Sheets CCI project; this has opened the door to many opportunities, which will, undoubtedly, be helpful in the future.

Abstract

The Greenland Ice Sheet is the largest ice mass in the northern hemisphere. Over the past decade, it has undergone substantial changes in e.g. mass balance, surface velocity, and ice thickness. The latter is reflected by surface elevation changes, which are detectable with altimetry. Therefore, this study exploits the advantages of radar and laser altimetry to analyze surface elevation changes and build a Digital Elevation Model of the ice sheet. Selected advantages are radar data's continuity in time and laser data's higher horizontal and vertical accuracy. Therefore, ESA Envisat and CryoSat-2 radar altimetry data are used in conjunction with laser data from NASA's ICESat and airborne ATM and LVIS instruments, and from ESA's airborne CryoVEx campaign.

The study is part of the ESA Ice Sheets CCI project. With the release of REAPER data, one goal is to use the more than two decades of ESA radar altimetry to develop a long-term surface elevation change product from 1992 to present. The optimal method is found by comparing ten different solutions submitted by the scientific community across the choice of altimeter and method: A combination of repeat-tracks and cross-overs. The former produces estimates along repeat ground-tracks while the latter exploits intersecting ground-tracks. The combination increases the spatial data coverage and reduces topographic errors. Two results based on Envisat data are presented here: The first repeat-track solution (2002 – 2010) of the Greenland Ice Sheet and a merged repeat-track and cross-over result from 2006 – 2010.

A 2×2 km Digital Elevation Model is built from combined radar and laser data. It is applicable for elevation change detection and correction of topographic errors. Current models have limitations as they are based on short observation periods from one sensor, limiting the spatial data coverage, or multiple years of data from various sensors, inheriting errors from intermediate elevation changes. The model here consists of Envisat and CryoSat-2 data from 2010 merged with ICESat, ATM, and LVIS data. Vertical radar errors are corrected with laser data. Thus, the Digital Elevation Model is referenced to a specific epoch in time and exploits the high spatial coverage of input data. An important finding in the study is disagreeing relocations of radar data depending on the method. Validation shows the preferred method to be the Point of Closest Approach with an a-priori Digital Elevation Model to extract the surface topography. The preferred spatial resolution of the model is 2×2 km for Envisat and CryoSat-2 LRM data near Jakobshavn Isbræ, i.e. over regions with both steep and smooth topography.

Resumé

Indlandsisen i Grønland er den største ismasse i den nordlige hemisfære. Over det sidste årti har Indlandsisen undergået store forandringer af blandt andet massebalancen, overfladehastigheder og istykkelse. Sidstnævnte afspejles ved højdeændringer, og disse kan måles ved hjælp af altimetri. Derfor omhandler dette studium udnyttelsen af fordelene ved radar- og laseraltimetri til at analysere højdeændringer samt bygge en højdemodel af Indlandsisen. Eksempler på fordele er, at radardata er kontinuerte i tid, mens laserdata har en højere horisontal og vertikal præcision. Til studiet kombineres radardata fra ESAs Envisat og CryoSat-2 med laserdata fra NASAs ICESat og flybårne instrumenter ATM og LVIS samt fra ESAs flykampagne CryoVEx.

Studiet er udført som en del af ESAs Ice Sheets CCI-projekt. Med offentliggørelsen af REAPER-data, er et af målene at anvende de mere end to årtiers ESA-radardata til højdeændringsbestemmelse fra 1992 og frem til i dag. Den optimale fremgangsmåde er fundet ved at sammenligne ti forskellige resultater, indsendt af det videnskabelige samfund, på basis af metode og altimeter: En kombination af repeat-tracks og cross-overs. Førstnævnte udnytter gentagende overfløjne satellitspor, mens sidstnævnte estimeres bestemmes, hvor sporene krydser. Kombinationen øger den rumlige datadækning og reducerer topografiske fejl. To resultater baseret på Envisat præsenteres her: De første repeat-track-resultater (2002 – 2010) over Indlandsisen samt kombinerede repeat-track og cross-over-resultater fra 2006 – 2010.

En 2×2 km højdemodel er udviklet fra kombinerede radar- og laserdata. Den kan anvendes i analyser af højdeændringer samt til at korrigere radardata for topografiske fejl. Nuværende modeller er begrænsede, i det de er bygget ud fra få års data fra én sensor, hvilket reducerer den rumlige datadækning, eller mange års data fra flere sensorer, hvormed fejl fra mellemliggende højdeændringer opstår. Denne højdemodel består af Envisat- og CryoSat-2-data fra 2010 kombineret med ICESat-, ATM- og LVIS-data. Vertikale fejl i radardata er korrigeret med laserdata. Dermed er en højdemodel udviklet, refereret til en specifik epoke, og som udnytter inputdatas høje rumlige dækning.

Et vigtigt resultat af studiet er forskelligartede forskydninger opnået ved at relokere radardata forskelligt. Validering viser, at den foretrukne fremgangsmåde er 'the Point of Closest Approach' med en a-priori højdemodel til at analysere overfladetopografien. Modellens foretrukne rumlige opløsning er 2×2 km for Envisat- og CryoSat-2 LRM-data opmålt nær Jakobshavn Isbræ, dvs. over områder med både store og små overfladehældninger.

Abbreviations

Abbreviation	Short for
AGU	American Geophysical Union
ATM	Airborne Topographic Mapper
Bs	Backscatter coefficient
CCI	Climate Change Initiative
CryoVEx	Cryosat Validation Experiment
DEM	Digital Elevation Model
DORIS	Doppler Orbit and Radio positioning Integration by Satellite
EGU	European Geosciences Union
ECV	Essential Climate Variable
ERS	Earth Remote Sensing
ESA	European Space Agency
GIMP	Greenland Ice Mapping Project
GrIS	Greenland Ice Sheet
GLAS	Geosciences Laser Altimeter Instrument
GPS	Global Positioning System
GRACE	Gravity Recovery and Climate Experiment
GSFC	Goddard Space Flight Center
ICESat	Ice, Cloud, and land Elevation Satellite
IV	Ice velocity
LA	Laser altimetry
LeW	Leading edge Width
LRM	Low Resolution Mode
LSq	Linear least-squares
LVIS	Land, Vegetation, and Ice Sensor
NASA	National Aeronautics and Space Administration
OCOg	Offset Center of Gravity
POCA	Point Of Closest Approach
POD	Precise Orbit Determination
PLF	Pulse-limited footprint
PS	Polar Stereographic
RA	Radar altimetry
REAPER	REprocessing of Altimeter Products for ERS
RL-DEM	Radar-Laser DEM
RMS	Root-Mean-Square

Abbreviation	Short for
RR	Round Robin
RT	Repeat-track
SNR	Signal-to-noise ratio
SAR	Synthetic Aperture Radar
SARIn	SAR Interferometry
SEC	Surface Elevation Changes
SMB	Surface Mass Balance
STD	Standard deviation
SPOT	Satellite Pour l'Observation de la Terre
TEC	Total Electron Content
TeS	Trailing edge Slope
XO	Cross-over

Contents

List of Figures	v
List of Tables	vii
1 Introduction	1
1.1 Structure of dissertation	5
2 Theory of altimeter measurements	7
2.1 The principle of radar altimetry	7
2.1.1 Waveform analyses and retracking	8
2.1.2 Error sources	13
2.2 The principle of airborne and spaceborne laser data	17
2.2.1 Waveform analyses and retracking	18
2.2.2 Error sources	20
2.3 Pulse- vs. beam-limited altimetry	22
2.4 Laser versus radar altimetry	25
2.5 Radar altimetry	27
2.5.1 Envisat	28
2.5.2 CryoSat-2	31
2.6 Airborne and spaceborne laser data	34
2.6.1 ICESat	34
2.7 Airborne laser-scanning observations	35
I Optimizing ice sheet-wide surface elevation change detection	37
3 Background and motivation	38
3.1 Methods for surface elevation change detection	42
4 The Round Robin exercise	45

CONTENTS

4.1	Main conclusions	45
4.2	Lessons learned	46
5	Perspectives and future work	48
 II A Digital Elevation Model of the Greenland Ice Sheet		51
6	Background and motivation	52
6.1	Observations	55
6.2	DEM conceptual algorithm and validation description	57
7	Discussion	58
7.1	Reasoning for including laser altimetry data	58
7.2	Selection of spatial interpolation technique: Collocation	59
7.3	Reasoning for including an external DEM	61
7.4	Comparison of RL-DEM with CryoSat-only model	69
8	Relocation of conventional radar altimetry data	74
8.1	Methodology	74
8.2	Results and outlook	75
9	Outlook and conclusions	80
 III ECV production and outlook		83
10	The first Envisat RT results	84
11	The first merged RT and XO results	87
12	Relocation methods' impact on volume changes	90
13	Perspectives and future work	95

CONTENTS

14 ECV parameters for surface change detection	97
15 Outlook and conclusions	102
Bibliography	105
A Derivation of method for Greenland Ice Sheet elevation change detection	118
B Envisat derived elevation changes of the Greenland Ice Sheet	144
C A Digital Elevation Model of the Greenland Ice Sheet	152
D Relocation of radar altimetry data over ice sheets	182
E Posters	191
E.1 Inter-comparison exercise of surface elevation changes by Jakobshavn Isbræ	191
E.2 A digital elevation model of the Greenland Ice Sheet	191
E.3 A digital elevation model of the Greenland Ice Sheet	191
E.4 Improving maps of ice sheet surface elevation changes	191
F Written contributions	197
G Least-squares collocation	200
G.1 Implementation	201
G.2 Advantages	203

CONTENTS

List of Figures

2.1	Altimetry principle	9
2.2	Radar altimetry over oceans	11
2.3	Retracking of radar altimetry data: Range correction	11
2.4	ICE-1 retracker	12
2.5	Envisat waveform parameters from the ICE-2 retracker	13
2.6	Slope-induced error	15
2.7	ICESat waveform	19
2.8	Gaussian-Centroid offset	21
2.9	Beam-limited footprint	23
2.10	Pulse-limited footprint	24
2.11	Envisat	29
2.12	CryoSat	32
2.13	ICESat	34
2.14	ATM repeat surveys	36
3.1	Round robin results: Surface elevation changes	40
3.2	Round robin results: Surface elevation change errors	41
3.3	Principle for surface elevation change detection	44
3.4	Good/ bad spatial distribution of repeated ground-tracks	44
7.1	Location of validation data	63
7.2	DEMs built with/without external elevation model	65
7.3	Radar and laser data locations for DEM development	66
7.4	CryoSat-2 DEM from 2012	71
8.1	Location of radar and laser data	75
8.2	Test of slope correction methods	78
8.3	Test of slope correction methods	79
10.1	Comparison between ICESat and Envisat RT SEC results from 2003 – 2009	85

LIST OF FIGURES

11.1 Preliminary merged RT and XO SEC results and corresponding errors	89
12.1 Original position of XO and RT solutions for the period 2006 – 2010	91
12.2 Relocated position of XO and RT solutions for the period 2006 – 2010	91
12.3 Original position of XO and RT solutions from 2006 – 2010 overlain surface elevation changes from 2007 – 2008	94
14.1 Change in ice velocities over Jakobshavn Isbræ	99
14.2 Change in surface elevation changes over Jakobshavn Isbræ . . .	100
14.3 Calving front locations over Jakobshavn Isbræ	101
G.1 Covariances and semi-variogram	202

List of Tables

2.1	Strengths and weaknesses of airborne and spaceborne laser and radar altimetry	25
2.2	Pulse-limited footprint info for Envisat	29
2.3	Envisat facts	30
2.4	CryoSat-2 facts	33
2.5	Information on airborne laser-scanner flights	35
7.1	Input values to collocation	60
7.2	Validation of the DEM against 2011 CryoVEx and ATM data	67
7.3	Validation of DEMs against CryoVEx and ATM data	68
7.5	Validation of CryoSat-2 DEM against 2011 CryoVEx and ATM data	73
12.1	Volume change estimates from 2006 – 2010 for differently re-located XO and RT solutions	92

LIST OF TABLES

1 Introduction

As the climate is changing, it is becoming increasingly important to gain an understanding of the extent to which this is happening. In order to do so, the European Space Agency has launched the Climate Change Initiative (ESA CCI) in which scientists and space agencies across Europe collaborate on 13 different essential climate variables (ECVs). Examples are ice sheets, sea ice, ocean color, and ozone ([European Space Agency, 2011a](#)). This work is part of the Ice Sheets CCI and the geographical area in focus is the Greenland Ice Sheet (GrIS).

The GrIS is the largest ice mass in the northern hemisphere. In the recent decades it has been subject to a large variability in mass balance, ice thickness, ice velocities, etc. E.g. [Sasgen et al. \(2012\)](#) and [Shepherd et al. \(2012\)](#) have considered the mass balance and, by comparing observations from different sensors, found an overall mass loss for the period 1992 – 2011. Both groups used data from the Gravity Recovery and Climate Experiment (GRACE), laser altimetry (LA) from the Ice, Cloud, and land elevation Satellite (ICESat), and surface mass balance minus discharge (SMB–D) estimates obtained using, e.g., the regional climate model RACMO2/GR and ice thicknesses from airborne radar data. [Sasgen et al. \(2012\)](#) focused on the period 2003 – 2009 and found that GRACE revealed a mass loss of $238 \pm 29 \text{ Gt yr}^{-1}$, ICESat $245 \pm 28 \text{ Gt yr}^{-1}$, and SMB–D $260 \pm 53 \text{ Gt yr}^{-1}$. [Shepherd et al. \(2012\)](#) found a combined mass loss of $142 \pm 49 \text{ Gt yr}^{-1}$ for the period 1992 – 2011, a trend, which increased to $263 \pm 30 \text{ Gt yr}^{-1}$ for the years 2005 – 2010. These numbers indicate a change in trends and thus that more work is needed in order to fully understand the changes.

In the Ice Sheets CCI, four parameters are to be derived, each resulting in a dataset made publicly available by ESA: Surface elevation changes (SEC), ice velocities, grounding line locations, and calving front positions. This Ph.D. study is related to the SEC product.

The aim is to use the more than two decades of available ESA radar altimetry (RA) data to produce a long-term time series of SEC starting in 1992. This is motivated by ESA having finished the REprocessing of Altimeter Products for European Remote Sensing (REAPER) project and releasing the ERS data in September 2014. The reprocessed data contain significant improvements relative to previous datasets, due to the application of Envisat RA-2 retrackerers, reprocessed Precise Orbit Solutions, improved ionospheric corrections, etc.

This has brought clear improvements in both the ocean (OPR) and waveform products (WAP) (European Space Agency, 2014a,d). The final SEC product derived in the CCI project will consist of observations from ERS-1 and -2, Envisat, CryoSat-2, and, in the future, Sentinel-3. The observation period starts with the ERS-1 Phase C in April 1992, and five-year running means are produced from 1992 – 1996, 1993 – 1997, and so forth. They will be provided as 5×5 km grids (Sørensen, 2012).

SEC estimates are typically derived using one of two methods: As repeat-tracks (RT; Sørensen et al. (2011)) in which the changes are found along repeated satellite ground-tracks, or cross-overs (XO; Khvorostovsky (2012)) where intersecting ground-tracks from ascending and descending orbits are exploited. One goal of this work is to assess whether the application of one of these methods, or a combination, provides the optimal method for an ice sheet-wide SEC detection from RA. The most accurate results are achieved when combining estimates from both methods relative to their respective errors. This allows for exploiting the high spatial coverage of RT data and the high accuracy of XO where slope effects due to the terrain largely can be ignored. The first ice sheet-wide RT results for the GrIS are derived from Envisat and presented by Sørensen et al. (2015).

The best-performing RA SEC solution was found after conducting a so-called Round Robin (RR) exercise (Part I). In this, the scientific community was asked to submit their best SEC estimate for a selected region using either Envisat or ICESat data. The region of interest was the highly dynamic Jakobshavn Isbræ drainage basin. Both datasets were included due to the few radar-based SEC solutions published for the GrIS, as well as their strengths and weaknesses: RA echoes are subject to e.g. surface penetration into the subsurface as well as slope-induced errors resulting from footprint diameters as high as 36 km (Envisat). Thus, topographic changes over the overflown region will shift the reflecting point from nadir to the Point of Closest Approach (POCA). This rectifies the measurement location, and for Envisat relocations can be as large as 18 km (Brenner et al., 1983; Hurkmans et al., 2012). LA echoes, with a shorter wavelength, measure the exact surface elevation. Furthermore, their footprints range from one to 60 m meaning that relocation errors are negligible. However, such observations are discontinuous in time due to limitations in flight costs (airborne) and the period of active lasers (ICESat), as well as a lack of penetration through thick clouds (Abdalati et al., 2010; Brenner et al., 1983, 2007; Ridley and Partington, 1988).

The methodology for the SEC derivation was decided upon by the RR participants, and ten submissions formed the basis for thorough inter-comparisons across RA vs. LA and RT vs. XO. Validation was conducted with airborne laser-scanner data acquired with the National Aeronautic and Space Administration's Airborne Topographic Mapper (NASA ATM) and in ESA's CryoSat Validation Experiment (CryoVEx) campaign. This located the largest RA-LA discrepancies over the ice margin, where surface topography may distort the signal and attribute the highest errors to RA data. RT performed better in the sense of a higher spatial coverage, although interpolation of the point measurements to a mean ground-track led to topography-induced errors. Such errors are ignored in XO due to the exploitation of overlapping ground-tracks. In spite of RA's larger errors, the validation showed such data to be capable of accurately resolving ice sheet-wide SEC estimates thereby illustrating a good potential for the final CCI SEC production ([Levinsen et al., 2015a](#); [Scharrer et al., 2013](#)).

In SEC analyses, it is important to correct for topography-induced errors depending on the altimeter and method: The aforementioned topography in-between ground-tracks (RT: LA + RA) as well as slope-induced errors (RT + XO: RA). Both effects can be corrected for using a Digital Elevation Model (DEM), as is e.g. done by [Qi and Braun \(2013\)](#) in a RT analysis of ICESat data.

Several GrIS DEMs exist, e.g. those by [Bamber et al. \(2001\)](#); [DiMarzio \(2007\)](#); [Helm et al. \(2014\)](#) and [Howat et al. \(2014\)](#). All models are based on either data from the 1980s and 1990s, a few or solely one year of data from one sensor, or approximately a decade of observations from various sensors. Parts I and III as well as [Zwally et al. \(2005\)](#) document not only significant but also spatially varying SEC trends during most of the applied data acquisition periods; these translate into errors in the respective DEMs. Combined with a limited spatial and temporal data coverage, or errors in input data, it is important to develop an updated DEM in order to continuously map surface changes relative to an accurate topography. Acknowledging such a need, a new DEM is built here (Part II). It is based on contemporary Envisat and CryoSat-2 RA from 2010 merged with ICESat, ATM, and Land, Vegetation, and Ice Sensor (LVIS) laser data agreeing in time and space. It is referred to as the RL-DEM. ATM and LVIS data are acquired in 2010, while additional ICESat, ATM, and LVIS data from 2009 are included after scaling them to 2010. The scaling is done by accounting for the intermediate elevation changes, as will be further explained later on. The result is an increased spatial data coverage and, there-

fore, RL-DEM accuracy. Vertical errors in RA data due to surface penetration are corrected using LA data. Horizontal errors from slope effects are accounted for by relocating RA data to the POCA as seen from the satellite. The final RL-DEM is developed by merging the corrected RA data with LA data.

CryoSat-2 operates in two modes over the GrIS: A Low Resolution Mode (LRM) in the interior and a Synthetic Aperture Radar Interferometry (SARIn) mode over the steep margins. The LRM is a conventional altimeter such as that on-board Envisat. Due to very similar flight altitudes and bandwidths for the two altimeters, the footprints are roughly the same size. Footprints in the SARIn mode have the same across-track resolution as in LRM while the along-track resolution is approximately 300 m. The technique and smaller footprint of the SARIn mode allow for denser and more accurate measurements than those achieved with previous RA altimeters. As only four months of CryoSat-2 data were available at the time the RL-DEM was developed, the combination of contemporary RA data is advantageous. The merging with LA data yields a DEM based on a large spatial data coverage and referenced to a specific epoch in time, namely 2010.

The RL-DEM will be provided in two projections, both referred to the WGS-84 ellipsoid: a 2×2 km equi-distant grid in Polar Stereographic format as well as an equi-angular map with a spatial resolution of $0.02^\circ\text{lat} \times 0.05^\circ\text{lon}$ (WGS-84). The temporal and spatial specifications supporting the RL-DEM development provides the model with a strong advantage over previous ones with similar resolutions (Bamber et al., 2001; Helm et al., 2014). The 2×2 km resolution makes the RL-DEM suitable for application in ice sheet-wide SEC analyses (Part I) as well as for relocating conventional RA data. The latter is documented through thorough analyses of relocation methods applied to Envisat and CryoSat-2 LRM data near Jakobshavn Isbræ (Appendix D). Currently, the majority of studies dealing with RA data over ice sheets do not dedicate particular attention to the relocation method used. A key conclusion of this study is that this needs to change, as the accuracy of the relocation is highly dependent on the applied method and spatial resolution of the a-priori surface topography. Validation against ATM shows the preferred solution for both datasets to be the POCA method using the Howat et al. (2014) Greenland Ice Mapping Project (GIMP) DEM regridded to a 2×2 km resolution for topography. This resolution thus is applicable over both the steep margin and smooth ice sheet interior. Further results using the POCA with the GIMP at 500 m indicate that the radar cannot resolve surface features at this horizontal scale over regions with a complex topography. A great number of studies use

RA data to derive surface elevation changes and interpolated volume- or mass changes (Helm et al., 2014; Li and Davis, 2008; Sørensen et al., 2015; Zwally et al., 2005, 2011). Therefore, care must be taken when relocating the observations as error associated with the technique will reduce the accuracy of the sought output.

The focus of the final part of this study builds upon the conclusions and ideas arisen from the first two. This regards a presentation of the first RT results developed from Envisat data (2002 – 2010) as well as a comparison with a SEC trend from ICESat data to explore and try to explain observed SEC differences. The comparison covers the period 2003 – 2009 during which both sensors were operational. It is followed by preliminary merged RT and XO SEC results for the period 2006 – 2010 and an analysis of how the choice of relocation method impacts volume changes inferred from the separate RT and XO data. This highlights not only the influence of the relocation method, but also the uncertainties related to volume changes' dependence on the amount and spatial distribution of input data. Finally, ideas are presented for future work to further our understanding of the physical signal inherent in radar data, and how the estimated SEC values may be used in conjunction with another ECV parameter, namely ice velocities.

1.1 Structure of dissertation

As described above, this Ph.D. study focuses on the GrIS. The work is split up into different parts, which is reflected in the structure of the dissertation: Firstly, the RR exercise is described in which an inter-comparison of ten SEC datasets over Jakobshavn Isbræ is carried out across the choice of altimeter and method. The resulting conclusions form the basis for finding the best-performing method for an ice sheet-wide SEC detection from RA. With the newly released REAPER data, the conclusions set the foundation for developing a continuous, long-term time series starting in 1992.

Conducting such an analysis using the RT method may require a DEM to correct for the surface topography. Hence, the second part describes the development of such a model from combined Envisat and CryoSat-2 RA and ICESat, ATM, and LVIS LA data; the RL-DEM. The reference epoch is 2010 and the spatial resolution is 2×2 km. Thus, the RL-DEM is useful for accurately correcting concurrent RA observations for surface topography, as in RT analyses, and for relocating the observations due to slope-induced errors. Finally, the last part presents results that have come out of the first two analyses as well

1.1 STRUCTURE OF DISSERTATION

as ideas for future work.

The basis for the first two parts relates to publications, and therefore reading of the journal papers prior to the corresponding sections is recommended. This provides the reader with a thorough understanding of the underlying work and thus a better understanding of the respective discussions. All publications and posters related to the Ph.D. study are included in Appendices [A](#) to [E](#).

2 Theory of altimeter measurements

In remote sensing, altimetry is used for estimating the elevation of a target surface such as oceans, sea ice, or land ice. In this work, both LA and RA data have been used, acquired in airborne and spaceborne campaigns, respectively. The RA observations stem from ESA's Envisat and CryoSat-2, while the spaceborne LA data are from NASA's ICESat ([European Space Agency, 2006, 2012](#); [Zwally et al., 2014](#)). The airborne laser-scanner data are acquired with NASA's ATM and LVIS instruments, as well as during ESA's CryoVEx campaign ([Blair and Hofton, 2012](#); [Krabill, 2012](#); [Skourup et al., 2011](#)). The airborne campaigns are conducted on a (semi-)annual basis starting in 1993, 1997, and 2003, respectively, while Envisat operated from 2002 – 2012 and ICESat from 2003 – 2009; CryoSat-2 was launched in 2010 and is still operational.

In the following, descriptions will be given of the principles behind measurements from the two types of sensors. This regards waveform analyses and retracking to retrieve the surface height, and the corrections necessary to apply hereto to ensure a reliable estimate. It is followed by an overview of the strengths and weaknesses connected to the datasets, thus clarifying the use of various combinations hereof in parts of this study. In all cases, the goal is to maximize the accuracy of the output in terms of spatial data coverage and minimum errors. Finally, each dataset is described, and details regarding the satellite orbit and measurement characteristics are provided.

More specifically, this section first introduces the concepts of RA and LA. A number of differences between the datasets exist, which are caused by different orbit altitudes, footprints, and measurement characteristics. This is described in detail to provide the reader with a thorough understanding of the observations involved in the study.

2.1 The principle of radar altimetry

The principle for height estimation from radar altimetry is based on the emission of an electromagnetic pulse to the surface and the two-way travel time from emission until the return echo by is received by the target. The energy of the return echo comprises the so-called waveform, and will be discussed in further detail in Section 2.1.1.

Fig. 2.1 demonstrates the concept. The elevation, H , above a given refer-

ence surface is given by the satellite altitude, S , minus the range, R_{corr} , i.e. (Fu and Cazenave, 2001):

$$H = S - R_{\text{corr}} \quad (2.1)$$

The reference surface is typically the ellipsoid. The satellite position and altitude are determined using a highly accurate precise orbit determination (POD) system such as the Global Positioning System (GPS) or the Doppler Orbit and Radio positioning Integration by Satellite (DORIS). In order to obtain the true range, it is necessary to correct for both geophysical and instrumental errors as well as the atmospheric index of refraction, n . As n is higher in the atmosphere than in vacuum, the velocity of the signal, v , is lowered, which increases the travel time. Thus,

$$\begin{aligned} R_{\text{corr}} &= R - \sum_j \Delta R_j \\ &= \frac{c t}{n} - \sum_j \Delta R_j \end{aligned}$$

where $R = R_0/n$ is the range from the satellite center of mass to the surface during the travel time t , c the speed of light ($299,792.458 \text{ km s}^{-1}$), $n = c/v$, and $\sum_j \Delta R_j$ the sum of the corrections. For land ice, which is considered in this work, the geophysical corrections arise from the:

1. Dry and wet troposphere,
2. Ionosphere,
3. Solid Earth tide,
4. Ocean loading tide,
5. Geocentric polar tide,

Examples of instrumental corrections are Doppler shifts of the echo, drifts of the on-board ultra-stable oscillators used for accurately converting the instrument time into e.g. UTC, and shifts of the satellite center of gravity (European Space Agency, 2006, 2012; Fu and Cazenave, 2001).

2.1.1 Waveform analyses and retracking

As mentioned above, altimetry is based on the emission and reception of electromagnetic pulses. The energy of the return signal gives the waveform, the shape of which depends on the reflecting surface. The range estimate is derived

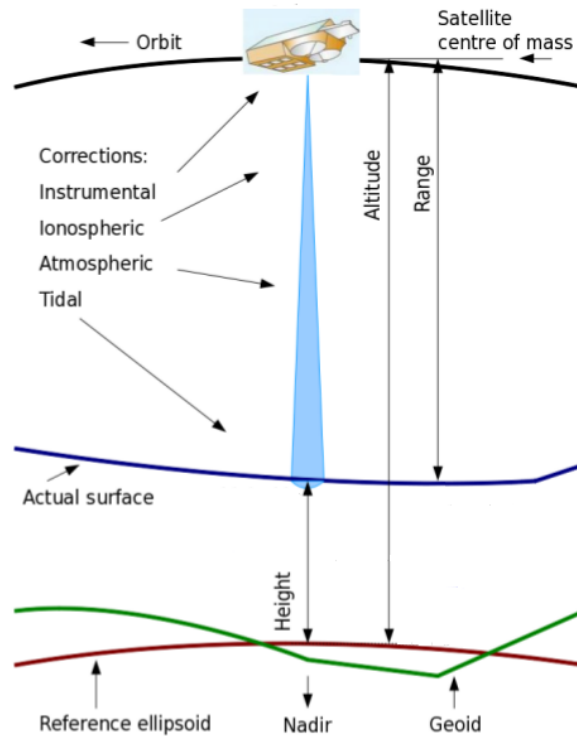


Figure 2.1 Principle of range measurements from spaceborne altimetry data (adapted from: [European Space Agency \(2012\)](#)).

by tracking, i.e. fitting a function to, the waveform twice. First, an on-board tracker filters the return signal into bins, providing a rough estimate of the surface characteristics within the range window. For Envisat, the number of bins is 128 meaning that each Ku-band waveform is composed of 128 samples. Secondly, an on-ground retracking is conducted to eliminate potential errors from a rough surface topography. This corrects the range by determining the offset between the center of the on-board range gate window, i.e. the point in which the range is determined, and the tracking point on the waveform. In case of topography, the latter may be offset by a number of range bins. An illustration of the retracking correction is provided later on in Fig. 2.3. Interrupted measurements may occur in case of rapid changes in the surface elevation: The on-board tracking anticipates the surface type at time $t = t + 1$ based on a brief processing of the signals received at times t , $t - 1$, $t - 2$, etc. Therefore, large topographic changes occurring at $t = t + 1$ results in the tracking function being unable to adjust and to lose lock. No data are acquired until the tracker once again has found a signal and locked onto it ([European Space Agency](#),

2011d; Ridley and Partington, 1988).

Retracking increases the precision of the range estimate and can be carried out in different ways. It is, however, out of the scope of this study to thoroughly analyze and compare different methods. Therefore, the following provides a description of both the temporal evolution of radar waveforms as well as which parameters can be extracted during retracking. The ICE-1 and ICE-2 retrackerers are introduced as both are used in the respective Ph.D. study. This provides a good understanding of how elevation estimates arrive and what information is inherent in the signals for use in further studies.

Fig. 2.2 illustrates the temporal evolution of a waveform from RA data over a horizontal, flat, and diffuse ocean surface. This is used for describing the situation over an idealized ice sheet surface. It is followed by an example of a GrIS echo as well as a description of how the waveform shape changes depending on the surface.

When a pulse is transmitted, it expands into a spherical shell until it intercepts the closest surface (T_0); in this case at nadir. The interception corresponds to the leading edge on the waveform. A circular region is illuminated, the area growing linearly in time, and forming what is known as the footprint. Backscatter of the signal occurs and part of the signal is reflected back to the satellite. The footprint area continues to grow until the back of the pulse intercepts the surface (T_1). This denotes the peak of the waveform, and the corresponding illuminated area is referred to as the pulse-limited footprint (PLF). The size of the PLF therefore depends on the leading edge width (LeW), which again depends on the characteristics of the illuminated surface. The trailing edge of the waveform follows after the peak and reflects echoes from points away from nadir. After the intersection of the entire pulse (T_2), the footprint continuously grows into an expanding annulus, and the waveform is attenuated by the antenna beam pattern (Fu and Cazenave, 2001; Ridley and Partington, 1988).

Over ice sheets, the situation is not as simple; the surface may be subject to changes in e.g. reflectivity, slope, and roughness within the illuminated area, all of which affect the waveform shape. The particular shape is modeled in the retracking procedure to correct for range errors due to deviations between the leading edge of the return waveform and the on-board altimeter tracking gate (Fig. 2.3).

The ICE-1 retracker is a so-called offset center of gravity (OCOG) module (Wingham et al., 1986), applied to ice sheet echoes from ERS (Bamber, 1994) and, in this study, Envisat (Section 11). It uses all samples in a waveform to

2.1 THE PRINCIPLE OF RADAR ALTIMETRY

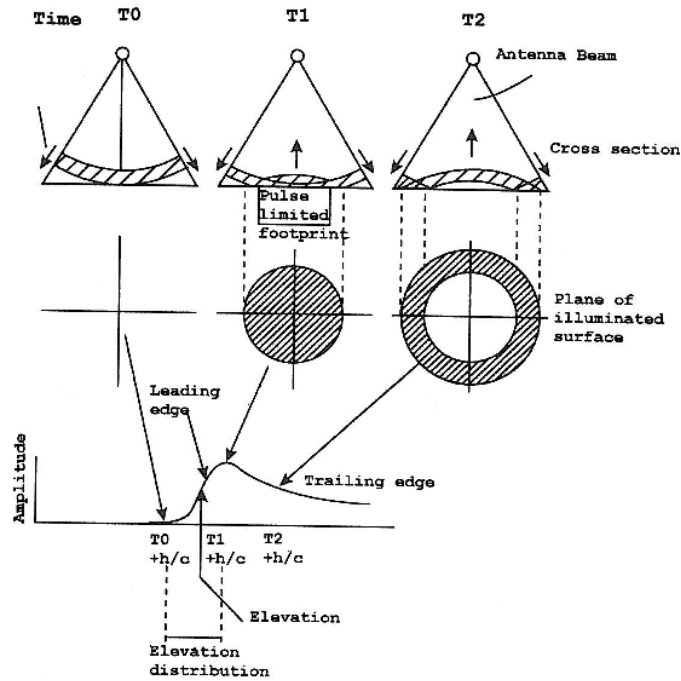


Figure 2.2 The development of a radar pulse over a planar and horizontal ocean surface (Ridley and Partington, 1988).

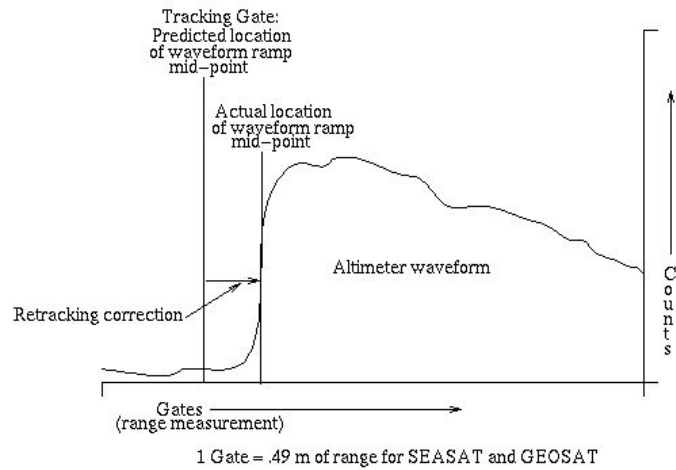


Figure 2.3 Range correction derived during retracking as the leading edge of the return waveform, and thereby the tracking point, is offset from the on-board altimeter tracking gate (National Aeronautics and Space Administration, 2014).

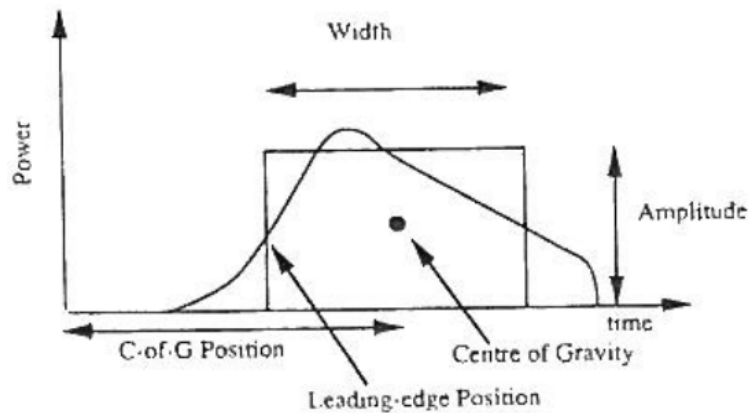


Figure 2.4 Illustration of the principle behind the ICE-1 retracker. It uses the Offset Center of Gravity and the width of a surrounding rectangular box to obtain the tracking point (Bamber, 1994).

estimate the COG and width of a rectangular box (Fig. 2.4). The amplitude of the box is given as twice the height of the COG, while the width is estimated from the waveform samples' values. The range estimate, i.e. tracking point, is found as the COG location minus the half-width. An important output parameter is the backscatter coefficient (Bs) (Bamber, 1994; Wingham et al., 1986).

The ICE-2 algorithm is based on the Brown (1977) waveform fitting (Legresy et al., 2005). The Brown model describes the return power from a rough surface as a convolution of the antenna gain, backscatter, and the range from the radar to the surface. The retracker uses all observations to find the waveform edge, and fit an error function to the leading edge and an exponentially decreasing function to the trailing edge. In Fig. 2.5, the original waveform is seen in blue and the retracked one in yellow. The figure illustrates the outputs of the retracker: The leading edge amplitude and width, the Bs, and the trailing edge slope (TeS). The tracking point corresponds to the half-power point on the leading edge.

As mentioned, the waveform parameters can be used to analyze the surface roughness (Legresy et al., 2005): The leading edge corresponds to the first interception of a radar echo with the surface, and hence a low LeW indicates little surface roughness, often associated with little accumulation and typical for the high-altitude, interior GrIS. Towards the coast, the surface roughness increases due to e.g. larger accumulation rates, mountains, and ice streams, and so does the LeW. The backscatter is a function of the same parameters,

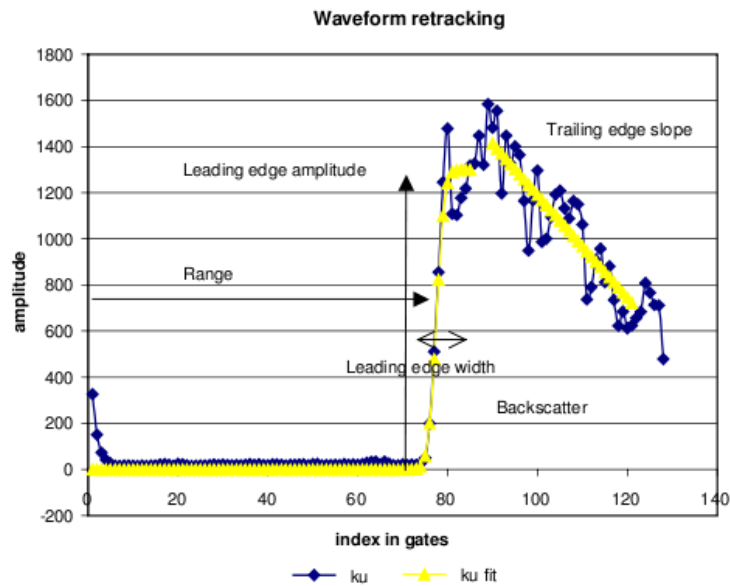


Figure 2.5 An Envisat waveform (blue) and the ICE-2 retracking fit hereto (yellow) from which the leading edge width, trailing edge slope, and backscatter coefficient can be extracted (Legresy et al., 2005).

although inversely proportional compared to the above: Bs is at a maximum in the interior because of the flat, smooth surface. Towards the coast, where surface slopes are larger, the energy received in the satellite is reduced, which lowers the Bs. The TeS relates to the off-nadir scatter received in the satellite. As the amount of this increases with the surface gradient, the highest, i.e. near-zero, TeS are found along the GrIS margin, while the values decrease inland (Legresy et al., 2005).

2.1.2 Error sources

Once the waveform has been analyzed and the range estimate retrieved, geophysical corrections need to be applied to the range. Then, knowing the satellite altitude, Eq. (2.1) can be used to deduct the surface elevation. The geophysical corrections account for range errors due to atmospheric conditions such as the amount of water vapour or the Total Electron Content (TEC), and Earth tides. The instrumental corrections have already been applied to data prior to their release and therefore are not a focus in the following. Instead, the section outlines the origin and order of magnitude of the corrections needed to be applied by the user, as well as describes an effect, which depends on

the texture of the snow/firn interface intersected by the radar echoes. The former regards atmospheric and tide-related effects as well as slope-induced errors due to topographic changes within the footprint; the latter concerns surface penetration of the radar echoes into the subsurface. Unless otherwise noted, the references used for the geophysical corrections are [European Space Agency \(2006, 2011c, 2012\)](#).

Troposphere

The troposphere is the lower part of the atmosphere and has a depth of approximately 10 km over the poles. It can be considered to consist of a wet and dry component, which have to be modeled independently.

The wet component reflects the liquid water content, which introduces a range error of up to 50 cm. The correction is modeled using humidity and temperature profiles from the European Centre for Medium-range Weather Forecasts (ECMWF) for both Envisat and CryoSat-2 data.

The dry correction results from the atmospheric dry gas component, taking into account the path delay from the atmosphere. This yields errors up to 2.3 m, i.e. a significant contribution. It is, however, nearly constant in time. Data from both satellites are corrected using ECMWF surface pressure profiles adjusted for the S1 and S2 (diurnal and semi-diurnal) tides.

Ionosphere

The ionosphere covers the upper part of the atmosphere from approximately 60 – 800 km altitude. This region is ionized, and its TEC varies over time, mostly due to solar activities. Examples of such are the daily cycle (very few free electrons during the night), changes between summer and winter, geomagnetic storms, and the 11-year sunspot cycle. The velocity with which the radar signals travel decreases with an increasing TEC. Since this is at a minimum over polar regions, typical errors here range from a few mm to 2 cm ([Brenner et al., 2007](#)).

The error is corrected for differently for the two satellites: For Envisat, daily Ku-band DORIS TEC maps are used, while CryoSat-2 data are adjusted using the Global Ionospheric Map (GIM) based on ionospheric data from GPS.

Solid Earth tide

This effect results from the deformation of the Earth's crust due to the Solar and Lunar gravitational attractions. It varies over the year with approximately 50 cm. Envisat data are corrected using the International Earth Rotation and Reference System Service (IERS) solid Earth tide model, while the Cartwright

model is applied to CryoSat-2 data (Cartwright and Taylor, 1971; International Earth Rotation and Reference Systems Service (IERS), 2014).

Ocean loading tide

Ocean loading tides result from the Solar and Lunar pull, and can perturb range estimates by several meters. It is modeled using the GOT00.2b model for Envisat and the FES2004 model for Cryosat-2 data (Cartwright et al., 1991; Lyard et al., 2006).

Geocentric polar tide

Small perturbations of the Earth's rotation axis, i.e. a polar motion, introduce a centrifugal force, which deforms the Earth's crust. It is a combination of the so-called Chandler wobble with a period of 433 days and another perturbation with a 369-day period. The total period is seven years. It introduces range errors of up to 2 cm and can be considered nearly constant for short observation periods. The correction for the two satellites is derived from historical pole location files.

Slope-induced errors

Typical radar footprints have radii ranging from 1 to 10 km, while topographic changes occur on spatial scales of m to km. Such changes will be reflected in the radar footprints. Cf. Brenner et al. (1983), a surface slope within the illuminated area will relocate the return signal from nadir to the POCA (Fig. 2.6). Thus, surface depressions such as the bottom of narrow outlet glaciers and troughs will be missed (Roemer et al., 2007). Furthermore, while the vertical error in, for instance, RT SEC estimates is assumed to cancel, the location representing the given estimate will be wrong.

The horizontal displacement from nadir can be assessed using the range and surface slope (denoted H and α , respectively, in Fig. 2.6) as:

$$D = H \times \sin(\alpha) \times \cos(\alpha) \tag{2.2}$$

where H is given in m and α in radians. Assuming small angles, the error in the measured range can be approximated by:

$$\begin{aligned} \Delta H &= H - H_m \\ &= \frac{H \times \alpha^2}{2} \end{aligned} \tag{2.3}$$

For a satellite altitude of 800 km, typical for Envisat, and a surface slope of 0.5° this yields $D = 7$ km and $\Delta H = 30$ m; slopes of 1° increase the errors to

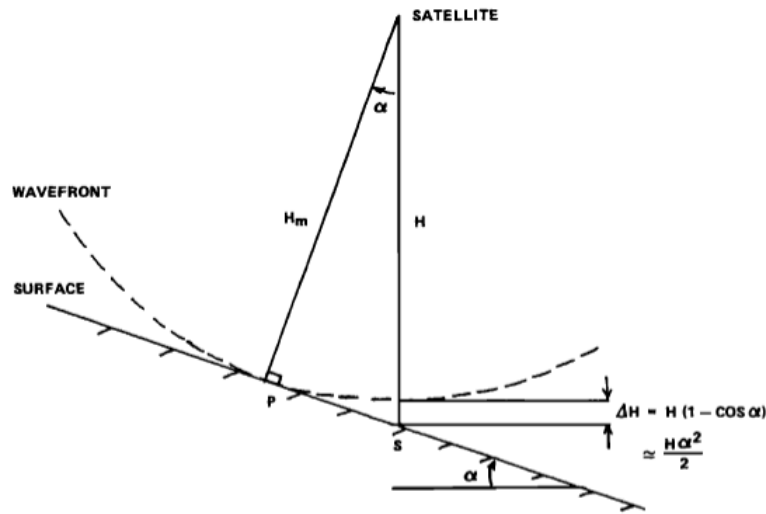


Figure 2.6 Slope-induced error in the radar echo as a surface slope, α , within the illuminated area shifts the reflecting point from nadir, S , to the Point of Closest Approach, P . The measured range is thereby H_m rather than H (Brenner et al., 1983).

$D = 14$ km and $\Delta H = 120$ m, respectively (Brenner et al., 1983; Hurkmans et al., 2012).

Slope-induced errors can be corrected for by e.g. adjusting the range estimate to nadir or by relocating the measurement location to the POCA; in any case, an a-priori model of the surface topography is needed, such as for deriving the surface slope and aspect. The topography may be extracted from a DEM. The study described in Section 8 compares two techniques for relocating the observations horizontally (Levinsen et al., 2015b). One of the methods is that described in Hurkmans et al. (2012), which relocates the observations using Eq. 2.4. The direction of the displacement is opposite the aspect, β . Given that $\beta = 0$ radians for north and increasing clockwise, the relocation vectors in the X and Y directions, dX and dY , are given as:

$$\begin{aligned} dX &= D \times \sin(\beta - \pi) \\ dY &= D \times \cos(\beta - \pi) \end{aligned} \tag{2.4}$$

Surface scatter, surface penetration, and volume scatter

Depending on the overflown region, radar echoes are subject to a certain amount of surface scatter, penetration into the subsurface, and volume scatter. Surface scatter predominates the shape of the return waveform over wet surfaces, as is typical over the ice sheet margins, while volume scatter dominates over drier regions such as the interior GrIS. The penetration depth can be derived from the extinction coefficient, which expresses the combined effect from absorption and scattering of the echoes. The former depends on the dielectric properties of the ice, derived using e.g. the radar frequency and temperature, while the latter depends on the number and radius of ice grains, the permittivity of free space and snow, etc. (Ridley and Partington, 1988).

The above explains why laser echoes, with a high frequency and thereby short wavelength, reflect off the surface, while radar echoes, with a longer wavelength, penetrate into the subsurface. Nghiem et al. (2005) found penetration depths for Ku-band data to exceed 1 m over the GrIS percolation zone, while Levinsen et al. (2015c) found the depths to vary between 1 and 4 m for points above 2000 m altitude (Appendix C). Sørensen et al. (2015) compared colocated ICESat and Envisat results (2003 – 2009) over the Equilibrium Line Altitude and found that effects such as penetration greatly affect RA-based SEC estimates (Appendix B). An example is an increased accumulation, which causes the physical surface to move upwards, as observed by ICESat; the lighter firn, however, increases the penetration depth, causing the reflecting layer to remain constant so Envisat measures a near-zero trend.

The effects from surface penetration and volume scatter can be reduced in two ways, either by measuring at times when the surface is wet, such as in the summer, or by using a threshold retracker: In ICE-2, the mean surface is estimated from the half-power (50%) position on the leading edge, whereas in a 10% threshold retracker, the volume part of the signal is reduced. As the volume part reflects the noisy nature of the waveform, the respective threshold increases the data accuracy (Davis, 1997; Ridley and Partington, 1988).

2.2 The principle of airborne and spaceborne laser data

As observations from both airborne and spaceborne campaigns are used in this thesis, a short introduction is given to the data types explaining their different nature. It is described how the height derivation differs from that for RA data, and an example of retracking of ICESat data is provided.

As in RA, laser echoes can be used to derive the elevation of a target surface.

Therefore, Eq. (2.1) still applies. However, due to different measurement characteristics for laser and radar campaigns, e.g. in terms of surface penetration and footprint size, the corrections inherent in R_{corr} need slight modifications. This will be clarified in Section 2.2.2 describing the error sources. One significant difference is that all laser data are corrected prior to their release. Hence, although new biases are discovered with time, e.g. the Gaussian-Centroid offset (Borsa et al., 2014), the user merely needs to perform an outlier rejection to ensure a high data accuracy.

2.2.1 Waveform analyses and retracking

An example of waveforms from ICESat data is given in Fig. 2.7. The top plot (a) shows the echo transmitted from the satellite and the bottom three return echoes from various surface types (b–d). An example of the retracking, based on the method applied to ICESat data, is described below (Yi et al., 2005; Zwally et al., 2002).

Observations over a flat, smooth surface, such as the interior GrIS, and no cloud cover increases the energy of the transmitted signal and saturates the waveform, resulting in a single, high peak (b). If instead a cloud cover is present, forward scattering occurs as the clouds scatter and attenuate the echoes. This distorts the shape of the waveform, giving it a long, asymmetric tail to the right (d). The two effects act to decrease and increase the measured elevation, respectively. In case of large surface slopes, such as along the GrIS margin, the waveform is broader and has more peaks (c). This may reflect multiple reflective surfaces within the footprint.

Cf. Fig. 2.7(a), the shape of a transmitted echo follows a Gaussian distribution. In case of small atmospheric effects and a Gaussian height distribution within a respective footprint, the return echo follows the same distribution. Therefore, ICESat data are retracked by fitting a Gaussian function to the two waveforms and extracting the two-way travel time from here (Zwally et al., 2002). The function is based on e.g. the number of peaks in the waveform, the respective amplitude(s), and the standard deviation (STD) of the peak(s). Cf. Section 2.2.2, the travel time is calculated from the centroid of the transmitted waveform to the center of the Gaussian fit to the return echo. This reduces effects from forward scattering, which would shift the centroid in time, and which have been proven to introduce errors of at least 1 m. The decision is therefore a compromise between reducing atmospheric effects in the waveforms and the introduction of Gaussian-Centroid errors, although on the cm-scale

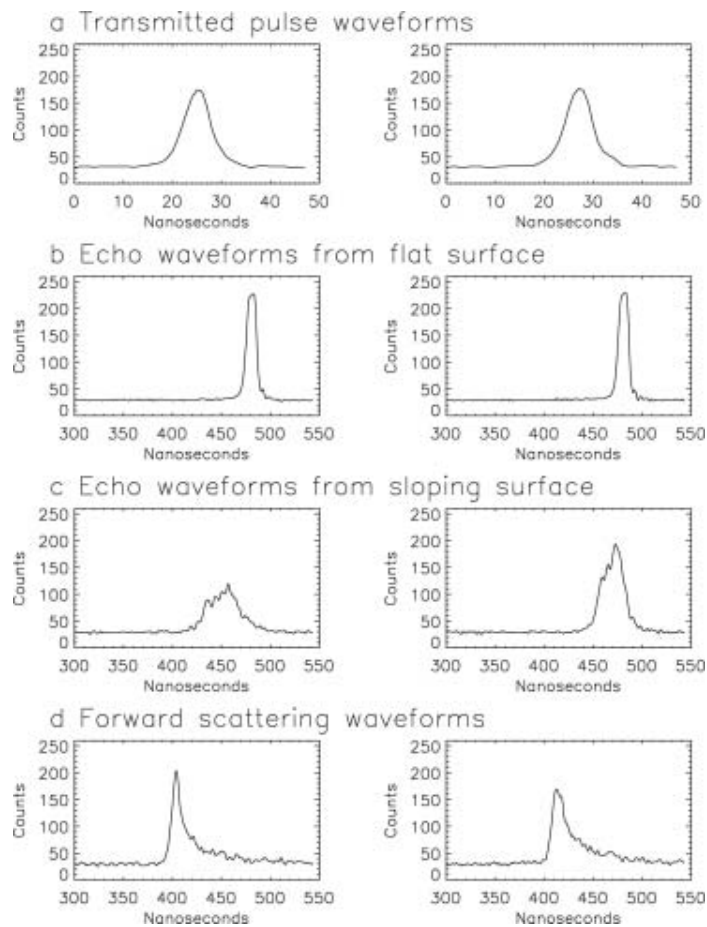


Figure 2.7 ICESat waveforms: The transmitted laser echo (top) and three return pulses over various surface types (Yi et al., 2005).

(Borsa et al., 2014); this is discussed in more detail in the section below. Having retracked the ICESat observations, data quality flags and waveform- and quality-related data rejection criteria can be applied to reduce systematic biases and remove problematic measurements, e.g. due to saturation of the echoes or topography within the footprint.

2.2.2 Error sources

Due to the different characteristics supporting each laser mission, the error sources for one mission may differ from that of another. For all missions, however, the troposphere adds a path delay, which must be accounted for, while the ionospheric delay either cancels or can be ignored due to the low flight altitude. The cancellation occurs due to the POD being carried out using GPS L1 and L2 carrier phases and pseudoranges, and the differencing of signals on the two frequencies removing any effects. The same is the case for satellite and receiver clock errors. The tropospheric error on ICESat data is approximately 2 cm, which is twice that for ATM (Krabill et al., 2002; Zwally et al., 2002).

For ICESat, POD techniques based on GPS data are used to determine the satellite position and altitude; errors herein are approximately 5 cm. Tides contribute with up to 1 cm. The largest error source arises from the precision of the pointing knowledge of the laser beam. Cf. Brenner et al. (2007) and Luthcke et al. (2005), this effect can be removed by modeling of Laser Reference System data and has been reduced to near-zero so potential range biases are nearly eliminated.

ICESat data are also affected by inter-campaign biases, which appear as range errors: Measurements are conducted using the on-board Geosciences Laser Altimeter System (GLAS) consisting of three lasers expected to have operated on a continuous basis. However, Laser 1 experienced a rapid energy decline shortly after launch and seized operation after 38 days. The remaining lasers were then switched on separately for two to three 33-day campaigns a year in order to maximize the science output for the remainder of the mission (Abshire et al., 2005). This introduced inter-campaign biases for measurements from different lasers, one of them being the Gaussian-Centroid offset in the processing of level 1 data (Borsa et al., 2014). When processing ICESat data (Section 2.2.1), two types of reference points are used (Fig. 2.8): The centroid of the waveform and the peak position of the Gaussian fit hereto. The corresponding time stamps for the transmitted and returned waveforms are then C_T , C_R and G_T , G_R , respectively. The travel time used for deriving the range estimate is given

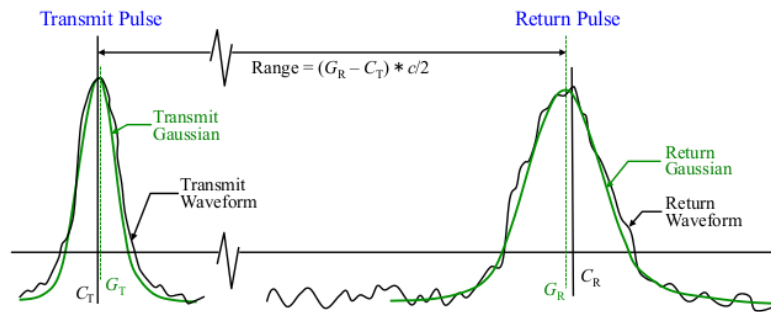


Figure 2.8 ICESat range derivation, with the transmitted and returned waveforms: Original (black) and the Gaussian fit hereto (green). The centroid positions, marking time stamps C_T and C_R , are given as solid black lines, while the dotted green lines indicate the peak positions of the Gaussian fits, G_T and G_R . Up until release R633, the time difference used for the range estimation was estimated as $T = G_R - C_T$, which introduced a range error corresponding to $G_T - C_T$ (Borsa et al., 2014).

as the respective time difference: Either $T = C_R - C_T$ or $T = G_R - G_T$. Either method yields similar results. Up until data release R633, however, the time difference of several datasets has been given as $T = G_R - C_T$, namely as a Gaussian-Centroid value. One of the datasets is the level 2 Antarctic and Greenland Ice Sheet Altimetry product (GLA12) used here. As the centroids and peak locations of the fits cannot be assumed to agree in time, this estimation of T introduces a range error corresponding to $G_T - C_T$. Cf. Borsa et al. (2014), the effect lowers the measured elevations by approximately 2 – 4 cm and SEC trends by 2 cm yr⁻¹.

The energy of the transmitted and received echoes varies depending on the presence of a cloud layer; this can be ignored with low-altitude flights thus giving an advantage to such. In case of a flat surface and no clouds, saturation of the return echo occurs, while a thin cloud layer will introduce forward scattering. This yields elevation errors on the order of cm to m (Brenner et al., 2007; Zwally et al., 2002). Fricker et al. (2005) derived a saturation correction for ICESat assuming no forward scattering and found that applying this to observations over the flat Bolivian Salar de Uyuni region reduced the root-mean-square (RMS) error between ICESat and GPS elevations from 4.9 cm to 3.2 cm and the elevation difference from -9.6 m to -1.9 cm. Mahesh et al. (2002) demonstrated that the forward scattering bias over Antarctica was typically below 1 m.

Errors in laser-scanner data arise from e.g. the pitch, roll, and yaw of the aircraft and instrument, as well as multi-path effects. The latter arises in case the direct path of the signal is blocked, which increases the travel time thus decreasing the final elevation estimate. The effect of the aircraft inertial navigation system pitch cancels when averaging and smoothing observations, while the roll introduces a cross-track error. Based on repeated 1993/1998 and 1994/1999 ATM flights, these effects contribute with SEC errors of no more than 1 cm yr^{-1} (Krabill et al., 2002).

2.3 Pulse- vs. beam-limited altimetry

In principle, two types of altimeters exist, namely the beam- and pulse-limited. Laser altimeters are beam-limited while most radar altimeters are pulse-limited. For the first type, the shape of the return echo depends on the width of the beam. The shape is illustrated in Fig. 2.7(b–d), while Fig. 2.9 demonstrates the principle behind estimating the footprint diameter. Given a satellite at altitude H , with an angular resolution θ_r , a frequency λ , and an antenna diameter D , the diameter of the respective footprint, D_s , can be estimated as:

$$\begin{aligned} D_s &= 2H \tan(\theta_r) = 2.44H \frac{\lambda}{D} \\ &= 2.44H \frac{c}{fD} \end{aligned} \tag{2.5}$$

where f denotes the frequency. This assumes a flat surface. The inverse relationship between D and D_s illustrates the disadvantage of beam-limited altimeters: Narrow beams require a large antenna, and due to spatial limitations on-board a satellite this introduces a physical constraint. The advantage is, however, that small ($\sim 1^\circ$) pointing errors away from nadir do not affect the range measurements significantly (Fu and Cazenave, 2001).

In pulse-limited altimetry, the return echo is limited by the length of the pulse. In conventional altimetry, as is the case for Envisat and CryoSat’s LRM mode, the footprint diameter depends on the satellite altitude and the compressed pulse length, τ . The concept is illustrated in Fig. 2.10, where:

$$\begin{aligned} r_p &= \text{Radius of the PLF} \\ l_p &= \text{Range resolution} \\ &= c\tau/2 \end{aligned} \tag{2.6}$$

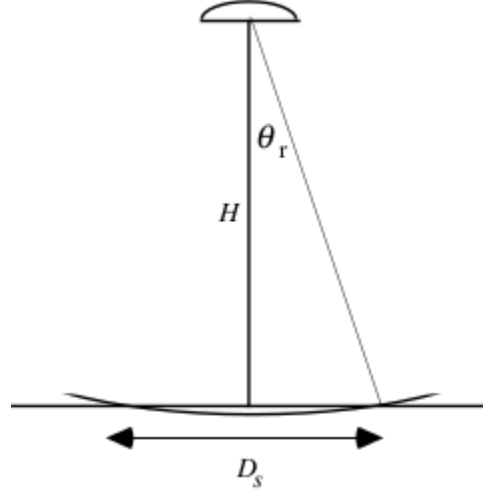


Figure 2.9 Beam-limited footprint of a circular aperture. It has the diameter, D_s , while the satellite altitude is H and the angular resolution is θ_r (Scripps Institution of Oceanography, University of San Diego).

The concept of pulse compression is described in the following: Pulse lengths of a few ns correspond to PLFs of a few km. Unfortunately, such a short pulse duration, described by the bandwidth, $B = 1/\tau$, requires a high transmission power, which reduces the lifetime of the system and risks conflicting with the satellite's power constraints. Increasing instead the pulse duration increases the range resolution and PLF thus decreasing the radar signal-to-noise ratio (SNR). None of this is feasible, and thus frequency-modulated pulses are used. In this case, the pulses are transmitted at one frequency and swept linearly to a lower frequency. Such pulses are referred to as "chirps". The specifics behind this technique are out of the scope of this study and therefore are not described in more detail here; in case of further interest for the topic, the reader is referred to Chelton et al. (1989); Fu and Cazenave (2001).

Based on the above and using trigonometry (Fig. 2.10), the radius of the PLF for a flat surface is given by:

$$\begin{aligned} r_p &= \sqrt{2Hl_p} = \sqrt{Hc\tau} \\ &= \sqrt{H \frac{c}{B}} \end{aligned} \quad (2.7)$$

Values for the above are provided for Envisat and CryoSat-2 data in Sections 2.5.1 and 2.5.2, respectively (European Space Agency, 2006, 2012; Fu and Cazenave, 2001).

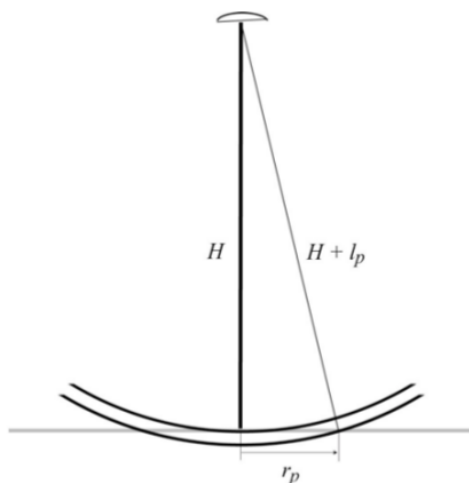


Figure 2.10 Radius of a pulse-limited footprint, r_p . It is illuminated when the trailing edge intersects the surface. l_p is the range resolution (Sandwell, 2011).

The above presents an idealized scenario over ice sheets where surface undulations exist. In such a case, a term representing the undulations, the Significant Wave Height (SWH), h_{SWH} , needs to be included. The corrected radius and compressed pulse length are (Sandwell, 2011):

$$\begin{aligned}
r_p^{\text{SWH}} &= \sqrt{Hc\tau_{\text{SWH}}}, \\
\tau_{\text{SWH}} &= \sqrt{\left(\frac{2l_p}{c}\right)^2 + \left(\frac{h_{\text{SWH}}}{c}\right)^2 \ln(2)} \\
&= \sqrt{\left(\frac{1}{B}\right)^2 + \left(\frac{h_{\text{SWH}}}{c}\right)^2 \ln(2)}
\end{aligned}$$

In general, $h_{\text{SWH}} = 4\Delta h$, i.e. four times the standard deviation from the surface height. The higher the value, the lower the quality of the measurements. Considering numbers typical for Envisat, i.e. $H = 800$ km and $B = 320$ MHz, a h_{SWH} of 2 m will result in $r_p = 0.85$ km and $r_p^{\text{SWH}} = 1.25$ km, i.e. a nearly 70% increase. In case of $h_{\text{SWH}} = 7$ m, the radius increases to 2.2 km. As surface undulations over the GrIS easily reach seven to ten meters (Bamber, 1994), the actual footprints here are significantly larger than the values estimated from Eq. (2.7).

2.4 Laser versus radar altimetry

Prior to introducing the applied datasets individually, differences between the data types are summarized to clarify the reasoning for the combinations. The main idea is that the strengths and weaknesses in one dataset compliment those of another to maximize the data accuracy and spatial resolution. Table 2.1 summarizes the respective pros and cons, and a brief description of each follows below.

Table 2.1 Strengths and weaknesses in the applied datasets, namely airborne and spaceborne laser data versus spaceborne radar altimetry.

Observation type	Strengths	Weaknesses
Radar altimetry	<ul style="list-style-type: none">– Continuous observations– Cloud penetration	<ul style="list-style-type: none">– Large footprint– Slope-induced errors– Losses lock– Surface penetration– Backscatter
Laser altimetry	<ul style="list-style-type: none">– High elevation accuracy– No slope-induced errors– No surface penetration– Maintains lock	<ul style="list-style-type: none">– Only penetrate optically thin clouds– Forward scattering from thin clouds– Saturation from high-energy returns– Discontinuous in time
Airborne laser	<ul style="list-style-type: none">– High elevation accuracy– No slope-induced errors– No surface penetration– Maintains track– Repeat flight lines	<ul style="list-style-type: none">– Limited to flight lines– Discontinuous in time

In 1991, ESA launched the first European Remote Sensing satellite, ERS-1, which marked the beginning of an era of continuous RA measurements from space. ERS-2 followed in 1995, seven years later came Envisat, and CryoSat-2 was launched in 2010. CryoSat-2 will be complimented by Sentinel-3 by late 2015. With repeat-cycles of 3 to 369 days, continuous observations of the Earth’s surface from 1991 until present are ensured. NASA’s ICESat operated from 2003 – 2009 and will be followed by its successor, ICESat-2, in 2017 ([European Space Agency, 2014b](#); [National Aeronautics and Space Administration, 2013](#); [Zwally et al., 2002](#)). The strength of RA is the capability of the radar signals to penetrate through the clouds thus measuring at a continuous rate.

This is unlike laser observations, which only penetrate optically thin clouds causing data gaps over regions with thick cloud cover. This is an issue over e.g. Southeast Greenland where the precipitation rates and cloud cover are at a maximum (Ettema et al., 2009).

Cf. Section 2.1.2, RA data are subject to slope-induced errors due to topographic variations within the large footprint. The narrow laser beam implies that such errors are not relevant in laser-based studies (Brenner et al., 1983; European Space Agency, 2006; Hurkmans et al., 2012; Krabill et al., 2002; Ridley and Partington, 1988; Zwally et al., 2002).

Once reaching the surface, the radar signal is subject to surface scattering and potentially subsurface volume scattering. The amount with which this happens depends on the physical properties of the subsurface. E.g. accumulation can increase the penetration depth so the reflecting surface seen by a radar is lowered. Instead, a laser, which is not subject to these effects, will observe an increase in the elevation. The laser will therefore see the physical surface, and the elevation difference between the reflective surfaces measured by the two altimeters will increase (Brenner et al., 2007; Ridley and Partington, 1988; Sørensen et al., 2015).

Laser altimeters can measure over the entire ice sheet, which is not the case for radar altimeters: Due to the larger radar footprint, topographic changes appear more abrupt than in laser echoes, which causes the on-board tracker to lose lock. Such a loss is not found in laser data. It can be accounted for by using a so-called open loop mode in which a DEM provides a priori knowledge of the surface topography. This has been used in the Poseidon-3 altimeter on-board ESA's Jason-2 (2008 – present) and will be used on-board Sentinel-3 (Aguirre et al., 2007; European Space Agency, 2011d).

Laser data are only acquired in the case of either no or thin clouds, and here saturation of the signal and forward scattering must be accounted for (Brenner et al., 2007; Yi et al., 2005). Cf. Section 2.2.1, this can be done during processing of the data.

Both airborne and spaceborne laser observations are limited in time. The former because they are confined to flight lines, which in turn are limited by logistics and costs, and the latter because of problems with the GLAS.

The strengths of the airborne laser campaigns correspond to those of the spaceborne. There is one clear difference, however, namely the ability to repeat previous flight lines due to an accurate tracking hereof using GPS and inertial

systems. This can ensure repeat passes over areas of particular interest: The ATM has been used to resurvey e.g. the Greenland outlet glaciers Jakobshavn Isbræ and Helheim several times thus allowing for an accurate SEC detection (Krabill et al., 2002; Milliman, 2014).

Many of the above reasons lead to the key difference between data from the two sensors: The elevation accuracy of laser data exceeds that of radar data. Laser observations have a cm-accuracy while comparisons of contemporary Envisat and ICESat data over Greenland show mean elevation differences of -9 ± 52 cm for surface slopes less than 0.1° ranging up to 2.7 ± 26 m for slopes up to 0.9° . LVIS data acquired one day apart revealed elevation differences for three nearly coincident tracks with means of 0.0 ± 0.11 m to 0.1 ± 0.6 m, respectively, while comparisons with the nearest ICESat campaign (L3I, separated three weeks in time) revealed differences from -0.02 ± 0.06 m to -0.09 ± 0.14 m, respectively. The LVIS-ICESat offsets likely reflect intermediate snowfall between the data acquisition periods. Compared to vertical errors in RA data, the offsets are, however, small (Brenner et al., 2007; Fricker et al., 2005; Hofton et al., 2008; Krabill et al., 2002).

Significant differences in the sensors' abilities to perform well both in time and space therefore exist.

2.5 Radar altimetry

The radar measurements used in this study are Ku-band data acquired with Envisat's RA-2 instrument and in CryoSat's LRM and SARIn modes. Envisat also measured in S-band, while CryoSat has an additional SAR mode. However, as none of these observations are used, they are not described in further detail below. Data from both sensors are downloaded directly from ESA via fast registration with Earth Online (European Space Agency, 2014c).

2.5.1 Envisat

On March 1st 2002, ESA launched Envisat (Fig. 2.11) into an 800 km, sun-synchronous orbit. It had a 35-day repeat cycle and reached latitudes of 82 degrees N/S. By late October 2010, the satellite was lowered by 17 km both to free the original orbit for other missions, as well as to extend Envisat's lifetime. This put the satellite into a drifting phase and reduced the repeat cycle to 30 days. Approximately 18 months later, on April 8th 2012, ESA lost contact with the satellite, which ended the ten year mission. The main objective with the mission was to ensure a data continuity from ERS; by following the same ground-tracks as ERS-2, the grounds were established for developing time series of ice sheet elevations and sea ice thicknesses, dynamic ocean circulation patterns, global and regional sea level changes, etc.

The measurements in this study are acquired with the "Radar Altimeter 2" (RA-2), which operated at two main frequencies: The Ku-band at 13.575 GHz and the S-band at 3.2 GHz; this corresponds to wavelengths of 2.2 cm and 9.3 cm, respectively. Incorporation of the latter allowed for in-situ corrections for ionospheric range delays. Envisat operated in three modes: The fine mode, with a bandwidth of 320 MHz, over oceans and most landmasses as well as the two coarser modes over moderate and rough terrain. Their bandwidths were 80 and 20 MHz, respectively. The on-board tracker decided whether the bandwidths should be increased or decreased based on the SNR of the waveform position relative to the values stored in the on-board memory. This ensured that the instrument remained locked and prevented uninterrupted measurements over regions with topographic changes. Using the three bandwidths to modulate the transmitted pulses, the corresponding compressed pulse lengths, range resolutions, and PLF diameters are given in Table 2.2. They are derived from Equations (2.6)–(2.7). The values for the three modes illustrate the strength of pulse compression: Increasing the bandwidth used to modulate the transmitted pulse minimizes the pulse length after the match filtering, which decreases the PLF; it should, however, be noted that the true footprints are presumably larger than the stated values.

Table 2.3 provides a number of facts for the mission, and it is clear that it used a Pulse Repetition Frequency (PRF) of 1.795 kHz, that the total number of samples of the waveform was 128, and that the antenna diameter was 1.2 m. Cf. Eq. (2.5), the characteristics resulted in beam-limited footprints with a diameter of approximately 36 km. Due to the orbit, the ground-track separation distance increased with a lower latitude. Hence, ground-tracks were separated by approximately 50 km at 60°N and 12 km at 80°. Finally, it should be re-

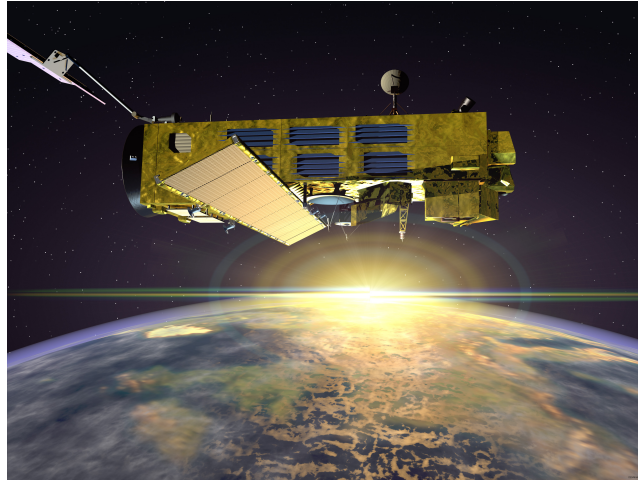


Figure 2.11 Envisat in orbit ([European Space Agency, 2001](#)).

Bandwidth [MHz]	Compressed pulse length [ns]	Range resolution [m]	PLF diameter [km]
320	3.1	0.5	1.7
80	12.5	1.9	3.5
20	50.0	7.5	6.9

Table 2.2 Bandwidths and calculated values for Envisat RA-2 pulse-limited footprints assuming a flat surface.

membered that unless otherwise noted, the range estimates are retracked with the ICE-2 model described in Section 2.1.1 ([European Space Agency, 2006, 2007](#); [Legresy et al., 2005](#)).

Parameter	Value
Mean altitude	800 km
Inclination	98.55°
Orbit	Sun-synchronous
Repeat-cycle	35 days
Orbits per cycle	501
Frequency	13.575 GHz
Wavelength	2.2 cm
Antenna beamwidth	1.3°
Antenna diameter	1.2 m
Beam-limited antenna footprint	36 km
PRF	1.795 kHz
Pulse width	20 μ s
Samples per echo	128

Table 2.3 Facts about the Envisat mission. As no data have been used after the lowering of the orbit in 2010, the numbers refer to the old orbit. Furthermore, only Ku-band measurements are used, and thus information regarding the S-band is not provided ([European Space Agency, 2006, 2011b](#)).

2.5.2 CryoSat-2

CryoSat-2 (Fig. 2.12(a)) was launched on April 8th 2010 with an expected lifetime of 3.5 years. This period has been exceeded, and the satellite is still operating continuously. The primary goal is to monitor thickness and mass changes of the Earth's marine and continental ice fields. This is done from a 730 km orbit covering the largest part of the northern and southern hemispheres to date, namely 88°N/S. The satellite has a repeat cycle of 369 days with a 30 day sub-cycle; facts about the mission are given in Table 2.4. Measurements are conducted with the SIRAL (SAR/Interferometric Radar Altimeter), which operates at Ku-band, and in three different modes depending on the surface type (Fig. 2.12(b)): The LRM, a SAR mode, and a SARIn mode.

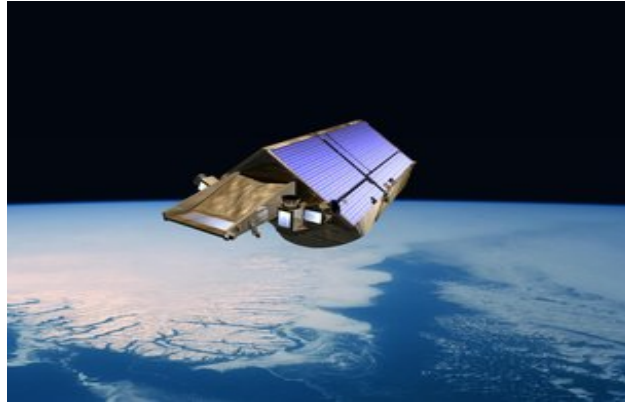
The LRM works as a conventional radar altimeter and is used over the interior ice sheet. Given a nearly similar altitude as Envisat and a bandwidth of 320 MHz, the diameter of the PLF is similar to that of Envisat's fine mode. Ground-tracks are separated by approximately 40 km at 66° and 15 km at 80°; the former boundary is further north than for Envisat due to the spatial confinement of the observations.

The SAR mode is used over sea ice, and data are processed using Doppler techniques to minimize the illuminated area on the surface in the along-track direction. Thus, small-scale topographic features such as floes and leads can be resolved. The Doppler processing allows for both detecting the direction of the arrival of surface echoes as well for measuring the respective time delay. Therefore, the footprint is defined independently in the two directions: The width in the across-track direction is similar to the pulse-limited value, while the along-track value is approximately 300 m. The latter is determined by the beam-limited area from the Doppler processing, which separates the return echoes into strips arranged across-track.

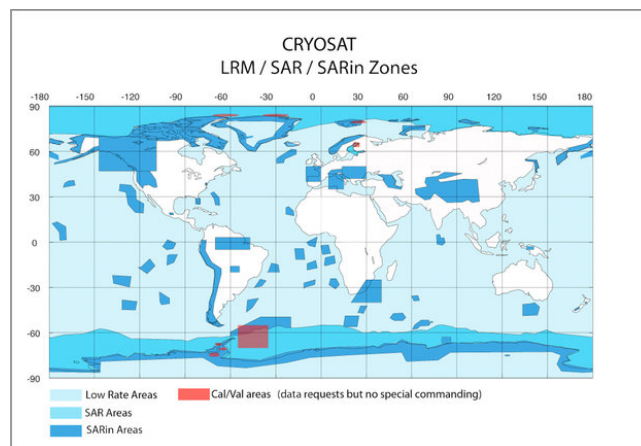
The SARIn mode combines SAR with interferometry by using not one but two antenna separated by 1 m. It is used over the margins. In case of surface slopes, return echoes will arrive in the antennae at different times, and the respective phase difference can be used to derive the exact location of the reflecting point. Hence, observations from this mode do not follow a repeat-track but rather the surface topography. One disadvantage is that the satellite might miss the bottom of troughs and narrow ice streams as the reflecting point is located somewhere up-slope from these. This is largely accounted for by increasing the PRF and samples per echo to allow for a denser detection of the surface. Combined with the smaller footprint, such data better accounts for the changing terrain than previous altimeters, which provides the observations

2.5 RADAR ALTIMETRY

with a strong advantage over sloping terrain ([Aresys, 2013](#); [European Space Agency, 2012](#); [Wingham et al., 2006](#)).



(a) In orbit



(b) Mode mask

Figure 2.12 CryoSat-2 in orbit (a) and the mask (b) incorporated in the altimeter to switch between operating modes relative to the type of surface below the satellite ([European Space Agency, 2003, 2010](#)).

Parameter	Value
Mean altitude	730 km
Inclination	92°
Orbit	Non sun-synchronous
Repeat-cycle	369 days with 30 day sub-cycle
Orbits per cycle	5,344
Frequency	13.575 GHz
Wavelength	2.2 cm
PRF	1.97 kHz (LRM), 18.181 kHz (SARIn)
Pulse width	44.8 μ s
Pulse bandwidth	320 MHz
Antenna beamwidth (3 dB)	1.06° along track \times 1.1992° across-track
Antenna diameter	Two reflectors: 1.2 \times 1.1 m
Beam-limited antenna footprint	33 km
Compressed pulse-length	3.125 ns
Range resolution	0.5 m
Samples per echo	128 (LRM), 512 (SARIn)

Table 2.4 Facts about the CryoSat-2 LRM and SARIn modes. Both data types are used in this study ([Aresys, 2013](#); [European Space Agency, 2012](#)).

2.6 Airborne and spaceborne laser data

The datasets described below are obtained from two different sources: All NASA data are downloaded through the National Snow and Ice Data Center (NSIDC) web-site ([Blair and Hofton, 2012](#); [Krabill, 2012](#); [Zwally et al., 2014](#)), while CryoVEx data are available in-house at DTU Space ([Skourup et al., 2011](#)).

2.6.1 ICESat

NASA's ICESat (Fig. 2.13) was launched on January 13th 2003 and operated until October 11th 2009. The main scientific purpose of the mission was the estimation of inter-annual and long-term elevation and mass balance changes of the polar ice sheets to increase our understanding of their contribution to a global sea level rise. Secondary purposes were the estimation of vertical cloud and aerosol structures, among others, which added an atmospheric aspect to the mission ([Zwally et al., 2002](#)).



Figure 2.13 ICESat in orbit ([National Snow and Ice Data Center, 2002](#)).

The satellite was launched into a 600 km orbit with an inclination angle of 94° . The satellite reaches latitudes of 86°N/S . Measurements were conducted with the GLAS consisting of three lasers, one operating at a time. Each laser emitted pulses with two wavelengths: 1024 nm (near-infrared) for altimetry and 532 nm (green) for the vertical distribution of clouds and aerosols. With an emission rate of 40 Hz, this created approximately 60 m footprints separated by 172 m along-track. Early on in the mission, an 8-day repeat cycle was implemented to obtain frequent repeats of calibration sites. Starting with Laser 2a, and thereby following the failure of Laser 1 in March 2003, a 91-day

cycle with a 33-day sub-cycle was used to account for the laser failure as well as to increase the spatial data coverage.

The ground-track separation distance for ICESat observations is approximately 10 km at 80° latitude and 50 km at 60°. A repeat-track error of ± 600 m implies that exact repeat ground tracks are rare; hence, XO measurements are preferred for achieving the desired SEC accuracy of $< 1.5 \text{ cm yr}^{-1}$ over ice sheets. This accuracy applies to spatial averages of XO estimates over areas of 100×100 km (Schutz et al., 2005; Zwally et al., 2002).

In this study, only high-quality elevation data are used, and a saturation correction flag is applied to reduce the effect from saturated echoes. Finally, observations with only one peak have been used to reduce errors from surface topography within the footprint.

2.7 Airborne laser-scanning observations

The three laser instruments are mounted on-board aircrafts; platforms typically used are the NASA DC-8 or P-3B for the ATM and LVIS, and Norlandair Twin Otters in the CryoVEx campaigns. Laser pulses are emitted to the surface, conically scanning the ground below the aircraft. Depending on the flight characteristics, such as altitude and off-nadir scan angle, larger or smaller swaths are illuminated, each consisting of larger or smaller footprints. Table 2.5 provides an overview of typical flight characteristics (Blair and Hofton, 2012; Hofton et al., 2008; Krabill, 2012; Krabill et al., 2002; RIEGL Laser Measurement Systems, 2010).

Instrument	Altitude [m]	Swath width [m]	Scan angle [deg]	Footprint [m]
ATM	400	140	15	1 – 3
LVIS	10,000	2,000	12	20
CryoVEx	300	300	60	0.78

Table 2.5 Information regarding flights with airborne laser scanners. Please note that the LVIS is a medium-altitude instrument whereas the ATM and CryoVEx flights are conducted at low altitudes.

The LVIS is a medium-altitude instrument while the remaining two are typically flown just below 500 m altitude. Common for all campaigns is the wish to repeat previous surveys as well as to explore new regions, so a constant focus

2.7 AIRBORNE LASER-SCANNING OBSERVATIONS

is given to areas of particular interest; in the polar regions, an example could be the observation of a sudden speed-up of an outlet glacier. The repeat flights are possible due to the use of GPS receivers and inertial navigation systems to detect the position of flight paths to within ± 5 cm. Thus, a minimum overlap with previous flights of 50% can be ensured, see Fig. 2.14 (Krabill et al., 2002). The instruments for both the LVIS and CryoVEx campaigns operate at the same near-infrared wavelength as ICESat (1064 nm) whereas the ATM instrument has a green-wavelength laser operating at 532 nm (Farrell et al., 2011; RIEGL Laser Measurement Systems, 2010).

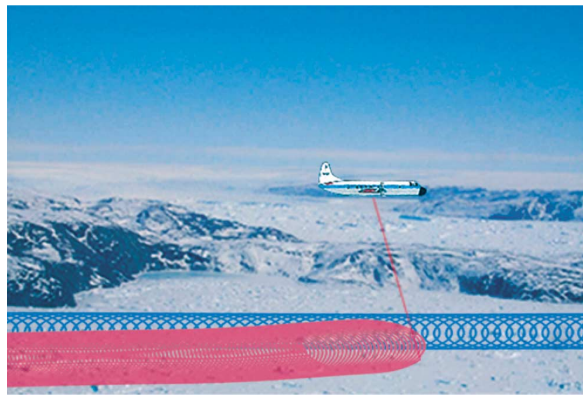


Figure 2.14 A 1994 (blue) ATM flight path resurveyed in 1999 (pink). In the intermediate period, the scan angle has been increased from 10° to 15° thereby increasing the swath width (Krabill et al., 2002).

Part I

Optimizing ice sheet-wide surface elevation change detection

The first part of this dissertation focuses on finding the best-performing method for SEC detection of the GrIS from radar altimetry. The final dataset will be based on a combination of ERS, Envisat, CryoSat-2, and Sentinel-3 data to provide a continuous time series starting in 1992. The method is decided upon after thorough inter-comparisons of ten SEC datasets provided by the scientific community. This inter-comparison exercise is conducted as part of the ESA Ice Sheets CCI project. The purpose is to find a method generally accepted by the community, and which forms the basis for the development of a 5×5 km product made available for scientists, modelers, and interested individuals.

The section below introduces two of the most frequently applied techniques for SEC detection, namely the RT and XO. From then on, the focus lies on the lessons learned and the conclusions drawn from the RR. Additionally, ideas are proposed for further work, both related to the submitted datasets as well as to the final, ice sheet-wide SEC product.

The paper describing the inter-comparison exercise and resulting conclusions is published in the *International Journal of Remote Sensing* and can be found in [Appendix A](#). A poster has also been presented at the 2013 EGU meeting; this is provided in [Appendix E.1](#). Gaining the optimal understanding of the section below follows from reading the journal paper. Finally, the publication describing the first RT results over the GrIS, derived from 2002 – 2010 Envisat data, is published in the *Remote Sensing of the Environment*. It is provided in [Appendix B](#), and the results are described in more detail in [Section 10](#).

3 Background and motivation

Several SEC studies of the Greenland and Antarctic Ice Sheets have been carried out using either LA or RA, e.g. by [Flament and Rémy \(2012\)](#); [Helm et al. \(2014\)](#); [Khvorostovsky \(2012\)](#); [Sørensen et al. \(2011\)](#); [Wingham et al. \(1998\)](#); [Zwally et al. \(2005, 2011\)](#). The analyses by [Sørensen et al. \(2011\)](#) and [Zwally et al. \(2005, 2011\)](#) convert the estimates into mass balance changes, which are indicative of not only the state of the cryosphere but also of the oceans ([Nuth et al., 2010](#); [Shepherd et al., 2012](#)): A negative SEC trend indicates a mass loss and hence a contribution to sea level rise. Given that reconciled estimates from a variety of sensors and models demonstrate an accelerating mass loss ([Sasgen et al., 2012](#); [Shepherd et al., 2012](#)), it is of high importance to continuously map SEC to increase our understanding of the changes and improve models for future predictions hereof.

Given the grand availability of temporally and spatially overlapping ESA RA, it is ideal to establish a long-term dataset of SEC; this work determines the optimal method for reaching that goal. More specifically, in the RR, the scientific community was encouraged to submit their best SEC estimate over a given region using either Envisat or ICESat data. The latter option was included due to the few radar-based SEC solutions over the GrIS. The test area was the Jakobshavn Isbræ drainage basin (68 – 71°N; 39 – 52°W) thereby covering the outlet glacier undergoing the largest changes ([Howat et al., 2011](#); [Joughin et al., 2014](#)). This is further confirmed in Section 14, where changes in two ECV parameters, SEC and IV, over a roughly 15-year period are presented. 11 solutions were received in the RR, based on both LA and RA data and derived using the RT and XO techniques. One was discarded as it was not comparable with the remaining data. The remaining ten solutions were divided relative to the method and named SEC-1 to SEC-10. This allowed for conducting thorough inter-comparisons across methodologies and sensors. The datasets were validated against contemporary SEC trends derived from ATM data. The respective analyses are explained in detail in the journal paper (Appendix A); there, Table 1 contains the background for each submission in terms of sensor and methodology, while Table 2 presents the corresponding observation periods and spatial resolutions. Seven ICESat solutions are provided and three based on Envisat data. The latter are retracked with the ICE-1, ICE-2 and with a NASA/Goddard Space Flight Center (GSFC) 10% threshold retracker ([Davis, 1997](#)). All algorithms contain all three waveform parameters. In spite of the choice of altimeter, two solutions cover the period of Envisat's

repeat orbit from 2002 – 2010, while the others cover the ICESat era from 2003 – 2009. Five solutions are based on RT and the remaining five on XO. Table 3 provides a brief overview of the processing details supporting each submission. However, due to our promise of keeping the participants anonymous, no specific information is provided neither there, nor here. In order to provide a brief overview of the different solutions, Figures 3.1 and 3.2 show the SEC estimates and corresponding errors. They are also provided in Figures 1 and 2 in the journal paper.

In order to still provide the reader with an understanding of the solutions, the sections below provide a brief introduction to the RT and XO methods. This is followed by a summary of the main conclusions and a discussion of the outcome of the RR. The latter regards, for example, how the RR could have been improved to enhance the terms for the inter-comparisons as well as interesting analyses of the final SEC time series.

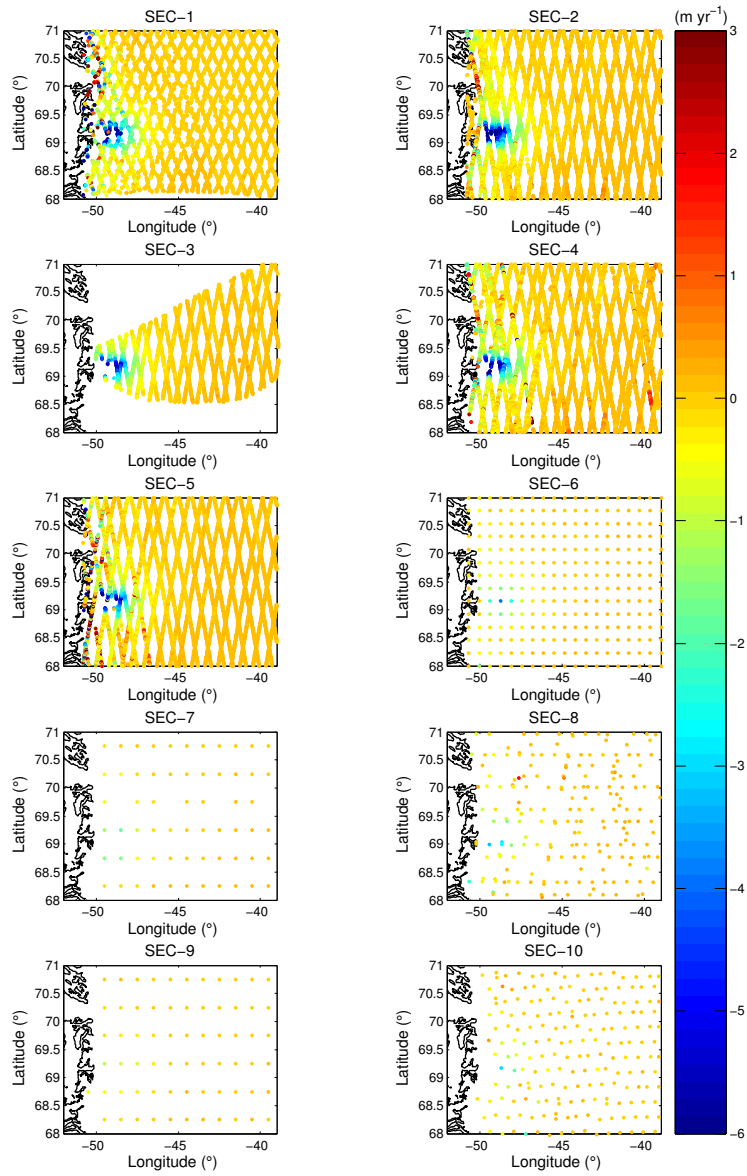


Figure 3.1 Surface elevation change estimates from repeat-track (participants SEC-1 to SEC-5) and cross-over (SEC-6 to SEC-10) analyses (Fig. 1 in the journal paper).

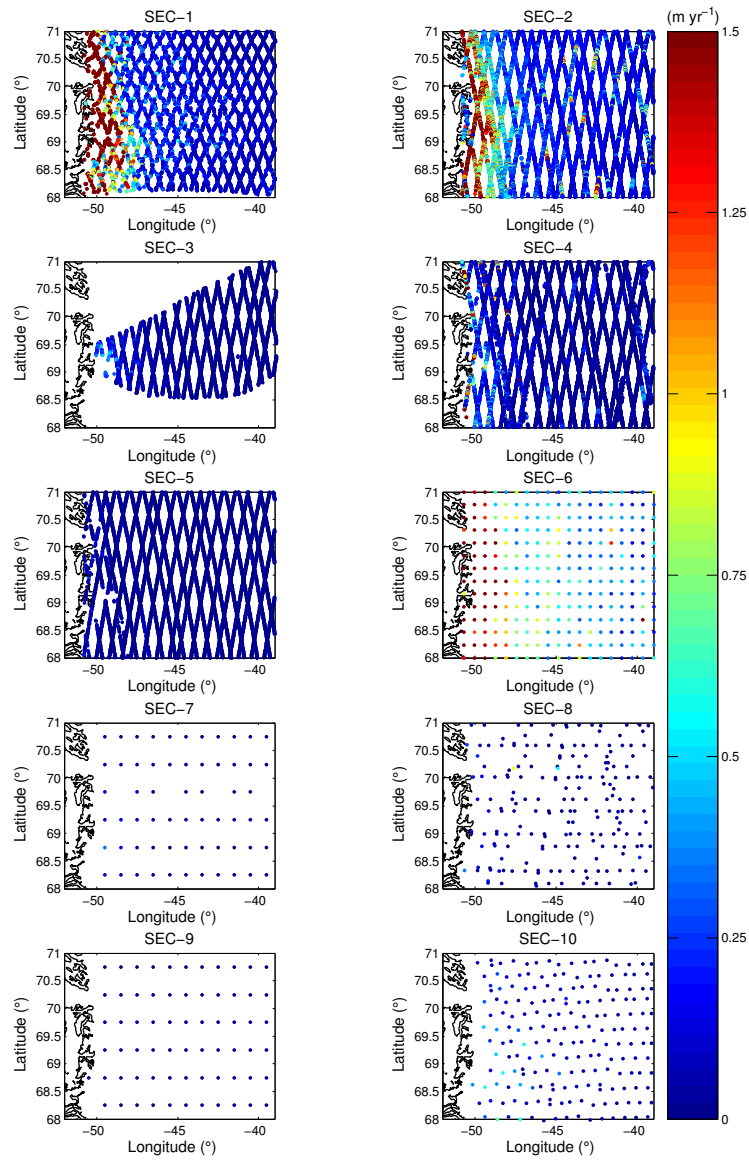


Figure 3.2 Surface elevation change errors from repeat-track (participants SEC-1 to SEC-5) and cross-over (SEC-6 to SEC-10) analyses (Fig. 2 in the journal paper).

3.1 Methods for surface elevation change detection

The following presents descriptions of selected XO and RT methods. They are based on the studies by [Khvorostovsky \(2012\)](#) and [Sørensen et al. \(2011\)](#). The solutions cover the GrIS and are based on Envisat and ICESat data, respectively. Both references are used as no ice sheet-wide RA RT solutions had been published by the time the analysis was conducted; the first of its kind is that by [Sørensen et al. \(2015\)](#) (Appendix B).

Fig. 3.3 illustrates three approaches, all of which will be described in the following. The first (a) regards the estimation of elevation differences in cross-over points between ascending and descending ground-tracks. This is advantageous as the SEC values are based on colocated elevations acquired at different times, which lowers estimation errors. However, due to measurement locations not being continuous in space, interpolation to a XO point is often necessary, which introduces interpolation errors. SEC detection in the latter two scenarios (b + c) is carried out in along-track segments. While such an approach increases the spatial data coverage, the lack of exact repeat ground-tracks introduces a need for correcting for the surrounding topography and hence, as before, interpolation errors.

In [Khvorostovsky \(2012\)](#), elevation pairs used for XO formation (Fig. 3.3(a)) are found between any two consecutive measurements on an ascending and descending orbit, respectively. Information such as elevation and signal parameters in the XO point are found by linearly interpolating the four points to this location. Biases between measurements on ascending and descending orbits are corrected for using the mean difference from observations on an ascending orbit relative to those from a descending orbit at another time, and vice versa. SEC estimates are obtained by defining a grid for the final solution and applying time series formation to the elevation pairs in each grid cell: As any surface changes within the same cycle are negligible, XO pairs are found for different cycles. In order to maximize the number of available pairs, the respective elevation differences are estimated relative to all cycles rather than just one reference cycle. This approach is described in more detail by [Davis and Ferguson \(2004\)](#) and further developed by [Khvorostovsky and Johannessen \(2009\)](#). After averaging the time series to give mean values for each grid cell, a linear or sinusoidal fit is applied to obtain the final SEC estimates.

Such an approach is sensitive to the spatial resolution of the model: The amount of observation points and thereby possible XO pairs increases with the size of the grid cell. However, if a given cell covers an area subject to a

large SEC variability over small distances, a large cell size will increase the risk of smoothing out the actual SEC signal in the averaging. This is particularly relevant over margin parts of the GrIS, and especially for RA as slope-induced errors relocate the measurements (Section 8), which reduces the availability of XO pairs.

In the work by [Sørensen et al. \(2011\)](#), three RT methods are tested for generating GrIS SEC values in along-track segments. The first two (Fig. 3.3(b)) are based on a cross-track projection where a reference surface is used to correct for the topography in-between ground-tracks. The reference surfaces are obtained from a DEM and generated from observations from two ICESat campaigns, respectively. In both cases, time series of elevation differences are generated for the along-track segments, and the mean elevation difference for each ICESat campaign in each segment is found. A linear least-squares (LSq) regression is applied to the mean values by also solving for the elevation offset in each segment, the mean time of a campaign, and a sine and cosine signal describing the seasonal signal. These approaches are highly sensitive to the spatial resolution and reference epoch of the reference surface: In case of a temporal offset between the data and reference surface, or the data used for developing the reference surface, intermediate SEC will introduce errors in the final result; different spatial resolutions may arise when using an external DEM such as the 1 km models developed by [DiMarzio \(2007\)](#); [Helm et al. \(2014\)](#). In this way, the reference surface might not fully capture the topography resolved in the observations, and this translates into the accuracy of the estimation values.

In the third method (Fig. 3.3(c)), the elevation is assumed to vary linearly with the position, time, and a seasonal signal. In each along-track segment, LSq is applied to find the SEC in the center point by also solving for the surface slopes and topography underlying the SEC. The disadvantage of this model is that in case of a strong correlation between the time and position, it cannot separate the two. This is exemplified in Fig. 3.4, which shows a good (left) and bad (right) distribution of ground-tracks: In the latter case, the ground-tracks are sequenced temporally, and thus the model cannot separate the signals coming from an elevation change and that from the local surface topography ([Ewert et al., 2012](#)).

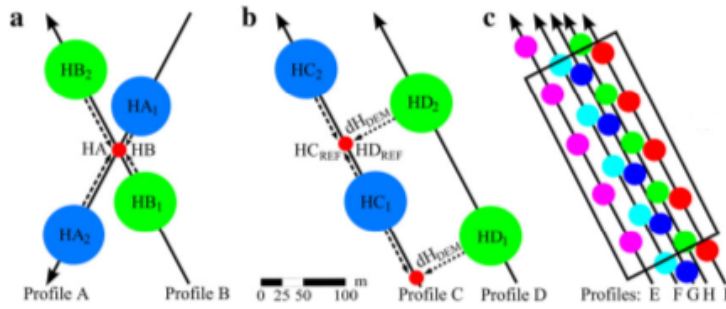


Figure 3.3 Three methods for surface elevation change detection: (a) The cross-over method in which the estimates are obtained where ascending and descending tracks intersect; (b) A cross-track projection using a reference surface to correct for the surface topography; (c) The application of linear least-squares to repeat-track observations (adapted from: [Moholdt et al. \(2010\)](#)).

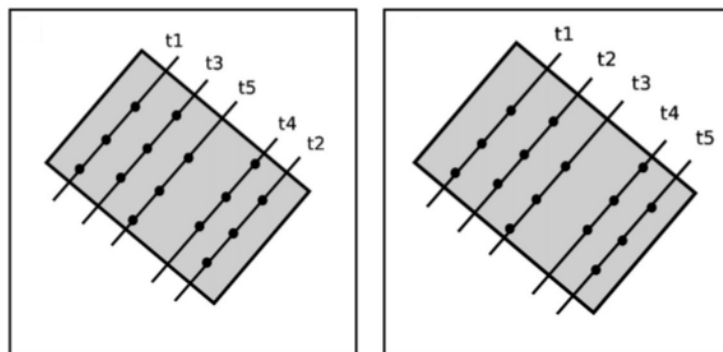


Figure 3.4 Examples of a good (left) and bad (right) spatial distribution of repeat ground-tracks (adapted from: [Ewert et al. \(2012\)](#)).

4 The Round Robin exercise

4.1 Main conclusions

Part of the RR includes validation of the solutions with a contemporary ATM SEC trend derived from either 2003 – 2009 or 2002 – 2010 data. Estimating the SEC differences and finding the mean and STD hereof (Table 5 in the journal paper) show the following:

- RT have the smallest mean SEC offsets.
Expected explanation: Most RT solutions are based on LA, and the ICESat footprint and applied spatial resolutions agree better with the ATM footprint than the XO grid cell sizes (Table 2 in the journal paper).
- RT have the largest STD.
Expected explanation: More RT than XO solutions are located at lower altitudes, i.e. in areas with a larger spatial SEC variability. This variability will increase the STD.

Thus, the larger XO mean values are a result of the typically larger grid cells causing part of the SEC signal to be lost when smoothing the observations. For instance, SEC-7 and SEC-9's $0.5^\circ\text{lat} \times 0.1^\circ\text{lon}$ resolution compared with the much smaller ICESat and Envisat footprints means that the resulting SEC may not accurately represent the true surface change. This was confirmed when a XO participant submitted a new dataset, where the grid cell size was downscaled to better agree with the footprint of the given sensor. The result was an improved agreement with validation data. The STD values for this method are, however, smaller than in RT studies as most XO pairs are located at higher altitudes.

SEC-1's results are based on a 5×5 km RT solution from Envisat. A key finding arises from validating the solution as it produces the best agreement with ATM. This is evident in the smallest mean and STD ($0.01 \pm 1.57 \text{ m yr}^{-1}$) and further confirmed in an inter-comparison of the result with SEC-3's LA RT solution: The coefficient of determination is 0.84, while a scatter plot of the respective SEC values yields a slope of 0.77. [Zwally et al. \(2005\)](#) presented the first RA-based GrIS SEC results. However, not only were the ERS data supplemented by ATM data and interpolation to obtain near-complete, ice sheet-wide coverage, the XO results were also mapped into 50×50 km grid cells meaning that much of the SEC signal over the margin was lost. Therefore, SEC-1's RT solution demonstrates, for the first time, the capability for RA to resolve SEC in all parts of the ice sheet, and at a 5×5 km posting.

In conclusion, the SEC time series to be developed in the CCI project will be based on a combination of RT and XO estimates to exploit the high spatial data coverage of the former and the high accuracy of the latter. In case of a random space-time distribution of the observations, the RT method will be replaced by a different approach. For example, an along-track method is developed for Envisat data from its last two years of observation: A DEM is subtracted from the radar heights to remove the topographic signal. Reference tracks are then selected, e.g. from one specific cycle, and divided into segments. By binning Envisat data into the segments, SEC can be estimated using the same mathematical approach as for RT, given that a minimum amount of data points is ensured. In Part III, the first-ever RT solution over the GrIS is presented along with a merged RT and XO result. Both are derived from Envisat data.

For the final time series, SEC estimates from the two products will be merged relative to the error variance. The solutions will therefore predominantly consist of combined RT and XO estimates in the interior and RT solutions along the ice and coastal margins. The spatial resolution will be 5×5 km. Cf. the validation and inter-comparison exercises, this is a fair compromise between the final SEC accuracy and the footprint of conventional radar altimeters. SEC from SARIn data will be regridded from original 3 km bins to the 5×5 km resolution.

4.2 Lessons learned

As noted in the journal paper, the participants' use of different observation periods, spatial resolutions, etc. complicate a direct comparison of the submissions. Therefore, a number of important lessons concerning initial requirements have been learned. All of them would have improved the outcome of the RR and strengthened the conclusions drawn when comparing the datasets:

- L.1 Specified observation period,
- L.2 Specified spatial resolution,
- L.3 Relocation of the RA observations is required,
- L.4 Adjusting the RA solutions for all waveform parameters (LeW, TeS, Bs) is required.

The use of a common observation period (L.1) would increase the basis for concluding on differences between the submitted datasets. An example arises from the results obtained in the two RT vs. XO analyses for LA (Table 6 in the journal paper) where such a requirement would eliminate temporal offsets

as a cause for the differing outcome. A proposed period is October 2003 – October 2009. During this time both Envisat and ICESat were operational, just as well as an equal number of summers and winters are ensured. It does not fully comply with the ATM observation times as the campaigns are mostly conducted in the months of April and May; however, due to ICESat’s periods of active lasers, completely agreeing acquisition times cannot be obtained.

Given one of the RR tasks being the determination of the optimal spatial resolution for the SEC dataset, specified resolutions for the RR submissions (L.2) would have been desirable. Proposed values are 1 km, 3 km, 5 km, and 10 km along-track segments and grid cell sizes. They serve as sufficient compromises between the footprints of the sensors, the possibility for resolving outlet glaciers and narrow valleys, capturing enough XO pairs to ensure confidence in the SEC estimates, and the accuracy of the final RA-based solutions.

An additional and highly important note relates to slope-induced errors in RA data (L.3). As neither SEC-9, nor SEC-10 have corrected for this effect, analyses involving the two solutions may be misleading, particularly for points in coastal regions. SEC-1 applied the POCA method where the observations are shifted to the closest location of the highest point within a given radius (Gray et al., 2013; Hawley et al., 2009). The Howat et al. (2014) GIMP DEM at a 90 m resolution was used for this purpose. However, cf. Section 8.2, the accuracy of the correction is highly dependent on the method and spatial resolution of the model used for generating the surface topography. This indicates that the relocation of SEC-1’s points is not as accurate as it might have been; the respective section provides an in-depth discussion hereof. Section 12 further documents the variability in volume changes when converting differently relocated SEC estimates into such.

A limitation in RA data is the dependency on the state of the reflecting surface: The penetration depth varies with snow characteristics resulting from, for example, a changing accumulation rate and firn air content (L.4). The highest SEC accuracy is achieved when correcting for all three waveform parameters, as is done by e.g. Flament and Rémy (2012); Khvorostovsky (2012); Sørensen et al. (2015). In the RR, SEC-1 and 9 accounted for all three parameters, while SEC-10 only considered Bs. Thus, the accuracy of SEC-10’s results is reduced due to lacking corrections for LeW and TeS as well as for slope-induced errors. This complicates direct comparisons with other submissions.

A potential additional requirement concerns the method used for the error estimation so these values would be directly comparable. However, the different approaches give rise to an interesting discussion. E.g. SEC-1, 3, 4, 7,

and 9 all provided the standard error of the trend. SEC-5 and 8 also included data errors, while SEC-6 returned the STD of the SEC values in each cell. The latter errors directly reflect a spatial variability in the surface topography, which explains why they are at a maximum over the highly dynamic regions. Although topographic effects will be reflected in the LSq error estimate, it does not necessarily capture all the physics of the surface. Hence, a recommendation is made for also considering data errors.

5 Perspectives and future work

A number of studies could be interesting given the availability of resubmitted RR datasets according to the ideas mentioned above. This concerns redoing the validation and inter-comparison of contemporary solutions to better draw firm conclusions, but with a particular focus on the analyses involving SEC-9 and SEC-10. This would require a relocation of the RA points, for SEC-9 to reduce the spatial resolution, and for SEC-10 to account for all three waveform parameters in the solution. Not only will such adjustments provide key information regarding the specific methods, it will also confirm that a downscaling of the grid cell will improve the validation results. The latter was demonstrated when one participant applied a downscaling and obtained better validation results.

Additional work could involve analyses of how different spatial resolutions affect the final SEC accuracy; conclusions based on such would stand stronger if based on contemporary observations.

Different results from the two sensors will occur for the reasons outlined in Section 2.4. The effect of RA echoes' dependency on the surface state is not yet fully understood, and hence a highly interesting analysis could involve the study of RA and LA data agreeing in time and space. An example could be airborne surveys with a Ku-band radar and a laser-scanner, conducted over an area with automated weather stations and people on the ground, potentially operating a ground-penetrating radar. To ensure fairly agreeing RA and LA reflecting point locations, the area should have as smooth a surface as possible. This would enable a full analysis of surface temperature, density, radar echoes from the sub-surface, etc. A grand and costly study, undoubtedly, but one that would shed important light on the impacts of varying surface characteristics. The estimation of mass changes from SEC data requires an in-depth analysis of the climatic conditions, particularly for RA data (Hurkmans et al., 2014;

[Sørensen et al., 2011](#); [Zwally et al., 2005, 2011](#)). Thus, performing such a study might improve the mass change estimation. The fact that we do need to further our knowledge in this field is outlined by [Sørensen et al. \(2015\)](#) (Appendix B) and described in Section 10.

As the final SEC dataset will be based on merged observations from a number of altimeters, another study related to the above is an analysis of waveform parameters to determine the related surface properties' impact on SEC. This is possible using observations following a repeat orbit as has been the case for both ERS-1 and -2 as well as Envisat. [Khvorostovsky \(2012\)](#) used data from all three satellites, retracked with a 10% threshold algorithm ([Davis, 1997](#)). The goal was to derive a XO trend over the GrIS for the period 1992 – 2008. The study involved an analysis of elevation, LeW, TeS, and Bs biases. The latter were found to range from -9.8 ± 0.5 dB to -1 ± 0.9 dB, while SEC estimates were adjusted by ± 10 cm yr⁻¹ when correcting for all waveform parameters. These numbers do not, however, contain information related to specific physical changes of the surface and subsurface over the observation period. As such a signal is inherent in all waveform parameters, and the CCI project generates five-year running means, investigations of temporal developments in the three parameters may further enhance our understanding of the RA elevation signal.

Part II

A Digital Elevation Model of the Greenland Ice Sheet

The second part of the dissertation demonstrates the capability of using radar and laser altimetry data to develop a DEM of the GrIS, the RL-DEM. It provides an elaborate insight into tests carried out for relocating the RA points, and for ensuring a maximized amount of surface detail in the model relative to the spatial data distribution. The RL-DEM is based on concurrent ESA Envisat and CryoSat-2 radar data merged with airborne and spaceborne laser data from NASA's ATM, LVIS, and ICESat. The reference epoch is 2010, and the RL-DEM is made available in two projections, both of which are referenced to the WGS-84 ellipsoid: A $0.02^\circ\text{lat} \times 0.05^\circ\text{lon}$ equi-angular grid in WGS-84, and an equi-distant Polar Stereographic (PS) 2×2 km grid.

The merging of observations from two types of sensors exploits the high temporal coverage of radar data, the high accuracy of SARIn data compared to conventional radar altimetry, and the high vertical and horizontal accuracy of laser data. A short observation period reduces errors from intermediate elevation changes. The combined result is a DEM with significant advantages relative to previous models, applicable for, e.g., surface elevation change detection or relocation of RA data.

Appendix C provides the paper describing the methodology for the DEM development as well as validation results. It further describes an analysis of penetration depths over the interior ice sheet, which is not seen in previous publications of DEMs. The paper is in review for publication in the AGU Earth and Space Science journal. As in Part I, a full understanding of the section below follows from reading the paper. An additional paper is provided in Appendix D, which describes the study of relocation methods. This has been submitted to The Cryosphere Discussions. Finally, Appendices E.2 and E.3 provide the posters presented at the 2014 EGU and AGU Fall meetings.

6 Background and motivation

DEMs are regular grids that provide information on the surface elevation of a given area. They serve many applications in remote sensing, such as for removing the topographic signal in SAR interferometric analyses of ice velocities, a process known as DEM elimination (Alsdorf and Smith, 1999; Joughin et al., 1996). In elevation change studies, the models can be used for correcting for topography in-between ground-tracks (Moholdt et al., 2010; Qi and Braun, 2013). Finally, Levinsen et al. (2013) and Nuth and Kääb (2011) constructed DEMs from stereographic imagery co-registered to laser data to increase the accuracy and spatial resolution of the observed elevation changes.

Regardless of the type of analysis, obtaining the most accurate results presupposes the availability of a DEM with a similar reference epoch as that of input data. With the availability of concurrent laser and radar data, this work focuses on combining the observations to develop an up-to-date GrIS DEM, referenced to a specific epoch. The accuracy of RA data is improved to increase the RL-DEM accuracy: LA data are assumed to define the 'true' surface, so vertical errors in RA data are corrected by adjusting the heights using the radar-laser elevation offsets from overlapping observation points. Horizontal errors are adjusted after performing an in-depth study of methods for relocating RA data (Levinsen et al. (2015b), Appendix D) and applying the preferred approach to the observations. The combined effect is a reduction of potential inter-satellite biases between the laser and radar sensors, while a requirement for short and simultaneous data acquisition periods reduces temporal variations in the penetration depth.

Several DEMs of the GrIS currently exist. They are based on observations from one or more sensors, accumulated over periods of one to approximately ten years. A description of a number of the DEMs is provided below, and through this the motivation for developing a new one becomes clear.

- (a) The model by Bamber et al. (2001) has a spatial resolution of 1×1 km. It is based on, e.g., 1985 – 1986 Geosat and 1994 – 1995 ERS data, 1991 – 1993 ATM data, and photogrammetric DEMs acquired by the Danish Geodata Agency (previously KMS) and the Geological Survey of Denmark and Greenland (GEUS). RMS errors along the coastal and ice margins are at least 100 m, and Scambos and Haran (2002) found that the model cannot resolve surface features with horizontal scales of up to

10 km. Furthermore, an inter-comparison with the GIMP DEM shows errors of the same order of magnitude as those documented through the RMS (Sørensen, 2012).

- (b) DiMarzio (2007) developed a DEM from 2003 – 2005 ICESat data. The observations have a high vertical accuracy, however are limited in both time and space: Observations are acquired in periods of active lasers and are sensitive to cloud cover. The largest cloud cover is typically found over the east coast, and therefore the amount and quality of observations over this region are reduced (Ettema et al., 2009).
- (c) The GIMP is posted at a 30 m resolution (Howat et al., 2014). It is constructed from e.g. 2003 – 2009 ICESat data to which DEMs from 2000 – 2010 ASTER and 2007 – 2008 SPOT-5 stereographic imagery is co-registered. The SPOT-5 imagery has a spatial resolution of 40 m and a vertical accuracy of less than 5 m in ice-covered regions; similar numbers for ASTER data are 30 m and 7 m, respectively (Korona et al., 2009; Tachikawa et al., 2011). The observations therefore resolve the GrIS surface with varying resolutions and accuracies. Validation with ICESat data shows RMS errors of elevation differences of 8.5 m over ice-covered terrain and 18.3 m over ice-free parts. The numbers are biased due to validation data being included in the DEM development. In spite of this, they do indicate that the model maps the GrIS surface well. Such a high-resolution model is applicable in many analyses such as for DEM elimination, where the input satellite imagery has a similar spatial resolution. However, vertical errors up to 100 m are found in regions with steep slopes and where the imagery is sparse, particularly in the north and along the southeast coast. Furthermore, the nominal reference period is 2007, and research indicates rapid and accelerating changes during data acquisition (as specified below), alternating both the surface slopes and elevation. This introduces elevation errors. The effect hereof is observed by Qi and Braun (2013): They found an underestimated thinning over Jakobshavn Isbræ when using the DiMarzio (2007) DEM rather than newer ATM data, better representing the actual topography at the time of measurement.
- (d) The work by Sørensen et al. (2011) focuses on RT SEC estimation by applying three different models to 2003 – 2008 ICESat data. The optimal approach is method 3 (Section 3.1), and part of the output is a mean surface topography; however, such one is subject to the effects seen in (b) and (c), i.e. temporal and spatial limitations as well as temporally-induced elevation offsets. It thereby does not represent the GrIS surface

at one specific point in time.

- (e) The [Helm et al. \(2014\)](#) CryoSat-2 model is built from one 369-day cycle of level 1B LRM and SARIn data starting in January 2012. The short observation period reduces errors from intermediate elevation changes however at the cost of a limited spatial data distribution. The latter is worsened by the radar’s inability to fully resolve the topography over regions with steep slopes, and therefore the margin regions with steep valleys, mountains, and rocks are poorly captured. This is confirmed in the validation against 2012 ATM data, showing mean elevation differences of 3.95 ± 133.6 m below 2200 m altitude and -0.01 ± 45.0 m above.

The intermediate elevation changes translating into errors are observed in a number of analyses, two of them related to this Ph.D. study: Sections 10 and 11 demonstrate the first results coming out of the Round Robin exercise (Part I), namely SEC estimates from Envisat derived using the RT technique (2002 – 2010) and merged RT and XO results from 2006 – 2010. Combined with results from [Sørensen et al. \(2011\)](#) and by [Khvorostovsky \(2012\)](#) based on 1992 – 2008 ERS and Envisat data, we not only find an overall pattern of thinning along the margin and a smaller thickening in the interior but also a change in trends with time. This has a significant impact when combining observations acquired over different time periods, also when correcting them relative to ICESat data ([Howat et al., 2014](#)) due to the seven-year observation period. A potential consequence will be incorrect adjustments of observations if based on a DEM containing such errors. An example is provided in Section 12 illustrating the difference in volume changes over Jakobshavn Isbræ when relocating three RT and three XO solutions differently.

In conclusion, previous models are subject to errors from year-long data acquisition times and/or a poor spatial data coverage. Therefore, developing a new DEM is highly relevant in order to accurately map surface changes relative to a time-specific topography and slopes. With the grand availability of concurrent RA and LA data, Envisat and CryoSat-2 data from 2010 are constrained by temporally and spatially overlapping ICESat, ATM, and LVIS data from 2009 and 2010. The 2009 data are corrected to the following year by accounting for the elevation changes, thus making for a 2010 reference epoch. This process is described in [Levinsen et al. \(2015c\)](#) and in more detail below. By merging the RA and LA data, the RL-DEM has clear advantages over those previously published, e.g.: Models built from mere or mostly radar data ([Bamber et al., 2001](#); [Helm et al., 2014](#)), as the echoes cannot accurately resolve the topography over regions with steep margins, and those built from data with long

acquisition periods (Bamber et al., 2001; Howat et al., 2014) due to errors from intermediate SEC.

The effect of the former is highlighted in a comparison of the RL-DEM with a model built from four years of CryoSat-2 data (Section 7.4). The CryoSat-only model was developed during the final stages of this Ph.D. study and thus was not involved in the analyses immediately below. The comparison does, however, point out the drawbacks of using mere RA data for DEM development in spite of the higher accuracy of SARIn data relative to conventional RA. It therefore solidifies the arguments supporting the methodology for the RL-DEM development.

The final RL-DEM is posted in two projections: WGS-84 with a spatial resolution of $0.02^\circ\text{lat} \times 0.05^\circ\text{lon}$, and in a 2×2 km PS grid. Such a resolution is a sufficient compromise between the RA and LA footprint sizes. Furthermore, the Round Robin exercise showed that a 5×5 km grid is sufficient for SEC detection from conventional radar data. Thus, given the SEC estimation from such observations in the Ice Sheets CCI project, the RL-DEM is optimal for inclusion in analyses based on observations acquired near or in 2010.

6.1 Observations

The datasets supporting the analysis as well as their temporal extent are summarized below:

CryoSat-2 = July – September 2010 LRM, SARIn

Envisat RA-2 = April – September 2010

ICESat = March & April 2009 + 2003–2009 dH/dt trend

LVIS = April & May 2009, 2010

ATM Qfit = April & May 2009, 2010

The CryoSat-2 data stem from the Level-2 intermediate (L2i) product published in the re-processed Baseline B release. At the time of analysis, only three months of data were available for 2010. In order to increase the spatial data coverage, Envisat RA-2 Geophysical Data Records (GDR) from cycles 88–92 were also implemented, covering the period from April to September. Observations from 2010 were preferred over later years to be able to include ICESat data for reducing DEM errors while minimizing interpolation errors from ICESat ceasing operation in 2009. The Envisat data are retracked with the ICE-2. The specific time frame agrees with the CryoSat-2, ATM, and LVIS

acquisition periods. ICESat data from March and April 2009 are included, covering a period of 34 days. Geophysical corrections as well as a relocation module are applied to RA data. Given that LA data are used to correct for vertical errors in RA data, the fact that LA data are confined to one period reduces errors from seasonal changes in the penetration depth.

Observations from 2009 are also included to increase the spatial data coverage. Prior to the inclusion, the ICESat and ATM heights are referenced to 2010: ICESat data by adding the 2003 – 2009 SEC trend derived from model 3 in [Sørensen et al. \(2011\)](#); ATM by deriving the 2009 – 2010 ATM SEC trends over regions with repeat surveys and interpolating them to 2009 data that are within 500 m of the repeat flight lines. By using observations slightly deviating from repeat flight lines, the spatial coverage is increased, while the distance for which observations can be adjusted is kept small to minimize errors from a spatial change in trends. Due to few repeat LVIS flights, and LVIS often following ICESat's ground-tracks, LVIS data from 2009 are used where the ICESat SEC trend is zero. This is typically found above 2000 m altitude.

2010 marked a record melt year over the GrIS: Examples are higher than average temperatures inducing surface melt, which lowered the albedo and amplified the melt. The changes were mostly confined to the southern part of the GrIS ([Bevis et al., 2012](#); [Richter-Menge and Overland, 2010](#); [Tedesco et al., 2011](#)). In spite of the melt event, a number of reasons make out for the 2009 to 2010 height adjustment being reasonable: I. Howat derived ATM SEC trends for repeat data over a region extending from Jakobshavn Isbræ to near the ice divide. He found no significant change in trends from 2009 – 2010 compared to previous years (I. Howat, pers. comm., December 2014). Furthermore, the availability of repeated LA data over the southern parts of the GrIS is sparse, and this leads to few overlapping laser and radar points (Fig. 7.3). Thus, the effect from a potentially anomalous SEC trend here is expected to be small.

All observations are referenced to the WGS-84 ellipsoid except for ICESat data, which are originally referenced to TOPEX/Poseidon. Prior to commencing the analysis, the ICESat datum is therefore adjusted to WGS-84.

6.2 DEM conceptual algorithm and validation description

An overview of the method used for developing the RL-DEM is provided below. It is adapted from Section 4.1 in the journal paper (Appendix C) and enables the reader to better follow the subsequent discussion.

1. Relocate Envisat, LRM, and SARIn data.
2. For radar points with laser observations within a specific radius, apply Inverse Distance Weighting (IDW) to derive a laser height at the radar location. To minimize errors from surface changes within the radius and the steep topography along the margin, the radius is 500 m for radar points below 2000 m altitude and 2 km for points above.
3. Estimate the radar-laser elevation offset: $dH = H_{RA} - H_{LA}$.
4. Reject dH values greater than two STD, 2σ , of the mean. This reduces errors from the location of laser points relative to radar data.
5. Recalculate the mean and σ . Then reject outliers exceeding 3σ .
6. Use collocation to spatially interpolate the dH values onto a grid: dH_{intp} (prediction values) and σ_{intp} (errors).
7. Correct the radar heights cf. $H = H_{RA} - dH_{intp}$.
8. In order to remove topography, thereby reducing potential interpolation errors, subtract the GIMP elevations from laser data and each corrected radar surface.
9. Use IDW to merge the residual surfaces into a grid. This yields dH_{comb} .
10. Finally, add the GIMP to dH_{comb} : $H_{RL-DEM} = H_{GIMP} + dH_{comb}$.

For information on the solution to the collocation system as well as advantages of its use, please see Appendix G.

The relocation of Envisat and CryoSat-2 LRM data is described in the study by [Levinsen et al. \(2015b\)](#) (Appendix D) and briefly in Section 8. CryoSat-2 SARIn data are relocated separately, as mentioned in [Levinsen et al. \(2015c\)](#) (Appendix C). The latter is done in spite of the Baseline B release already being corrected for slope-induced errors. However, a number of the observations have not been accurately relocated and are still subject to a 2π phase ambiguity. Furthermore, ESA's relocation is carried out using the [Bamber et al. \(2001\)](#) DEM, which cf. this and other studies ([Scambos and Haran, 2002](#); [Sørensen, 2012](#)) contains significant errors. As the L2i product allows for a separate relocation, the one carried out here is based on the GIMP and therefore increases the horizontal data accuracy relative to that in the official release.

7 Discussion

In the following, a number of elements concerning the methodology are discussed in the order in which they are relevant for the DEM development. It regards the inclusion of laser data and the GIMP as well as the use of collocation as interpolation tool. It is followed by a comparison of the RL-DEM with an external DEM developed solely from CryoSat-2 data; this specifically highlights the advantages of including other types of observations in the RL-DEM development. Finally, a brief description of the [Levinsen et al. \(2015b\)](#) relocation study is provided along with a summary of the conclusions and ideas for further work.

7.1 Reasoning for including laser altimetry data

The use of LA data to correct the Envisat and CryoSat-2 surface elevations is a compromise between the accuracy of the final DEM and the amount of surface detail contained in the footprint of the given sensor. This is due to the errors inherent in RA data. [Nghiem et al. \(2005\)](#) found penetration depths for Ku band RA data to exceed 1 m in the interior ice sheet, while this study showed values up to approximately 4 m (Appendix C: Fig. 4). To this date, we do not have the full understanding required to accurately model the penetration depth in all surface schemes; hence, LA data were included to account for the radar-laser elevation offset between otherwise contemporary observations. This was done by estimating the elevation differences, dH , in overlapping observation points and spatially interpolating the dH values to correct the radar heights. In order for such an interpolation to give the optimal results, observations from the two sensors should ideally observe the same surface signal. For several reasons, all of them connected, this cannot be ensured:

- (i) Different footprint diameters,
- (ii) Variations in surface topography,
- (iii) Slope-induced errors,
- (iv) The size of the search radius for overlapping observations.

Elements (i), (iii) are described in detail in the journal papers in Appendices C and D ([Levinsen et al., 2015b,c](#)), while this section focuses on (ii), (iv). Section 12 highlights the importance of the choice of relocation method as varying results are obtained when relocating RT and XO solutions over Jakobshavns Isbræ differently. The search radii between neighboring laser/ radar points have

been fixed at 500 m for radar points below 2000 m altitude and 2 km for points above. The map of surface slopes (Appendix C: Fig. 3) indicates inter-changing values within short distances at lower altitudes due to mountains, crevasses, narrow valley glaciers, etc. For this reason, topographic changes may occur within the radius. Thus, given a surface slope, the sensors do not necessarily resolve the same surface signal, which would translate into incorrect radar-to-laser height adjustments. This effect has been minimized with the different search radii thereby separating the surface regimes. The altitude limit is a compromise between the steep margin topography and the low altitudes far inland in the north. This is reflected in the spatial distribution of dH values (Appendix C: Fig. 1) in spite of the highest density of spaceborne observations occurring in the north. Hence, LA data are included both to correct the radar heights, increasing the confidence in using them for DEM development, and to maximize the spatial data coverage and DEM accuracy.

7.2 Selection of spatial interpolation technique: Collocation

Collocation is a geostatistical interpolation tool (Appendix G). In this study it is used for spatially interpolating the radar-laser elevation residuals, dH , to correct the radar heights. The reasoning for the choice of statistical approach is discussed in the following. The main reason is that the solution is based on the assumption of a zero mean, and its ability to transfer scattered observation points onto a predefined grid. This fits well with the residuals being distributed above and below zero meters due to their dependence on the RA/LA data location (Appendix C: Fig. 1), and their locations being confined to agreeing RA and LA ground-tracks and flight lines. While IDW merely accounts for the spatial distribution of data, which is relevant when estimating dH , collocation accounts for their spatial correlation based on the data values. This is highly important for accurately reproducing the dH estimates.

Collocation makes use of the spatial correlation between the observations and/or estimation points. Thus, two measurements conducted in close proximity of each other are assumed to be highly correlated. This basic assumption allows for reproducing the pattern of input values for prediction points close to observation points, while the error increases with distance. Furthermore, observations in a cluster are assigned smaller weights than single points. Such features are particularly advantageous given the irregular distribution of RA

Table 7.1 Input values for applying collocation to the CryoSat-2 and Envisat elevation residuals, dH : Correlation length and input data error.

Sensor	Corr. length [km]	Input error [m]
CS-2: LRM	524.6	2.1
CS-2: SARIn	605.9	3.1
EV: RA-2	554.5	2.4

and LA points.

The computations are carried out using GRAVSOFTE GEOGRID (Forsberg and Tscherning, 2008), which requires the following inputs: The correlation length and a data error. The former corresponds to the separation distance, i.e. 'lag', where half the variance is reached; the latter accounts for the fact that two measurements at the same location should ideally yield similar results, however do not. In this work, the respective values are found through semi-variogram analyses (see Fig. G.1 where the nugget effect represents the data error while half the range denotes the correlation length). Assuming second order stationarity, i.e. that the mean, variance, and covariance only depend on the lag and therefore are constant in space, yields the numbers given in Table 7.1 (Bohling, 2005; Nielsen, 2009). Table 1 in Levinsen et al. (2015c) holds the statistics for the residuals input to the collocation routine, namely the mean, STD, and range of dH .

Table 7.1 reveals that the largest correlation length and input error are found for SARIn data. This reflects the SARIn points' confinement to margin areas where the magnitude of dH reflects the steep topography and hence the sensitivity towards the LA vs. RA point location. This increases the input error, while the correlation length demonstrates the overall improvement of such data relative to conventional altimetry: The specifications of the SARIn mode improve the horizontal and vertical data accuracy.

Table 1 in Levinsen et al. (2015c) reveals a negative mean(dH) for all RA datasets. This reflects penetration of the RA signal, so the reflecting layer seen by the laser is higher than that seen by the radar. A more in-depth description and interpretation of dH is given in the paper, while here the focus is the advantage of using collocation: The solution depends on the spatial data distribution rather than data values. Therefore, the combination of contemporary Envisat and CryoSat-2 data is highly beneficial for lowering DEM errors. This is clear from Fig. 2(b) in Levinsen et al. (2015c), in which the errors are

calculated from Gaussian quadratic summation of the collocation interpolation errors, i.e.

$$\sigma_{DEM} = \sqrt{(\sigma_{intp}^{EV})^2 + (\sigma_{intp}^{CS})^2}$$

The values range from 0.4 m in the interior to 4.0 m near the coast. Minima depict the location of RA points after which the errors increase with distance. Collocation minimizes estimation errors, and the distribution-dependent weighting of the large number of elevation residuals allows for reproducing these values to a high degree. Confidence is therefore provided in the adjustment of the RA elevations using the radar-laser elevation residuals.

7.3 Reasoning for including an external DEM

This section deals with the external DEM used for adjusting for surface topography when merging the corrected Envisat and CryoSat-2 data with laser data. In this case, the external model is the GIMP.

When building a DEM, a compromise has to be made between the accuracy and spatial resolution of the model. The merging of observations increases the spatial data coverage, however may introduce elevation offsets. This occurs in case of differing observation times, and due to the sensors resolving the surface with varying resolutions and accuracies. If instead using just one sensor, a long observation period is typically required to ensure enough data to reduce the model uncertainty. This results, however, in the temporal offsets mentioned above. An exemption is found with CryoSat-2: Normally, altimeters have a repeat-cycle of approximately one month, which increases the amount of repeat-tracks within a short time frame *and* the on-ground spacing of ground-tracks. CryoSat-2's repeat-cycle is 369 days with the exact intention of maximizing the spatial data distribution. Furthermore, the SARIn mode allows for properly tracking the reflecting point hence causing the observations to deviate from a repeat-track.

Summarizing the above, the goal of this work is to develop a DEM with both a high spatial resolution and accuracy. This is achieved by:

- Correcting vertical errors in radar data using contemporary laser data,
- Correcting horizontal errors in radar data by relocating the measurements,
- Developing the DEM from all available laser and radar data,

- Including an external DEM to reduce errors from topography, and to provide surface heights in-between flight lines and satellite ground-tracks.

The GIMP model is introduced after the Envisat, LRM, and SARIn heights have been corrected. The model is re-gridded to the RL-DEM resolution and subtracted from the laser and radar heights thereby reducing them to the ellipsoid. Afterward, the residual surfaces are merged with IDW, and the GIMP is added back. IDW is carried out with GRAVSOFTE GEOGRID (Forsberg and Tscherning, 2008) using the 20 nearest neighbors in each quadrant surrounding the respective estimation point.

The reasoning for including the GIMP is to reduce interpolation errors and provide a topographic signal in the resulting model. This is clarified in Fig. 7.2 and Table 7.2, which demonstrate the effect from including/excluding the GIMP, both in terms of the amount of resolved surface detail and the corresponding validation against ATM and CryoVEx data from 2011. The validation data are acquired closest in time to the reference epoch, given the inclusion of 2010 ATM data in the analysis and the lack of CryoVEx flights that same year. A map of the ATM and CryoVEx flight lines is provided in Fig. 7.1. It shows a larger temporal and spatial ATM data sampling and that a smaller fraction of the CryoVEx flight lines are located over regions with steep surface gradients. Fig. 7.2(a) shows the DEM when including the GIMP, i.e. the RL-DEM, and (b) that without. (c) gives the elevation difference, dH_{extDEM} , i.e. (a)–(b). The locations of LA data and dH points are overlain the RL-DEM in Fig. 7.3. The validation is based on elevation differences between the respective model and validation data, i.e. $dH_{\text{valid}} = H_{\text{DEM}} - H_{\text{valid}}$, and only observations within a 500 m search radius are used.

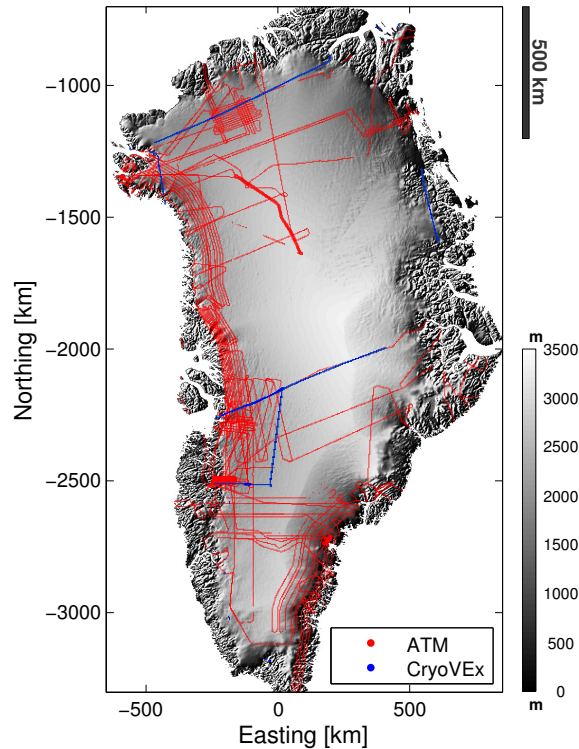


Figure 7.1 Location of validation data from 2011 ATM and CryoVEx flights. The observations are overlain the RL-DEM in Fig. 7.2(a).

It is found that the surface in Fig. 7.2(b) is generally higher than that by validation data: Below 2200 m altitude, dH_{valid} ranges from approximately 150 ± 360 m (CryoVEx) to 110 ± 310 m (ATM), while at higher altitudes the number for both systems is 0 ± 20 m. The agreement between validation data and the surface in (a) is very good for observations above 2200 m altitude, while slight offsets are found at lower elevations. In both cases, dH_{valid} is approximately zero, while the STD ranges from 10 m to 60 m, depending on the dataset and elevation. When comparing the ATM and CryoVEx results, a number of things should be noted: The statistics are positively affected by a larger ATM data sampling, which lowers the STD, while validation against CryoVEx data over the margin increases the STD. Furthermore, offsets will be introduced when comparing point measurements (ATM, CryoVEx) with a model with a grid spacing much higher than that.

The DEM in Fig. 7.2(b) suffers from the inability to fully resolve the surface topography, and to a much larger extent depicts the position of input data; the latter is particularly clear in the dH_{extDEM} pattern in (c) where near-zero values are found in and along ground-tracks. The 500 m counters reveal that

the quality of the model is lowered towards the ice and coastal margins as well as with a lowering latitude due to the decreasing amount of observations. Thus, the region with the largest offsets in (b) depicts that where few or no observations are present in Fig. 7.3.

Overall, the following observations are made for the parts of the GrIS where input data are available:

- Along flight lines and ground-tracks: $dH_{\text{extDEM}} = 0$ m, i.e. the two models agree.
- Within $(\Delta\phi = 0.05^\circ, \Delta\lambda = 0.02^\circ)$ of flight lines and ground-tracks: Interchanging positive and negative dH_{extDEM} signals depending on the location of RA points relative to the estimation point. Ex: If RA points are located up-slope from the estimation point $dH_{\text{extDEM}} > 0$ m, while $dH_{\text{extDEM}} < 0$ m if the RA points are located down-slope. This indicates that the IDW routine cannot accurately reproduce the true surface.
- Outside $(\Delta\phi, \Delta\lambda)$ of the ground-tracks: $dH_{\text{extDEM}} > 0$ m. The IDW process for Fig. 7.2(b) markedly fails, which is particularly visible in the margin parts of the GrIS due to the sparsity of input data.

In regions where neither RA nor LA data exist, $dH_{\text{extDEM}} < 0$ m. This is explained by interpolation errors.

The above demonstrates that when solely interpolating RA and LA data, IDW cannot accurately reproduce the surface topography otherwise known from the GrIS. Instead, it tends to overestimate the heights, which helps explaining the offsets found in the validation. When including an external surface, the topographic signal included in this is transferred into the DEM where RA or LA data are few or lacking. This is mostly found along margin parts of the ice sheet. In spite of the GIMP's 2007 reference epoch, this markedly improves the quality of the RL-DEM: The validation shows that near-zero means and low STD of dH_{valid} are produced.

The decision of using the GIMP is based on tests of DEMs built from a number of external models, namely those described in Section 6 with the exception of [DiMarzio \(2007\)](#) due to the short observation period and the sparse data acquisition periods. A DEM was built using each one, and validation was conducted with 2011 ATM and CryoVEx data. Furthermore, cross-comparisons of the final models were carried out to see how they compared. Separate validations of the DEMs could have been carried out. It would not, however, provide relevant information for the DEM development. E.g. ICESat data might perform well in the validation while the on-ground separation distance

7.3 REASONING FOR INCLUDING AN EXTERNAL DEM

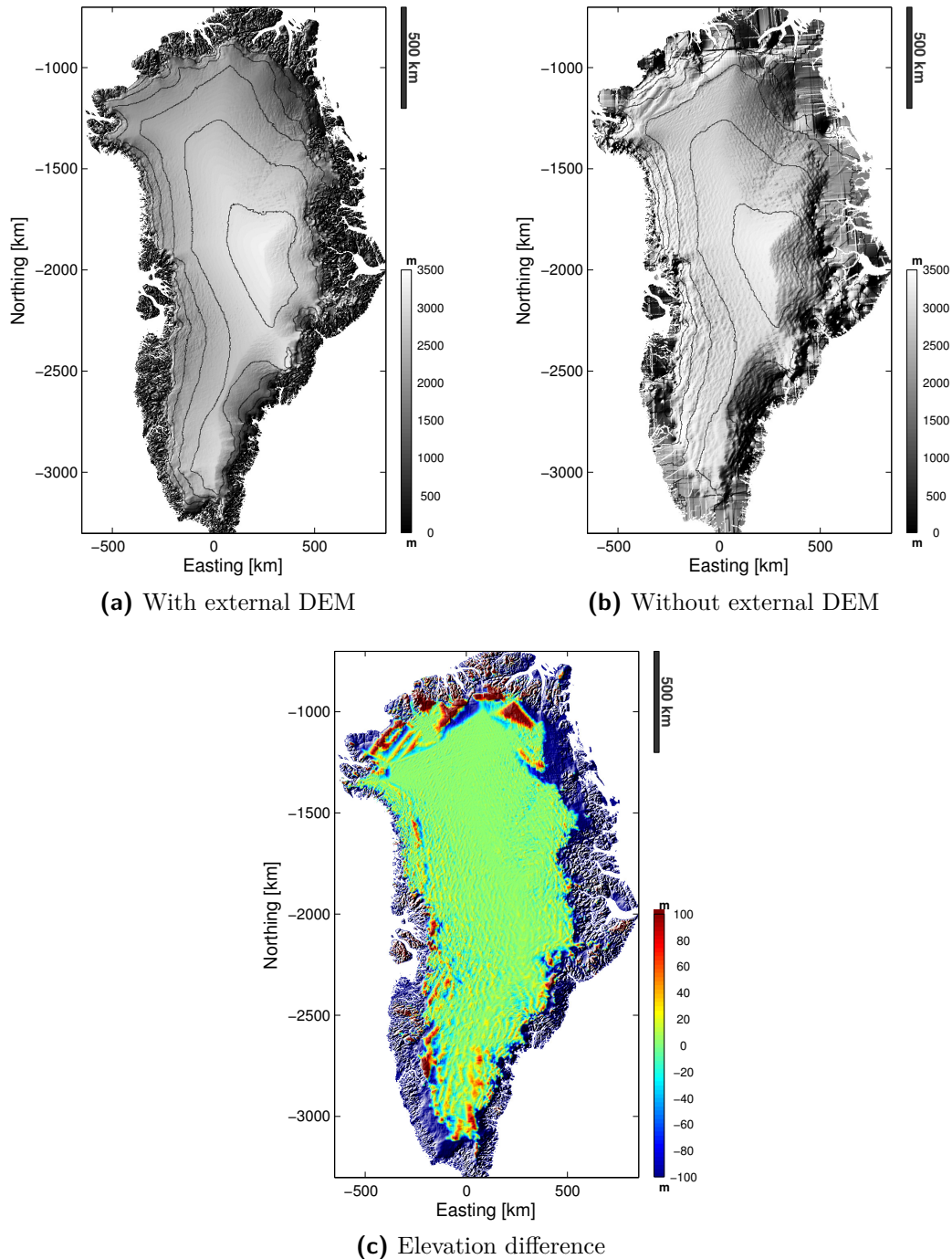


Figure 7.2 DEMs when including (a)/ excluding (b) an external DEM to correct for topography. 500 m elevation contours are overlain. (c) Elevation differences, i.e. $c = a - b$. Please note that the DEM in (a) is the RL-DEM, i.e. Fig. 2(a) in [Levinson et al. \(2015c\)](#) (Appendix C), although without the contours.

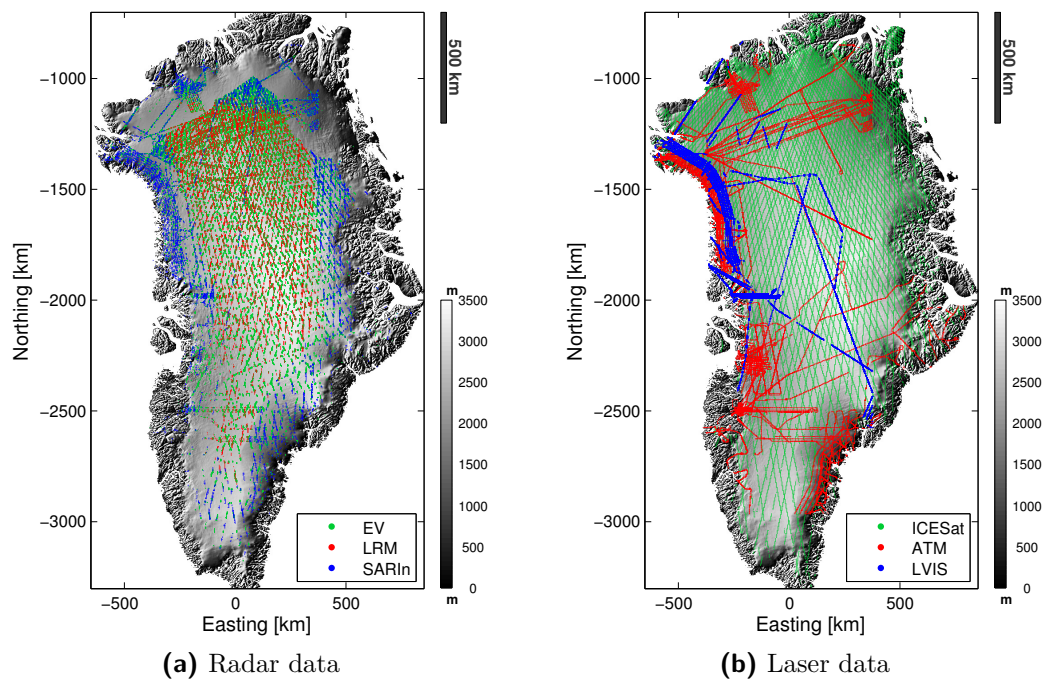


Figure 7.3 Locations of dH estimates along Envisat and CryoSat-2 LRM ground-tracks and in SARIn data points (a), based on all available ICESat, ATM, and LVIS data (b). The observations are overlain the RL-DEM in Fig. 7.2(a).

7.3 REASONING FOR INCLUDING AN EXTERNAL DEM

Table 7.2 Validation of DEM against 2011 CryoVEx and ATM data for the model built *with* (top) and *without* (bottom) an external DEM to reduce topographic errors. The search radius for neighboring DEM and validation points is 500 m, and elevation differences are derived cf. $dH_{\text{valid}} = H_{\text{DEM}} - H_{\text{valid}}$. The mean and STD (σ) are estimated. Please note that the values for the model developed *with* an external DEM is also provided in Table 2 in [Levinson et al. \(2015c\)](#) (Appendix C).

	Above 2200 m			Below 2200 m		
	# of points	mean [m]	σ [m]	# of points	mean [m]	σ [m]
W/ DEM						
ATM	3,860	0.1	7.9	15,094	1.2	30.2
CryoVEx	195	-1.6	13.8	869	0.1	59.9
W/out DEM						
ATM	3,860	-0.8	23.2	15,107	110.0	306.2
CryoVEx	195	-1.7	17.1	869	154.6	356.6

of the ground-tracks would introduce errors when implementing the observations in a 2×2 km model.

Table 7.3 provides the results of the validation, which was carried out similarly to above, although this time including all validation points. It is found that the mean and STD with the GIMP are smaller for all altitudes, and that these values increase for the remaining three surface models. Thus, the GIMP provides the optimal model for accounting for the surface topography not covered/resolved by the RA and LA data. Overall, the mean and STD for DEM points above 2200 m altitude are quite similar as they range from -0.2 ± 13 m (GIMP; ATM) to -2.6 ± 25 m (ICESat; ATM). The largest differences are found at lower altitudes, which correlates with the region where slope-induced errors in RA data, short or long observation periods, and the specific techniques have the largest impact. E.g. the values for the DEM based on the [Helm et al. \(2014\)](#) model confirm the large offsets with 2012 ATM data as posted in the paper, thereby demonstrating the advantage of combining observations from different sensors to increase the amount of resolved surface detail. Overall, the results with the GIMP support the finding described in the paper (Appendix C: Tables 3 and 4): That the optimal DEM is developed using the GIMP.

Table 7.3 Validation of DEMs derived using an external elevation model against 2011 ESA CryoVEx and ATM data. The search radius for neighboring DEM and validation points is 500 m, and elevation differences are given as $dH_{valid} = H_{DEM} - H_{valid}$.

Sensor	Validation data	Above 2200 m			Below 2200 m		
		# of points	mean [m]	σ [m]	# of points	mean [m]	σ [m]
CryoSat	CryoVEx	400	-2.2	17.5	1,718	14.7	93.2
	ATM	7,710	-0.3	14.3	30,066	38.6	168.8
GIMP	CryoVEx	400	-1.7	17.3	1,726	3.0	63.6
	ATM	7,710	-0.2	13.0	30,119	0.5	49.3
Bamber	CryoVEx	400	-2.1	17.7	1,636	5.6	55.9
	ATM	7,708	-1.2	22.2	27,349	2.0	59.9
ICESat	CryoVEx	400	-0.9	19.1	1,722	12.3	110.0
	ATM	7,710	-2.6	25.0	30,113	33.3	171.9

7.4 Comparison of RL-DEM with CryoSat-only model

In the study by Nilsson (2015), a $0.01^\circ\text{lat} \times 0.025^\circ\text{lon}$ DEM of the GrIS is developed from CryoSat-2 data from July 2010 to August 2014 with a reference epoch in 2012. The model is compared against the RL-DEM and validated against ATM and CryoVEx data from 2011. In order to fully understand the results of the validation and comparison, the background for the DEM development is first described.

The CryoSat-only DEM is developed as a side-product during SEC estimation to extract the topographic signal from the surface heights. For this reason, it is confined to ice-covered regions only. The method is similar to that described by Zwally et al. (1990), i.e. a local, bi-quadratic surface modeling approach. More specifically, an iterative, distance-weighted, least-squares minimization is used for gridding the observations. A minimum of ten data points is required for the fitting procedure to work, and so the search radius is variable to ensure that the requirement is met. The radius is set to vary between 5 km and 25 km. The distance weighting factor, W , is determined as:

$$W = \frac{1}{1 + \left(\frac{D}{D_c}\right)^2}$$

where D is the distance from the prediction point to a given observation and D_c is a weighting factor set to the resolution of the grid cell. This ensures a greater weighting of observations closer to the prediction point, and that the local topography is preserved. An iterative fitting procedure is carried out in which outliers are removed, e.g. due to negative surface elevations or too large errors. In this case, a bilinear fit is applied instead, and if this does not work, the search radius is increased and the fitting routine reapplied. If a reliable result still has not been produced, IDW is applied using the 20 nearest DEM elevations to fill the missing value.

Prior to gridding the observations, a correction for surface penetration is applied. It assumes a constant bias in space, and separate values are derived for the LRM and SARIn modes. The penetration depths are estimated as the mean elevation difference between CryoSat-2 and ATM data for the years 2011 – 2013. The observations are acquired in the months of February to June and April to May, respectively. The resulting values are 0.46 m for the LRM mode and 0.60 m for SARIn data, respectively, which are added to the heights.

The CryoSat-2 DEM is seen in Fig. 7.4(a) where (b) shows elevation differences as the RL-DEM minus the model in (a). The RL-DEM is visualized in

Fig. 7.2(a) here and Fig. 2(a) in [Levinsen et al. \(2015c\)](#) (Appendix C), and the comparison is made for coordinates where the two DEMs intersect.

Keeping in mind the earlier RL-DEM reference epoch and the spatial pattern of SEC values (see e.g. Figures 10.1(a,b) and 11.1(a)), the elevation differences are expected to be positive over regions subject to a thinning. Positive or near-zero values are expected over the interior due to two things: The 2012 melt event increasing the reflecting surface seen by CryoSat-2 by approximately 0.6 m and the different ways of accounting for surface penetration. The RL-DEM study estimated penetration depths from 1 m to 4 m (Appendix C: Fig. 4) while [Nilsson \(2015\)](#) found values between 0.46 m and 0.60 m. Given near-zero SEC in the interior, the RL-DEM heights are expected to be higher than or nearly equal the CryoSat-2 DEM heights.

Fig. 7.4(b) shows zero or slightly positive elevation differences in the interior, while Table 7.4 demonstrates positive mean elevation differences both at higher and lower altitudes. The STD, however, are large and range from 75.7 m above 2200 m altitude to 250.3 m below. Firm conclusions on the exact size of the elevation offsets thereby cannot be drawn. The high STD may reflect that the CryoSat-2 model shows less surface topography than the RL-DEM in spite of being built from four years of observations to increase the spatial data coverage. The elevation offsets therefore indicate that the CryoSat-2 model cannot accurately reproduce the surface topography. The most distinct difference between the two DEMs is found at lower altitudes as the CryoSat-2 heights are generally higher, except for by Jakobshavn Isbræ and a few locations by the margin, where the pattern is reversed. These locations do not, however, necessarily agree with locations of an expected thinning. The reversed pattern over Jakobshavn Isbræ indicates that the large thinning rates outweighs the generally overestimated DEM heights. Other significant elevation offsets correlate with:

- Locations of troughs and narrow valleys illustrating the radar's lacking ability to resolve such features over regions with steep topography,
- The geographical boundary between the LRM and SARin modes. This is, to some extent, visible in Fig. 7.3(a).

A more elaborate description of potential reasons for the elevation offsets is provided below.

Validation of the CryoSat-2 DEM against ATM and CryoVEx data from 2011 (Table 7.5) reveal large elevation offsets at lower altitudes resulting from too high DEM heights. This is mostly clear through the validation with ATM

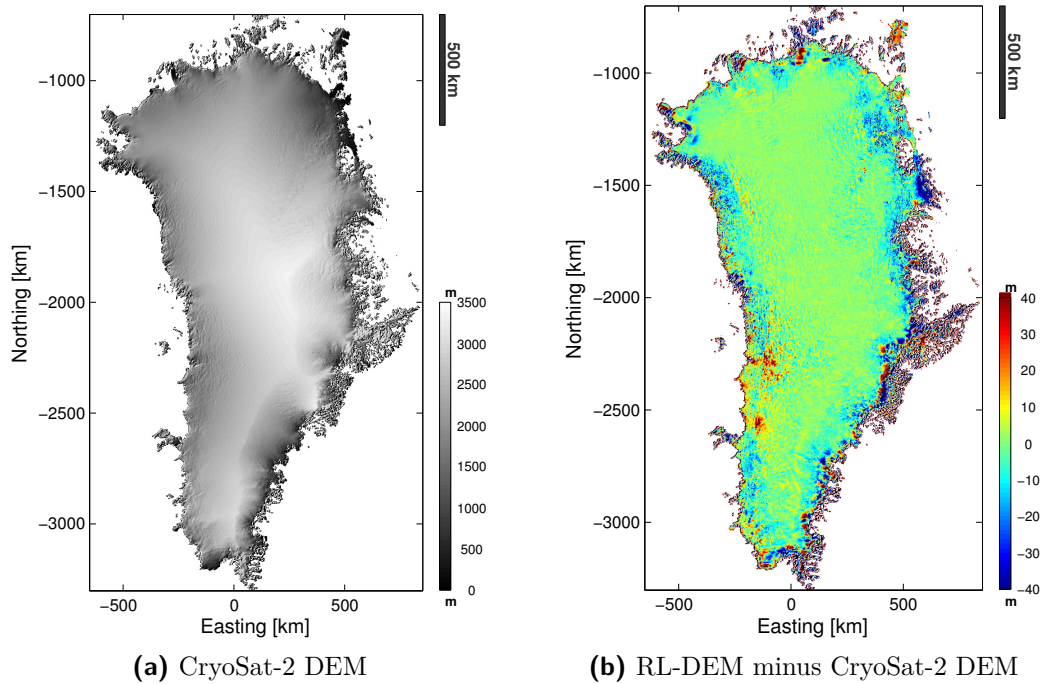


Figure 7.4 The Nilsson (2015) CryoSat-2 DEM (a) and elevation differences between the RL-DEM and the CryoSat-2 model (b). Please note that the CryoSat-2 heights have been extracted over points intersecting with the RL-DEM.

Table 7.4 Mean and STD are estimated for RL-DEM and CryoSat-2 DEM elevation differences. Please note that the CryoSat-2 heights have been extracted over points intersecting with the RL-DEM.

	Above 2200 m			Below 2200 m		
	# of points	mean [m]	σ [m]	# of points	mean [m]	σ [m]
RL-DEM – CS-2	227,892	1.5	75.7	216,093	27.4	250.3

where elevation differences of 28.4 ± 171.5 m are found for points below 2200 m altitude against 11.7 ± 51.6 m with CryoVEx. The better agreement with CryoVEx data may be explained by the fewer validation points over the steep margins (Fig. 7.1). When comparing the validation results with those of the RL-DEM (Table 7.2, top panel), a few points are that the mean and STD for points above 2200 m altitude are similar while offsets at lower altitudes are larger with the CryoSat-2 model. The latter highlights the inability of radars to fully resolve the margin topography, as was also found in the CryoSat-2 model by Helm et al. (2014), and which created the motivation for including both laser data and the GIMP in the RL-DEM.

Validation of the CryoSat-2 DEM was expected to improve relative to that of the RL-DEM. This is due to the CryoSat-2 model being produced on a $0.01^\circ\text{lat} \times 0.025^\circ\text{lon}$ grid, reducing validation biases from the DEM grid spacing relative to the size of the laser footprints. The expectation is not met, and several possible explanations exist for this, all of which may also explain the elevation offsets relative to the RL-DEM:

- In spite of the advantages with the SARIn mode, the radar still cannot resolve the bottom of troughs, narrow valleys, outlet glaciers, etc. This translates into interpolation errors in the gridding procedure.
- Noticeable differences in the range estimation between the LRM and SARIn modes, as also noticed in a 2010 – 2014 SEC map from A. Shepherd, University College London (pers. comm., June 2014).
- The choice of method. As the search radius can be increased to 25 km, a distance over which significant surface changes may occur, the resulting heights may not be realistic. Depending on the topography, the bilinear fit may not provide realistic elevations either.
- A large melt event in July 2012 (Nghiem et al., 2012) increased the surface height observed by CryoSat-2. The study by Nilsson et al. (2015) over the North Greenland Eemian Ice Drilling Project camp showed an elevation increase of 56 ± 26 cm when comparing CryoSat-2 data after the melt event (August – September) with those before (May – June). The observations are obtained from the L1b product and retracked with a 20% threshold, meaning that the surface part of the signal is enhanced. The positive rate of change reflects a higher reflecting layer, i.e. lower penetration depth, potentially due to the formation of dense ice layers.
- The correction for surface penetration. As the actual depth depends on snow characteristics, which may be variable in space, the underlying assumption of a spatially constant bias is not valid. Furthermore, the Nilsson (2015) biases are estimated from three years of observations, i.e.

Table 7.5 Validation of the Nilsson (2015) CryoSat-2 DEM against 2011 CryoVEx and ATM data. The search radius for neighboring points is 500 m, and the mean and STD are estimated for elevation differences derived cf. $dH_{\text{valid}} = H_{\text{DEM}} - H_{\text{valid}}$. Please note that the CryoSat-2 heights have been extracted over points intersecting with the RL-DEM.

	Above 2200 m			Below 2200 m		
	# of points	mean [m]	σ [m]	# of points	mean [m]	σ [m]
ATM	3,274	1.5	7.4	11,484	28.4	171.5
CryoVEx	189	-1.1	14.3	682	11.7	51.6

a longer time period than that used for the RL-DEM, and one that covers the 2012 melt event. The end result is likely to be more realistic penetration depths in the RL-DEM study.

Advantages of the method by Nilsson (2015) are the weighting of observations closer to a prediction point higher than those further away, the long observation period, and the use of SARIn data to increase the spatial data coverage. In spite of this, several aspects of the model affect the quality of the outcome, which decreases the amount of resolved surface detail and the agreement with validation data. The model therefore cannot act as an accurate, stand-alone DEM of the GrIS.

8 Relocation of conventional radar altimetry data

The study by [Levinsen et al. \(2015b\)](#) (Appendix D) compares two techniques for relocating Envisat and CryoSat-2 LRM data near Jakobshavn Isbræ. The results are validated against ATM to find the preferred method over regions with both steep terrain as well as smoother topography. Envisat and ATM data are acquired in May 2010 and LRM data in July 2010, the period closest in time where observations were available.

The main outcome of the study is that the accuracy of the relocation is highly dependent on the technique and spatial resolution of the a-priori DEM used for generating the surface topography. This is demonstrated by the significantly different relocation vectors obtained when slightly modifying the technique, as well as in validation of the results. As RA data are applicable for deriving, e.g., surface elevation, volume and mass changes ([Helm et al., 2014](#); [Hurkmans et al., 2012, 2014](#); [Li and Davis, 2008](#); [Sørensen et al., 2015](#); [Zwally et al., 2005, 2011](#)), potential errors in the relocation will transfer directly into these estimates. Currently, the majority of studies dealing with RA data over ice sheets do not dedicate particular attention to the relocation method used; this study suggests that more attention is needed to ensure a reliable correction.

8.1 Methodology

Several techniques for adjusting for slope-induced errors have been described in literature, e.g. by [Bamber \(1994\)](#); [Brenner et al. \(1983\)](#); [Remy et al. \(1989\)](#) and [Hurkmans et al. \(2012\)](#). As mentioned in the journal paper (Appendix D), the techniques applied here relocate the observations horizontally, so the measured range agrees with the POCA. One technique, referred to as 'the POCA', directly relocates the observations from nadir to the POCA, while the other uses the satellite altitude and the surface slope and aspect to derive the relocation vectors. The latter method is described by [Hurkmans et al. \(2014\)](#), and discards observations with local slopes exceeding 1.5° . The relocation vectors are given in Eq. (2.4). The techniques assume a non-uniform, respectively constant, slope within the illuminated area, and they use an a-priori DEM to generate the surface topography. Here, a-priori data originate from either Envisat or ATM or the GIMP DEM regridded to four different spatial resolutions for each dataset. This eliminates errors from external data and reduces those from RA data, while the variable DEM resolutions provide a minimum hori-

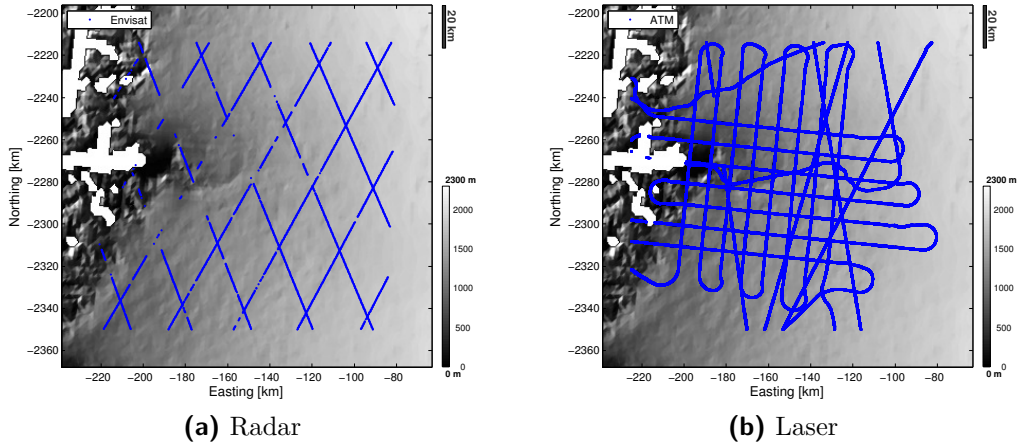


Figure 8.1 Location of observation points used for purposes of relocation: (a) Envisat, and (b) ATM data.

zontal scale for topographic features, which the radar is capable of resolving. The latter is found over regions with steep topography.

The largest focus is given to the study of Envisat data as they are located over steep terrain where slope-induced errors are most significant. Following this correction, CryoSat-2 LRM data acquired inland from Jakobshavn Isbræ are relocated. The details related to the relocation techniques are described in Section 3 in the journal paper, while Fig. 8.1 here illustrates the location of the Envisat ground-tracks (a) and ATM flight lines (b) over Jakobshavn.

8.2 Results and outlook

Figures 8.2 – 8.3 present a subset of the relocated Envisat data over Jakobshavn Isbræ. They are also visualized in Fig. 1(a)–(c) in [Levinsen et al. \(2015b\)](#) (Appendix D).

The figures demonstrate that the relocation is highly dependent on the technique, mostly regarding the spatial resolution of a-priori data. Over the interior ice sheet, the relocations in Fig. 8.2 are fairly consistent for the GIMP at low spatial resolutions (> 4 km) while the largest variations are found at lower elevations with steeper topography. In no case, however, do all solutions agree, neither with respect to the direction nor magnitude of the displacement, and this in spite of a number of the relocations being based on the same set of equations. Generally larger relocation vectors are found with the method de-

scribed by [Hurkmans et al. \(2012\)](#) than with the POCA, likely owing to the local slope approximation over regions with complex topography.

Validation of the relocated Envisat data against ATM (Appendix D: Table 1) reveals the POCA as the preferred method, and that the optimal results are obtained with the GIMP DEM regrided to a 2 km resolution. Applying the POCA to LRM data reveals the same result (Appendix D: Table 2), indicating that the resolution is applicable over both margin and inland parts of the GrIS. It further clarifies the applicability of the RL-DEM in relocation analyses. Additional tests of Envisat data with the GIMP at a 500 m posting were carried out based on the assumption that the higher resolution would improve the results over Jakobshavn Isbræ. This was not found, leading to the conclusion that the radar simply cannot resolve small-scale surface features over regions with steep slopes. It is an important result, which indicates faults in e.g. the relocation carried out by participant SEC-1 in the Round Robin exercise (Section 4.2).

The analyses demonstrate that the accuracy of the relocation is highly dependent on the approach: The relocated points simply do not overlap. The displacement depends on the spatial distribution and spatial and temporal resolution of the a-priori data. Location and elevation errors are inherent in RA data, and ATM data are confined to flight lines biasing the relocation towards the direction of densest data coverage. This means that local maxima may be missed. The GIMP has a higher spatial resolution however sees features that the RA likely cannot see. Furthermore, when correcting data acquired after the GIMP's 2007 reference epoch, the intermediate surface changes are not accounted for. Therefore, no matter the approach, it is impossible to know the true location of the reflecting point.

In spite of this, a number of techniques are proposed for further testing. Based on the consistent results with CryoSat-2 LRM, they are to be applied to Envisat data over the ice margin:

- T-a An iterative POCA method based on Envisat data for generating surface topography,
- T-b Using the POCA method based on the GIMP regrided to eight different resolutions starting at 500 m and ending at 4 km. For each computation, the resolution is increased by 500 m,
- T-c The POCA based on more contemporary LA data than those available for the study with ATM.

The approach in T-a is similar to that applied by Helm et al. (2014), and validation of the results would reveal the accuracy of relocation. The advantage is that no external observations are used such that errors from, e.g., different data acquisition times are reduced. T-b would reveal more specific information on the horizontal scale of spatial features to be resolved by the radar. This is important for understanding the observations seen with the radar and for maximizing the accuracy of the relocation. The final technique (T-c) is applicable given a larger spatial LA data availability. Such may be obtained when both the ATM and LVIS are operated, and in case of temporal overlaps with ICESat's periods of active lasers. However, due to the limitation of LA data in time and space, the highest accuracy of T-c is expected to be obtained over the smooth interior where local surface depressions are fewer and smaller than those closer to the ice margin.

8.2 RESULTS AND OUTLOOK

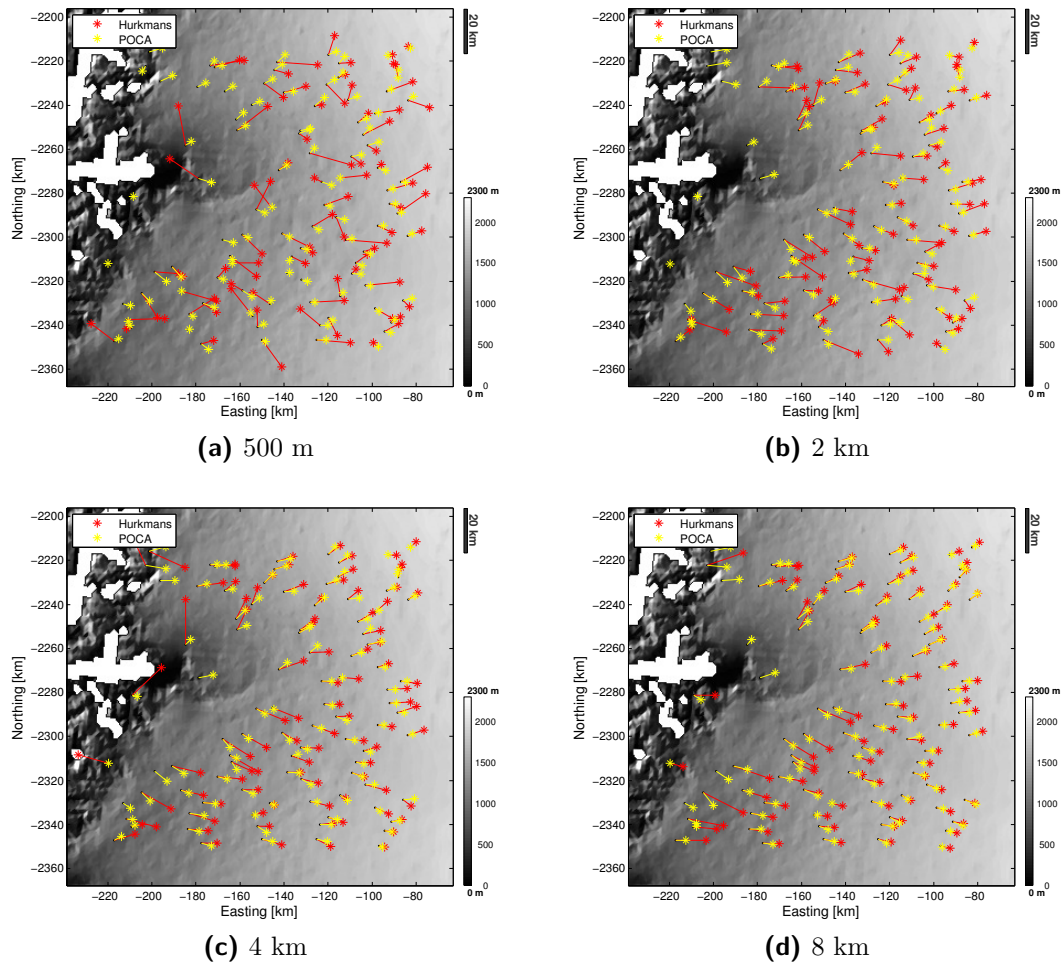


Figure 8.2 Relocated Envisat data over Jakobshavn Isbræ overlain the RL-DEM. The relocations are carried out using the method described in [Hurkmans et al. \(2012\)](#) as well as the POCA. All computations are based on the GIMP regrided to (a) 500 m, (b) 2 km, (c) 4 km, (d) and 8 km postings, respectively.

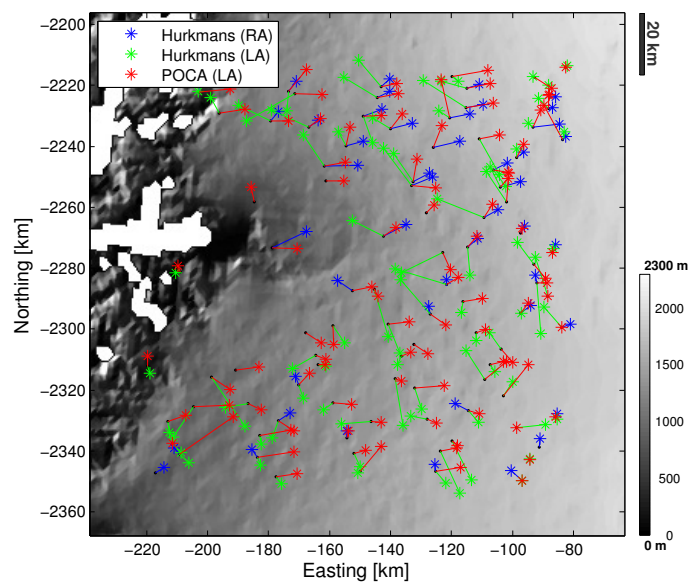


Figure 8.3 Relocated Envisat data over Jakobshavn Isbræ overlain the RL-DEM. The relocations are carried out using the method described in [Hurkmans et al. \(2012\)](#), where Envisat and ATM data, respectively, are used to develop a local DEM, as well as the POCA based on ATM data.

9 Outlook and conclusions

In this work, a DEM of the GrIS has been developed from contemporary Envisat and CryoSat-2 radar data merged with ATM, LVIS, and ICESat laser data. It is referred to as the RL-DEM. Radar echoes are subject to e.g. slope-induced errors and to penetration into the subsurface. This acts to lower the horizontal and vertical data accuracy, respectively. The former effect is mostly pronounced in conventional altimetry such as from Envisat and CryoSat-2 LRM.

In order to prevent the effects from translating into DEM errors, both are adjusted for in this work: The [Levinsen et al. \(2015b\)](#) study showed the preferred method for relocating Envisat and CryoSat-2 LRM data to be the POCA using the GIMP DEM regridded to a 2 km resolution to generate the surface topography. Originally, a 500 m resolution was obtained for LRM data, which therefore was applied in the DEM development. However, later work showed 2 km to be preferred, which will be implemented at a later stage. CryoSat-2 SARIn data were relocated separately by applying a correction for a 2π phase ambiguity error. A particularly important outcome of the [Levinsen et al. \(2015b\)](#) study is the relocation vectors' sensitivity to different methods and DEM resolutions, which may translate into errors in derived surface elevation, volume or mass changes.

The vertical errors were accounted for using contemporary airborne and spaceborne laser data. By estimating the radar-laser elevation offsets, the radar heights were adjusted towards the true surface thereby ensuring confidence in the estimates. This was ensured due to the use of the spatial interpolation tool collocation for interpolating the residuals: This accounts for the spatial data distribution and errors and allows for accurately reproducing the input values. Thus, no matter the reason for a given residual, e.g. a physical error or inter-satellite biases, collocation reproduces the signal, which is then added back to the radar elevation. Therefore, the RL-DEM could have been developed without laser data, which would, however, compromise the vertical RL-DEM accuracy. This was not desirable.

As seen in Fig. 7.3, few laser and radar points exist along the coastal margin and with a lowering latitude. This is due to the short observation period, the satellite orbit, and the flight lines. Interpolating input data to the entire ice sheet to develop the DEM would therefore compromise the accuracy over regions with a sparse data coverage. This is demonstrated in Fig. 7.2(b) where few surface details are resolved, particularly relative to (a) where an external

model, the GIMP, was used to adjust for the missing topography. Validation of the two models is given in Table 7.2; a comparison with ATM and ESA CryoVEx data from 2011 shows elevation offsets exceeding 100 m for (b) whereas mean elevation differences and standard deviations for (a) decrease to 0 m and 10 – 60 m, respectively. Including the GIMP was therefore a compromise between the amount of resolve surface detail and the RL-DEM accuracy. The drawdown from keeping to RA is demonstrated by Helm et al. (2014) and Nilsson (2015), who built DEMs from one and four years of CryoSat-2 data, respectively, and could not properly resolve the surface detail along the coastal and ice margins.

Based on the above, a contemporary DEM of the GrIS is now available. The reference epoch is 2010. The RL-DEM is referenced to the WGS-84 ellipsoid and published in both a 2×2 km polar-stereographic and $0.02^\circ\text{lat} \times 0.05^\circ\text{lon}$ WGS-84 projection, respectively. The analyses setting the grounds for the DEM development as well as the foundation of contemporary observations have greatly improved the horizontal and vertical accuracy, hence providing the DEM with an advantage over previous models.

Part III

ECV production and outlook

The third and final part of the dissertation sums up the first two by providing the first results following from the Round Robin exercise as well as an outlook and ideas for further work, based on the results obtained during the Ph.D. study. It regards both the first repeat-track results over the Greenland Ice Sheet as well as a merged repeat-track and cross-over result. Both are derived using Envisat data. It involves a study of the impact of elevation changes upon volume changes when the underlying radar data are relocated differently. A discussion of future work involves the application of the 2010 RL-DEM for Envisat elevation change detection when the satellite's drifting orbit prevented repeat-track analyses. It also involves the possible use of two ECV parameters in conjunction, namely surface elevation changes and ice velocities. This is based on a study by [Hurkmans et al. \(2014\)](#), who explored the correlation between gradients of the two parameters. Finally, a comparison of changes in ice velocities and elevation changes over an approximately 15-year time period is presented, followed by a summary of the results obtained during the Ph.D. study. This outlines both the first results of the Ice Sheets CCI project as well as those generated over the past three years.

The repeat-track results from Envisat are described in the journal paper provided in Appendix B. It is published in the Remote Sensing of the Environment. The remaining work presented below is carried out for this specific study and has not yet been published.

10 The first Envisat RT results

As mentioned previously, one of the goals in the Ice Sheets CCI project is the derivation of a long-term SEC trend of the GrIS from RA. Cf. Part I describing the Round Robin exercise, the optimal method for an ice sheet-wide change detection is obtained from a combined RT and XO module. If the observations do not follow a repeat ground-track, application of the RT method is not possible and another approach will be implemented. In the case of Envisat data from 2010 – 2012, an along-track method is applied where the observations are binned into segments (Section 4.1). This section presents the first Envisat RT results over the GrIS (Appendix B). They are estimated from observations acquired during the satellite’s repeat orbit, namely from November 2002 until October 2010, and retracked with the ICE-2. The estimation is based on method (c) in Section 3.1 in the study by [Sørensen et al. \(2011\)](#). It performs a LSq adjustment adapted to RA data by also including the three waveform parameters Bs, LeW, and TeS, in the regression. This is similar to the method by [Flament and Rémy \(2012\)](#) applied to observations over Antarctica. The model in this work takes it one step further by also adjusting for seasonal variations in the surface elevation.

By applying the model to observations divided into 1000 m along-track segments, the obtained SEC estimates are as presented in Fig. 1 in the journal paper (and in a smaller version here in Fig. 10.1(b)). They show a clear thinning along the margin, which is most distinct on the west coast. Furthermore, the three outlet glaciers Jakobshavn Isbræ, Kangerdlugssuaq, and Helheim are clearly visible, all showing a thinning. Of these, Jakobshavn Isbræ shows the largest draw-down, consistent with the glacier experiencing the largest mass loss and surface velocities ([Howat et al., 2011](#); [Joughin et al., 2014](#)). In the interior ice sheet, a slight thickening is observed. Overall, the results agree well with those obtained from 2003 – 2009 ICESat RT data ([Hurkmans et al., 2014](#); [Sørensen et al., 2011](#)) and GRACE data from that same period ([Khan et al., 2010](#)); the latter study shows how a mass loss has moved up the west coast compared to previous years, consistent with the spatial distribution of elevation changes. One interesting feature is the thickening on the northeast coast, near Storstrømmen glacier in Kong Frederik VIII land, when the region north hereof shows the opposite pattern. The thickening is also observed by [Thomas et al. \(2009\)](#), who compared ATM SEC rates from repeat flights in 1994 – 1999 with those from 1999 – 2007, and by J. Nilsson, who estimated SEC from 2010 – 2014 CryoSat-2 data using both a XO and a plane-fitting module ([Nilsson, 2015](#)).

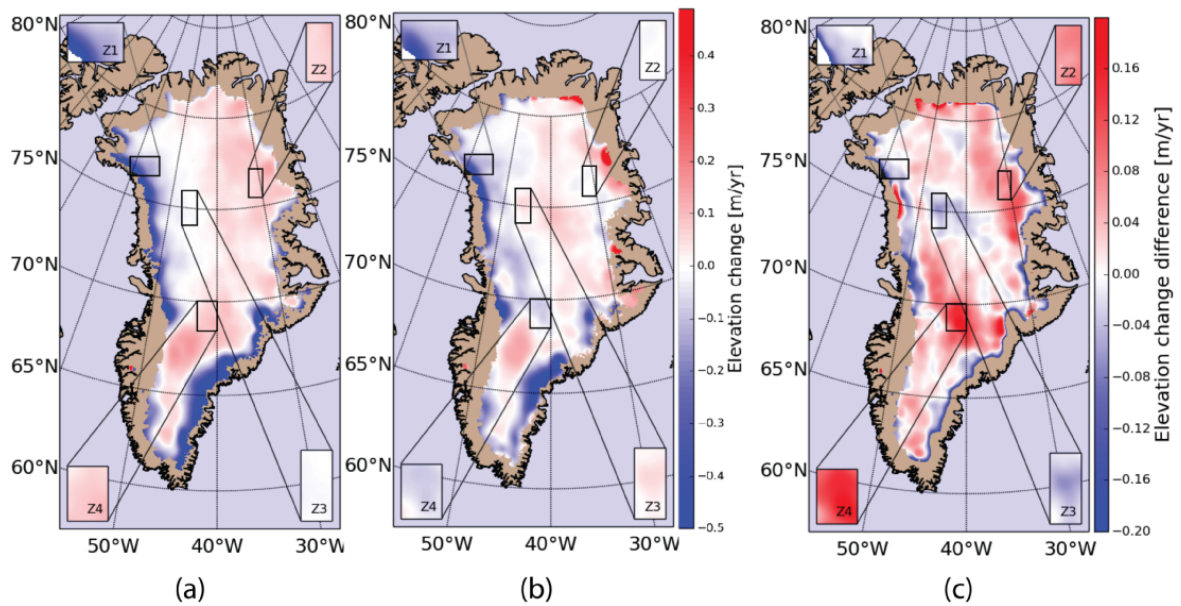


Figure 10.1 Comparison of repeat-track surface elevation changes over Greenland from ICESat (a) and Envisat (b), and the difference between the results (c). The observation period is 2003 – 2009. This is Fig. 4 in the journal paper. The regions labeled Z1 – Z4 indicate areas singled out for interpreting the different SEC signals. The interpretations are aided by modeled changes of accumulation rate and firn air content (Fig. 5 in the journal paper).

The above confirms the conclusion from the RR, namely the potential for using RA data to accurately resolve SEC throughout the ice sheet. However, as the [Sørensen et al. \(2015\)](#) study further shows, care must be taken when interpreting the SEC signal. This is concluded after comparing colocated 2003 – 2009 RT results from Envisat and ICESat; the latter data originate from the work by ([Sørensen et al., 2011](#)). The comparison is confined to observations above the equilibrium line altitude (ELA) as defined from the HIRHAM5 regional climate model (RCM) ([Lucas-Picher et al., 2012](#)). This serves to use snow parameters to explain potential differences in the SEC signal.

Fig. 10.1 illustrates the SEC estimates obtained from the two sensors while Fig. 5 in the journal paper presents two climatic parameters used for interpreting the differences: changes in the accumulation rate and in the firn air content. They are derived from the HIRHAM5 RCM and a firn densification model, respectively. Additional parameters were analyzed, such as the surface temperature and density, but none of them showed a clear correlation with the SEC differences. Four different zones (Z1 – Z4) are singled out to focus the interpretation. An example here is provided from Z1: Envisat observes a smaller thinning than ICESat, which is consistent with a decreasing accumulation rate and firn air content. The former is likely to explain the ICESat signal, as a thinning already occurs, while the latter does the Envisat signal: When the firn air content is reduced, the density of the subsurface snow/firn increases, which increases the height of the reflecting layer seen by the radar.

The overall conclusion of the comparison is that no single parameter can fully explain the observed differences; this forms the basis for the conclusion of applying caution in RA-based SEC studies. However, when performing this comparison and interpretation, the following must be remembered:

- The uncertainties associated with changes in the accumulation rate and firn air content are as high as 20% and 40%, respectively,
- Due to ICESat’s limited data acquisition periods, the observations are not acquired simultaneously,
- The different footprints mean that the sensors resolve different surface signals,
- Relocation errors may have an influence: At the time the study was conducted, the relocation analyses (Appendix D; [Levinsen et al. \(2015b\)](#)) had not been completed. As the method described by [Hurkmans et al. \(2012\)](#) shifted the points upslope, which is in accordance with theory, this method was applied with the [Bamber et al. \(2001\)](#) DEM used for topography. Such a strategy resembles that in most RA-based studies

over ice sheets. However, Table 1 in Appendix D shows that the approach used in [Hurkmans et al. \(2012\)](#) is associated with great uncertainties, and Section 3 and Tables 3 + 4 in Appendix C demonstrate that the [Bamber et al. \(2001\)](#) DEM contains errors much larger than those in other DEMs. Therefore, while this does not change the magnitude of the observed SEC signal, it does mean that the error of their distribution in space presumably has not been minimized to the degree possible. Although the largest errors are expected to occur below the ELA, it still does complicate the direct comparison with ICESat data.

All in all, RA data are indeed applicable for an ice sheet-wide SEC detection. However, we do need to further our understanding of the climatic signal in the subsurface to better understand what the radar actually sees. This requires the inclusion of climate models to better understand the changes in snow characteristics. Although none of the climatic parameters fully and singlehandedly explain the RA-LA SEC offsets, they do provide important information on the physics behind the differences.

11 The first merged RT and XO results

The following serves to present a preliminary merged RT and XO SEC product from Envisat data. As the long-term CCI SEC product consists of five-year running means ([Sørensen, 2012](#)), the period from 2006 – 2010 is chosen for this study. It provides a fair basis for comparison with the 2002 – 2010 RT data, while the observation period ends before Envisat was put into a drifting phase. The RT trend is produced in a manner similar to the above, again in 1000 m along-track segments. XO data are processed using the method by [Khvorostovsky \(2012\)](#), described in Section 3.1, and binned into $0.2^\circ\text{lat} \times 0.5^\circ\text{lon}$ grid cells. The observations are retracked with the ICE-1 rather than ICE-2. The reasoning is found in the processing of ERS data for the final product, which originate from the REAPER dataset ([European Space Agency, 2014a](#)): The REAPER data contain ranges derived with both an Envisat-style ICE-1 and the ICE-2 retrackers, and thereby contain all three waveform parameters. However, the ICE-2 results are currently subject to large biases and noise meaning that care must be taken when assessing the data quality (Steven Baker, pers. comm., September 2014). In order to minimize errors from retracking the ERS and Envisat data differently, the ICE-1 was preferred. The main difference between this dataset and that from the ICE-2 is that the ICE-1 product does not

contain all three waveform parameters. As such, the only correction performed in the LSq adjustment for both RT and XO data is for Bs.

Building on the relocation analyses, the two SEC products are relocated using the POCA with the GIMP DEM regrided to a 2 km posting. They are then merged into a $0.05^\circ\text{lat} \times 0.125^\circ\text{lon}$ grid, i.e. approximately 5×5 km, using GRAVSOFTE collocation (Appendix G) (Forsberg and Tscherning, 2008).

The results are presented in Fig. 11.1. Similarly to Fig. 1 in the Sørensen et al. (2015) paper, they show the large thinning on the west coast, particularly near Jakobshavn Isbræ and north hereof (a). The thinning over the Helheim glacier is clearly visible, while that over Kangerdlugssuaq is not as pronounced. This may reflect the less abrupt mass changes observed during that same period by Howat et al. (2011), who investigated the yearly changes over the period 2000 – 2011. As in the 2002 – 2010 RT changes, the southern GrIS appears to be thinning, whereas the interior and the area near Storstrømmen glacier are thickening. The region north of Storstrømmen is thinning. The SEC errors (b) are estimated as the mean residual between the model fit and input observations. They reach a maximum of 0.31 m yr^{-1} with the highest values located on the west and northeast coasts. This is consistent with regions experiencing the largest SEC and hence reflect both the rapid surface changes as well as the dynamic topography captured by the RA footprint. Another noticeable feature in the error map is the overall higher errors in the south, arising from the increasing separation distance between ground-tracks, which decreases the availability of RT and XO points. Furthermore, XO errors at lower altitudes are typically higher than RT errors, potentially owing to the topographic variability within the grid cells. Reasons for XO errors are discussed in greater detail in Section 12 below.

As the overall spatial SEC pattern agrees with those observed with ICESat and Envisat (Section 10), this first merged solution therefore does resolve changes on both a basin- and ice sheet-scale. This serves as a promising start.

The final data product will be derived from merging the RT and XO estimates weighted by their corresponding errors. Hence, the interior will be covered by combined RT and XO data while the solution along the margin predominantly will consist of RT data. Another thing to note is the application of the ICE-1 retracker rather than the ICE-2. This means that the tracking point is found differently, which may result in a range offset. Furthermore, in spite of the REAPER data containing all three waveform parameters, the only parameter corrected for here is the Bs. The effect of this is elaborated upon in Section 13.

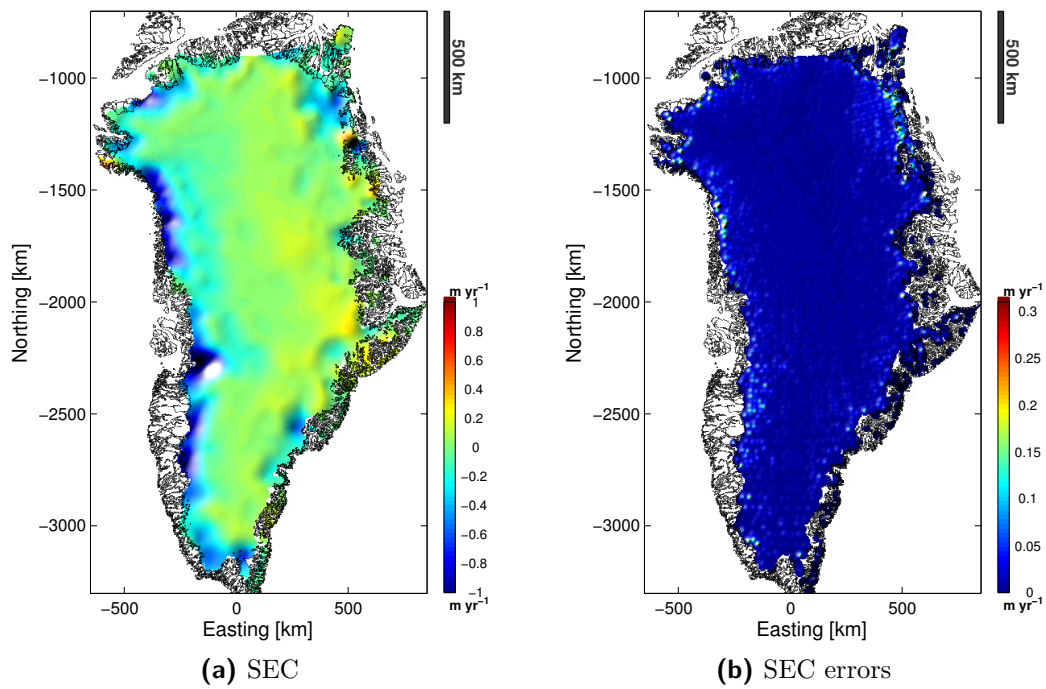


Figure 11.1 Preliminary SEC results (a) and corresponding error map (b) from Envisat when merging separate repeat-track and cross-over results using collocation. The observation period is 2006 – 2010. Please note the different scales on the colorbars.

12 Relocation methods' impact on volume changes

As discussed earlier, relocation methods can be associated with great uncertainties. In order to explore potential consequences, an analysis is made where the RT and XO solutions from 2006 – 2010 are relocated separately in three different ways after which the estimates are converted into volume changes, $\frac{dV}{dt}$. The focus area is that over the Jakobshavn Isbræ drainage basin as it was also used in the Round Robin exercise.

More specifically, a 100×100 km area is chosen near the glacier outlet. The RT and XO estimates within this region are selected and relocated separately. The latter occurs with the POCA based on the GIMP regrided to 500 m and 2 km postings, respectively, as well as the [Hurkmans et al. \(2012\)](#) method, also using the GIMP at 2 km. The POCA method demonstrates the effect of applying a high, respectively, low resolution model of surface topography to RA data; the [Hurkmans et al. \(2012\)](#) method using the GIMP at the otherwise optimal spatial resolution still produces an offset.

Following relocation, the RT data are interpolated onto a 1×1 km grid cf. the size of the along-track segments. Similarly, XO data are interpolated onto a 15×20 km grid corresponding to the $0.5^\circ\text{lon} \times 0.2^\circ\text{lat}$ resolution. Using SI units, the volume change estimate is derived and converted into $\text{km}^3 \text{yr}^{-1}$ cf.:

$$\frac{dV}{dt} = \left(\sum_{i=1}^N A_i \frac{dH_i}{dt} \right) \times 10^{-9}$$

A_i corresponds to the area of the respective grid cell as mentioned above. The location and estimation values of the input SEC data are shown in Fig. 12.1. As in the remaining figures in this section, both solutions are plotted as point values rather than 1×1 km or 15×20 km cells. This is done to better illustrate the range of the SEC estimates as well as the effect of the relocation. Fig. 12.1 shows that only 11 XO points are available, which is far less than the 320 RT points. XO data are mostly confined to higher altitudes rather than the drainage basin, and the SEC values range from -4.4 to 0 m yr^{-1} . Most signals are more positive than -1.5 m yr^{-1} . RT data cover greater parts of the fast-moving drainage basin. The SEC signals span -7.2 to 0 m yr^{-1} with most values higher than -4.5 m yr^{-1} . Fig. 12.2 shows the position of all relocated XO points, while a subset is presented for RT. The subset is made as plotting of all the RT points would make it difficult to obtain a clear image of the displacements.

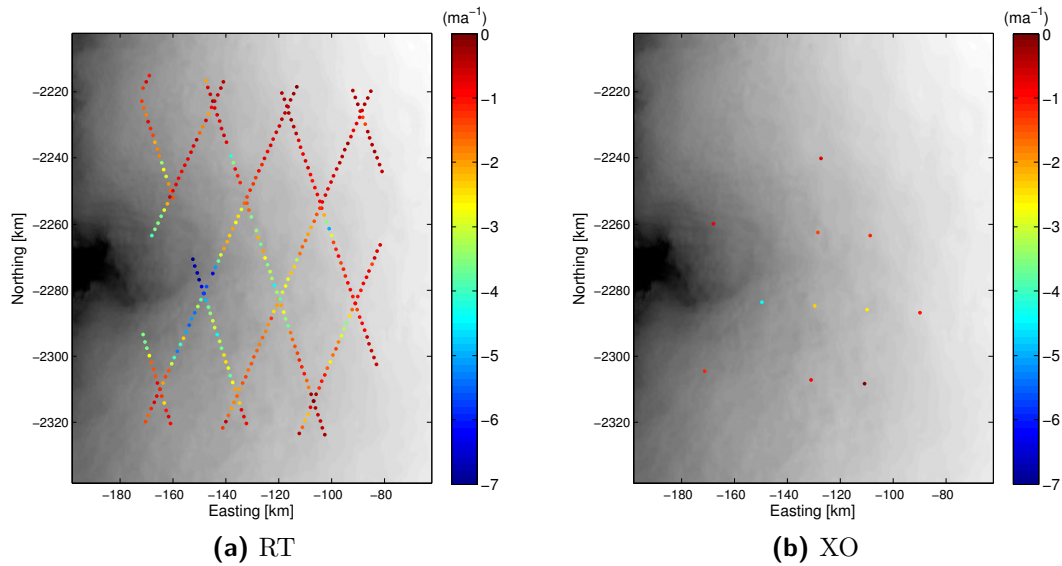


Figure 12.1 Original location of surface elevation change estimates derived using the repeat-track (a) and cross-over (b) methods. The observation period is 2006 – 2010.

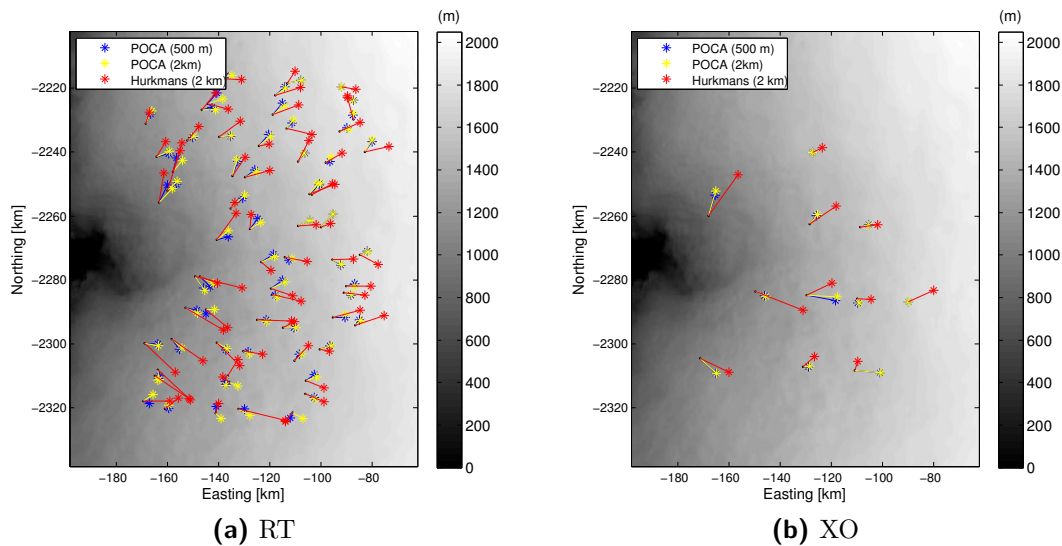


Figure 12.2 Relocated location of surface elevation changes derived using the repeat-track (a) and cross-over (b) methods. The observation period is 2006 – 2010. Due to the large amount of repeat-track points, (a) only shows every fifth observation. This makes it easier to visualize the effect of the relocation.

Method	Volume change [km ³ yr ⁻¹]	Deviation from mean (method) [%]	Deviation from mean (total) [%]
RT Hurk (2 km)	-24.02	-6.15	-48.01
RT POCA (500 m)	-21.93	3.08	-35.13
RT POCA (2 km)	-21.93	3.07	-35.14
XO Hurk (2 km)	-8.91	9.36	45.10
XO POCA (500 m)	-10.27	-4.49	36.71
XO POCA (2 km)	-10.31	-4.87	36.48

Table 12.1 Volume change estimates from three differently relocated repeat-track and cross-over solutions. The observation period is 2006 – 2010. The deviation from the mean per method (second column) and for both methods combined (third column) are also shown.

Volume changes are derived for all datasets, and deviations from the mean value are calculated both relative to the specific method (either RT or XO) and to the combined estimate. The results are presented in Table 12.1. All values of volume change are negative, signifying a volume loss. The RT method produces the highest loss. It has a mean value of 22.63 km³ yr⁻¹ and reflects the ground-tracks crossing parts of the fast-moving basin. The XO values are lower, with a mean of 9.83 km³ yr⁻¹. This is due to two of things: The location of the points at higher altitudes where smaller surface changes occur, and the large grid cells, which result in part of the SEC signal being lost when averaging the observations. The same observation was made in the Round Robin exercise. Additional errors may arise from the fact that the XO points are relocated during post-processing, not pre-processing, such that grid cells may be wrongly located, and that these locations may do not necessarily correspond to the exact XO point location. The mean volume loss for the two methods is 16.23 km³ yr⁻¹.

When considering the volume losses with respect to the mean for each method (second column, Table 12.1), the two POCA relocations yield similar results for both RT and XO; the former estimate is, however, more than twice that of the latter. Similarly, the RT result based on the [Hurkmans et al. \(2012\)](#) method is approximately three times as high as that for XO. Within the RT segment, variations of $\frac{dV}{dt}$ reach 9.23% while those for XO data reach 14.23% (column 2). When compared with the combined mean, the numbers change to 12.88% and 8.62%, respectively (column 3).

[Hurkmans et al. \(2012\)](#) lowered the volume change error by 14% relative to

ICESAT/ATM data by applying this relocation method to Envisat data. Assuming the rates from the 2 km RT POCA approach to be more realistic (Appendix D: Table 1), this study suggests that the volume change error can be reduced even further. The choice of relocation method therefore has a significant impact on the estimation accuracy.

Whereas deviations from the separate RT or XO mean values are typically around 10% percent, those with respect to the combined mean range from $\pm 35\%$ to $\pm 48\%$. Particularly the latter numbers are very high. Fig. 12.3 shows the SEC values from Fig. 12.1 overlain elevation changes derived by co-registering stereoscopic imagery from SPOT-5 to contemporary ATM and ICESat data. This reduces horizontal and elevation-dependent errors in the imagery and allows for resolving the changes with a resolution of 100 m. The observation period is 2007 – 2008 (Levinsen et al., 2013). It is clear that the RT and XO locations do not cover the fastest-changing parts of the glacier, and this indicates that the full volume loss cannot be resolved even with RT data. Therefore, the percentile deviations send a highly important signal: That we need to tread carefully when interpreting volume changes from altimetry data. In case the volume changes are used to infer mass changes, a similar 'warning' applies here.

The issue is highlighted by Simonsen et al. (2015), who compared volume and mass changes from ICESat data with those from combined ICESat and airborne laser-scanner data. The studied region was the Godthåbsfjord drainage basin on the west coast of Greenland. The airborne campaigns covered the outlet glaciers, unlike the ICESat ground-tracks at higher altitudes. The inclusion of airborne data doubled the estimated mass loss and thereby made a substantial contribution to the observed changes. This indicates that the combination of data allowed for a more realistic change detection than that from ICESat data alone.

In order to put the values estimated in this work into a perspective, published values of volume and mass losses are presented in the following: Helm et al. (2014) estimated an ice sheet-wide volume loss of $146 \text{ km}^3 \text{ yr}^{-1}$ using 2003 – 2009 ICESat data, while Nilsson (2015) found $224 \text{ km}^3 \text{ yr}^{-1}$ from 2011 – 2014 CryoSat-2 data. Howat et al. (2011) published mass changes from combined discharge and SMB estimates and found Jakobshavn Isbræ's total mass loss to vary between 25 Gt yr^{-1} and 34 Gt yr^{-1} in the years 2006 – 2010. Shepherd et al. (2012) found a GrIS mass loss of 263 Gt yr^{-1} from 2005 – 2010. The studies indicate that the changes over Jakobshavn Isbræ represent

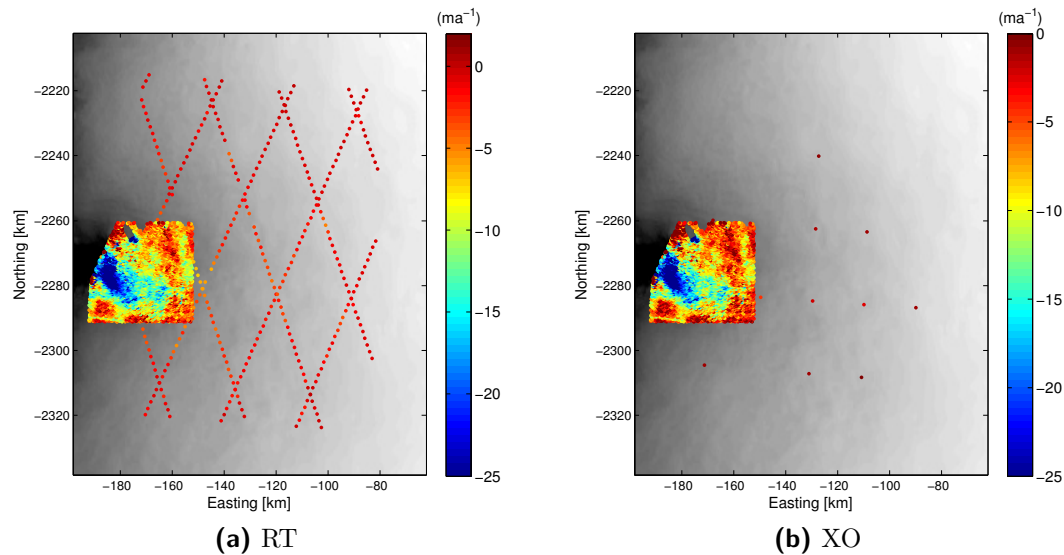


Figure 12.3 Original location of Envisat surface elevation changes from 2006 – 2010 derived using the repeat-track (a) and cross-over (b) methods. The values are overlain elevation changes from 2007 – 2008 derived from SPOT-5 imagery co-registered to ICESat and ATM data. They are obtained from the study by [Levinson et al. \(2013\)](#). Please note the different color scale compared to Fig. 12.1.

approximately 10% of the total ice sheet. It supports the finding that the RT estimates are the ones best representing the truth, however that they underestimate the total change. This underlines the effect of the number and spatial distribution of RT and XO points: Errors are introduced when interpolating the point values to the 100×100 km observation area; these are largest for the 11 XO points, which simply cannot reproduce a realistic pattern of changes. In conclusion, care must be taken in analyses of volume and mass changes from altimetry data, and the choice of relocation method will affect the resulting accuracy when using RA data.

13 Perspectives and future work

Following the estimation of a 2002 – 2010 SEC trend from Envisat data, the next step is to make a similar study of 2010 – 2012 data from the satellite’s drifting phase. A brief description of the applied along-track method is provided in Section 4.1. The model requires a DEM to subtract a topographic signal from the elevations. As the RL-DEM developed in this study (Part II) has a 2×2 km resolution, and the final SEC product is gridded to 5×5 km, the respective resolution is sufficient for accurately aiding the SEC estimation. It will therefore be included in the process. Cf. the relocation study (Appendix D) and the RL-DEM’s 2010 reference epoch, an additional benefit is its applicability in relocating the Envisat data. As such, it will be applied for this purpose as well.

Given the availability of a routine for Envisat RT estimation using both ICE1 and ICE2 retracked data, a straightforward study would be to analyze the effect of waveform parameters on SEC when using either retracker. [Khvorostovsky \(2012\)](#) investigated the effects from Bs and all three waveform parameters combined using 1992 – 2008 ERS and Envisat data, retracked using a 10% threshold algorithm provided by NASA/GSFC ([Davis, 1997](#)). He found a mean correction for all waveform parameters of 0.9 ± 1.7 cm yr⁻¹. The range of the correction was ± 10 cm yr⁻¹. As such, the effect on the SEC signal is relatively small. It does, however, provide important information for furthering our understanding of the physical signal inherent in radar data, such as regarding surface penetration. Therefore, one study could involve separate investigations of Bs, LeW, and TeS on the ICE-2-derived SEC signal. In case of a future REAPER ICE-1 release containing all three waveform parameters, a similar study could be carried out on those data. Additionally, a comparison of ICE-1 with ICE-2 while only correcting for Bs would provide information on potential differences between the signal in each dataset.

Another step is to correlate SEC with climatic signals, such as changes in the firn air content and accumulation rate, surface density and temperature, etc. Direct comparisons are complicated due to different spatial resolutions and uncertainties of the data and models, as was e.g. highlighted by [Lucas-Picher et al. \(2012\)](#). They compared regional climate model output calculated at different spatial resolutions over the GrIS. HIRHAM5 simulations of summer and winter temperature and precipitation patterns at 0.05° and 0.25° resolutions were compared with ERA-Interim reanalysis model output interpolated onto a 0.75° grid. They found a good overall agreement between large-scale patterns

from all outputs, however that the high-resolution model more accurately reproduced the expected spatial weather patterns relative to topography: Snow accumulation peaks over the coasts were better captured, and an intensification of precipitation over fjord systems was observed. Furthermore, the mountains along the coast were higher than in lower-resolution models resulting in a colder climate. At the same time, however, particularly a winter warm temperature bias was found when compared with automated weather station data. The source may be located in the model specifications, as e.g. a poor vertical resolution of an input model would prevent it from accurately representing the katabatic winds prevailing over the ice sheet, or the cloud cover affecting the amount and distribution of incoming radiation.

However, with today's availability of observations and model output, a comparison of RA SEC trends with climatic data might still yield important information aiding the interpretation of the RA signal.

When working with RA data, the margins may be poorly resolved due to the satellite losing lock and the large footprint. In this case, a number of methods exist for preventing a reduced spatial coverage of SEC estimates. [Zwally et al. \(2005\)](#) supplemented ERS-1 and -2 data with ATM data, while [Hurkmans et al. \(2014\)](#) found the gradient of changes in ice velocities (IV) to correlate with the gradient of SEC. Both studies cover the GrIS, and the advantage of the latter is the inclusion of another output parameter from the Ice Sheets CCI project, namely IV.

[Hurkmans et al. \(2014\)](#) found the highest correlation over dynamically thinning regions, such as those containing Jakobshavn Isbræ, Kangerdlugssuaq, Helheim and, to a lesser degree, the Upernavik glacier. In those cases, space-time kriging with an external drift (ST-KED) was applied for deriving the SEC. The method thus was confined to margin regions. In ST-KED, a semi-variogram was fitted both in space and time, and the two were combined by assuming a linear relationship between the SEC rate and IV. It was applied for ice velocities exceeding 70 m yr^{-1} and regression slope lower than -2 . Over other regions, ordinary kriging was applied.

The external drift component is ideal over regions with sparse altimetry data or strong velocity gradients. Drawdowns of the method are the lack of accounting for the gradient in accumulation as this may affect the SEC pattern, and that one cannot assume a constant correlation over such large basins as those implemented here. It works well when the main reason for SEC is dynamic thinning, but this pattern may change during the observation period, hence lowering the accuracy of the output. However, given the grand availability of

IV produced in the CCI project, merging of the two parameters is ideal for increasing the spatial coverage of SEC estimates. At present stage, winter IV from Phase 1 of the project cover:

- The northern basins using 1991/1992 ERS-1 data,
- The margin using 1995/1996 ERS-2 data,
- The margin using 2006 – 2010 ALOS/PALSAR data,
- The Upernavik glacier using 1992 – 2011 ERS-1 and -2, ALOS/PALSAR and Envisat/ASAR data, whenever available,
- The Academy, Hagen and Petermann glaciers using 1995/1996 ERS-2 and 2009/2010 ALOS/PALSAR data,
- Jakobshavn Isbræ using 1995/1996 ERS-2 and 2008/2009, 2009/2010 ALOS/PALSAR data.

The IV maps have a spatial resolution of 500 m. More information on the temporal and spatial distribution of IV estimates can be found in [Shepherd \(2012\)](#); [Sørensen \(2012\)](#). The work mentioned above is carried out during Phase 1 of the project, which runs from March 2012 to February 2015. Phase 2 will take place from March 2015 to February 2018. In this latter project phase, IV estimates will be generated for the entire GrIS as well as nine specific, major outlet glaciers. The computations will be based primarily on Sentinel-1 (launched April 2014) and 2012/2013 Radarsat data, combined with ERS-1 and -2 and Envisat data when necessary. Therefore, with CryoSat-2's continued operation, the expected launch of Sentinel-3A in late 2015 ([European Space Agency, 2015](#)), and the repeated IV maps over the margin, the foundation is formed for exploiting the high-resolution IV data for SEC mapping over regions with lacking altimetry data.

14 ECV parameters for surface change detection

Following on from the SEC results in Section 11 and the production of IV maps mentioned above, the focus of this section is a comparison of results over time to consider the change in trends. All values are generated in the Ice Sheets CCI project and are applicable for detection of surface changes over ice sheets. The observation area covers Jakobshavn Isbræ, and the results confirm why this region was chosen for the Round Robin exercise (Part I).

Based on the IV data availability, and the first, five-year running means from RT and XO estimates being available for the years 1996 – 2000, the following is considered: IV maps from 1995/1996 ERS-2 and 2008/2009 ALOS/PALSAR data, and RT and XO solutions from 1996 – 2000 ERS-2 and 2006 – 2010 Envisat data. The results are presented in Figures 14.1 – 14.2, which also show a change in trends over the period. The SEC values from 1996 – 2000 are generated in the same way as those in Section 11, i.e. by separately relocating the RT and XO measurements and merging them onto a $0.05^\circ\text{lat} \times 0.125^\circ\text{lon}$ grid.

For IV (Fig. 14.1), it is clear that a major speed-up over the main trunk has occurred and that velocities have increased with up to 800 m yr^{-1} . The velocities have increased throughout most of the area, particularly over the region covering and surrounding the trunk. A few negative values are found, indicating a slow-down. This may be attributed to errors resulting from a lack of coherence due to snowfall, decreasing the image-to-image correlation. The significant speed-up is consistent with results from [Joughin et al. \(2010\)](#), who found a more than doubling of the speeds over Jakobshavn when comparing 2000/2001 and 2005/2006 velocities from RADARSAT data.

The SEC results (Fig. 14.2) show an increased thinning throughout the region. During the first five-year period, only slightly negative values are found, which decrease to yielding a stronger thinning with time. The negative pattern does not reflect the specific location of the glacier outlet and trunk, as does the IV maps. This is likely due to the $1 \times 1 \text{ km}$ RT and $0.2^\circ\text{lat} \times 0.5^\circ\text{lon}$ XO measurements being regridded onto an approximately $5 \times 5 \text{ km}$ map, thus preventing the resolution of features with smaller horizontal scales.

Overall, however, the pattern of an increased thinning correlates with an increased speed-up. The change in trends reflects an increased dynamic mass loss. This could not be concluded from altimetry data alone and hence illustrates the need for both datasets to better interpret the changes. The timing is consistent with periods of warming leading to the disintegration of the glacier's floating tongue in 2003 and thus to increased flow speeds ([Joughin et al., 2004, 2010](#)). Furthermore, it is in agreement with the study by [Howat et al. \(2011\)](#) as well as other results from the CCI project: The former showed an increased ice discharge resulting from a significant change in ice flow rate (2000 – 2011), while the latter demonstrated rapid retreats of the calving front (Fig. 14.3). The calving front locations are derived from Envisat Advances Synthetic Aperture Radar (ASAR) imagery acquired in the summers 2003 to 2010; they make

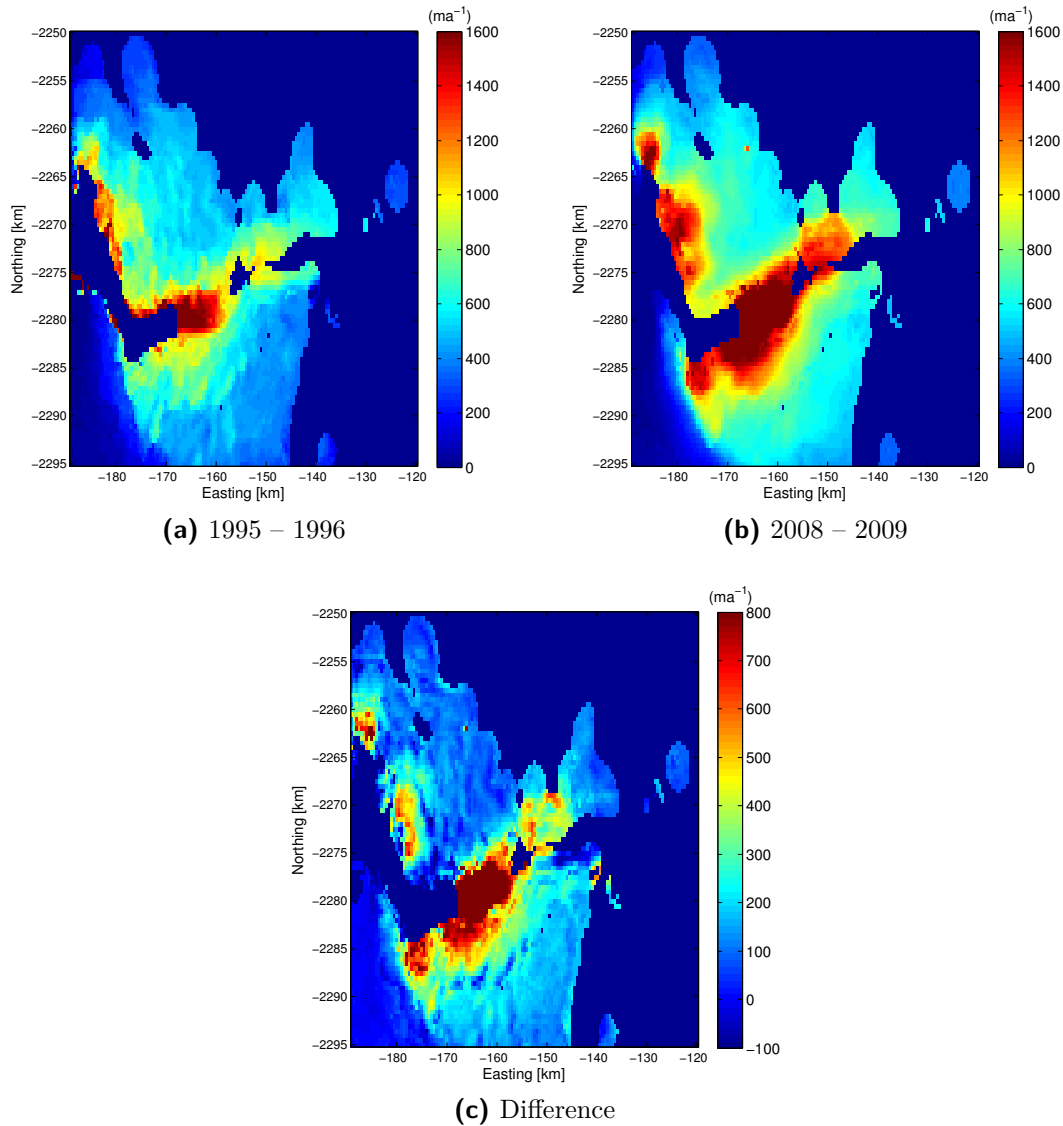


Figure 14.1 Ice velocities over Jakobshavn Isbræ for the winters 1995/1996 (a) and 2008/2009 (b) as well as the difference in trends (c). They are derived from ERS-2 and ALOS/PALSAR data, respectively, and generated in the Ice Sheets CCI project.

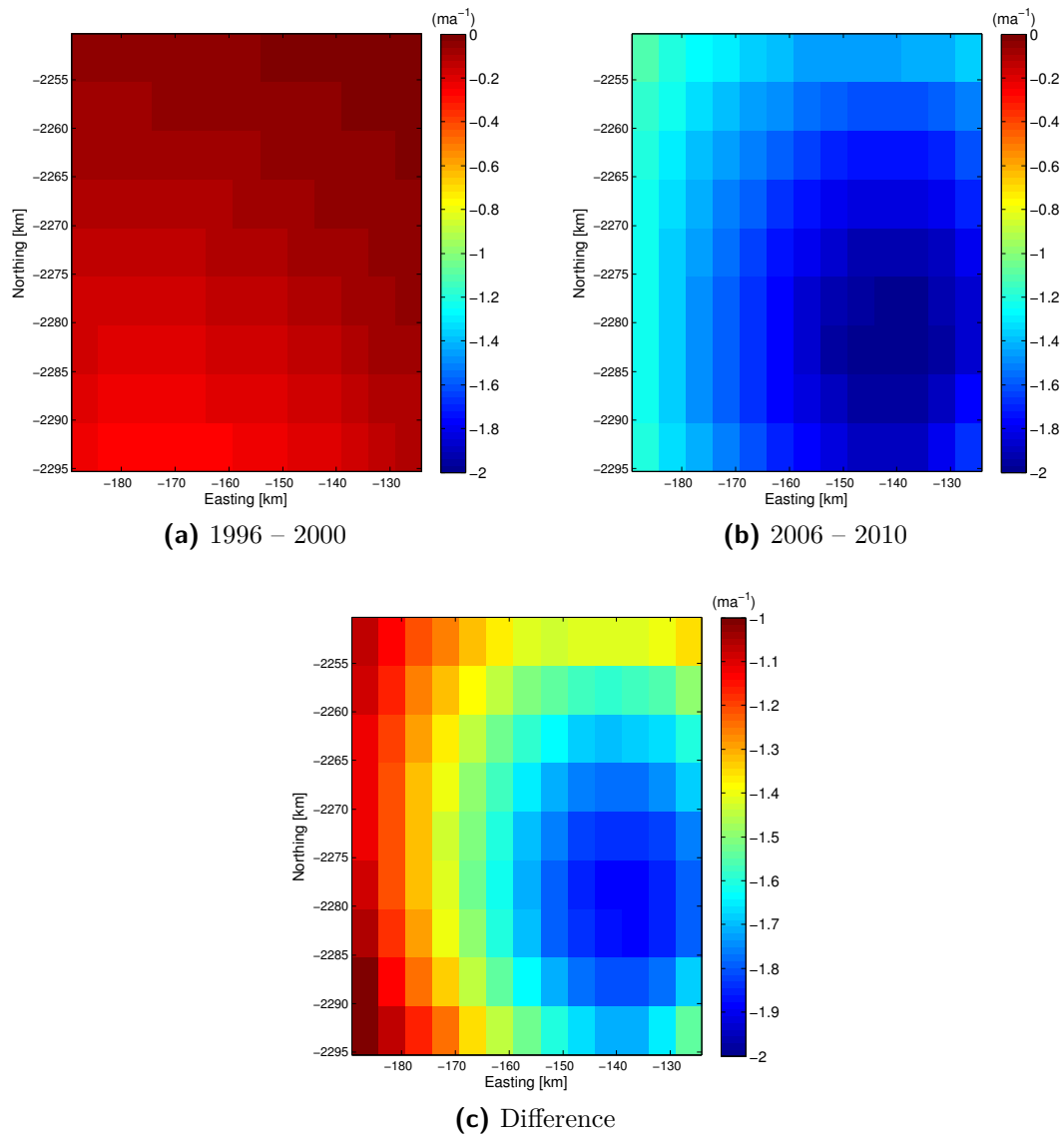


Figure 14.2 Surface elevation changes over Jakobshavn Isbræ for the periods 1996 – 2000 (a) and 2006 – 2010 (b) as well as the difference in trends (c). They are derived from RT and XO solutions from ERS-2 and Envisat data merged onto a 5×5 km grid. The values are generated in the Ice Sheets CCI project.

out a third parameter to be derived in the Ice Sheets CCI project (Sørensen, 2012).

The above demonstrates a dynamic mass loss and thereby that the method described by Hurkmans et al. (2014) is indeed applicable for SEC detection when few or no altimetry data are available. It further documents the significant surface changes having occurred by Jakobshavn Isbræ over the past nearly two decades, and that these are observable using a number of techniques and datasets. Any further analyses of the observations are beyond the scope of this Ph.D. study. The mass loss consists of a SMB and a dynamic component (Andersen et al., 2015), and particularly the latter is not yet well understood (Joughin et al., 2012; Straneo and Heimback, 2013). Therefore, finally, the above explains why the region is the subject of a great many studies, such as the Round Robin, to comprehend the complex nature of the change signal.

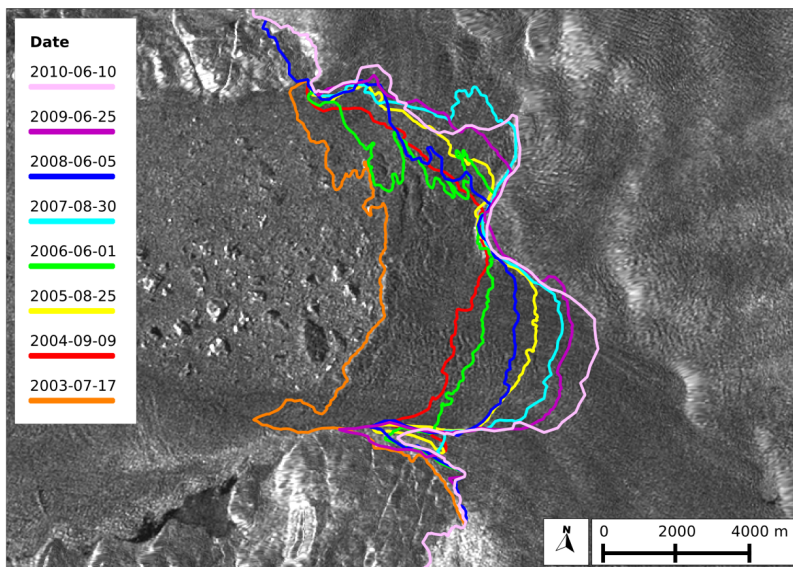


Figure 14.3 Calving front locations over Jakobshavn Isbræ derived from Envisat ASAR imagery acquired in the summers 2003 – 2010. The estimates are generated in the Ice Sheets CCI project.

15 Outlook and conclusions

The focus area of this Ph.D. study is the GrIS. It was carried out as part of the Ice Sheets CCI project, where one goal is to derive continuous, ice sheet-wide SEC time series starting in 1992. The time series will be based on merged ESA radar altimetry data from ERS-1 and -2, Envisat, CryoSat-2, and, in the future, Sentinel-3. This is made possible after the recent release of ERS REAPER data, which significantly increased the accuracy of the observations ([European Space Agency, 2014a,d](#)). The time series generated in the CCI project will be provided as five-year running means gridded to a 5×5 km resolution ([Sørensen, 2012](#)).

In this Ph.D. study, a so-called Round Robin exercise was carried out to find the optimal approach for the elevation change detection. Ten different solutions submitted by the scientific community were inter-compared relative to the choice of altimeter and method. Through validation against contemporary SEC trends from ATM data, two important conclusions were drawn: Repeat-track solutions from radar altimetry can be used for resolving ice sheet-wide elevation changes, and a combined repeat-track and cross-over module yields the most accurate results. The latter results from the exploitation of the high spatial coverage of repeat satellite ground-tracks, while errors from slope effects are reduced in intersections between ascending and descending orbits.

Therefore, the first, ice sheet-wide repeat-track result from Envisat's repeat orbit (2002 – 2010) is presented here along with a repeat-track and cross-over result from the period 2006 – 2010. The latter is also based on Envisat data and consists of a direct merging of the two datasets. Both RT and XO results reveal a thinning, which is mostly distinct along the west coast, and a thickening of the interior. This is in accordance with the pattern observed by e.g. [Sørensen et al. \(2011\)](#). Locations of the maximum errors agree with regions with steep topography, indicating that they reflect both the rapid surface changes with time as well as the dynamic topography within the area illuminated by the radar.

When the space-time distribution of radar echoes is random, the repeat-track method has to be replaced by a different approach. This is the case for both CryoSat-2 SARIn and 2010 – 2012 Envisat data. One solution is the application of an along-track algorithm where the elevation changes are derived relative to a reference track. A DEM can then be used to correct the radar heights for topography.

Acknowledging the need for an up-to-date reference DEM, such one is de-

veloped here. It is based on Envisat and CryoSat-2 radar data from 2010 combined with ICESat, ATM, and LVIS laser data; the RL-DEM. Laser data are acquired in 2009 and 2010, and observations from the first year are adjusted to the latter by accounting for the elevation changes. This increases the spatial data coverage and reduces the RL-DEM errors. Vertical errors in radar data are corrected by assuming laser data to span the true surface and adjusting the radar heights relative hereto; this accounts for subsurface penetration of the echoes. Horizontal errors are reduced by relocating the Envisat, LRM, and SARIn data separately. This is done to achieve the highest accuracy possible for each dataset. The result is a 2×2 km DEM referenced to the WGS-84 ellipsoid and with a reference epoch in 2010. The use of a short observation period provides the RL-DEM with a strong advantage over other models, particularly those built from radar data: They are usually developed from observations acquired over longer time periods, hence introducing vertical errors from intermediate elevation changes, or a short time period, which compromises the amount of resolved surface detail. The RL-DEM instead exploits the advantages of each dataset to increase the accuracy in both time and space.

The Round Robin exercise showed that elevation change maps with a 5×5 km resolution is sufficient for an ice sheet-wide elevation change detection from radar altimetry. This indicates that the RL-DEM is suitable for application in such analyses. During the process related to the DEM development, a number of things became clear, two of which are mentioned here: That the relocation of radar data is highly dependent on the applied method, and that the RL-DEM is suitable for relocating radar data with measurement characteristics similar to Envisat's.

The above was found in an elaborate study of relocation methods to account for slope-induced errors in conventional radar altimetry data. A number of approaches were tested on Envisat data over Jakobshavn Isbræ and on CryoSat-2 LRM data over the interior ice sheet. The observations were acquired in 2010, and all methods relocated the points horizontally to ensure agreeing locations and measured ranges. The analyses revealed significant inconsistencies both with respect to the direction and distance of the displacement: Some points were shifted down-slope to locations closer to the glacier outlet and ice margin, while other displacement vectors intersected in spite of the observations lying within the same footprint. Validation against contemporary ATM data revealed the Point of Closest Approach (POCA) method to yield the optimal results, and that this required a model at a 2 km resolution for both datasets to generate the surface topography. This resolution therefore is applicable over

regions with a steep as well as smooth surface topography. The main conclusion of the study was that a number of relocation methods are associated with significant errors, which will reduce the accuracy in the respective analyses of, e.g., surface elevations or derived volume and mass changes. Caution therefore is necessary when selecting the technique.

When converting the relocated repeat-track and cross-over estimates from 2006 – 2010 into volume changes, a number of things were found: The choice of relocation method affected the volume changes, and depending on the approach, variations of approximately 10% to 50% occurred. Furthermore, as the repeat-track locations do not necessarily coincide with regions subject to the largest surface changes, not even these data alone can fully resolve the signal of change. Repeat-track estimates therefore underestimate the volume changes. This issue is even larger for cross-over data as they represent averages over larger regions, and because the points are typically located at higher altitudes. As additional offsets in elevation change estimates, and thereby volume changes, result from the radar echoes being subject to e.g. surface penetration and volume scatter, care therefore must be taken when using altimetry data for surface-based analyses over ice sheets.

Bibliography

- W. Abdalati, H. Zwally, R. Bindenschadler, B. Csatho, S. Farrell, H. Fricker, D. Harding, R. Kwok, M. Lefsky, T. Markus, A. Marshak, T. Neumann, S. Palm, B. Schutz, B. Smith, J. Spinhirne, and C. Webb. The ICESat-2 Laser Altimetry Mission. *Proceedings of the IEEE*, 98(5):735–751, May 2010. doi: 10.1109/JPROC.2009.2034765.
- J. B. Abshire, X. Sun, H. Riris, J. M. Sirota, J. F. McGarry, S. Palm, D. Yi, and P. Liiva. Geoscience Laser Altimeter System (GLAS) on the ICESat Mission: On-orbit measurement performance. *Geophys. Res. Lett.*, 32(21), 2005. ISSN 1944-8007. doi: 10.1029/2005GL024028.
- M. Aguirre, B. Berruti, J.-L. Bezy, M. Drinkwater, F. Heliere, U. Klein, C. Mavrocordatos, and P. Silvestrin. The Ocean and Medium-Resolution Land Mission for GMES Operational Services. ESA Bulletin 131, European Space Agency, 2007.
- D. E. Alsdorf and L. C. Smith. Interferometric SAR observations of ice topography and velocity changes related to the 1996, Gjalp subglacial eruption, Iceland. *Int. J. Remote Sens.*, 20(15-16):3031–3050, 1999. doi: 10.1080/014311699211606. URL <http://dx.doi.org/10.1080/014311699211606>.
- M. Andersen, L. Stenseng, H. Skourup, W. Colgan, S. Khan, S. Kristensen, S. Andersen, J. Box, A. Ahlstrøm, X. Fettweis, and R. Forsberg. Basin-scale partitioning of Greenland ice sheet mass balance components (2007–2011). *Earth Planet. Sci. Lett.*, 409:89–95, 2015. doi: 10.1016/j.epsl.2014.10.015.
- Aresys. Cryosat footprints. Aresys Technical Note 1.1, March 2013.
- J. L. Bamber. Ice sheet altimeter processing scheme. *Int. J. Remote Sens.*, 15(4):925–938, 1994. doi: 10.1080/01431169408954125. URL <http://dx.doi.org/10.1080/01431169408954125>.
- J. L. Bamber, S. Ekholm, and W. B. Krabill. A new, high-resolution digital elevation model of Greenland fully validated with airborne laser altimeter data. *J. Geophys. Res. - Sol. Ea.*, 106(B4):6733–6745, 2001. doi: 10.1029/2000JB900365.
- M. Bevis, J. Wahr, S. A. Khan, F. B. Madsen, A. Brown, M. Willis, E. Kendrick, P. Knudsen, J. E. Box, T. van Dam, D. J. Caccamise, B. Johns, T. Nylén, R. Abbott, S. White, J. Miner, R. Forsberg, H. Zhou,

BIBLIOGRAPHY

- J. Wang, T. Wilson, D. Bromwich, and O. Francis. Bedrock displacements in Greenland manifest ice mass variations, climate cycles and climate change. *Proc. Natl. Acad. Sci. U.S.A.*, 109(30):11944–11948, 2012. doi: 10.1073/pnas.1204664109.
- B. Blair and M. Hofton. IceBridge LVIS L2 Geolocated Surface Elevation Product. <http://nsidc.org/data/docs/daac/icebridge/ilvis2/>, Boulder, Colorado USA: NASA DAAC at the National Snow and Ice Data Center, 2012. Checked June 2014.
- G. Bohling. Introduction to Geostatistics and Variogram Analysis. <http://www.ecst.csuchico.edu/~juliano/csci693/Presentations/2008w/Materials/Kalkundrikar/DOCS/Variograms.pdf>, Kansas Geological Survey, October 2005.
- A. A. Borsa, G. Moholdt, H. A. Fricker, and K. M. Brunt. A range correction for ICESat and its potential impact on ice-sheet mass balance studies. *The Cryosphere*, 8(2):345–357, 2014. doi: 10.5194/tc-8-345-2014. URL <http://www.the-cryosphere.net/8/345/2014/>.
- A. C. Brenner, R. A. Bindshadler, R. H. Thomas, and H. J. Zwally. Slope-induced errors in radar altimetry over continental ice sheets. *J. Geophys. Res. - Oceans*, 88(C3):1617–1623, 1983. doi: 10.1029/JC088iC03p01617.
- A. C. Brenner, J. P. DiMarzio, and H. J. Zwally. Precision and Accuracy of Satellite Radar and Laser Altimeter Data Over the Continental Ice Sheets. *IEEE T. Geosci. Remote.*, 45(2):321–331, 2007. doi: 10.1109/TGRS.2006.887172.
- G. Brown. The average impulse response of a rough surface and its applications. *Antennas and Propagation, IEEE Transactions on*, 25(1):67–74, Jan 1977. ISSN 0018-926X. doi: 10.1109/TAP.1977.1141536.
- D. E. Cartwright and R. J. Taylor. New computation in the tide-generating potential. *Geophys. J. Roy. Astr. S.*, 23:45–74, 1971.
- D. E. Cartwright, R. D. Ray, and B. V. Sanchez. Oceanic tide maps and spherical harmonic coefficients from Geosat altimetry. *NASA Technical Memorandum 104544*, July 1991. Goddard Space Flight Center, Greenbelt, Maryland, USA.

BIBLIOGRAPHY

- D. B. Chelton, E. J. Walsh, and J. L. MacArthur. Pulse compression and sea level tracking in satellite altimetry. *J. Atmos. Oceanic Technol.*, 6:407–439, June 1989. doi: [http://dx.doi.org/10.1175/1520-0426\(1989\)006<0407:PCASLT>2.0.CO;2](http://dx.doi.org/10.1175/1520-0426(1989)006<0407:PCASLT>2.0.CO;2).
- C. H. Davis. A robust threshold retracking algorithm for measuring ice-sheet surface elevation change from satellite radar altimeters. *IEEE Trans. Geosc. Remote Sens.*, 35(4):974–979, 1997. doi: 10.1109/36.602540.
- C. H. Davis and A. C. Ferguson. Elevation change of the Antarctic ice sheet, 1995-2000, from ERS-2 satellite radar altimetry. *IEEE Trans. Geosc. Remote Sens.*, 42(11):2437–2445, 2004. doi: 10.1109/TGRS.2004.836789.
- A. Dermanis. Kriging and collocation - A comparison. *Manuscripta geodaetica*, 9:159–167, 1984.
- J. P. DiMarzio. GLAS/ICESat 1 km Laser Altimetry Digital Elevation Model of Greenland. <http://nsidc.org/data/nsidc-0305.html>, 2007.
- J. Ettema, M. R. van den Broeke, E. van Meijgaard, W. J. van de Berg, J. L. Bamber, J. E. Box, and R. C. Bales. Higher surface mass balance of the Greenland ice sheet revealed by high-resolution climate modeling. *Geophys. Res. Lett.*, 36, 2009. doi: 10.1029/2009GL038110.
- European Space Agency. Europe’s environmental satellite. http://www.esa.int/Our_Activities/Observing_the_Earth/Envisat/Europe_s_Environment_Satellite, November 2001. Checked July 2014.
- European Space Agency. CryoSat takes significant step towards final completion. http://www.esa.int/Our_Activities/Observing_the_Earth/CryoSat/CryoSat_takes_significant_step_towards_final_completion2, August 2003. Checked July 2014.
- European Space Agency. *ENVISAT RA-2/MWR Level 2 User Manual*, June 2006.
- European Space Agency. *ENVISAT RA-2/MWR Product Handbook*, 2.2 edition, February 2007.
- European Space Agency. CryoSat - Scientific Objectives. http://www.esa.int/Our_Activities/Observing_the_Earth/The_Living_Planet_Programme/Earth_Explorers/CryoSat-2/Objectives, January 2010. Checked July 2014.

BIBLIOGRAPHY

- European Space Agency. ESA Climate Change Initiative. <http://www.esa-cci.org/>, 2011a.
- European Space Agency. RA-2. http://www.altimetry.info/html/missions/envisat/instruments/ra2_en.html, 2011b. Checked July 2014.
- European Space Agency. Geophysical corrections. http://www.altimetry.info/html/alti/dataflow/processing/geophys_corr/welcome_en.html, 2011c. Checked July 2014.
- European Space Agency. On-board reception and tracking. http://www.altimetry.info/html/alti/principle/waveform/onboard_tracking_en.html, 2011d. Checked July 2014.
- European Space Agency. *CryoSat Product Handbook*. ESRIN, ESA and Mullard Space Sciences Laboratory, and University College London, April 2012.
- European Space Agency. *REAPER - Product handbook for ERS Altimetry reprocessed products*, 3.1 edition, August 2014a. URL <https://earth.esa.int/documents/10174/1511090/Reaper-Product-Handbook-3.1.pdf>.
- European Space Agency. Altimetry Missions. http://www.esa.int/Our_Activities/Observing_the_Earth/Copernicus/Altimetry_missions, April 2014b. Checked July 2014.
- European Space Agency. ESA Earth Online. <https://earth.esa.int/web/guest/pi-community/apply-for-data>, 2014c. Checked October 2014.
- European Space Agency. Reprocessed ESA ERS Altimetry (REAPER) dataset now available. <https://earth.esa.int/web/guest/missions/esa-operational-eo-missions/ers/news/-/article/reprocessed-esa-ers-altimetry-reaper-dataset-now-available>, September 2014d.
- European Space Agency. Sentinel-3. <https://earth.esa.int/web/guest/missions/esa-future-missions/sentinel-3>, 2015. Checked January 2015.
- H. Ewert, A. Groh, and R. Dietrich. Volume and mass changes of the Greenland ice sheet inferred from ICESat and GRACE. *J. Geodyn.*, 59–60:111–123, 2012. doi: 10.1016/j.jog.2011.06.003.

BIBLIOGRAPHY

- S. L. Farrell, T. Markus, R. Kwok, and L. Connor. Laser altimetry sampling strategies over sea ice. *Ann. Glaciol.*, 52(57):69–76, 2011.
- T. Flament and F. Rémy. Dynamic thinning of Antarctic glaciers from along-track repeat radar altimetry. *J. Glaciol.*, 58(211):830–840, 2012.
- R. Forsberg and C. C. Tscherning. An overview manual for the GRAVSOFTE Geodetic Gravity Field Modelling Programs. Technical Report 2, DTU Space; University of Copenhagen, August 2008.
- H. A. Fricker, A. Borsa, B. Minster, C. Carabajal, K. Quinn, and B. Bills. Assessment of ICESat performance at the salar de Uyuni, Bolivia. *Geophys. Res. Lett.*, 32(21), 2005. ISSN 1944-8007. doi: 10.1029/2005GL023423.
- L. L. Fu and A. Cazenave. *Satellite Altimetry and Earth Sciences: A Handbook of Techniques and Applications*. Academic Press, 2001.
- L. Gray, D. Burgess, L. Copland, R. Cullen, N. Galin, R. Hawley, and V. Helm. Interferometric swath processing of Cryosat data for glacial ice topography. *The Cryosphere*, 7(6):1857–1867, 2013. doi: 10.5194/tc-7-1857-2013. URL <http://www.the-cryosphere.net/7/1857/2013/>.
- R. L. Hawley, A. Shepherd, R. Cullen, V. Helm, and D. J. Wingham. Ice-sheet elevations from across-track processing of airborne interferometric radar altimetry. *Geophys. Res. Lett.*, 36(22), 2009. doi: 10.1029/2009GL040416.
- V. Helm, A. Humbert, and H. Miller. Elevation and elevation change of Greenland and Antarctica derived from CryoSat-2. *The Cryosphere*, 8(4):1539–1559, 2014. doi: 10.5194/tc-8-1539-2014. URL <http://www.the-cryosphere.net/8/1539/2014/>.
- B. Hofmann-Wellenhof and H. Moritz. *Physical Geodesy*. Springer-Verlag Wien, 2. edition, 2005.
- M. A. Hofton, J. B. Blair, S. B. Luthcke, and D. L. Rabine. Assessing the performance of 20 – 25 m footprint waveform lidar data collected in ICESat data corridors in Greenland. *Geophys. Res. Lett.*, 35(24), 2008. doi: 10.1029/2008GL035774.
- I. M. Howat, Y. Ahn, I. Joughin, M. R. van den Broeke, J. T. M. Lenaerts, and B. Smith. Mass balance of Greenland’s three largest outlet glaciers, 2000–2010. *Geophys. Res. Lett.*, 38(12), 2011. ISSN 1944-8007. doi: 10.1029/2011GL047565.

BIBLIOGRAPHY

- I. M. Howat, A. Negrete, and B. E. Smith. The Greenland Ice Mapping Project (GIMP) land classification and surface elevation datasets. *The Cryosphere*, 8(4):1509–1518, 2014. doi: 10.5194/tc-8-1509-2014. URL <http://www.the-cryosphere.net/8/1509/2014/>.
- R. T. W. L. Hurkmans, J. L. Bamber, and J. A. Griggs. Brief communication "Importance of slope-induced error correction in volume change estimates from radar altimetry". *The Cryosphere*, 6(2):447–451, 2012. doi: 10.5194/tc-6-447-2012. URL <http://www.the-cryosphere.net/6/447/2012/>.
- R. T. W. L. Hurkmans, J. L. Bamber, C. H. Davis, I. R. Joughin, K. S. Khvorostovsky, B. S. Smith, and N. Schoen. Time-evolving mass loss of the Greenland Ice Sheet from satellite altimetry. *The Cryosphere*, 8(5):1725–1740, 2014. doi: 10.5194/tc-8-1725-2014. URL <http://www.the-cryosphere.net/8/1725/2014/>.
- International Earth Rotation and Reference Systems Service (IERS). IERS Conventions (2003). Technical Report 32, IERS Conventions Center, 2014. URL http://202.127.29.4/cddisa/data_base/IERS/Technical_Notes/IERS_Technical_Note_No_32.pdf.
- I. Joughin, R. Kwok, and M. Fahnestock. Estimation of ice-sheet motion using satellite radar interferometry: Method and error analysis with application to Humboldt Glacier, Greenland. *J. Glaciol.*, 42(142):564–575, 1996.
- I. Joughin, W. Abdalati, and M. Fahnestock. Large fluctuations in speed on Greenland's Jakobshavn Isbræ glacier. *Nature*, 432:608–610, 2004. doi: 10.1038/nature03130.
- I. Joughin, B. E. Smith, I. M. Howat, T. Scambos, and T. Moon. Greenland flow variability from ice-sheet-wide velocity mapping. *J. Glaciol.*, 56(197):415–430, 2010. doi: 10.3189/002214310792447734.
- I. Joughin, R. B. Alley, and D. M. Holland. Ice-Sheet Response to Oceanic Forcing. *Science*, 338(6111):1172–1176, 2012. doi: 10.1126/science.1226481.
- I. Joughin, B. E. Smith, D. E. Shean, and D. Floricioiu. Brief Communication: Further summer speedup of Jakobshavn Isbræ. *The Cryosphere*, 8(1):209–214, 2014. doi: 10.5194/tc-8-209-2014. URL <http://www.the-cryosphere.net/8/209/2014/>.

BIBLIOGRAPHY

- S. A. Khan, J. Wahr, M. Bevis, I. Velicogna, and E. Kendrick. Spread of ice mass loss into northwest Greenland observed by GRACE and GPS. *Geophys. Res. Lett.*, 37(6), 2010. doi: 10.1029/2010GL042460.
- K. Khvorostovsky. Merging and analysis of elevation time series over Greenland ice sheet from satellite radar altimetry. *IEEE Trans. Geosc. Remote Sens.*, 50, 1:23–36, 2012. doi: 10.1109/TGRS.2011.2160071.
- K. Khvorostovsky and O. M. Johannessen. Merging of ERS-1, ERS-2 and Envisat altimeter data over the Greenland ice sheet. Technical Report 307, Nansen Environmental and Remote Sensing Center, December 2009. URL <http://www.nersc.no/sites/www.nersc.no/files/Report307.pdf>.
- J. Korona, E. Berthier, M. Bernard, F. Remy, and E. Thouvenot. SPIRIT. SPOT 5 stereoscopic survey of Polar Ice: Reference Images and Topographies during the fourth International Polar Year (2007–2009). *ISPRS J. Photogramm.*, 64(2):204–212, 2009. URL <http://dx.doi.org/10.1016/j.isprsjprs.2008.10.005>.
- W. B. Krabill. ATM L2 Icessn Elevation, Slope, and Roughness, Version 2. <http://nsidc.org/data/ilatm2.htm>, Boulder, Colorado USA: NASA DAAC at the National Snow and Ice Data Center, 2012. Checked June 2014.
- W. B. Krabill, W. Abdalati, E. Frederick, S. Manizade, C. Martin, J. Sonntag, R. Swift, R. Thomas, and J. Yungel. Aircraft laser altimetry measurement of elevation changes of the Greenland Ice Sheet: technique and accuracy assessment. *J. Geodyn.*, 34:357–376, 2002. doi: 10.1016/S0264-3707(02)00040-6.
- B. Legresy, F. Papa, F. Remy, G. Vinay, M. van den Bosch, and O.-Z. Zanife. ENVISAT radar altimeter measurements over continental surfaces and ice caps using the ICE-2 retracking algorithm. *Remote Sens. Environ.*, 95(2): 150–163, 2005. doi: 10.1016/j.rse.2004.11.018.
- B. Legrésy, F. Rémy, and F. Blarel. Along track repeat altimetry for ice sheets and continental surface studies. *Proceedings of the Symposium on 15 years of Progress in Radar Altimetry, Venice, Italy*, 181:ESA–SP614, 13–18 March 2006.
- J. Levinsen, I. M. Howat, and C. C. Tscherning. Improving maps of ice-sheet surface elevation change using combined laser altimeter and stereoscopic elevation model data. *J. Glaciol.*, 59(215), 2013. doi: 10.3189/2013JoG12J114.

BIBLIOGRAPHY

- J. Levinsen, K. Khvorostovsky, F. Ticconi, A. Shepherd, R. Forsberg, L. Sørensen, A. Muir, N. Pie, D. Felikson, T. Flament, R. Hurkmans, G. Moholdt, B. Gunter, R. Lindenbergh, and M. Kleinherenbrink. ESA ice sheet CCI: derivation of the optimal method for surface elevation change detection of the Greenland ice sheet – round robin results. *Int. J. Remote Sens.*, 36 (2):551–573, 2015a. doi: 10.1080/01431161.2014.999385.
- J. F. Levinsen, S. B. Simonsen, L. S. Sørensen, and R. Forsberg. Brief communication: Relocation of radar altimetry data over ice sheets. *The Cryosphere Discuss.*, 2015b. Submitted.
- J. F. Levinsen, B. E. Smith, L. S. Sørensen, K. Khvorostovsky, S. B. Simonsen, and R. Forsberg. A Digital Elevation Model of the Greenland Ice Sheet based on combined laser and radar altimetry. *Earth and Space Science*, 2015c. In review.
- Y. Li and C. Davis. Decadal Mass Balance of the Greenland and Antarctic Ice Sheets from High Resolution Elevation Change Analysis of ERS-2 and Envisat Radar Altimetry Measurements. In *Geoscience and Remote Sensing Symposium. IGARSS 2008. IEEE International*, volume 4, pages 339–342, July 2008. doi: 10.1109/IGARSS.2008.4779727.
- P. Lucas-Picher, M. Wulff-Nielsen, J. H. Christensen, G. Aðalgeirsdóttir, R. Mottram, and S. B. Simonsen. Very high resolution regional climate model simulations over Greenland: Identifying added value. *J. Geophys. Res. - Atmos*, 117(D2), 2012. doi: 10.1029/2011JD016267.
- S. B. Luthcke, D. D. Rowland, T. A. Williams, and M. Sirota. Reduction of ICESat systematic geolocation errors and the impact on ice sheet elevation change detection. *Geophys. Res. Lett.*, 32, L21S05, 2005. doi: 10.1029/2005GL023689.
- F. Lyard, F. Lefevre, T. Letellier, and O. Francis. Modelling the global ocean tides: modern insights from FES2004. *Ocean Dynam.*, 56:394–415, 2006. doi: 10.1007/s10236-006-0086-x.
- A. Mahesh, J. D. Spinhirne, D. P. Duda, and E. W. Eloranta. Atmospheric Multiple Scattering Effects on GLAS Altimetry – Part II: Analysis of Expected Errors in Antarctic Altitude Measurements. *IEEE Trans. Geosci. Remote Sensing*, 40(11), 2002.
- T. Milliman. Operation IceBridge Planning Tool. <http://icebridge.sr.unh.edu/>, 2014. Checked July 2014.

BIBLIOGRAPHY

- G. Moholdt, C. Nuth, J. O. Hagen, and J. Kohler. Recent elevation changes of Svalbard glaciers derived from ICESat laser altimetry. *Remote Sens. Environ.*, 114(11):2756–2767, 2010. doi: 10.1016/j.rse.2010.06.008.
- National Aeronautics and Space Administration. ICESat & ICESat-2. <http://icesat.gsfc.nasa.gov/index.php>, May 2013. Checked July 2014.
- National Aeronautics and Space Administration. Retracking Correction. http://icesat4.gsfc.nasa.gov/radar_data/data_processing/retrack.php, July 2014. Checked November 2014.
- National Snow and Ice Data Center. Products & Services. <http://nsidc.org/pubs/notes/42/>, December 2002.
- S. V. Nghiem, K. Steffen, G. Neumann, and R. Huff. Mapping of ice layer extent and snow accumulation in the percolation zone of the Greenland ice sheet. *J. Geophys. Res. - Earth*, 110(F2), 2005. ISSN 2156-2202. doi: 10.1029/2004JF000234.
- S. V. Nghiem, D. K. Hall, T. L. Mote, M. Tedesco, M. R. Albert, K. Keegan, C. A. Shuman, N. E. DiGirolamo, and G. Neumann. The extreme melt across the Greenland ice sheet in 2012. *Geophys. Res. Lett.*, 39(20), 2012. ISSN 1944-8007. doi: 10.1029/2012GL053611.
- A. A. Nielsen. *Geostatistics and Analysis of Spatial Data*. Informatics and Mathematical Modelling, Technical University of Denmark, DTU, Richard Petersens Plads, Building 321, DK-2800 Kgs. Lyngby, 2009.
- J. Nilsson. *Cryosphere monitoring from satellite and aircrafts*. PhD thesis, National Space Institute, Technical University of Denmark, January 2015.
- J. Nilsson, P. Vallelogna, S. B. Simonsen, L. S. Sørensen, R. Forsberg, D. Dahl-Jensen, M. Hirabayashi, K. Goto-Azuma, C. S. Hvidberg, H. A. Kjær, and K. Satow. Greenland 2012 melt event effects on CryoSat-2 radar altimetry. *Geophys. Res. Lett.*, 2015. In review.
- C. Nuth and A. Kääb. Co-registration and bias corrections of satellite elevation data sets for quantifying glacier thickness change. *The Cryosphere*, 5(1):271–290, 2011. doi: 10.5194/tc-5-271-2011. URL <http://www.the-cryosphere.net/5/271/2011/>.
- C. Nuth, G. Moholdt, J. Kohler, J. O. Hagen, and A. Kääb. Svalbard glacier elevation changes and contribution to sea level rise. *J. Geophys. Res. - Sol. Ea.*, 115(F1), 2010. doi: 10.1029/2008JF001223.

BIBLIOGRAPHY

- W. Qi and A. Braun. Accelerated Elevation Change of Greenland's Jakobshavn Glacier Observed by ICESat and IceBridge. *IEEE Geosci. Remote Sens. Lett.*, 10(5):1133–1137, 2013. doi: 10.1109/LGRS.2012.2231954.
- F. Remy, P. Mazzega, S. Houry, C. Brossier, and J. Minster. Mapping of the Topography of Continental Ice by Inversion of Satellite-Altitude Data. *J. Glaciol.*, 35(119):98–107, 1989. doi: 10.3189/002214389793701419.
- J. Richter-Menge and J. Overland. Arctic Report Card 2010. http://www.arctic.noaa.gov/report10/ArcticReportCard_full_report.pdf, 2010.
- J. K. Ridley and K. C. Partington. A Model of Satellite Radar Altimeter Return from Ice Sheets. *Int. J. Remote Sens.*, 9(4):601–624, 1988. doi: 10.1080/01431168808954881.
- RIEGL Laser Measurement Systems. 2D laser scanner LSM-Q240i. Technical report, RIEGL Laser Measurement Systems, 2010.
- S. Roemer, B. Legrésy, M. Horwath, and R. Dietrich. Refined analysis of radar altimetry data applied to the region of the subglacial Lake Vostok/Antarctica. *Remote Sens. Environ.*, 106(3):269–284, 2007. doi: <http://dx.doi.org/10.1016/j.rse.2006.02.026>.
- D. T. Sandwell. *Radar altimetry*, 2011. URL <http://topex.ucsd.edu/rs/altimetry.pdf>.
- I. Sasgen, M. van den Broeke, J. L. Bamber, E. Rignot, L. S. Sørensen, B. Wouters, Z. Martinec, I. Velicogna, and S. B. Simonsen. Timing and origin of recent regional ice-mass loss in Greenland. *Earth Planet Sc. Lett.*, 333:293–303, 2012.
- T. A. Scambos and T. Haran. An image-enhanced DEM of the Greenland ice sheet. *Ann. Glaciol.*, 34(1):291–298, 2002. doi: 10.3189/172756402781817969.
- K. Scharrer, J. F. Levinsen, and F. Ticconi. Product Validation and Algorithm Selection Report for the Ice_Sheets_cci project of ESA's Climate Change Initiative. Version 1.2, April 2013. Available from: <http://www.esa-icesheets-cci.org/>.
- B. E. Schutz, H. J. Zwally, C. A. Shuman, D. Hancock, and J. P. DiMarzio. Overview of the ICESat mission. *Geophys. Res. Lett.*, 32, L21S01, 2005. doi: 10.1029/2005GL024009.

BIBLIOGRAPHY

- Scripps Institution of Oceanography, University of San Diego. Principles of Synthetic Aperture Radar. topex.ucsd.edu/rs/sar_summary.pdf. Checked July 2014.
- A. Shepherd. Data Access Requirements Document for the Ice_Sheets_cci project of ESA's Climate Change Initiative. Version 1.7.6, September 2012. Available from: <http://www.esa-icesheets-cci.org/>.
- A. Shepherd, E. R. Ivins, G. A. V. R. Barletta, M. J. Bentley, S. Bettadpur, K. H. Briggs, D. H. Bromwich, R. Forsberg, N. Galin, M. Horwath, S. Jacobs, I. Joughin, M. A. King, J. T. M. Lenaerts, J. Li, S. R. M. Ligtenberg, A. Luckman, S. B. Luthcke, M. McMillan, R. Meister, G. Milne, J. Mouginot, A. Muir, J. P. Nicolas, J. Paden, A. J. Payne, H. Pritchard, E. Rignot, H. Rott, L. S. Sørensen, T. A. Scambos, B. Scheuchl, E. J. O. Schrama, B. Smith, A. V. Sundal, J. H. van Angelen, W. J. van de Berg, M. R. van den Broeke, D. G. Vaughan, I. Velicogna, J. Wahr, P. L. Whitehouse, D. J. Wingham, D. Yi, D. Young, and H. J. Zwally. A Reconciled Estimate of Ice-Sheet Mass Balance. *Science*, 338(6111):1183–1189, 2012. doi: 10.1126/science.1228102. URL <http://www.sciencemag.org/content/338/6111/1183.abstract>.
- S. B. Simonsen, V. R. Barletta, R. Forsberg, and L. Sandberg Sørensen. Reconciled freshwater flux into the Godthåbsfjord system from satellite and airborne remote sensing. *Int. J. Remote Sens.*, 36(1):361–374, 2015. doi: 10.1080/01431161.2014.995277.
- H. Skourup, V. Barletta, I. Einarsson, R. Forsberg, C. Haas, V. Helm, S. Hendricks, S. M. Hvidegaard, and L. S. Sørensen. *ESA CryoVEx 2011: Airborne field campaign with ASIRAS radar, EM induction sounder and laser scanner*. DTU Space, National Space Institute, Technical University of Denmark, 1 edition, 2011.
- L. S. Sørensen. Product Specification Document for the Ice_Sheets_cci project of ESA's Climate Change Initiative. Version 1.2, August 2012. Available from: <http://www.esa-icesheets-cci.org/>.
- L. S. Sørensen, S. B. Simonsen, K. Nielsen, P. Lucas-Picher, G. Spada, G. Adalgeirsdottir, R. Forsberg, and C. S. Hvidberg. Mass balance of the Greenland ice sheet (2003 – 2008) from ICESat data – the impact of interpolation, sampling and firn density. *The Cryosphere*, 5(1):173–186, 2011. doi: 10.5194/tc-5-173-2011.

BIBLIOGRAPHY

- L. S. Sørensen, S. B. Simonsen, R. Meister, R. Forsberg, J. F. Levinsen, and T. Flament. Envisat-derived elevation changes of the Greenland ice sheet, and a comparison with ICESat results in the accumulation area. *Remote Sens. Environ.*, 160:56–62, April 2015. doi: 10.1016/j.rse.2014.12.022.
- F. Straneo and P. Heimback. North Atlantic warming and the retreat of Greenland’s outlet glaciers. *Nature*, 504:36–43, 2013. doi: 10.1038/nature12854.
- T. Tachikawa, M. Kaku, A. Iwasaki, D. Gesch, M. Oimoen, Z. Zhang, J. Danielson, T. Krieger, B. Curtis, J. Haase, M. Abrams, R. Crippen, and C. Carabaja. ASTER Global Digital Elevation Model Version 2 – Summary of Validation Results. Technical report, NASA Land Processes Distributed Active Archive Center and the Joint Japan-US ASTER Science Team, August 2011.
- M. Tedesco, X. Fettweis, M. R. van den Broeke, R. S. W. van de Wal, C. J. P. P. Smeets, W. J. van de Berg, M. C. Serreze, and J. E. Box. The role of albedo and accumulation in the 2010 melting record in Greenland. *Environ. Res. Lett.*, 6(1):014005, 2011.
- R. Thomas, E. Frederick, W. Krabill, S. Manizade, and C. Martin. Recent changes on Greenland outlet glaciers. *J. Glaciol.*, 55(189):147–162, 2009. doi: 10.3189/002214309788608958.
- D. Wingham, C. Francis, S. Baker, C. Bouzinac, D. Brockley, R. Cullen, P. de Chateau-Thierry, S. Laxon, U. Mallow, C. Mavrocordatos, L. Phalippou, G. Ratier, L. Rey, F. Rostan, P. Viau, and D. Wallis. CryoSat: A mission to determine the fluctuations in Earth’s land and marine ice fields. *Adv. Space Res.*, 37(4):841–871, 2006. doi: 10.1016/j.asr.2005.07.027.
- D. J. Wingham, C. G. Rapley, and H. D. Griffiths. New techniques in satellite altimeter tracking systems. Proceedings of the IGARSS Symposium, Zurich SP-254, European Space Agency, September 1986. Edited by T. D. Guyenne and J. J. Hunt.
- D. J. Wingham, A. J. Ridout, R. Scharroo, R. J. Arthern, and C. K. Shum. Antarctic Elevation Change from 1992 to 1996. *Science*, 282(5388):456–458, 1998. doi: 10.1126/science.282.5388.456.
- D. Yi, H. J. Zwally, and S. Sun. ICESat measurement of Greenland ice sheet surface slope and roughness. *Ann. Glaciology*, 42(1):83–89, 2005. doi: 10.3189/172756405781812691.

BIBLIOGRAPHY

- H. Zwally, B. Schutz, W. Abdalati, J. Abshire, C. Bentley, A. Brenner, J. Bufton, J. Dezio, D. Hancock, D. Harding, T. Herring, B. Minster, K. Quinn, S. Palm, J. Spinhirne, and R. Thomas. ICESat's laser measurements of polar ice, atmosphere, ocean, and land. *J. Geodyn.*, 34(3–4): 405–445, 2002. doi: 10.1016/s0264-3707(02)00042-x.
- H. J. Zwally, A. C. Brenner, J. A. Major, T. V. Martin, and R. A. Bindshadler. Satellite radar altimetry over ice, Vol. 1. Processing and corrections of Seasat data over Greenland. NASA Reference Publication 1233, National Aeronautics and Space Administration, 1990.
- H. J. Zwally, M. B. Giovinetto, J. Li, H. C. Cornejo, M. A. Beckley, A. C. Brenner, J. L. Saba, and D. Yi. Mass changes of the Greenland and Antarctic ice sheets and shelves and contributions to sea-level rise: 1992 – 2002. *J. Glaciol.*, 51(175):509–527, 2005.
- H. J. Zwally, J. Li, A. Brenner, M. Beckley, H. G. Cornejo, J. DiMarzio, M. B. Giovinetto, T. A. Neumann, J. Robbins, J. L. Saba, D. Yi, and W. Wang. Greenland ice sheet mass balance: distribution of increased mass loss with climate warming; 2003 – 2007 versus 1992 – 2002. *J. Glaciol.*, 57(201): 88–102, 2011.
- H. J. Zwally, R. Schutz, C. Bentley, J. Bufton, T. Herring, J. Minster, J. Spinhirne, and R. Thomas. GLAS/ICESat L1 and L2 Global Altimetry Data. http://nsidc.org/data/docs/daac/glas_icesat_l1_l2_global_altimetry.gd.html, Boulder, Colorado USA: NASA DAAC at the National Snow and Ice Data Center, 2014. Checked October 2014.

A Derivation of method for Greenland Ice Sheet elevation change detection

Multiple methods exist for surface elevation change detection of ice-covered regions, e.g. the repeat-track or cross-over techniques (Khvorostovsky, 2012; Moholdt et al., 2010; Sørensen et al., 2011; Zwally et al., 2005, 2011).

This study focuses on arriving at the optimal method for an ice sheet-wide estimation over the Greenland Ice Sheet. It is achieved through an inter-comparison of ten solutions provided by the scientific community. The solutions cover the Jakobshavn Isbræ drainage basin and are based on either repeat-track or cross-over analyses using either Envisat or ICESat data. Inter-comparisons across datasets and techniques demonstrated that a combination of the two is preferred, and that radar altimetry data are applicable for elevation change detection even over margin regions. Thus, it is possible to exploit the large spatial data coverage in repeat-track analyses and the high accuracy in cross-over points to obtain highly accurate SEC maps from radar altimetry data.

The work leading to this conclusion is described in the paper below:

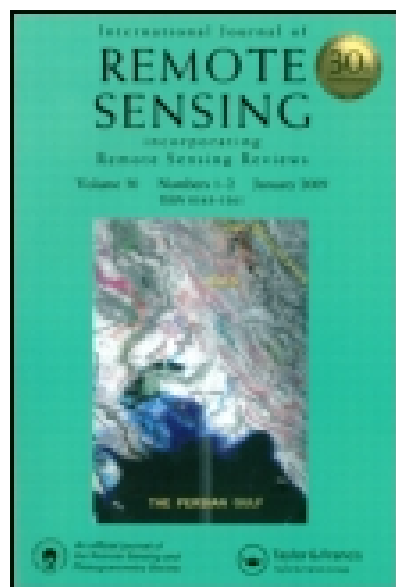
Authors : J. F. Levinsen, K. Khvorostovsky, F. Ticconi, A. Shepherd, R. Forsberg, L. S. Sørensen, A. Muir, N. Pie, D. Felikson, T. Flament, R. Hurkmans, G. Moholdt, B. Gunter, R. C. Lindenbergh, M. Kleinherenbrink
Title : ESA Ice Sheets CCI: Derivation of the optimal method for surface elevation change detection of the Greenland Ice Sheet – Round Robin results
Journal : International Journal of Remote Sensing
Publication date : January 19th 2015
DOI : 10.1080/01431161.2014.999385

This article was downloaded by: [DTU Library]

On: 20 January 2015, At: 02:16

Publisher: Taylor & Francis

Informa Ltd Registered in England and Wales Registered Number: 1072954 Registered office: Mortimer House, 37-41 Mortimer Street, London W1T 3JH, UK



[Click for updates](#)

International Journal of Remote Sensing

Publication details, including instructions for authors and subscription information:

<http://www.tandfonline.com/loi/tres20>

ESA ice sheet CCI: derivation of the optimal method for surface elevation change detection of the Greenland ice sheet - round robin results

J.F. Levinsen^a, K. Khvorostovsky^b, F. Ticconi^{cd}, A. Shepherd^c, R. Forsberg^a, L.S. Sørensen^a, A. Muir^e, N. Pie^f, D. Felikson^f, T. Flament^c, R. Hurkmans^g, G. Moholdt^h, B. Gunter^{ij}, R.C. Lindenberghⁱ & M. Kleinherenbrinkⁱ

^a DTU Space, National Space Institute, Technical University of Denmark, 2800 Kongens Lyngby, Denmark

^b NN, Nansen Environmental and Remote Sensing Centre, 5006 Bergen, Norway

^c School of Earth and Environment, University of Leeds, Leeds LS2 9JT, UK

^d Remote Sensing and Product Unit, EUMETSAT, 64295 Darmstadt, Germany

^e Department of Earth Sciences, University College London, London WC1E 6BT, UK

^f Center for Space Research, University of Texas, 3925 West Braker Lane, Suite 200, Austin, TX 78759-5321, USA

^g Bristol Glaciology Centre, School of Geographical Sciences, University of Bristol, Bristol BS8 1SS, UK

^h Scripps Institution of Oceanography, Institute of Geophysics and Planetary Physics, La Jolla, CA 92093-0225, USA

ⁱ Department of Geoscience & Remote Sensing, Delft University of Technology, 2600 GA Delft, the Netherlands

^j School of Aerospace Engineering, Georgia Institute of Technology, Atlanta, GA 30332-0150, USA

Published online: 19 Jan 2015.

To cite this article: J.F. Levinsen, K. Khvorostovsky, F. Ticconi, A. Shepherd, R. Forsberg, L.S. Sørensen, A. Muir, N. Pie, D. Felikson, T. Flament, R. Hurkmans, G. Moholdt, B. Gunter, R.C. Lindenbergh & M. Kleinherenbrink (2015) ESA ice sheet CCI: derivation of the optimal method for

surface elevation change detection of the Greenland ice sheet - round robin results, International Journal of Remote Sensing, 36:2, 551-573, DOI: [10.1080/01431161.2014.999385](https://doi.org/10.1080/01431161.2014.999385)

To link to this article: <http://dx.doi.org/10.1080/01431161.2014.999385>

PLEASE SCROLL DOWN FOR ARTICLE

Taylor & Francis makes every effort to ensure the accuracy of all the information (the "Content") contained in the publications on our platform. However, Taylor & Francis, our agents, and our licensors make no representations or warranties whatsoever as to the accuracy, completeness, or suitability for any purpose of the Content. Any opinions and views expressed in this publication are the opinions and views of the authors, and are not the views of or endorsed by Taylor & Francis. The accuracy of the Content should not be relied upon and should be independently verified with primary sources of information. Taylor and Francis shall not be liable for any losses, actions, claims, proceedings, demands, costs, expenses, damages, and other liabilities whatsoever or howsoever caused arising directly or indirectly in connection with, in relation to or arising out of the use of the Content.

This article may be used for research, teaching, and private study purposes. Any substantial or systematic reproduction, redistribution, reselling, loan, sub-licensing, systematic supply, or distribution in any form to anyone is expressly forbidden. Terms & Conditions of access and use can be found at <http://www.tandfonline.com/page/terms-and-conditions>

ESA ice sheet CCI: derivation of the optimal method for surface elevation change detection of the Greenland ice sheet – round robin results

J.F. Levinsen^{a*}, K. Khvorostovsky^b, F. Ticconi^{c,d}, A. Shepherd^c, R. Forsberg^a, L.S. Sørensen^a, A. Muir^e, N. Pie^f, D. Felikson^f, T. Flament^c, R. Hurkmans^g, G. Moholdt^h, B. Gunter^{i,j}, R.C. Lindenberghⁱ, and M. Kleinherenbrinkⁱ

^aDTU Space, National Space Institute, Technical University of Denmark, 2800 Kongens Lyngby, Denmark; ^bNN, Nansen Environmental and Remote Sensing Centre, 5006 Bergen, Norway; ^cSchool of Earth and Environment, University of Leeds, Leeds LS2 9JT, UK; ^dRemote Sensing and Product Unit, EUMETSAT, 64295 Darmstadt, Germany; ^eDepartment of Earth Sciences, University College London, London WC1E 6BT, UK; ^fCenter for Space Research, University of Texas, 3925 West Braker Lane, Suite 200, Austin, TX 78759-5321, USA; ^gBristol Glaciology Centre, School of Geographical Sciences, University of Bristol, Bristol BS8 1SS, UK; ^hScripps Institution of Oceanography, Institute of Geophysics and Planetary Physics, La Jolla, CA 92093-0225, USA; ⁱDepartment of Geoscience & Remote Sensing, Delft University of Technology, 2600 GA Delft, the Netherlands; ^jSchool of Aerospace Engineering, Georgia Institute of Technology, Atlanta, GA 30332-0150, USA

(Received 27 June 2014; accepted 28 October 2014)

For more than two decades, radar altimetry missions have provided continuous elevation estimates of the Greenland ice sheet (GrIS). Here, we propose a method for using such data to estimate ice-sheet-wide surface elevation changes (SECs). The final data set will be based on observations acquired from the European Space Agency's Environmental Satellite (ENVISAT), European Remote Sensing (ERS)-1 and -2, CryoSat-2, and, in the longer term, Sentinel-3 satellites. In order to find the best-performing method, an intercomparison exercise has been carried out in which the scientific community was asked to provide their best SEC estimates as well as feedback sheets describing the applied method. Due to the hitherto few radar-based SEC analyses as well as the higher accuracy of laser data, the participants were asked to use either ENVISAT radar or ICESat (Ice, Cloud, and land Elevation Satellite) laser altimetry over the Jakobshavn Isbræ drainage basin. The submissions were validated against airborne laser-scanner data, and intercomparisons were carried out to analyse the potential of the applied methods and to find whether the two altimeters were capable of resolving the same signal. The analyses found great potential of the applied repeat-track and cross-over techniques, and, for the first time over Greenland, that repeat-track analyses from radar altimetry agreed well with laser data. Since topography-related errors can be neglected in cross-over analyses, it is expected that the most accurate, ice-sheet-wide SEC estimates are obtained by combining the cross-over and repeat-track techniques. It is thus possible to exploit the high accuracy of the former and the large spatial data coverage of the latter. Based on CryoSat's different operation modes, and the increased spatial and temporal data coverage, this shows good potential for a future inclusion of CryoSat-2 and Sentinel-3 data to continuously obtain accurate SEC estimates both in the interior and margin ice sheet.

1. Introduction

As the climate is changing, a need has arisen for scientists and space agencies across the globe to combine their efforts into establishing long-term data records to observe the

*Corresponding author. Email: JFL@space.dtu.dk

changes. This has led the European Space Agency to establish the Climate Change Initiative (ESA CCI) in which 13 essential climate variables are analysed, such as sea ice, ozone, fire, and ice sheets (ESA 2011a). This work is part of the ice sheet CCI for which the focus area is the Greenland ice sheet (GrIS). The motivation is an increased mass loss, e.g. demonstrated by Zwally et al. (2011), who used laser and radar altimetry and found an increase of 164 ± 5 Gt year⁻¹ from 1992–2002 to 2003–2007. Shepherd et al. (2012) compared mass balance estimates from the input–output method, laser altimetry, and gravimetry, and for reconciled estimates for 1992–2000 and 2000–2011, respectively, found that the mass loss rose from -51 ± 65 Gt year⁻¹ to -211 ± 37 Gt year⁻¹.

In order to increase our understanding of the changes, the goal of this work is to develop a method for creating ice sheet-wide maps of surface elevation changes (SEC) based on ESA radar altimetry from the European Remote Sensing (ERS) satellites, Environmental Satellite (ENVISAT), CryoSat-2, and Sentinel-3. This will enable the construction of time series running from 1992 until the present date. In order to find the optimal method for SEC production, a broad collaboration between relevant cryospheric and climate-related research groups is carried out. This is done in a so-called round robin (RR) exercise where members of the scientific community are contacted and encouraged to submit their best estimates as well as in-depth descriptions of the applied method. Here, we present the outcome of this exercise. The submitted results are intercompared and validated against airborne laser-scanner data, and the resulting conclusions form the basis for the final GrIS SEC production.

2. Surface elevation change studies from altimetry

Observations from both laser altimetry (LA) and radar altimetry (RA) are used in several SEC studies of the ice sheets, e.g. by Zwally et al. (2005, 2011), Sørensen et al. (2011), Flament and Rémy (2012), Khvorostovsky (2012), and Helm, Humbert, and Miller (2014). Common approaches are the repeat-track (RT) and cross-over (XO) techniques, where measurements along repeated ground-tracks or in XO locations between ascending and descending satellite passes are explored. The different methods are described by Slobbe, Lindenbergh, and Ditmar (2008), Moholdt et al. (2010), and Gunter et al. (2014).

For a number of reasons, the altimeters resolve the surface signal to varying degrees and precisions: laser data from the National Aeronautics and Space Administration (NASA) Ice, Cloud, and land Elevation Satellite (ICESat) illuminate about 60 m-wide ellipses, while echoes from ENVISAT have pulse-limited footprints of 2–10 km. Hence, RA signals reflect greater amounts of topography, reflected by slope-induced errors (see below). Furthermore, the echoes are subject to surface penetration and volume scatter, which introduce elevation errors. Nghiem et al. (2005) found penetration depths to exceed 1 m for Ku-band data over Greenland, while Forsberg, Keller, and Jacobsen (2002), for C-band data, found 15–20 m in the dry accumulation zone near the Geikie plateau, which decreased to zero towards lower altitudes. Such errors are not found in LA as the echoes reflect directly off the surface (Brenner et al. 1983, 2007; Ridley and Partington 1988; Bamber 1994). This explains the findings by Brenner, DiMarzio, and Zwally (2007) in a comparison of ICESat and ENVISAT surface elevations over Greenland and Antarctica. They found a laser elevation precision of 14–50 cm depending on the surface slope, and elevation differences ranging from 9 ± 52 cm for slopes less than 0.1° to 2.7 ± 26 m for slopes up to 0.9° . The effect therefore varies when moving from the sloping, often

specular coastal margin to the smoother interior with smaller surface roughness (Legresy et al. 2005; Remy et al. 2012, Sørensen et al. 2014).

Slope-related errors can be attributed to two things: for RA, the large footprint means that the reflecting point over a sloping surface rarely coincides with nadir but rather somewhere up-slope. In this case, one can either correct the range measurement to the sub-satellite point, or the elevation measurement by e.g. adding a term based on the surface slope. For a 1° surface slope and a satellite altitude of 800 km, this error can shift measurement locations up to 14 km from nadir and introduce a vertical offset of approximately 120 m (Brenner et al. 1983; Hurkmans, Bamber, and Griggs 2012).

In RT analyses, an error results from the footprint rarely being exactly repeat. It is, however, larger for RA as e.g. ICESat is capable of performing off-nadir manoeuvres to better repeat previous ground-tracks (Schutz et al. 2005). In any case, the local surface topography in-between ground-tracks must be considered. This can be done by estimating the slope bias from the distance between ground-tracks as well as the surface slope between them, the latter derived from an external digital elevation model (DEM) (Slobbe, Lindenbergh, and Ditmar 2008).

RT analyses from RA therefore suffer from two types of slope-induced errors, which significantly increase data errors. Advantages are thus given to LA-based analyses, or to XO studies where measurements in overlapping ground-track locations are explored; hence, effects from the local topography can be ignored.

3. The round robin exercise

The ice sheet CCI RR was announced through personal invitations, postings on the CCI website (www.esa-icesheets-cci.org/), and on the e-mailing list for snow and ice related research, CRYOLIST (www.cryolist.org/). In order to establish a basis for intercomparing the results, the participants were given an observation area and instructions on which data to use. They were asked to submit their best SEC estimates, errors, and feedback sheets describing pre- and post-processing steps, estimation specifications, computational time, etc. This allowed for intercomparing the applied approaches.

The focus area was the Jakobshavn Isbræ drainage basin ($68\text{--}71^\circ$ N; $39\text{--}52^\circ$ W), and the participants could use either ICESat or ENVISAT data. Laser data were included due to their high elevation accuracy and the sparsity of recent RA SEC studies of the GrIS. If a DEM was needed, the Greenland Ice Mapping Project (GIMP) model by Howat, Negrete, and Smith (2014), originally posted at a 90 m resolution, was recommended.

In total, 11 submissions were received, one of which was discarded as the results were not comparable with the remaining data sets. Table 1 shows the sensor and method used by the participants as well as the submitted output parameters; a more elaborate description of the methodologies is given in Section 3.2 and by Scharrer, Levinsen, and Ticconi (2013). In order to anonymize the results, the participants are referred to as SEC-1, SEC-2, ..., SEC-10, the order in which they are named being random. Three participants used ENVISAT data and the remaining seven used ICESat. Of these, five groups applied the XO technique and the remaining five RT.

Some groups submitted both elevation time series and SEC estimates. In the former, the formation of time series is first made, e.g. one for each grid cell, after which typically linear least-squares regression is used to fit a trend to the surface elevations. The direct estimates are made when fitting a trend to elevation differences (dH) versus the temporal difference between the data acquisition times (dt).

Table 1. Sensors and methods used for the SEC production as well as the final data parameters submitted by the round robin participants.

Participant	Sensor	Method	Output parameters
SEC-1	ENVISAT	Repeat-track	dH/dt (time series)
SEC-2	ICESat	Repeat-track	dH/dt
SEC-3	ICESat	Repeat-track	dH/dt
SEC-4	ICESat	Repeat-track	dH/dt
SEC-5	ICESat	Repeat-track	dH/dt
SEC-6	ICESat	Cross-overs	dH/dt , XO differences
SEC-7	ICESat	Cross-overs	dH/dt
SEC-8	ICESat	Cross-overs	dH/dt
SEC-9	ENVISAT	Cross-overs	dH/dt (time series)
SEC-10	ENVISAT	Cross-overs	dH/dt (time series)

The submissions are validated against airborne laser-scanner data acquired from NASA's Airborne Topographic Mapper (ATM). Such data are used due to their high accuracy and spatial data coverage (Krabill et al. 2002). Finally, a number of submissions are intercompared to analyse the applied techniques and sensors. Thus, analyses of cross-over *versus* repeat-track results and radar *versus* laser altimetry are carried out, to test the validity of the applied methods and investigate the performance of RA relative to LA. On the basis of the extensive amount of submissions across sensors and methods, the final conclusions form the basis for the optimal RA SEC solution for the GrIS.

3.1. Temporal extent and spatial resolution

Table 2 lists the spatial resolution and temporal extent of the submissions. The observation periods are mainly based on the operational period of the given sensor. Two ENVISAT data sets span the period from 2002 to 2010 corresponding to the 35-day repeat cycle, while the third covers the ICESat observation period from 2003 to 2009. The remaining submissions are based on ICESat and also cover 2003–2009. The laser acquisitions are, however, limited by the period of active altimeters and thus are carried out in two or three 35-day intervals per

Table 2. Observation period, spatial density, and spatial resolution of the round robin SEC products.

Participant	Observation period	Spatial density	Spatial resolution
SEC-1	Sep 2002–Oct 2010	Along ENVISAT tracks	5.0 km along-track segments
SEC-2	Oct 2003–Oct 2009	Along ICESat tracks	0.7 km along-track segments
SEC-3	Feb 2003–Oct 2009	Along ICESat tracks	1.0 km along-track segments
SEC-4	Oct 2003–Oct 2009	Along ICESat tracks	0.5 km along-track segments
SEC-5	Sep 2003–Oct 2009	Along ICESat tracks	1.0 km along-track segments
SEC-6	Feb 2003–Oct 2009	Grid cells covering 100% of area	8.0 km \times 8.0 km grid cells
SEC-7	Oct 2003–Oct 2009	Grid cells covering about 93% of area	0.5° lat \times 0.1° lon grid cells
SEC-8	Feb 2003–Oct 2009	Grid cells covering about 95% of area	1.2 km \times 1.2 km grid cells
SEC-9	Sep 2003–Oct 2009	Grid cells covering about 97% of area	0.5° lat \times 0.1° lon grid cells
SEC-10	Oct 2002–Oct 2010	Grid cells covering about 90% of area	10.0 km \times 10.0 km grid cells

year (NASA 2013a, 2013b). No ENVISAT solutions cover the period from the lowering of the orbit in October 2010 until it ceased operation in March 2012. The spatial resolution and density of prediction points depend on the method, and thus RT has a higher spatial coverage than XO due to the better ground coverage. The RT solutions are estimated for along-track segments, while the remaining solutions are given for grid cells centred on each XO location; the size of both, and thus the measurement spacing, varies from hundreds of metres to several kilometres. While most RT results cover the entire observation area, that from SEC-3 is confined to the drainage basin.

3.2. Methodology

The feedback sheets reveal that the ICESat data processing is very similar, with common data rejection criteria for the saturation index, the incident beam co-elevation angle, the return signal's gain value, and the return waveform having only one peak. Table 3 lists the details of the RR product generation, and it is found that all RT groups apply linear least-squares (LSq) techniques, namely weighted, unweighted, and multivariate LSq. SEC-2 fits a plane to near repeat-tracks, solving for both surface slope and dH/dt .

Table 3. Overview of the repeat-track and cross-over methodologies used by the RR participants.

Participant	Processing specifications	External data	Error estimation
SEC-1	LSq; relocation: POCA backscatter correction: inherent in LSq solution	GIMP DEM	Standard error of the trend
SEC-2	LSq; plane fitting	N/A	RMS of plane fits
SEC-3	Multivariate LSq	Basin mask InSAR velocities*	Standard error of the trend
SEC-4	Weighted LSq; assumes SEC to vary linearly with position	Ice mask	Standard error of the trend
SEC-5	Unweighted LSq	N/A	Error from LSq covariance matrix + RMS of elevation difference residuals
SEC-6	Linear-sinusoidal fit to elevation differences	N/A	Standard error of dH/dt values within each cell
SEC-7	Linear-sinusoidal fit to elevation difference time series	N/A	Standard error of the trend
SEC-8	Unweighted LSq fit to elevation difference time series	N/A	Error from LSq covariance matrix + RMS of elevation difference residuals;
SEC-9	Linear-sinusoidal fit to elevation difference time series; backscatter correction for $dH, d\sigma^0$ correlation >0	N/A	Standard error of the trend
SEC-10	Linear-sinusoidal fit to elevation difference time series; backscatter correction for $dH, d\sigma^0$ correlation >0.5	ECMWF ERA- Interim surface pressure derived dry troposphere correction [†]	Standard error of the trend

Notes: 'LSq' abbreviates linear least-squares regression and 'POCA' the point of closest approach method.

*Ice velocities are obtained from the work of Joughin et al. (2010).

[†]The European Centre for Medium-Range Weather Forecasts Interim Reanalysis (ECMWF ERA-Interim) correction is described in the work of ESA (2011b).

SEC-3 solves for dH/dx , dH/dy , and dH/dt , whereas SEC-1 also solves for the waveform parameters, i.e. backscatter, trailing edge slope, and leading edge width (Legresy et al. 2005). Only one group relocates the RA points: SEC-1 who uses a point of closest approach (POCA) method (Gray et al. 2013; Hawley et al. 2009). The errors from SEC-1, SEC-3, and SEC-4 are given as the standard errors of the LSq fit. SEC-2 uses the one from the plane fitting and SEC-5 that from the unweighted LSq covariance matrix combined with the RMS of the elevation estimation residuals within each along-track segment.

The SEC estimation is carried out similarly for SEC-7, SEC-9, and SEC-10, who apply a linear-sinusoidal fit to time series of elevation differences. SEC-9 filtered observations with noise levels of the waveforms exceeding five counts. SEC-6 submitted the median dH/dt signal from all values within each grid cell, whereas SEC-8 applies an unweighted LSq fit, in which data errors are included through data covariance matrices (e.g. Gunter et al. 2014; Khvorostovsky 2012; Zwally et al. 2005). The error estimates from SEC-7, SEC-9, and SEC-10 are given as the standard errors of the time series trends, while SEC-6's errors represent the standard deviations (STDs) of the SEC values in each grid cell. Finally, SEC-9 and SEC-10 have corrected the SEC estimates for backscatter effects when the correlation between elevation differences (dH) and changes in the received backscatter power ($d\sigma^0$) is either positive or exceeds 0.5, respectively. The relation between the two is given by $dH = dH - d\sigma^0 \times (dH/d\sigma^0)$ (Arthern 1997; Khvorostovsky 2012). SEC-9 applies additional corrections for the leading edge width and trailing edge slope.

The RA data sets are based on three different retrackers, namely ESA's ICE-1 and ICE-2 as well as a 10% threshold retracker (Davis 1997; ESA 2011b). However, cf. Khvorostovsky (2013), although SEC estimates do differ prior to correcting for waveform information, they agree afterwards. Hence, in spite of the retrackers applying different corrections, comparable results are obtained.

3.3. Validation

The RR results are validated against SEC trends derived from ATM data. The campaigns are carried out yearly, except for in 2004, in the months April, May, and August. In order to ensure temporal consistency, two separate trends are derived for 2003–2009 and 2002–2010, respectively. The focus area is the main trunk of Jakobshavn ($68.5\text{--}70^\circ\text{ N}$; $47\text{--}50.5^\circ\text{ W}$), where the largest surface changes are observed (Joughin et al. 2014; Liu et al. 2012; Nielsen et al. 2013). The ATM trends are derived by fitting a linear trend as well as cyclic terms to the observations. In order to make a proper ground truth, only values based on a minimum of three observation periods are used.

The validation is carried out by subtracting the ATM dH/dt trend from the RR values. This is done by, for each RR point, finding all available ATM observations within a polygon surrounding the point. The size of the polygon is determined by the spatial resolution used in the respective submission (Table 2). The given ATM values are averaged to find the mean, which is subtracted from the RR value to give $dH/dt_\Delta = dH/dt_{RR} - dH/dt_{ATM}$. Finally, the mean and STD of dH/dt_Δ are estimated. The method of averaging the ATM values within each grid cell is chosen to account for: (1) the respective measurements not necessarily being conducted in the exact coordinate of the grid cell centres, and (2) the spatial resolutions applied by the RR participants.

This is typically not a problem for small search areas such as the along-track segments used in RT analyses, which are confined to the ground-track and limited by the altimeter's footprint. For larger spatial resolutions, however, correspondingly larger variations in the SEC signal may occur, thereby affecting the statistics.

4. Results

The following sections present the RR results along with their validation and intercomparison.

4.1. The round robin exercise

Figures 1 and 2 show the participants' elevation change estimates and corresponding errors. The results are presented according to the use of RT and XO, respectively. The errors are derived in various ways, such as from the standard error of the trend, or by including covariance matrices. Therefore, the values are not directly comparable. They do, however, provide important information on the accuracy of the different methods and thus are included after all.

The RT results are given in dense grids covering the entire observation area, and both RA and LA resolve the SEC values quite well. SEC-1's ENVISAT results are particularly interesting as they illustrate the possibility of using radar altimetry to observe surface changes throughout the area and thus also along the coastal and ice margins. The estimates from both sensors agree well in the interior, whereas a small offset is found by the coastal margin where ICESat data (SEC-2–SEC-5) show a larger thinning.

The associated errors decrease with an increasing elevation and are near-zero in the interior ice sheet. Therefore, the errors are described relative to their respective altitude, i.e. for locations above and below 2000 m (Table 4). Where no elevations are submitted, the GIMP DEM is used as a reference. For RT measurements below 2000 m, the LA results from SEC-2 and SEC-4 reveal maximum errors of 3 and 3.8 m year⁻¹, respectively, while the values from SEC-3 and SEC-5 reach approximately 0.5 m year⁻¹. SEC-1's RA errors are larger and reach 39 m year⁻¹. For measurements above 2000 m, the errors generally decrease due to the smoother surface exposed to smaller changes (Sørensen et al. 2011). Thus, SEC-1's errors have decreased to a maximum of 0.9 m year⁻¹, SEC-2's to 1.9 m year⁻¹, SEC-3's to 0.2 m year⁻¹, and SEC-5's to 0.1 m year⁻¹. The maximum error from SEC-4 is similar for both areas although more values are closer to zero (99% less than 1 m year⁻¹ over high elevation area against 97% at lower elevations).

SEC-1's ENVISAT results are particularly interesting as they illustrate the possibility of using RA to observe surface changes even along the coastal margin, where surface topography, due to high slopes and undulations, and penetration of the radar echoes distort the measurements. The results contain the largest errors, however still provide an important insight into the surface changes. Additional differences between the measured SEC signals from RA and LA result from ENVISAT's footprint, preventing it from resolving small ice streams, the fact that the satellite cannot be pointed cross-track to ensure precise repeat-tracks, as well as the ICESat observation period being shorter by 2 years.

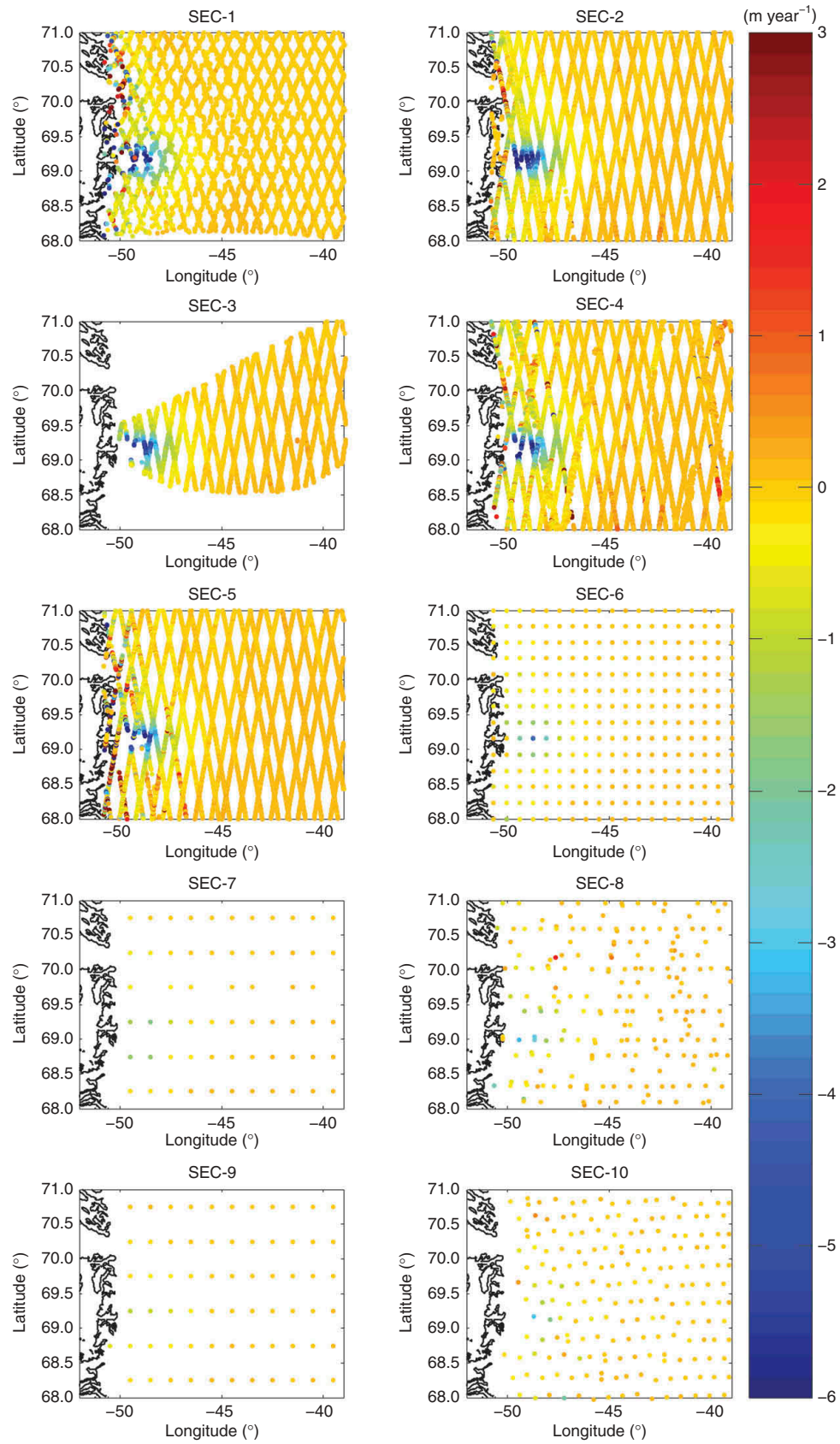


Figure 1. Surface elevation change estimates derived using repeat-tracks (participants SEC-1 to SEC-5) and cross-overs (SEC-6 to SEC-10).

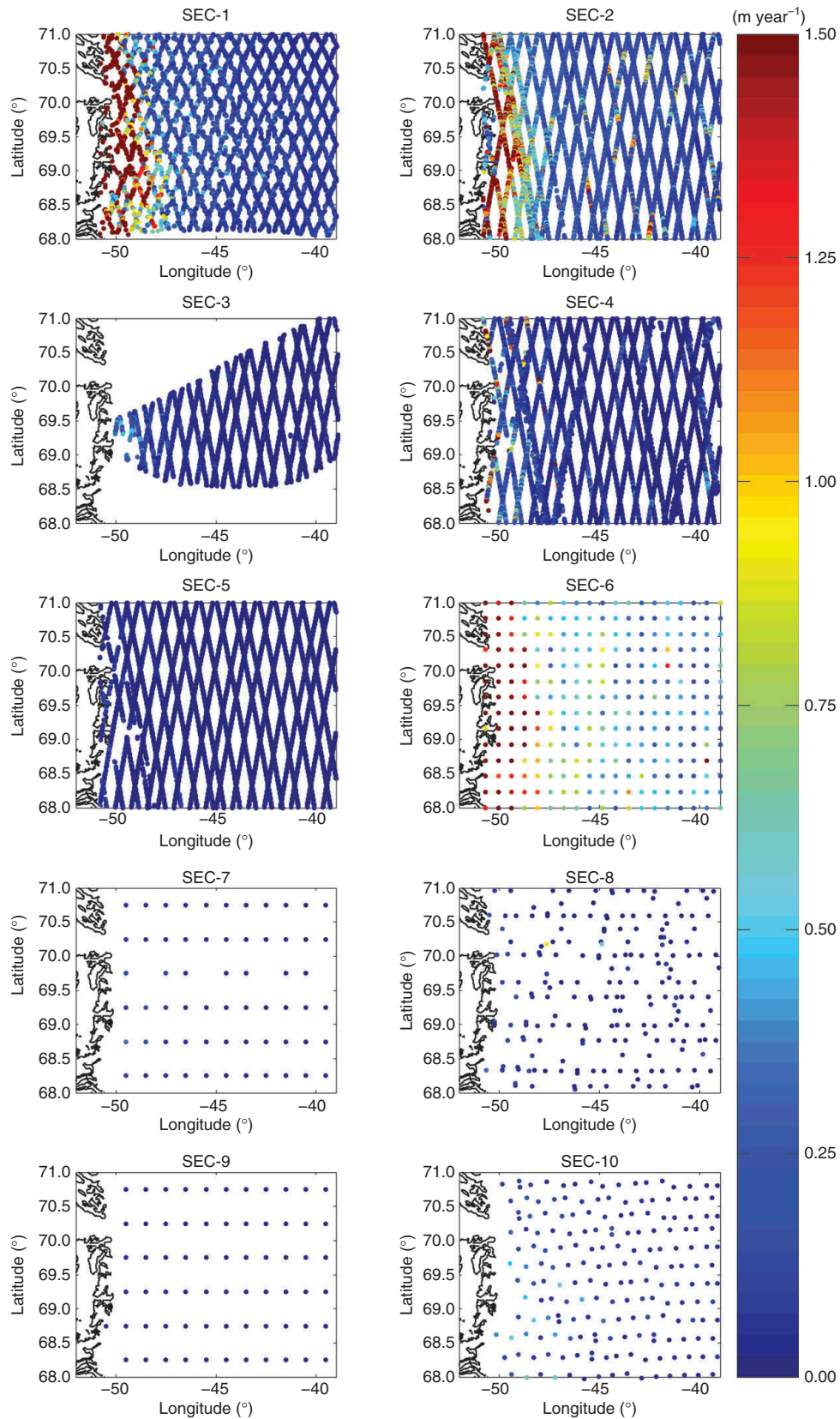


Figure 2. Surface elevation change errors from repeat-track (participants SEC-1 to SEC-5) and cross-over (SEC-6 to SEC-10) analyses.

Table 4. Mean and maximum errors for repeat-track (SEC-1 to SEC-5) and cross-over (SEC-6 to SEC-10) analyses.

Participant	Number of points	Below 2000 m		Number of points	Above 2000 m	
		Mean error (m year ⁻¹)	Max. error (m year ⁻¹)		Mean error (m year ⁻¹)	Max. error (m year ⁻¹)
SEC-1	3394	2.52	38.88	8132	0.11	0.89
SEC-2	10,186	0.68	3.03	20,630	0.20	1.86
SEC-3	1213	0.09	0.49	5848	0.02	0.24
SEC-4	6697	0.20	3.84	13,819	0.04	3.83
SEC-5	3113	0.02	0.42	6959	0.01	0.06
SEC-6	94	1.28	3.45	172	0.46	1.51
SEC-7	43	0.09	0.35	20	0.02	0.05
SEC-8	59	0.09	0.93	135	0.02	0.55
SEC-9	46	0.02	0.05	21	0.01	0.02
SEC-10	137	0.21	0.67	53	0.07	0.44

The XO results, SEC-6 to SEC-10, do not fully resolve the large thinning observed along the drainage basin and coastal margin using RT. This can be explained by the XO estimates being found by gridding the observations into cells, thereby losing part of the SEC signal due to the applied smoothing. As the RR participants have used differently sized grid cells, observations from the same sensor do not agree in space; the only overlap is found for SEC-7 and SEC-9 due to the submissions coming from the same research institution. Interior dH/dt estimates agree well for the two sensors, thereby illustrating the capabilities in this region regardless of the applied method and type of altimeter. The data errors (Table 4) for LA measurements below 2000 m reach a maximum of 3.5 m year⁻¹ for SEC-6, 0.4 m year⁻¹ for SEC-7, and 0.9 m year⁻¹ for SEC-8. The maximum errors of the radar-based submissions are 0.1 m year⁻¹ and 0.7 m year⁻¹, respectively. As was observed using RT, estimates over higher elevations have smaller errors: SEC-6's errors have decreased to 1.5 m year⁻¹ while those for SEC-7 and SEC-8 decreased to 0.1 and 0.6 m year⁻¹. The RA errors are 0.0 m year⁻¹ for SEC-9 and 0.4 m year⁻¹ for SEC-10, respectively.

When comparing the values estimated using a similar method (column 4, Table 3), i.e. SEC-1, 3, 4, 7, 9, and SEC-10, giving the standard error of the trend, it is clear that the XO errors are typically lower. The reason for SEC-6 deviating from this is the estimation of the standard error of the dH/dt values instead. The lower XO errors indicate that such analyses produce the highest accuracy as slope effects from the local topography can be ignored. The method does, however, for RA require an initial slope correction of data. Because of the spatial distribution of ground-tracks, XO points are limited in space, particularly along the coastal margin. The opposite is found with RT, which has a high spatial coverage, however, a lower accuracy due to the lack of exact repeat ground-tracks.

In the following, results from SEC-7 and SEC-9 are given for the validation exercise; they are, however, not considered in detail neither here, nor in the intercomparison. This is due to the size of the grid cells (0.5° lat × 0.1° lon, i.e. approximately 50 km × 50 km) relative to the respective footprint sizes: the spatial resolution cannot accurately reproduce the changes visible with neither sensor.

4.2. Validation using airborne laser-scanner data

Validation is carried out using ATM data. Two SEC trends are derived for 2003–2009 and 2002–2010, respectively; Figure 3 provides an example of the former. The mean and STD of the RR minus ATM SEC trends, dH/dt_{Δ} , are estimated (Table 5). Due to the observation area being confined to the lowest part of the glacier and consequently the relatively small data sampling, the validation is not split up relative to the altitude.

The statistics for the RT measurements confirm the advantage of the validation method for the relatively small along-track segments: near-zero means indicate very good agreements with validation data. For SEC-2 to SEC-5, this results from the high accuracy of LA data as well as the spatial resolutions consistent with the ICESat footprint. For SEC-1, whose results are based on ENVISAT RA and a spatial resolution of $5 \text{ km} \times 5 \text{ km}$, the agreement is quite remarkable: this data set has the smallest mean and STD of all RT measurements, namely 0.01 m year^{-1} and 1.57 m year^{-1} , respectively. The statistics are, undoubtedly, affected by the highest amount of validation points. However, the validity of SEC-1's results is further confirmed in an intercomparison below, where scatter plots of LA and RA RT measurements reveal a coefficient of determination, R^2 , of 0.84. Both results confirm the capability of using RA data to resolve SEC estimates even in margin regions of the ice sheet.

In spite of the low RT mean values, the STDs are generally higher than for XO. A possible explanation is that the validation points used for the RT comparison are located

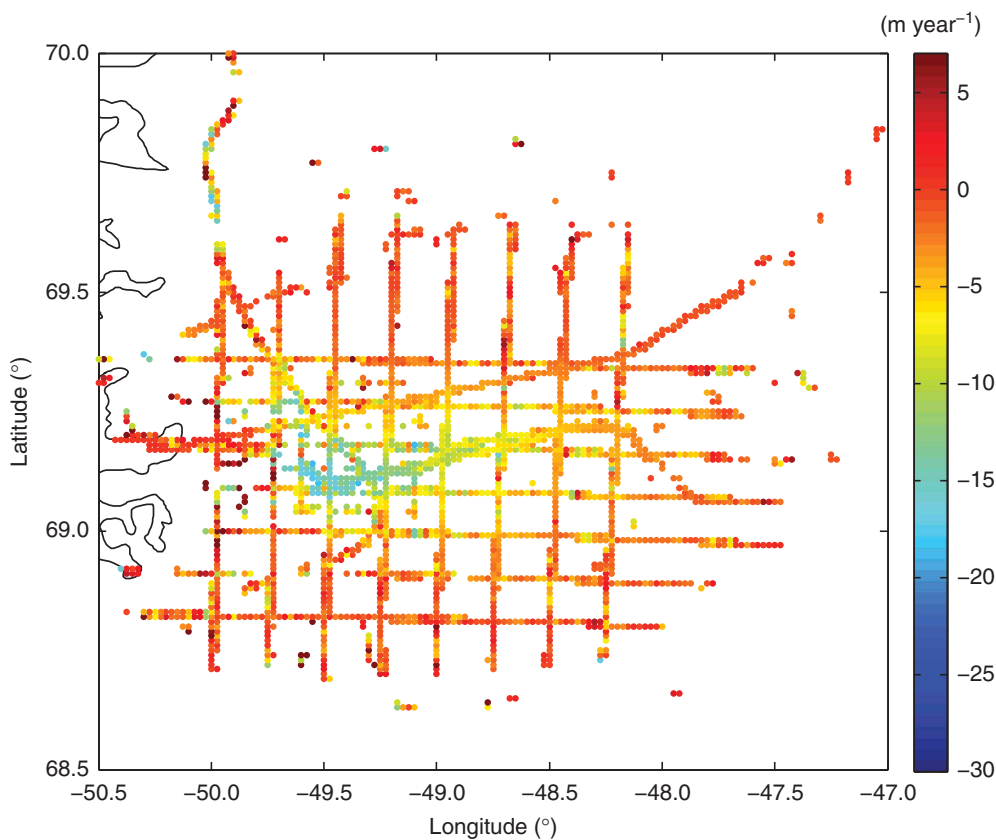


Figure 3. Validation data: surface elevation changes derived from 2003–2009 ATM data. As the ATM flights largely cover the same flight lines, the 2002–2010 trend (not shown) is given along the same coordinates.

Table 5. Results obtained from the validation of the round robin datasets using dH/dt trends derived from ATM data.

Participant	Number of points	Mean (dH/dt_{Δ}) (m year^{-1})	STD (dH/dt_{Δ}) (m year^{-1})
SEC-1	670	0.01	1.57
SEC-2	296	0.56	3.78
SEC-3	140	0.81	2.20
SEC-4	104	0.13	3.89
SEC-5	165	0.56	3.78
SEC-6	26	1.89	3.01
SEC-7	11	1.29	1.31
SEC-8	5	1.54	1.38
SEC-9	13	1.53	1.27
SEC-10	17	2.42	2.86

Notes: The search radius used for overlapping grid cells is given by the spatial resolution of the respective submissions, just as the temporal coverage of the validation trends corresponds to that of the submissions (Table 2). dH/dt_{Δ} gives the dH/dt difference between the round robin and ATM values, and the mean and STD hereof are presented.

close to and along the coastal margin, whereas those for XO typically have only a few observations in this region and most at high altitudes. As the margin region is subject to the largest surface changes, a varying surface topography means that these patterns can change even within hundreds of metres (Levinsen, Howat, and Tscherning 2013). This may explain the relatively high RT STD.

This topographic difference also clarifies the smaller STD for XO measurements. Their respective means are generally higher, which is a result of the different RR SEC routines as well as the typically larger grid cells. The latter may complicate the process of obtaining agreeing ATM and RR results as any variations in the dH/dt trends are smoothed out in the averaging. The typically larger spatial resolutions in XO analyses reduce the number of validation points and increase the mean difference, namely from 0.41 m year^{-1} for RT to 1.73 m year^{-1} for XO. Therefore, when considering the XO results, it should be noted that the average number of observations for the comparison is 14 against 275 for the RT analyses.

The higher mean values are exactly observed for the remaining XO observations, where SEC-6 has a spatial resolution of $8 \text{ km} \times 8 \text{ km}$ while that for SEC-7 and SEC-9 is as large as $50 \text{ km} \times 50 \text{ km}$. SEC-8 has the smallest cells and thus should reveal the optimal agreement with ATM data; however, given such a small spatial resolution, only five validation points are available, and hence the respective mean and STD are not believed to fully represent the data set.

SEC-10 has the largest mean of 2.42 m year^{-1} ; the STD is 2.86 m year^{-1} , i.e. second-highest after SEC-6. Similarly to SEC-1, the work is based on ENVISAT data. However, although the size of the grid cells agrees well with the RA footprint, no relocation of the estimation points has been carried out. This introduces errors when compared with a laser-based data set and hence explains the large offset.

As mentioned above, SEC-6 has the highest XO STD of 3.01 m year^{-1} . Comparing Table 4, the data set also has large errors; see Section 5 for more details on the reason.

Based on the above, the validation has shown the following:

- RT measurements provide the best validation results with near-zero means. This supports the application of a high spatial resolution and the exploitation of the large data coverage to be achieved with RT; both contribute to a high agreement with validation data.
- RT measurements are, however, subject to larger STD due to more of the observations being located at lower altitudes with a greater spatial SEC variability.
- SEC-1's RT results are based on RA and a $5 \text{ km} \times 5 \text{ km}$ resolution. In spite of slope-induced errors, the data set has illustrated the capabilities of RA to accurately resolve SEC trends both inland and in margin parts of the ice sheet, although with errors exceeding those from LA, particularly at lower altitudes.
- Validation points for XO measurements are few in space, which bias the statistics. This is due to the larger grid cells in which parts of the SEC signal are lost due to smoothing of the observations. The result is generally higher mean differences.

4.3. Intercomparison of round robin results

In order to thoroughly analyse the applied methods, a number of intercomparisons are made. As before, only observations within similar spatial domains are compared. This is achieved by using search radii based on the spatial resolutions of the data sets in question. The given methods are then assessed by finding overlapping estimation points and differencing the SEC values herein ('diff'). The mean and root mean square errors (RMSEs) of these differences are calculated, and scatter plots are used for estimating the coefficient of determination and the slope of the regression (Figure 4 and Table 6).

The following analyses are carried out.

- (1) *Laser: repeat-track versus cross-overs – SEC-3 versus SEC-8*
The results from SEC-3 proved to be very accurate, the spatial resolutions are similar, and both data sets cover the period February 2003–October 2009. This analysis opens the way to testing the capabilities for ICESat change detection using XO.
- (2) *Laser: repeat-track versus cross-overs – SEC-5 versus SEC-8*
The observations from SEC-5 span September 2003–October 2009, i.e. one summer less than SEC-8. The data sets do, however, have similar spatial resolutions.
- (3) *RT: laser versus radar altimetry – SEC-1 versus SEC-3*
Both data sets proved to be highly accurate in the validation.
- (4) *XO: laser versus radar altimetry – SEC-8 versus SEC-10*
SEC-7 and SEC-9 are not representative due to the large grid cells, and the method for deriving dH/dt estimates is most similar to that for SEC-8 and SEC-10.
- (5) *Radar: repeat-track versus cross-overs – SEC-1 versus SEC-10*
The two data sets are the most similar considering spatial and temporal resolutions.

The first analyses are based on the highly accurate LA data to validate the outcome, and hence quality, of the RT and XO methods. Both types of altimeters are then tested for RT

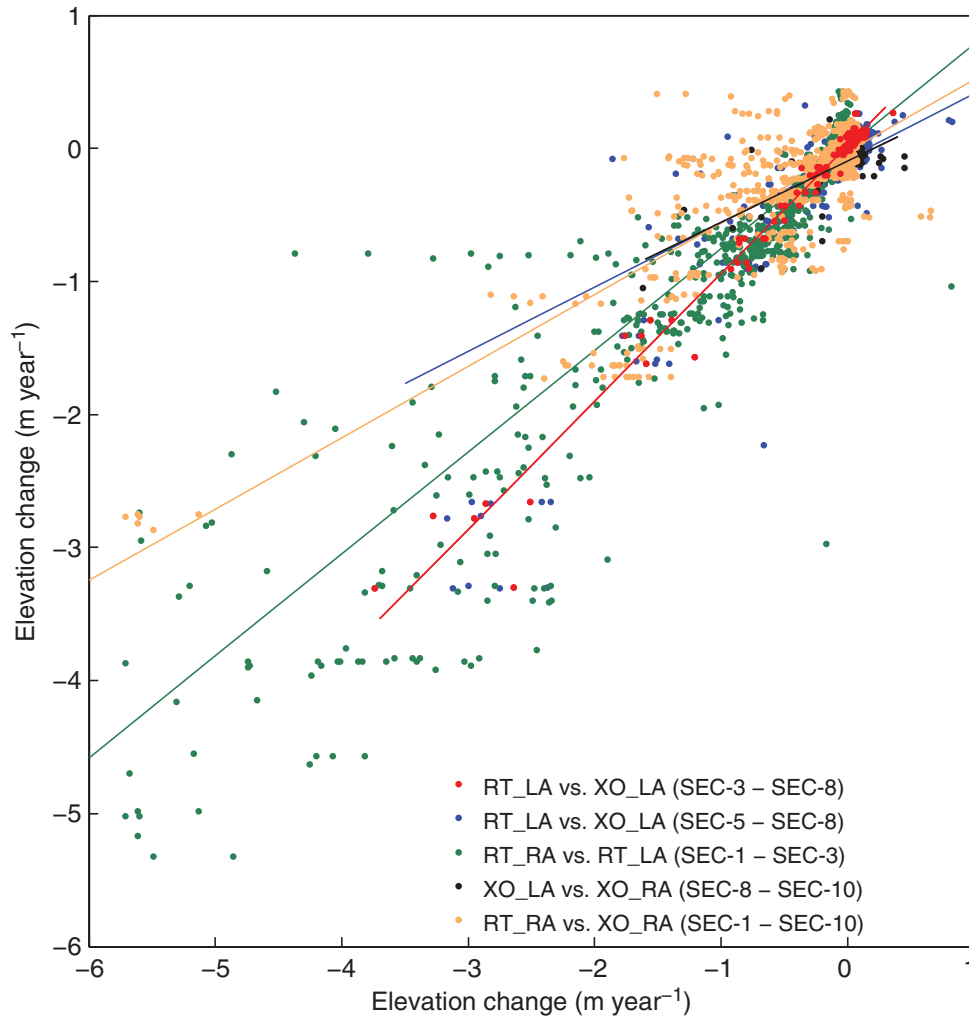


Figure 4. Scatter plots from intercomparing the selection of the round robin results: cross-overs *versus* repeat-tracks for radar and laser altimetry and radar *versus* laser altimetry for both methods. The *x*-axis depicts the first-mentioned submission in the legend and the *y*-axis depicts the latter. See Table 6 for the corresponding statistics.

Table 6. Results obtained from the intercomparison of the selection of the round robin results.

Participants	Method	Sensor	Search radius (km)	# of points	Mean (diff) (m year ⁻¹)	<i>R</i> ²	Slope
SEC-3–SEC-8	RT versus XO	Laser	1	226	-0.03	0.98	0.96
SEC-5–SEC-8	RT versus XO	Laser	1	493	-0.13	0.39	0.49
SEC-1–SEC-3	RT	Radar <i>versus</i> laser	5	3935	-0.07	0.84	0.77
SEC-8–SEC-10	XO	Radar <i>versus</i> laser	10	76	0.08	0.53	0.46
SEC-1–SEC-10	RT versus XO	Radar	5	2050	-0.05	0.66	0.54

Note: The search radius used for finding overlapping grid cells is based on the spatial resolution given in Table 2, while ‘diff’ holds the dH/dt difference for the groups in question.

and XO observations separately to see whether RA performs equally well as LA. A final intercomparison based on RA is made to test whether RT and XO are capable of resolving the same SEC signal. In the analyses involving SEC-3, it should be noted that those observations are limited to the drainage basin. As SEC-1’s and SEC-8’s results become

more noisy outside this area, intercomparisons with SEC-3 may be biased to give better agreements than those obtained for other comparison exercises.

The two laser analyses yield R^2 of 0.98 and 0.39 and slopes of the regression of 0.96 and 0.49, respectively. This indicates that both RT and XO measurements from ICESat are capable of resolving SEC trends within the drainage basin, but that they are indeed affected by the more noisy SEC-5 signal. This data set covers a larger region, making it more exposed to spatial changes in the SEC trend, which are lost in the averaging of XO estimates. This naturally introduces an offset.

The analyses of RA *versus* LA data show an offset in the resolved SEC signal. As neither of the compared data sets is based on the same temporal or spatial resolution, firm conclusions cannot be drawn. It is, however, clear that the altimeters resolve the rate of thinning differently. The RT measurements – based on the highly accurate SEC-1 and SEC-3 – agree well, which are positive considering the different types of altimeters as well as the geographical constraint to the quickly changing drainage basin. Thus, RT analyses from RA provide comparable results with those from LA. The XO measurements show a poorer correlation, with SEC-8 resolving a greater variation in the SEC signal. This is partly due to the different altimeters and spatial resolutions, and partly to the lack of relocation of the SEC-10 measurements, the latter thus demonstrating the necessity for doing so.

Hence, the above also explains the observed disagreement in the final analysis, namely that of RT and XO for RA data. The observations from SEC-1 proved to be highly accurate, and therefore the observed difference is believed to result from the methods used for obtaining the results – not the use of either RT or XO.

To summarize, the best SEC results for the given sensors and techniques arise from LA: SEC-3's RT solution and SEC-8's XO method; RA: SEC-1's RT solution and SEC-9's XO method. The latter is based on the lack of relocating SEC-10, the smaller SEC-9 errors, and the corresponding better validation results. Therefore, it is believed that the lowering of the spatial resolution to better agree with the RA footprint will significantly improve the results. The respective data sets are further discussed below.

5. Discussion

Figure 5 illustrates the relationship between the RR elevations and dH/dt values. A random subset has been plotted to optimize the visualization. Where elevations have not been supplied, they have been derived from the GIMP DEM. Generally agreeing, near-zero dH/dt values are found in the interior while disagreements occur nearer the coastal margin. This pattern follows that of the error estimates, which increase with a lowering altitude. The observed changes in the interior are small, and both LA and RA perform well, regardless of the method. The largest offsets are found for SEC-10 due to the missing relocation. Closer to the coastal margin, a disagreement arises due to data errors, different data locations, and different routines applied for the SEC estimation. Most XO results are near-zero due to the data locations typically being on higher elevations, far from the glacier outlet, as well as averaging of the observations over larger grid cells. Collaborations with one of the XO participants demonstrated the effect of the latter: a simple experiment in which the results were downscaled to $1\text{ km} \times 1\text{ km}$ grid cells revealed a much better agreement with validation data and hence a significant improvement of the data accuracy. This further illustrated the advantage of applying a spatial resolution corresponding to the given footprint size (B. Gunter, pers. comm.).

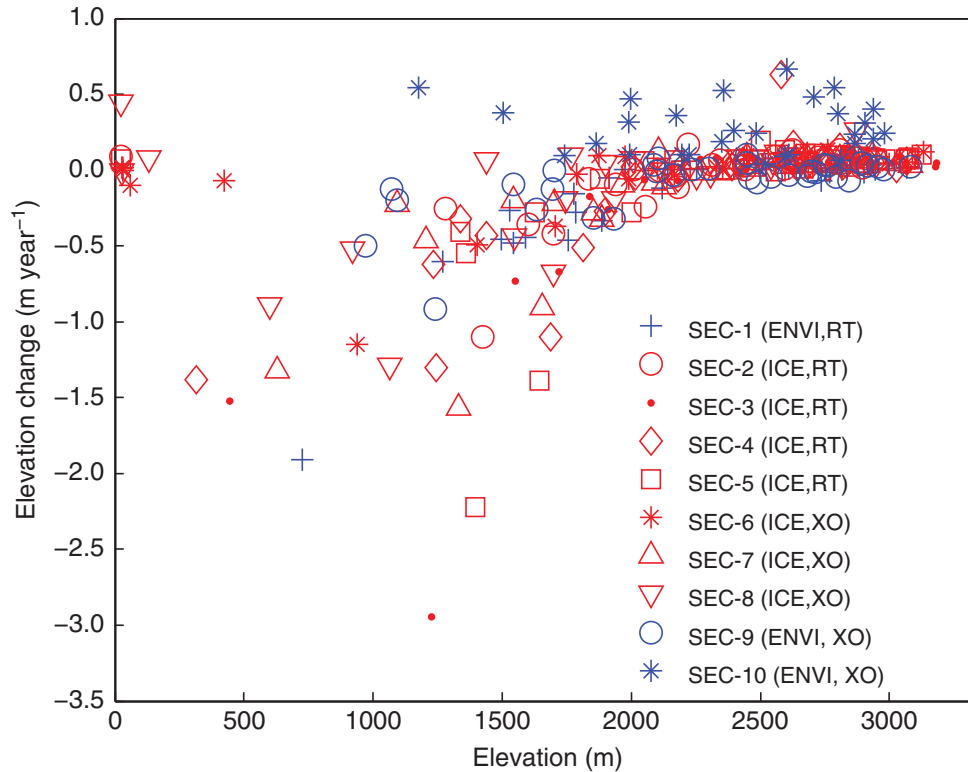


Figure 5. Subset of surface elevation *versus* dH/dt values.

RA and LA not being able to resolve the same SEC signal means that differences will arise when converting the results to estimates of mass balance changes. The statistics for the respective intercomparisons are indicative of this difference. Since the SEC-1 and SEC-3 RT estimates exhibit a higher accuracy, and due to the few XO points, the RT analysis is investigated further. The focus lies on the coastal region, i.e. observations below 2000 m altitude. This yields 713 estimation points with a mean(diff) of -13 cm year^{-1} , i.e. a larger difference than for the whole area, -7 cm year^{-1} . For mass balance estimates, assuming only ice and an ice density of $\rho_{\text{ice}} = 917 \text{ kg m}^{-3}$, this corresponds to an additional mass loss of 20 Gt year^{-1} for an area, A , of $1.7 \times 10^5 \text{ km}^2$. The change rate has been estimated cf. $dM/dt = \rho_{\text{ice}} \times (A \times dH/dt)$, i.e. without accounting for SEC changes due to firn compaction and surface mass balance variability as in the work of Hurkmans et al. (2014). Considering a total GrIS mass loss of $263 \pm 30 \text{ Gt year}^{-1}$ for the period 2005–2010 (Shepherd et al. 2012), the SEC offset corresponds to a difference of 7%, i.e. a relatively small contribution. The above is a crude estimate for the specific observation area and based on observations with different spatial resolutions and observation periods. A more in-depth investigation of the RA-LA SEC differences was done by Sørensen et al. (2014), who compared 2003–2009 SEC trends derived from ICESat and ENVISAT data, respectively, and sampled to a similar spatial resolution. They found a correlation with changes in the accumulation rate and firn air content, and that the specific pattern is highly complex as it varies for different climatic zones and conditions. A full understanding of the changes therefore requires in-depth analyses of accumulation, air content of the firn, surface temperature, melt, etc. This indicates that the offsets found in the RA *versus* LA intercomparisons only represent this specific region.

Part of the RA-LA SEC differences is due to backscatter of the RA echoes, an effect that varies throughout the ice sheet and is at a maximum in the interior (Legresy et al.

2005). Several studies have demonstrated that it has a large seasonal cycle and varies greatly with the length of the observation period, however that it makes a small contribution to elevation change rates: Wingham et al. (1998) found an average SEC correction of 1.1 cm year^{-1} with variations of approximately $\pm 30 \text{ cm year}^{-1}$ for 1992–1996 ERS data over Antarctica; over Greenland, Zwally et al. (2005) found a mean and STD of $0.02 \pm 2.36 \text{ cm year}^{-1}$ from 1992–2002 ERS data, while Khvorostovsky (2012) found a mean correction of $0.35 \text{ cm year}^{-1}$ with variations exceeding $\pm 3 \text{ cm year}^{-1}$, for 1992–2008 ERS and ENVISAT data. The correction therefore provides an important, however small, contribution to the final SEC estimates.

The fact that the adjustment does indeed affect the change detection has led to a deeper investigation of the correction's impact on the RA submissions and the potential conversion of these into estimates of mass balance changes; all participants accounted for backscatter, and one participant agreed to submit additional results for analyses covering both given observation area and entire GrIS. For the Jakobshavn Isbræ basin, the mean dH/dt signal changed by 1 cm year^{-1} while variations ranged from -19 cm year^{-1} to $+11 \text{ cm year}^{-1}$. For the ice sheet, the mean was 6 cm year^{-1} with variations from -77 cm year^{-1} to $+39 \text{ cm year}^{-1}$. Converting a 1 cm year^{-1} backscatter correction into mass balance changes, and using a GrIS area of $2.166 \times 10^6 \text{ m}^2$, yields mass losses of approximately 2 Gt year^{-1} and 20 Gt year^{-1} , respectively, for the two areas. The latter corresponds to a $<10\%$ adjustment of the GrIS volume rate and therefore makes a relatively small improvement. This confirms that the adjustment for backscatter does make a small contribution to the SEC estimation and, therefore, the conversion hereof into mass balance changes.

An interesting observation in the ICESat data sets is that in spite of the participants using the same data release (R33) and some the same method, e.g. RT with LSq, the results differ. This is partly due to varying processing and estimation schemes, such as slightly different data rejection criteria and LSq techniques, i.e. weighted, unweighted, and multivariate approaches, respectively. An additional reason is the inter-campaign biases, which vary with time, thus affecting the accuracy of the ICESat elevation measurements. Different groups have obtained different bias estimates for the same data set, and none of them have applied the Gaussian-centroid part of the bias as discussed by Borsa et al. (2014). In spite of this, SEC-3's results are found to be highly accurate and thus demonstrate an optimal solution for change detection using LA. The group that provided these data solved for the surface slope and elevation changes using a multivariate LSq technique, and residual elevations from the regression exceeding 5 m were iteratively discarded to ensure each estimation value to be based on ≥ 10 footprints from at least four epochs covering a minimum of 2 years. Furthermore, the method rejected SEC estimates when the standard error exceeded 0.5 m year^{-1} , ensuring the inclusion of estimates with a high accuracy only.

Minimizing the errors is important. However, in order to ensure confidence in the final results, it is equally important for the errors to reflect the nature of the observation area. This is possible when using the methods by SEC-5, SEC-6, and SEC-8: the estimates from SEC-5 and SEC-8 are based on contributions from the dH/dt trend as well as the observations themselves, the data errors being included by adding a data covariance matrix into the least-squares fit. SEC-6's errors are computed as STDs of the dH/dt values within any given grid cell, thereby providing more of a measure of the surface variability within each grid cell than an assessment of the accuracy of the technique. As such, an observed SEC variability translates into the error estimates, hence explaining the generally higher XO values particularly near the coastal margin. Thus, both methods yield

larger errors mainly in highly dynamic and topographically rough areas, and this presumably makes the estimates more realistic.

In spite of all RR contributions not being directly comparable, several intercomparisons across methods and altimeters were possible. Thus, the unique value of the round robin exercise is the ability to evaluate the submissions regarding methodology, pre- and post-processing steps, etc. The main outcomes of the round robin are the great potential of both RT and XO analyses, best visible for LA due to the higher data accuracy, and, most importantly, also clear for RA RT analyses: investigations of SEC-1's results demonstrate RA's capabilities of resolving SEC throughout the GrIS, albeit with larger errors than in LA studies. Therefore, an iterative linear least-squares approach applied to RA RT data in which e.g. surface slope and backscatter parameters (leading edge width, trailing edge slope, and backscatter) are solved for is promising. The XO analyses show that LA accurately resolves the SEC signal, and that RA is capable of the same given relocation of the measurements and the spatial resolution corresponding to the altimeter footprint. Therefore, SEC-9's linear-sinusoidal fit with the application of a backscatter correction and for smaller grid cells is expected to provide the best RA XO results.

Thus, a combination of RT and XO modules will allow for exploiting the respective high spatial coverage and high accuracy to precisely map SEC throughout the ice sheet, i.e. both in interior and margin regions. Based on the results from SEC-1, a spatial resolution of $5.0 \text{ km} \times 5.0 \text{ km}$ is a sufficient trade-off between the resolution achievable with RA and the final SEC accuracy. This shows great potential for the creation of an extensive SEC data set based on RA from ERS, ENVISAT, CryoSat-2, and, in the longer term, Sentinel-3. Not only will it yield a time series based on more than two decades of observations; the greater amounts of observations overlapping in time and space will also help in reducing estimation errors.

Due to different observation periods and flight times, completely agreeing acquisition times of the data used in the RR analysis cannot be achieved. This will introduce a difference between the RR and ATM validation dH/dt trends, which, if not accounted for, affects the comparison of the two types of data. The airborne campaigns are typically conducted in April/May or August, whereas ICESat data are only available in the periods of active lasers. Thus, when comparing a trend based on ATM data obtained in May with the one derived from altimetry data acquired in e.g. October/November, the intermediate surface elevation changes must be accounted for. This elevation difference can, theoretically, be corrected for using a positive degree day model such as that of van den Broeke et al. (2010). It is based on the RACMO2/GR regional atmospheric climate model for Greenland (van Meijgaard et al. 2008) as well as observations from three automatic weather stations located in Jakobshavn's ablation zone. It calculates the degree day factors for snow and ice, respectively, i.e. a measure of the melt per positive degree-day. Given the knowledge on what is melting, an estimate of the vertical surface change can be found. Problems with such a model are e.g. the sparsity of weather stations throughout the ice sheet, and the lack of observations of the exact composition of the surface material (e.g. ice, firn, or snow). Further complications arise as it does not account for precipitation, for which the rates are the highest in the southern parts of the GrIS (Ettema et al. 2009; Sasgen et al. 2012). As the precipitation pattern changes both in time and space, the exact rates at which this occurs are needed. They are, however, unknown. The lack of observations also distort mass balance approaches, where flux-balance and surface mass balance estimates can be used to infer the vertical surface change. Additional error sources are the poorly known density needed for such estimates as well as the seasonal variability of all of the above.

This indicates the difficulty in estimating an accurate vertical correction term to be applied to the ATM SEC trends. However, when applying the model and using a threshold temperature of $T_0 = -5^\circ\text{C}$ in order to include (nearly) all melt days, it is found that the largest elevation difference from either snow or ice is a few metres, i.e. less than the dynamical thinning observed in the area.

6. Conclusions

Several studies have been performed on the estimation of SEC of the Greenland ice sheet using altimetry, e.g. Zwally et al. (2005, 2011), Sørensen et al. (2011), Khvorostovsky (2012). The most commonly applied methods are the repeat-track (RT) and cross-over (XO) techniques based on either laser or radar altimetry. In order to assess the quality of the respective SEC solutions, an intercomparison exercise was conducted with contributions from the scientific community. Based on the findings, the best-performing SEC solution for ESA radar altimetry was identified. Ten data sets were analysed covering the Jakobshavn Isbræ drainage basin and derived using either radar (ENVISAT) or laser altimetry (ICESat). Intercomparisons of RT *versus* XO studies and laser *versus* radar data were performed, and the solutions were validated against SEC trends from temporally consistent and spatially collocated NASA ATM data. The conclusions can be summarized as follows.

- The spatial resolution of SEC estimates is higher with RT than with XO. Thus, RT allows for better resolving the surface changes along the coastal margin, such as along narrow ice streams.
- The XO method is advantageous as slope-induced errors from local topography can be ignored, however at the cost of a lower spatial data coverage. Validation shows a systematic bias, likely due to the spatial resolutions exceeding the altimeter footprint size. Smoothing of the data thereby removes part of the SEC signal, particularly in margin regions. Therefore, using grid cells consistently sized relative to the footprint, the method is most suitable in the smooth interior ice sheet.
- In spite of the differences between the surface signals resolved using laser and radar altimetry, validation and intercomparisons have revealed that radar data, particularly in RT analyses, can be used for accurately mapping SEC even in regions with high surface gradients.

For the ESA CCI SEC generation, we therefore propose a hybrid method in which RT and XO results are merged in order to maximize the spatial coverage and minimize the estimation errors. The merging will be carried out using geostatistical interpolation tools, i.e. the optimal gridding procedures known from collocation/simple kriging (Dermanis 1984; Goovaerts 1997; Hofmann-Wellenhof and Moritz 2005). The final SEC product will have a spatial resolution of $5\text{ km} \times 5\text{ km}$, which is a good compromise between the resolution obtained with radar altimetry, the spatial data availability, and data errors. This is e.g. demonstrated by SEC-1 who used the same resolution to map elevation changes both in margin and interior regions. When to use RT, XO, or combined results is based on a weighting of the error variances. The grid will predominately consist of RT results near repeat ground-tracks and along the coastal margin, the latter due to their higher spatial coverage, while XO estimates are found where ascending and descending ground-tracks intersect. Due to steep slopes along the margin, displacing measurement locations up-

slope from nadir, XO locations are mostly confined to higher grounds. Results obtained from this method are, however, used over as large a region as possible.

The RT and XO algorithms are already implemented among the CCI project partners and the effort for merging them into a transparent and fully operational set up is ongoing. Thus, a prototype of ENVISAT SEC is currently available at the ESA website (<http://products.esa-icesheets-cci.org/>), and the 2002–2010 results are demonstrated by Sørensen et al. (2014). The implementation of ERS and CryoSat-2 data has begun, the latter to bridge the gap between ENVISAT and Sentinel-3. The launch of Sentinel-3 is expected to take place in mid-2015 (ESA 2013). The production of the final SEC grids is thereby underway.

Acknowledgements

We thank the European Space Agency Climate Change Initiative (ESA CCI) for supporting the analysis, and the round robin participants for taking the time to submit data sets and elaborate feedback sheets. We also thank B. Gunter for his extensive contribution to the analysis. The ICESat GLAS and ATM data were downloaded from NSIDC while ENVISAT data were available through ESA.

Disclosure statement

No potential conflict of interest was reported by the authors.

Funding

This study was supported by the European Space Agency through the Ice_Sheets_CCI [grant number 4000104815/11/I-NB].

References

- Arthern, R. J. 1997. “The Impact of Climate Variability on the Determination of Ice-Sheet Mass Balance Using Satellite Radar Altimetry.” PhD diss., University of London, United Kingdom.
- Bamber, J. L. 1994. “Ice Sheet Altimeter Processing Scheme.” *International Journal of Remote Sensing* 15: 925–938. doi:10.1080/01431169408954125.
- Borsa, A. A., G. Moholdt, H. A. Fricker, and K. M. Brunt. 2014. “A Range Correction for ICESat and Its Potential Impact on Ice Sheet Mass Balance Studies.” *The Cryosphere* 8: 345–357. doi:10.5194/tc-8-345-2014.
- Brenner, A. C., R. A. Blindschadler, R. H. Thomas, and H. J. Zwally. 1983. “Slope-Induced Errors in Radar Altimetry over Continental Ice Sheets.” *Journal of Geophysical Research – Oceans* 88: 1617–1623. doi:10.1029/JC088iC03p01617.
- Brenner, A. C., J. P. DiMarzio, and H. J. Zwally. 2007. “Precision and Accuracy of Satellite Radar and Laser Altimeter Data over the Continental Ice Sheets.” *IEEE Transactions on Geoscience and Remote Sensing* 45 (2): 321–331. doi:10.1109/TGRS.2006.887172.
- Davis, C. H. 1997. “A Robust Threshold Retracking Algorithm for Measuring Ice-Sheet Surface Elevation Change from Satellite Radar Altimeters.” *IEEE Transactions on Geoscience and Remote Sensing* 35 (4): 974–979. doi:10.1109/36.602540.
- Dermanis, A. 1984. “Kriging and Collocation – A Comparison.” *Manuscripta Geodaetica* 9: 159–167.
- ESA. 2011a. “ESA Climate Change Initiative.” <http://www.esa-cci.org/>
- ESA. 2011b. “ENVISAT ALTIMETRY Level 2 User Manual.” Version 1.4. Issued October 2011. https://earth.esa.int/pub/ESA_DOC/ENVISAT/RA2-MWR/PH_light_1rev4_ESA.pdf
- ESA. 2013. “Sentinel 3.” <https://earth.esa.int/web/guest/missions/esa-future-missions/sentinel-3>
- Ettema, J., M. R. van den Broeke, E. van Meijgaard, W. J. van de Berg, J. L. Bamber, J. E. Box, and R. C. Bales 2009. “Higher Surface Mass Balance of the Greenland Ice Sheet Revealed by

- High-Resolution Climate Modeling.” *Geophysical Research Letters* 36. doi:10.1029/2009GL038110.
- Flament, T., and F. Rémy. 2012. “Dynamic Thinning of Antarctic Glaciers from Along-Track Repeat Radar Altimetry.” *Journal of Glaciology* 58 (211): 830–840. doi:10.3189/2012JoG11J118.
- Forsberg, R., K. Keller, and S. M. Jacobsen. 2002. “Airborne Lidar Measurements for Cryosat Validation.” In *Geoscience and Remote Sensing Symposium, 2002. IGARSS '02. 2002 IEEE International*, Vol. 3, June 24–28, 1756–1758. Piscataway, NJ: IEEE.
- Goovaerts, P. 1997. “Geostatistics for Natural Resources Evaluation.” *Applied Geostatistics Series*. Oxford: Oxford University Press. ISBN 0–19–511538–4.
- Gray, L., D. Burgess, L. Copland, R. Cullen, N. Galin, R. Hawley, and V. Helm. 2013. “Interferometric Swath Processing of Cryosat Data for Glacial Ice Topography.” *The Cryosphere* 7 (6): 1857–1867. doi:10.5194/tc-7-1857-2013.
- Gunter, B. C., O. Didova, R. E. M. Riva, S. R. M. Ligtenberg, J. T. M. Lenaerts, M. A. King, M. R. van den Broeke, and T. Urban. 2014. “Empirical Estimation of Present-Day Antarctic Glacial Isostatic Adjustment and Ice Mass Change.” *The Cryosphere* 8 (2): 743–760. doi:10.5194/tc-8-743-2014.
- Hawley, R. L., A. Shepherd, R. Cullen, V. Helm, and D. J. Wingham. 2009. “Ice-Sheet Elevations from Across-Track Processing of Airborne Interferometric Radar Altimetry.” *Geophysical Research Letters* 36: 22. doi:10.1029/2009GL040416.
- Helm, V., A. Humbert, and H. Miller. 2014. “Elevation and Elevation Change of Greenland and Antarctica Derived from Cryosat-2.” *The Cryosphere* 8: 1539–1559. doi:10.5194/tc-8-1539-2014.
- Hofmann-Wellenhof, B., and H. Moritz. 2005. *Physical Geodesy*. 2nd ed. Wien: Springer-Verlag.
- Howat, I. M., A. Negrete, and B. E. Smith. 2014. “The Greenland Ice Mapping Project (GIMP) Land Classification and Surface Elevation Datasets.” *The Cryosphere Discussions* 8: 453–478. doi:10.5194/tcd-8-453-2014.
- Hurkmans, R. T. W. L., J. L. Bamber, C. H. Davis, I. R. Joughin, K. S. Khvorostovsky, B. S. Smith, and N. Schoen. 2014. “Time-Evolving Mass Loss of the Greenland Ice Sheet from Satellite Altimetry.” *The Cryosphere* 8: 1725–1740. doi:10.5194/tc-8-1725-2014.
- Hurkmans, R. T. W. L., J. L. Bamber, and J. A. Griggs. 2012. “Brief Communication ‘Importance of Slope-Induced Error Correction in Volume Change Estimates from Radar Altimetry’.” *The Cryosphere* 6: 447–451. doi:10.5194/tc-6-447-2012.
- Joughin, I., B. E. Smith, I. M. Howat, T. Scambos, and T. Moon. 2010. “Greenland Flow Variability from Ice-Sheet-Wide Velocity Mapping.” *Journal of Glaciology* 56 (197): 415–430. doi:10.3189/002214310792447734.
- Joughin, I., B. E. Smith, D. E. Shean, and D. Floricioiu. 2014. “Brief Communication: Further Summer Speedup of Jakobshavn Isbræ.” *The Cryosphere* 8: 209–214. doi:10.5194/tc-8-209-2014.
- Khvorostovsky, K. 2012. “Merging and Analysis of Elevation Time Series over Greenland Ice Sheet from Satellite Radar Altimetry.” *IEEE Transactions on Geoscience and Remote Sensing* 50 (1): 23–36. doi:10.1109/TGRS.2011.2160071.
- Khvorostovsky, K. 2013. “Analysis of the Greenland Ice Sheet Elevation Time Series from Satellite Altimetry.” In *European Geosciences Union Meeting*, Vienna, April 7–12. poster ID: EGU2013-10054.
- Krabill, W. B., W. Abdalati, E. Frederick, S. Manizade, C. Martin, J. Sonntag, R. Swift, R. Thomas, and J. Yungel. 2002. “Aircraft Laser Altimetry Measurement of Elevation Changes of the Greenland Ice Sheet: Technique and Accuracy Assessment.” *Journal of Geodynamics* 34 (3–4): 357–376. doi:10.1016/S0264-3707(02)00040-6.
- Legresy, B., F. Papa, F. Remy, G. Vinay, M. van den Bosch, and O.-Z. Zanife. 2005. “ENVISAT Radar Altimeter Measurements over Continental Surfaces and Ice Caps Using the ICE-2 Retracking Algorithm.” *Remote Sensing of Environment* 95: 150–163. doi:10.1016/j.rse.2004.11.018.
- Levinsen, J. F., I. M. Howat, and C. C. Tscherning. 2013. “Improving Maps of Ice-Sheet Surface Elevation Change Using Combined Laser Altimeter and Stereoscopic Elevation Model Data.” *Journal of Glaciology* 59 (215): 524–532. doi:10.3189/2013JoG12J114.
- Liu, L., J. Wahr, I. M. Howat, S. A. Khan, I. Joughin, and M. Furuya. 2012. “Constraining Ice Mass Loss from Jakobshavn Isbræ (Greenland) Using InSAR-Measured Crustal Uplift.” *Geophysical Journal International* 188: 994–1006. doi:10.1111/j.1365-246X.2011.05317.x.

- Moholdt, G., C. Nuth, J. O. Hagen, and J. Kohler. 2010. "Recent Elevation Changes of Svalbard Glaciers Derived from ICESat Laser Altimetry." *Remote Sensing of Environment* 114: 2756–2767. doi:10.1016/j.rse.2010.06.008.
- NASA. 2013a. "Operation IceBridge – IceBridge Data Portal." <http://nsidc.org/icebridge/portal/>
- NASA. 2013b. "Laser Operational Periods." http://nsidc.org/data/icesat/laser_op_periods.html
- Nghiem, S. V., K. Steffen, G. Neumann, and R. Huff. 2005. "Mapping of Ice Layer Extent and Snow Accumulation in the Percolation Zone of the Greenland Ice Sheet." *Journal of Geophysical Research – Earth Surface* 110 (F2). doi:10.1029/2004JF000234.
- Nielsen, K., S. A. Khan, G. Spada, J. Wahr, M. Bevis, L. Liu, and T. van Dam. 2013. "Vertical and Horizontal Surface Displacements near Jakobshavn Isbræ Driven by Melt-Induced and Dynamic Ice Loss." *Journal of Geophysical Research: Solid Earth* 118: 1837–1844. doi:10.1002/jgrb.50145.
- Remy, F., T. Flament, F. Blarel, and J. Benveniste. 2012. "Radar Altimetry Measurements over Antarctic Ice Sheet: A Focus on Antenna Polarization and Change in Backscatter Problems." *Advances in Space Research* 50 (8): 998–1006. doi:10.1016/j.asr.2012.04.003.
- Ridley, J. K., and K. C. Partington. 1988. "A Model of Satellite Radar Altimeter Return from Ice Sheets." *International Journal of Remote Sensing* 9: 601–624. doi:10.1080/01431168808954881.
- Sasgen, I., M. van den Broeke, J. L. Bamber, E. Rignot, L. S. Sørensen, B. Wouters, Z. Martinec, I. Velicogna, and S. B. Simonsen. 2012. "Timing and Origin of Recent Regional Ice-Mass Loss in Greenland." *Earth and Planetary Science Letters* 333–334: 293–303. doi:10.1016/j.epsl.2012.03.033.
- Scharrer, K., J. F. Levinsen, and F. Ticconi. 2013. "Product Validation and Algorithm Selection Report for the Ice_Sheets_cci project of ESA's Climate Change Initiative." <http://www.esa-icesheets-cci.org/>
- Schutz, B. E., H. J. Zwally, C. A. Shuman, D. Hancock, and J. P. DiMarzio. 2005. "Overview of the ICESat Mission." *Geophysical Research Letters* 32 (21): 1944–8007. doi:10.1029/2005GL024009.
- Shepherd, A., E. R. Ivins, A. Geruo, V. R. Barletta, M. J. Bentley, S. Bettadpur, K. H. Briggs, D. H. Bromwich, R. Forsberg, N. Galin, M. Horwath, S. Jacobs, I. Joughin, M. A. King, J. T. M. Lenaerts, J. Li, S. R. M. Ligtenberg, A. Luckman, S. B. Luthcke, M. McMillan, R. Meister, G. Milne, J. Mouginot, A. Muir, J. P. Nicolas, J. Paden, A. J. Payne, H. Pritchard, E. Rignot, H. Rott, L. S. Sorensen, T. A. Scambos, B. Scheuchl, E. J. O. Schrama, B. Smith, A. V. Sundal, J. H. van Angelen, W. J. van de Berg, M. R. van den Broeke, D. G. Vaughan, I. Velicogna, J. Wahr, P. L. Whitehouse, D. J. Wingham, D. Yi, D. Young, and H. J. Zwally. 2012. "A Reconciled Estimate of Ice-Sheet Mass Balance." *Science* 338: 1183–1189. doi:10.1126/science.1228102.
- Slobbe, D., R. Lindenbergh, and P. Ditmar. 2008. "Estimation of Volume Change Rates of Greenland's Ice Sheet from ICESat Data Using Overlapping Footprints." *Remote Sensing of Environment* 112: 4204–4213. doi:10.1016/j.rse.2008.07.004.
- Sørensen, L. S., S. B. Simonsen, R. Meister, T. Flament, R. Forsberg, and J. F. Levinsen. 2014. "Envisat Derived Elevation Changes of the Greenland Ice Sheet, and a Comparison to Icesat Results in the Accumulation Area." *Remote Sensing of the Environment*, In review.
- Sørensen, L. S., S. B. Simonsen, K. Nielsen, P. Lucas-Picher, G. Spada, G. Adalgeirsdottir, R. Forsberg, and C. S. Hvidberg. 2011. "Mass Balance of the Greenland Ice Sheet (2003–2008) from ICESat Data – the Impact of Interpolation, Sampling and Firn Density." *The Cryosphere* 5: 173–186. doi:10.5194/tc-5-173-2011.
- van den Broeke, M., C. Bus, J. Ettema, and P. Smeets. 2010. "Temperature Thresholds for Degree-Day Modelling of Greenland Ice Sheet Melt Rates." *Geophysical Research Letters* 37. doi:10.1029/2010GL044123.
- van Meijgaard, E., L. H. van Ulft, W. J. van de Berg, F. C. Bosveld, B. J. J. M. van den Hurk, G. Lenderink, and A. P. Siebesma. 2008. "The KNMI Regional Atmospheric Climate Model." Version 2.1, Tech. Rep. 302. The Royal Netherlands Meteorological Institute, De Bilt. <http://a.knmi2.nl/bibliotheek/knmipubTR/TR302.pdf>
- Wingham, D. J., A. J. Ridout, R. Scharroo, R. J. Arthern, and C. K. Shum. 1998. "Antarctic Elevation Change from 1992 to 1996." *Science* 282: 456–458. doi:10.1126/science.282.5388.456.

- Zwally, H. J., M. B. Giovinetto, J. Li, H. G. Cornejo, M. A. Beckley, A. C. Brenner, J. L. Saba, and D. Yi. 2005. "Mass Changes of the Greenland and Antarctic Ice Sheets and Shelves and Contributions to Sea-Level Rise: 1992–2002." *Journal of Glaciology* 51: 509–527. doi:[10.3189/172756505781829007](https://doi.org/10.3189/172756505781829007).
- Zwally, H. J., J. Jun, A. C. Brenner, M. A. Beckley, H. G. Cornejo, J. Dimarzio, M. B. Giovinetto, T. A. Neumann, J. Robbins, J. L. Saba, D. Donghui, and W. Wang. 2011. "Greenland Ice Sheet Mass Balance: Distribution of Increased Mass Loss with Climate Warming; 200307 versus 19922002." *Journal of Glaciology* 57: 88–102. doi:[10.3189/002214311795306682](https://doi.org/10.3189/002214311795306682).

B Envisat derived elevation changes of the Greenland Ice Sheet

The Round Robin exercise showed that a combination of the repeat-track and cross-over techniques provide the optimal elevation change estimates throughout the Greenland Ice Sheet. Here, one part of the results are published, namely a repeat-track analysis of Envisat data from 2002 – 2010. The model is based on model 3 in [Sørensen et al. \(2011\)](#), which has been adapted to radar altimetry data by adjusting for the waveform parameters: The backscatter coefficient, leading edge width, and trailing edge slope, cf. [Flament and Rémy \(2012\)](#); [Legrésy et al. \(2006\)](#).

Separate surface elevation change results have been derived for the ICESat period 2003 – 2009 ([Sørensen et al., 2011](#)) to enable a comparison of results over the accumulation zone. Furthermore, four five-year running mean segments are estimated for two locations on the ice sheet to better understand the more local changes in the signal. The periods are 2003 – 2007, 2004 – 2008, 2005 – 2009, and 2006 – 2010, and the observation areas cover Jakobshavn Isbræ and Kong Frederik VIII land.

This work is described in the paper below:

Authors : L. S. Sørensen, S. B. Simonsen, R. Meister, R. Forsberg,
J. F. Levinsen, T. Flament
Title : Envisat derived elevation changes of the Greenland ice sheet,
and a comparison to ICESat results in the accumulation area
Journal : Remote Sensing of the Environment
Published online : January 28th 2015
DOI : 10.1016/j.rse.2014.12.022



Envisat-derived elevation changes of the Greenland ice sheet, and a comparison with ICESat results in the accumulation area



Louise Sandberg Sørensen^{a,*}, Sebastian B. Simonsen^a, Rakia Meister^a, René Forsberg^a, Joanna F. Levinson^a, Thomas Flament^{b,c,1}

^a DTU Space, Technical University of Denmark, Geodynamics Department, DK-2800, Kgs. Lyngby, Elektrovej, Bldg. 328, Denmark

^b Laboratoire d'Etudes en Géophysique et Océanographie Spatiales, 14 avenue Edouard Belin, 31400 Toulouse, France

^c Centre for Polar Observation and Modelling, University of Leeds, Woodhouse Lane, LS2 9JT Leeds, United Kingdom

ARTICLE INFO

Article history:

Received 16 September 2014

Received in revised form 23 November 2014

Accepted 14 December 2014

Available online 28 January 2015

Keywords:

Ice sheet

Mass balance

Radar altimetry

Laser altimetry

Cryosphere changes

ABSTRACT

We show, for the first time over the Greenland ice sheet, that an along track method for deriving rates of elevation change can successfully be applied to Envisat radar altimetry data (2002–2010). The results provide improved resolution and coverage compared to previous results obtained from cross-over methods.

Also, we find that temporal changes in the elevation change rate can be derived from Envisat data, and show clear examples of this by generating five-year running means for selected areas of the Greenland ice sheet. For a period between 2003 and 2009, the elevation of the ice sheets was measured by both the laser altimeter on board ICESat and the radar altimeter on board Envisat. We compare rates of elevation change derived from ICESat and Envisat for this time span in which both sensors were operating. We focus on the area above the equilibrium line altitude, in order to specifically derive information on snow parameters. A comparison of the elevation changes observed by the two sensors shows a complex pattern, which can be explained regionally by model output describing the changes in both firn air content and accumulation rates.

© 2015 Elsevier Inc. All rights reserved.

1. Introduction

Satellite altimetry has proven to be a valuable tool for assessing the changes of the Greenland ice sheet (GrIS), and results that agree with other geodetic methods are obtained (Sasgen et al., 2012; Shepherd et al., 2012). The repeated elevation measurements from altimeters can be used to estimate the change in snow or ice volume, and this volume can be converted into a mass change under assumptions of fluctuations in the firn layer and the densities involved (Pritchard et al., 2012; Sørensen et al., 2011; Zwally et al., 2011).

Both radar altimetry and laser altimetry have been used for studying the changes of GrIS (e.g. Johannessen et al., 2005; Khan et al., 2014; Khvorostovsky, 2012; Legresy et al., 2005; Li and Davis, 2008; Pritchard et al., 2009; Shepherd and Wingham, 2007; Sørensen et al., 2011; Thomas et al., 2008; Zwally et al., 2011). Laser and radar altimetry measurements of ice-covered regions are associated with different strengths and weaknesses; radar altimetry covers the longest time series, started by the launch of the European Remote-Sensing satellite, ERS-1, in 1991, which was followed by

ERS-2, Envisat and currently, CryoSat-2. Prior satellite missions only monitored parts of the GrIS due to the inclination of the satellites (Davis et al., 1998; Zwally et al., 1989).

Satellite laser altimetry is available solely from the Ice, Cloud and land Elevation Satellite (ICESat) mission which was operational in the period 2003–2009, and limited to two to three campaigns of approximately one month duration per year (Abshire et al., 2005). Because of the short wavelength of the laser instrument, the signal is reflected from the air–snow interface while the radar signal, with the longer wavelength, might penetrate into the snow pack (Arthern et al., 2001; Ridley and Partington, 1988). The radar reflecting surface depends on the ratio between the surface and the volume backscatter which is a function of several different properties such as snow density, crystal structure and surface roughness. This complicates the conversion of elevation changes observed with radar altimetry into mass changes.

In some early studies by Zwally et al. (2005) and Johannessen et al. (2005), ERS1 and ERS2 radar data were used for the periods 1992–2002 and 1992–2003, respectively, to estimate the rate of elevation changes from a cross-over (XO) analysis (using points where ascending and descending tracks cross). In a more recent study, Khvorostovsky (2012) includes additional data from Envisat in the XO analysis, extending the time period up to 2008. Both Khvorostovsky (2012) and Johannessen et al. (2005) found a general

* Corresponding author.

E-mail address: srss@space.dtu.dk (L.S. Sørensen).

¹ LEGOS, Toulouse, now at University of Leeds.

pattern of interior thickening and thinning near the edges of the ice sheet.

Repeat-track (RT) methods, which are often applied in the analysis of ICESat data, use all available data and not only data from XO locations, resulting in an unprecedented level of details in the pattern of the observed elevation change (Pritchard et al., 2009). The measurements used in the RT analyses are actually rarely exactly repeated, meaning that the underlying topography must be estimated in order to evaluate dH/dt . With tracks of similar orientation being processed separately, it is not necessary to account for the elevation bias between ascending and descending tracks, as it is for the XO method. Flament and Rémy (2012) successfully used a RT method on Envisat radar data over Antarctica, and to our knowledge no such results have so far been published for GrIS. Levinsen et al. (2014) do compare XO and RT results over the Jakobshavn drainage basin though.

The aim of this paper is to derive and investigate rates of elevation change (dH/dt) from Envisat data over the GrIS, by applying a RT method. We compare the Envisat results with temporally overlapping, previously published results from ICESat (Sasgen et al., 2012; Sørensen et al., 2011), in the area above the equilibrium line altitude (ELA), to investigate the different natures of the two sensor types.

2. Envisat data

Envisat was launched by the European Space Agency (ESA) in 2002, and was operating until April 2012 (Batoula et al., 2011). The Envisat Radar Altimeter 2 (RA-2) data used in this study cover the time period from November 2002 to October 2010 (corresponding to cycles 11–93); in which period Envisat was in a 35-day repeat orbit. Hereafter, the orbit was changed and this repeat orbit was abandoned.

The RA-2 was a dual frequency nadir-looking radar altimeter, with a pulse limited footprint of varying size (2–10 km), depending on the local ice sheet topography. The along-track distance between each measurement is 370 m.

The level-2 (L2) Envisat data provide geolocated height estimates from both the use of the ICE2 (Legresy et al., 2005) and ICE1 (Wingham et al., 1986) waveform retracers, together with several geophysical corrections and waveform shape parameters. The results presented in this study are based on heights retracked with the ICE2 retracker. The data were obtained directly from ESA in the form of the Envisat Level-2 Radar Altimetry Geophysical Data Record (GDR) product.

2.1. Preprocessing

The Envisat L2 data have to be preprocessed prior to the elevation change analysis. During the retracking process, ESA assigns data a “valid” or “invalid” flag. The invalid data can be caused by a number of scenarios, including lack of tracking record, waveform filters set to 0, if the radar return signal is not received in a predefined time window, or if the leading edge, or power is smaller than noise (Batoula et al., 2011). In this work, only “valid” data were used. Several geophysical corrections were applied, including the corrections for atmospheric delay caused by the dry and wet troposphere as well as the ionosphere, and those for the geocentric pole and solid Earth tides (Batoula et al., 2011). The sum of corrections was subtracted from the retracked height. In addition, only data from ice covered areas are used.

3. Method for deriving elevation changes

The RT method is used to estimate elevation changes (dH/dt) along the Envisat ground track, with a resolution of 1000 m. The method resembles the third method of Sørensen et al. (2011, M3). According to Flament and Rémy (2012) and Legrésy et al. (2006), the method has been adapted to radar altimetry, by performing a least-squares

regression on all data in 1000 m along-track segments of the satellite track. The regression parameters are given by

$$\begin{aligned}
 H(x, y, t) = & H_0(\bar{x}, \bar{y}, \bar{t}) + dH/dt(t - \bar{t}) \\
 & + dBs(Bs - \bar{Bs}) + dLeW(LeW - \bar{LeW}) \\
 & + dTeS(TeS - \bar{TeS}) \\
 & + sx(x - \bar{x}) + sy(y - \bar{y}) \\
 & + \alpha \cos(\omega t) + \beta \sin(\omega t) \\
 & + \varepsilon(x, y, t).
 \end{aligned} \tag{1}$$

H_0 is the mean altitude of a given track segment. dBs , $dLeW$ and $dTeS$ are the model parameters for the backscatter coefficient (Bs), leading edge width (LeW), and trailing edge slope (TeS) from the ICE2 retracker. These are waveform parameters and are included in the adjustment because it has been shown that variations in these waveform shape parameters are correlated with variations in the elevation (Davis et al., 2005; Legresy et al., 2005; Legrésy et al., 2006; Wingham et al., 1998; Zwally et al., 2005), and sx and sy describe the surface topography by its slope. We include a term describing the seasonal variations in surface elevation, $S(t)$, and assume that this can be represented by the following expression, with $T = 365$ days being the period and φ being the phase,

$$\begin{aligned}
 S(t) = & D \cos\left(\frac{2\pi}{T}t + \phi\right) \\
 = & \alpha \cos(\omega t) + \beta \sin(\omega t).
 \end{aligned}$$

The overbar indicates the mean of the measurements in the given segment, and ε is the residual (the difference between the model and the observation values).

We apply a 3σ outlier rejection similar to that of Flament and Rémy (2012) based on the residuals, but do so in an iterative procedure. When outliers have been rejected, the standard deviation of the segment residuals is calculated again and the remaining data are evaluated against this. This is done repeatedly until no further observations are rejected. To ensure a robust solution, we only provide a dH/dt estimate for track segments in which more than 130 data points are available for the fitting procedure after the outlier rejection (Flament & Rémy, 2012).

In areas with sloping topography, a radar signal will not be reflected from nadir but from the closest point to the satellite within the (beam-limited) satellite footprint (Brenner et al., 1983; Brenner et al., 2007). We therefore apply a slope-induced error correction to relocate the dH/dt estimate to the actual location of the radar returns (Hurkmans et al., 2012). This is done using an independent DEM (Bamber et al., 2001), representing the local topography for each dH/dt estimate.

4. Elevation change results

Fig. 1 shows dH/dt over GrIS, derived from Envisat data in the period 2002–2010 by applying the algorithm described in Section 3. A clear pattern of thinning (blue) along a large fraction of the ice margin is seen, and especially near large outlet glaciers, such as Jakobshavn Isbræ located on the west coast of Greenland, great thinning is observed. In the interior of the ice sheet Fig. 1 shows only modest deviations from $dH/dt = 0$.

Temporal variations in the elevation change pattern for the area around Kong Frederik VIII Land in Northeast Greenland and Jakobshavn Isbræ in West Greenland, are shown in Figs. 2 and 3. These two areas were chosen as examples because they represent areas which are currently changing. Jakobshavn has been extensively studied throughout the past decade and has undergone major changes (Howat et al., 2011; Joughin et al., 2014), while the glaciers in Kong Frederik VIII Land has been studied recently by Khan et al. (2014). The four plots for each location show the results for the partly overlapping five-year

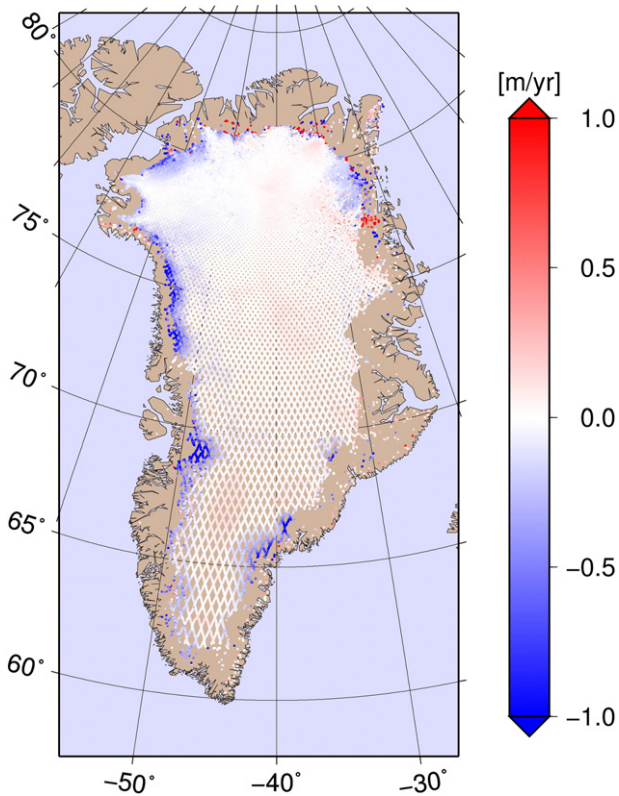


Fig. 1. Rate of elevation change [m/yr] of GrIS derived from 2002 to 2010 Envisat radar altimetry.

periods; 2003–07, 2004–08, 2005–09 and 2006–10, respectively. The latter time period is shorter than the others by two months because of the change in orbit in October 2010. The thinning rate in Kong Frederik VIII Land becomes increasingly larger as time progresses (Fig. 2), while near Jakobshavn the temporal changes show a more complex behavior (Fig. 3).

5. Comparison of Envisat and ICESat results

Sørensen et al. (2011) used a RT algorithm similar to the one used in this study to estimate rates of elevation change derived from ICESat laser altimetry. The mean annual surface elevation change from ICESat data above the equilibrium line altitude (ELA), which is defined by the HIRHAM5 regional climate model (RCM) (Lucas-Picher et al., 2012), is shown in Fig. 4a for the period from September 2003 to October 2009 (Nielsen et al., 2014, Sasgen et al., 2012). For comparison, a result based on Envisat data for the same time period is generated and is shown in Fig. 4b. Both RT results have been interpolated onto a 5 km grid and a Gaussian filter with a radius of 25 km has been applied to suppress short wavelength features to ease the comparison of the two.

In terms of rate of elevation change above the ELA, ICESat shows a thinning of the southeastern and northwestern margins of the GrIS and a slight thickening in the interior (Fig. 4a). The thickening is most pronounced in Northeast GrIS and also northwest of the South Dome. A similar pattern is found in the Envisat results, however here a band of thinning is observed across the GrIS from the catchment area of Jakobshavn Isbræ in the west to the catchment area of the Kangerdlussuaq glacier in the east. Fig. 4c shows the difference between the rate of elevation change based on Envisat and ICESat data above the ELA, given by

$$\frac{dH}{dt}_{\Delta} = \frac{dH}{dt}_{ICESat} - \frac{dH}{dt}_{Envisat} \quad (2)$$

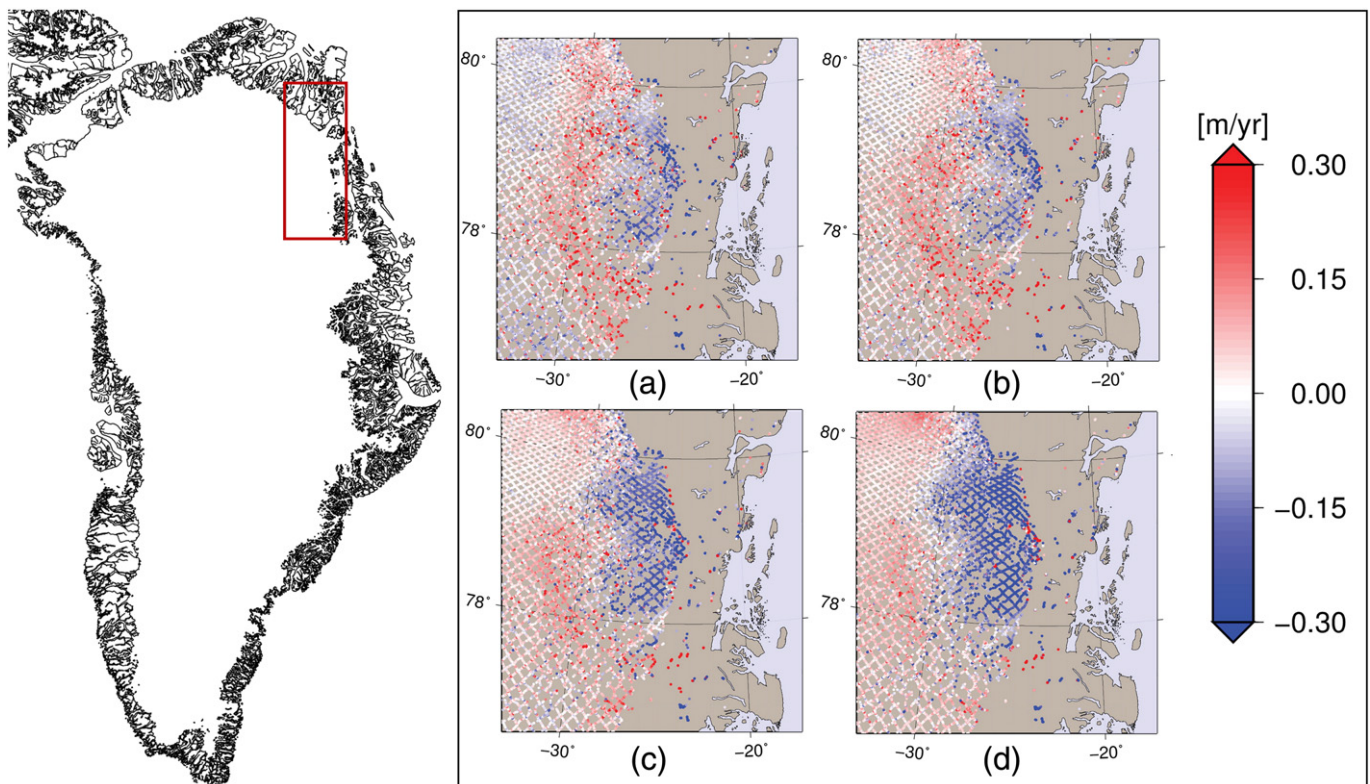


Fig. 2. Rate of elevation change [m/yr] in Kong Frederik VIII Land in northeast Greenland, for four different five-year time spans: (a) 2003–2007, (b) 2004–2008, (c) 2005–2009, and (d) 2006–2010.

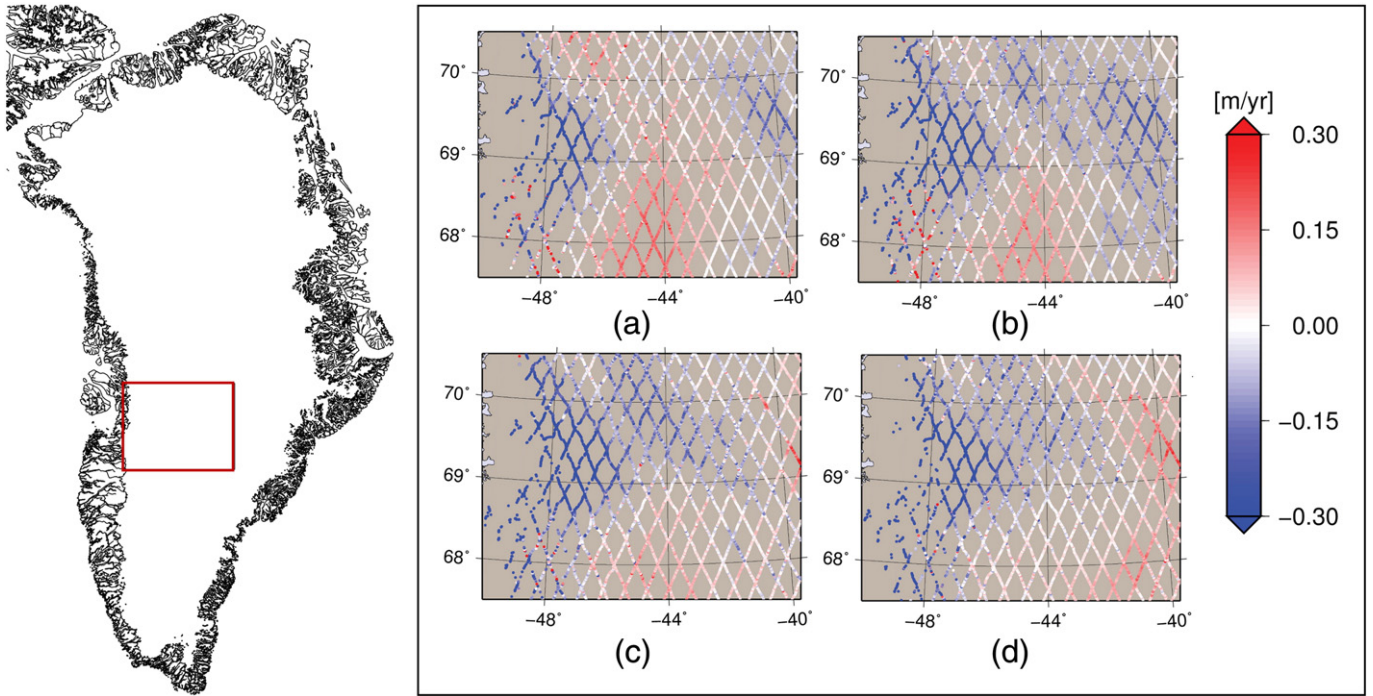


Fig. 3. Rate of elevation change [m/yr] near Jakobshavn Isbræ, for four different five-year time spans: (a) 2003–2007, (b) 2004–2008, (c) 2005–2009, and (d) 2006–2010.

In the interior of the ice sheet a predominately positive $\frac{dH}{dt}|_{\Delta}$ is observed, indicating a faster rate of elevation change seen from ICESat than from Envisat. A difference in the observed rate of elevation change from the two satellites implies a temporal change in the physical properties of the subsurface snow/firn in the accumulation area, which affects radar penetration (Ridley & Partington, 1988). Here, the rate of change in surface temperature, accumulation, melt and surface mass balance modeled by the high resolution HIRHAM5 RCM (Lucas-Picher et al., 2012) have been investigated, and so have the surface density

and firn air content modeled by an off-line coupled firn densification model (Sørensen et al., 2011). None of the fields showed a clear correlation with the observed difference in elevation change from the two satellites. It was, however found that especially the change in air content of the firn column and the change in accumulation rate can help to interpret the pattern of $\frac{dH}{dt}|_{\Delta}$. The change in accumulation for the ICESat period 2003–09 is shown in Fig. 5a while the modeled change in firn air content is shown in Fig. 5b. The uncertainty of the change in firn air content is assumed to be 40%, while the uncertainty in the

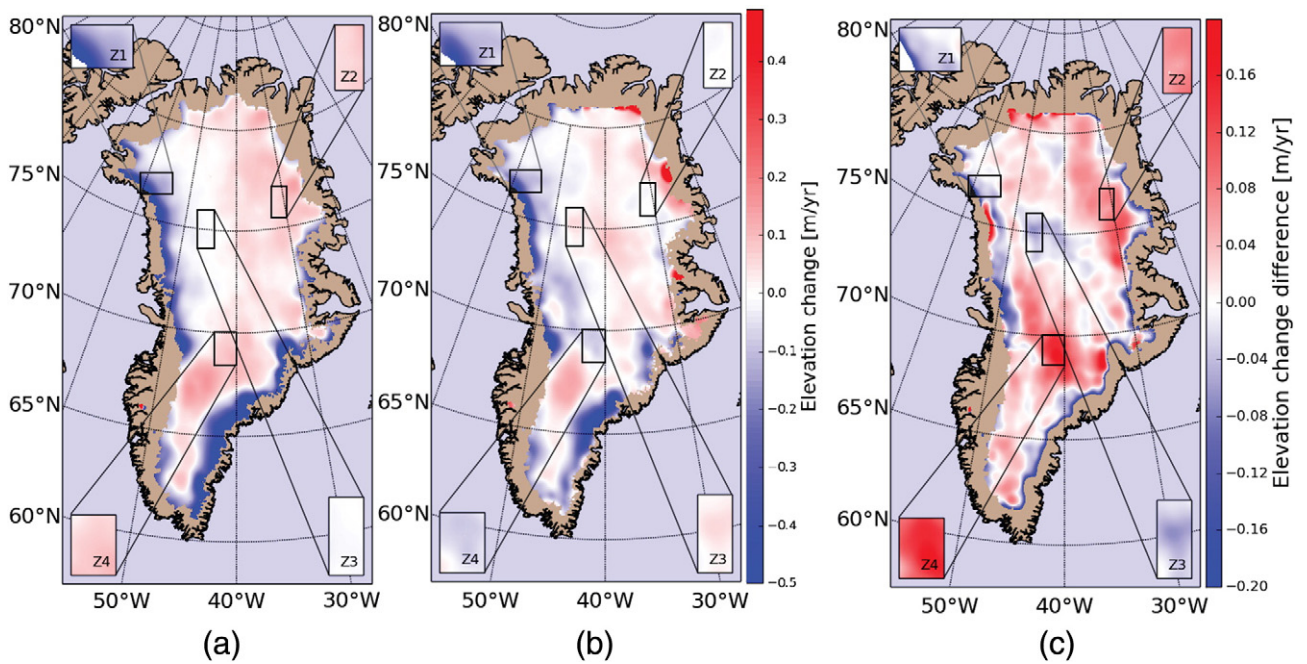


Fig. 4. Rate of elevation change [m/yr] of the GrIS above the ELA derived from 2003 to 09 ICESat (a) and Envisat (b) data, respectively. (c) The difference between the rate of elevation change seen from ICESat and Envisat (Eq. (2)). The areas Z1–Z4 indicate zones of interest for the interpretation of the results. All data sets have been smoothed by a Gaussian filter with a radius of 25 km to suppress short wavelengths.

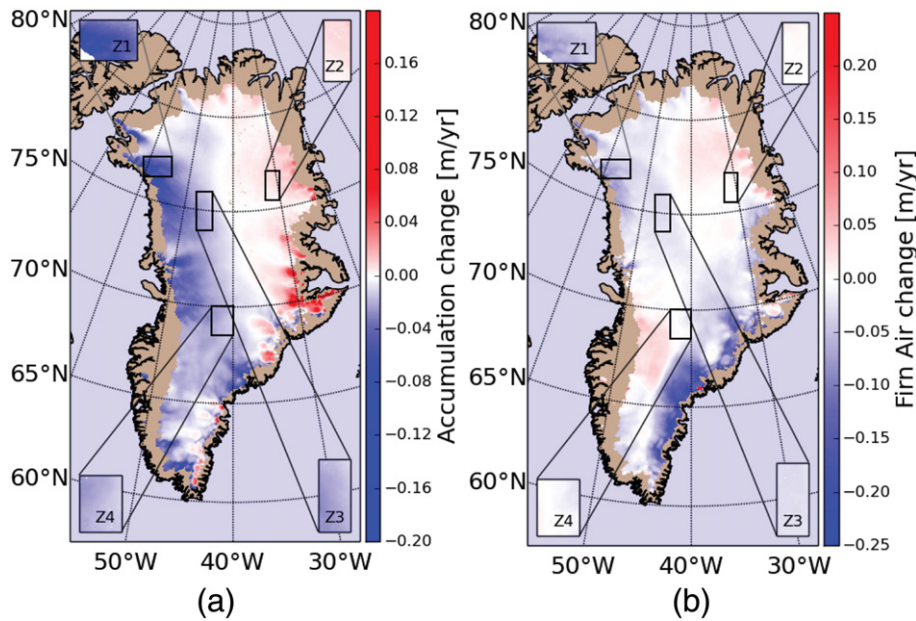


Fig. 5. (a) The change in accumulation rate [m/yr], and (b) change in air content of the firn column [m/yr] over the 2003–2009 time span. Both fields are modeled by an off-line coupled firn densification model (Sørensen et al., 2011).

change in accumulation is 20% (Simonsen et al., 2013). The uncertainties on the Envisat and ICESat elevation changes are the means of the uncertainties in each zone, derived through the least-squares fit.

The complex pattern in Fig. 4c is difficult to summarize and therefore the following discussion will focus on four specific zones, each representing different $\frac{dH}{dt}|_{\Delta}$ scenarios. The locations of the four zones are already shown in Figs. 4 and 5.

In zone 1, located close to the ELA, both satellites observe a downward movement of the surface elevation. The downward movements observed by ICESat (-22.3 ± 6.1 cm/yr) is faster than the one from Envisat (-16.4 ± 5.6 cm/yr), leading to negative $\frac{dH}{dt}|_{\Delta}$ values. At least part of the thinning observed by ICESat is caused by a decrease in accumulation rate (see Fig. 5a), and the fact that Envisat observes a smaller thinning rate can be explained by a negative trend in firn air content in the area, meaning higher densities and shallower penetration depth. The mean change in accumulation rate in zone 1 is -5.3 ± 1.1 cm/yr, while the mean change in firn air content is -5.4 ± 2.2 cm/yr. In this zone, which is located close to the ELA, one might suspect the inclusion of ice lenses to play a critical role in the location of the reflective surface seen by Envisat, especially in a warming climate (Box, Yang, Bromwich, & Bai, 2009).

Zone 2 in northeast Greenland is characterized by positive $\frac{dH}{dt}|_{\Delta}$ values, with a mean value of 7.0 ± 2.2 cm/yr. Here, Envisat observes an almost zero (-0.5 ± 2.8 cm/yr) rate of elevation change, and ICESat observes the physical surface to move upwards with a mean velocity of 6.5 ± 1.6 cm/yr. An explanation of this scenario is that even though the physical surface moves upwards caused by an increase in accumulation rate apparent in the area, the radar reflection surface remains constant due to lighter firn, causing the penetration depth increases. The model predictions do show this pattern with an increasing accumulation rate and firn air change, but the mean values of 0.7 ± 0.1 cm/yr and 0.3 ± 0.1 cm/yr, respectively, are not sufficient to fully explain the observations.

Zone 3 is located high on the ice sheet in the northern part of Greenland. In zone 3, negative $\frac{dH}{dt}|_{\Delta}$ values of on average -3.5 ± 1.8 cm/yr are found, caused by ICESat observing only a small elevation change, almost zero, while Envisat observes a positive rate of change. This scenario is consistent with the model results presented in Fig. 5. The upward movement of the reflective surface suggests denser firn conditions, which is

supported by the negative trend of -2.5 ± 1.0 cm/yr in firn air content seen in Fig. 5b. The upward movement of the Envisat reflective surface could also be explained by a sudden introduction of a strong reflective surface, i.e. ice lenses, within the penetration depth of the radar signal.

The largest positive values of $\frac{dH}{dt}|_{\Delta}$ on the GrIS (12.8 ± 2.5 cm/yr) are found within zone 4, located high on the ice sheet, east of the Jakobshavn Isbræ. Here, ICESat observes an average increase in surface elevation of 7.3 ± 1.8 cm/yr while Envisat observes the opposite, with an average of -5.4 ± 3.2 cm/yr. The positive $\frac{dH}{dt}|_{ICESat}$ could be explained by an increase in accumulation rate causing the physical surface to move upwards. An increase in air content in the firn making the firn easily penetrated by the radar could result in a smaller $\frac{dH}{dt}|_{Envisat}$ but it would hardly be negative as the observations show. The model results also contradict the observations by predicting a negative trend in accumulation rate (-2.0 ± 0.4 cm/yr) and a firn air change close to zero within zone 4. This inconsistency suggests other sources of elevation changes, such as ice dynamics.

6. Discussion and conclusion

We find that the presented RT method provides robust Envisat-derived $\frac{dH}{dt}$ estimates covering a larger fraction of the GrIS with a higher resolution than what has previously been provided by XO methods (e.g. Khvorostovsky, 2012).

The radar system onboard Envisat might lose track when the satellite moves from ocean to the steep topography, which is typical for the coastal areas of Greenland. This means that generally more ICESat results than Envisat results will be available in these regions. We compare ICESat and Envisat results above the ELA only, where the data coverage is more comparable, but the difference in coverage between the two missions might explain the fact that ICESat observes a larger area of thinning in southeast Greenland than Envisat. Another distinct feature visible in the difference patterns is the thin blue line in Fig. 4c along the eastern side of the ELA on the west coast, could be partly explained by a non-perfect relocation and preferential sampling of high points of the radar returns. In this lower altitude (wetter) area, Envisat should not suffer as much from penetration variability.

The high spatial resolution Envisat RT results enable investigations into variations in elevation change for smaller areas than previously

studied. We have presented the area of Kong Frederik VIII Land and the catchment area of Jakobshavn Isbræ. In Kong Frederik VIII Land, the GRIS regime drainage is governed by outlet glaciers of the North Greenland ice stream; Nioghalvfjærdsfjorden (79°25'N, 22°8'W), Zachariae Isstrøm (78°53'N, 21°8'W) and Storstrømmen (77°10'N, 22°45'W). The area shows a decrease in the extent of positive surface elevation change with time, and also a significant increase in thinning. This may be related to actual elevation changes, or be a result of changes in penetration depth of the Envisat radar. The elevation change of the outlet glaciers is more easily interpreted, where changes in the firn can be neglected. Both Nioghalvfjærdsfjorden and Storstrømmen follow the pattern of changing from a thickening regime to thinning over the four time spans, whereas Zachariae Isstrøm shows elevation loss for all the four time spans.

The rate of elevation change in the catchment area of Jakobshavn Isbræ, as shown in Fig. 3, shows a complex pattern of the relationship between elevation decrease and increase, and further investigations into radar penetration of the area have to be carried out before conclusions can be reached. In general, the extent of thinning appears to be increasing over the four time spans.

The least-square regression used to derive elevation changes from Envisat data includes information about the waveform parameters: the backscatter, leading edge width and trailing edge slope. This information can be used to suppress the influence of changes in the reflective properties of the surface on elevation changes. Despite the inclusion of the additional terms in the regression, we find that the rate of elevation change seen from Envisat and ICESat, respectively, differs. Part of the difference between the ICESat and Envisat results could possibly be attributed to the fact that ICESat measures only three months per year, but since what we compare are longer term trends, this should only have minor influence.

The pattern of difference is not uniform, and we find that we can explain some of the differences on a regional level if we include information of changes in air content as well as accumulation rates in the analysis.

We recommend treading carefully when using radar data to determine ice mass changes, and suggest that the use of radar altimetry to assess ice sheet volume change could include a bias-correction by using models of climate-dependent movement of the reflective surface. Such a correction might improve results, but may inherit the uncertainties of the introduced firn compaction model. Such a correction would depend on which retracker is used. With the additional information derived from ICESat, the period of coinciding measurement may be used to validate the firn models in a similar fashion as for airborne radar altimetry in Simonsen et al. (2013), and help to improve both firn and climate models.

Acknowledgments

The study was supported by the European Space Agency (ESA) through the Ice_Sheets_CCI (4000104815/11/I-NB). Rakia Meister was funded by ESA through the ICEMASS STSE. Envisat data were acquired through ESA, and ICESat data through NSIDC. We want to thank the two reviewers who provided constructive comments which helped improve the manuscript.

References

- Abshire, J.B., Sun, X., Riris, H., Sirota, J.M., McGarry, J.F., Palm, S., et al. (2005). Geoscience Laser Altimeter System (GLAS) on the ICESat mission: On-orbit measurement performance. *Geophysical Research Letters*, 32(21).
- Arthern, R., Wingham, D., & Ridout, A. (2001). Controls on ERS altimeter measurements over ice sheets: Footprint-scale topography, backscatter fluctuations, and the dependence of microwave penetration depth on satellite orientation. *J. Geophys. Res. Atmos.* (1984–2012), 106(D24), 33471–33484.
- Bamber, J.L., Ekholm, S., & Krabill, W.B. (2001). A new, high-resolution digital elevation model of Greenland fully validated with airborne laser altimeter data. *J. Geophys. Res. Solid Earth* (1978–2012), 106(B4), 6733–6745.
- Batoula, S., Urien, S., Soulat, F., Muir, A., Roca, M., & Cotton, D. (2011). Envisat altimetry level 2 user manual. *Issue*, 1, 4.
- Box, J.E., Yang, L., Bromwich, D.H., & Bai, L.-S. (2009). Greenland ice sheet surface air temperature variability: 1840–2007. *Journal of Climate*, 22(14), 4029–4049.
- Brenner, A.C., Bindschadler, R.A., Thomas, R.H., & Zwally, H.J. (1983). Slope-induced errors in radar altimetry over continental ice sheets. *J. Geophys. Res. Oceans* (1978–2012), 88(C3), 1617–1623.
- Brenner, A.C., DiMarzio, J.P., & Zwally, H.J. (2007). Precision and accuracy of satellite radar and laser altimeter data over the continental ice sheets. *IEEE Trans. Geosci. Remote Sens.*, 45(2), 321–331.
- Davis, C.H., Kluever, C.A., & Haines, B.J. (1998). Elevation change of the southern Greenland ice sheet. *Science*, 279(5359), 2086–2088.
- Davis, C.H., Li, Y., McConnell, J.R., Frey, M.M., & Hanna, E. (2005). Snowfall-driven growth in East Antarctic ice sheet mitigates recent sea-level rise. *Science*, 308(5730), 1898–1901.
- Flament, T., & Rémy, F. (2012). Dynamic thinning of Antarctic glaciers from along-track repeat radar altimetry. *Journal of Glaciology*, 58(211), 830–840.
- Howat, I.M., Ahn, Y., Joughin, I., van den Broeke, M.R., Lenaerts, J., & Smith, B. (2011). Mass balance of Greenland's three largest outlet glaciers, 2000–2010. *Geophysical Research Letters*, 38(12).
- Hurkmans, R., Bamber, J., & Griggs, J. (2012). Brief communication "Importance of slope-induced error correction in volume change estimates from radar altimetry". *The Cryosphere*, 6(2), 447–451.
- Johannessen, O.M., Khvorostovsky, K., Miles, M.W., & Bobylev, L.P. (2005). Recent ice-sheet growth in the interior of Greenland. *Science*, 310(5750), 1013–1016.
- Joughin, I., Smith, B., Shean, D., & Floricioiu, D. (2014). Brief communication: Further summer speedup of Jakobshavn Isbræ. *The Cryosphere*, 8(1), 209–214.
- Khan, S.A., Kjær, K.H., Bevis, M., Bamber, J.L., Wahr, J., Kjeldsen, K.K., et al. (2014). Sustained mass loss of the northeast Greenland ice sheet triggered by regional warming. *Nature Climate Change*, 4(4), 292–299.
- Khvorostovsky, K.S. (2012). Merging and analysis of elevation time series over Greenland ice sheet from satellite radar altimetry. *IEEE Trans. Geosci. Remote Sens.*, 50(1), 23–36.
- Legrésy, B., Papa, F., Remy, F., Vinay, G., van den Bosch, M., & Zanife, O.-Z. (2005). ENVISAT radar altimeter measurements over continental surfaces and ice caps using the ICE-2 retracking algorithm. *Remote Sensing of Environment*, 95(2), 150–163.
- Legrésy, B., Rémy, F., & Blarel, F. (2006). Along track repeat altimetry for ice sheets and continental surface studies. *Proceedings of the Symposium on 15 years of Progress in Radar Altimetry, Venice, Italy, 13–18 March 2006. Vol. 181*, (ESA-SP614, Paper).
- Levinsen, J.F., Khvorostovsky, K., Ticconi, F., Shepherd, A., Forsberg, R., Sørensen, L.S., et al. (2015). ESA Ice Sheets CCI: Derivation of the optimal method for surface elevation change detection of the Greenland Ice Sheet – Round Robin results. *International Journal of Remote Sensing*, 36(2), 551–573.
- Li, Y., & Davis, C.H. (2008). Decadal mass balance of the Greenland and Antarctic ice sheets from high resolution elevation change analysis of ERS-2 and ENVISAT radar altimetry measurements. *Geoscience and Remote Sensing Symposium, 2008. IGARSS 2008. IEEE International, Vol. 4*. (pp. IV–339). IEEE.
- Lucas-Picher, P., Wulff-Nielsen, M., Christensen, J.H., Adalgeirsdóttir, G., Mottram, R.H., & Simonsen, S.B. (2012). Very high resolution regional climate model simulations over Greenland: Identifying added value. *Journal of Geophysical Research*, 117(D), 02108.
- Nielsen, K., Sørensen, L.S., Khan, S.A., Spada, G., Simonsen, S.B., & Forsberg, R. (2014). Towards constraining glacial isostatic adjustment in Greenland using ICESat and GPS observations. *Earth on the edge: Science for a sustainable planet* (pp. 325–331). Springer: IUGG.
- Pritchard, H.D., Arthern, R.J., Vaughan, D.G., & Edwards, L.A. (2009). Extensive dynamic thinning on the margins of the Greenland and Antarctic ice sheets. *Nature*, 461(7266), 971–975.
- Pritchard, H., Ligtenberg, S., Fricker, H., Vaughan, D., Van den Broeke, M., & Padman, L. (2012). Antarctic ice-sheet loss driven by basal melting of ice shelves. *Nature*, 484(7395), 502–505.
- Ridley, J.K., & Partington, K. (1988). A model of satellite radar altimeter return from ice sheets. *Remote Sensing*, 9(4), 601–624.
- Sasgen, I., van den Broeke, M., Bamber, J.L., Rignot, E., Sørensen, L.S., Wouters, B., et al. (2012). Timing and origin of recent regional ice-mass loss in Greenland. *Earth and Planetary Science Letters*, 333, 293–303.
- Shepherd, A., Ivins, E.R., Geruo, A., Barletta, V.R., Bentley, M.J., Bettadpur, S., et al. (2012). A reconciled estimate of ice-sheet mass balance. *Science*, 338(6111), 1183–1189.
- Shepherd, A., & Wingham, D. (2007). Recent sea-level contributions of the Antarctic and Greenland ice sheets. *Science*, 315(5818), 1529–1532.
- Simonsen, S.B., Stenseng, L., Adalgeirsdóttir, G., Fausto, R., Hvidberg, C.S., & Lucas-Picher, P. (2013). Assessing a multilayered dynamic firn-compaction model for Greenland with ASIRAS radar measurements. *Journal of Glaciology*, 59(215), 545–558.
- Sørensen, L., Simonsen, S., Nielsen, K., Lucas-Picher, P., Spada, G., Adalgeirsdóttir, G., et al. (2011). Mass balance of the Greenland ice sheet (2003–2008) from ICESat data – The impact of interpolation, sampling and firn density. *The Cryosphere*, 5(1), 173–186 (5:173–186).
- Thomas, R., Davis, C., Frederick, E., Krabill, W., Li, Y., Manizade, S., et al. (2008). A comparison of Greenland ice-sheet volume changes derived from altimetry measurements. *Journal of Glaciology*, 54(185), 203–212.
- Wingham, D., Rapley, C., & Griffiths, H. (1986). New techniques in satellite altimeter tracking systems. *Proceedings of IGARSS'86 Symposium* (pp. 1339–1344) (Ref. ESA SP-254).

- Wingham, D.J., Ridout, A.J., Scharroo, R., Arthern, R.J., & Shum, C. (1998). Antarctic elevation change from 1992 to 1996. *Science*, 282(5388), 456–458.
- Zwally, H.J., Bindschadler, R.A., Brenner, A.C., Major, J.A., & Marsh, J.G. (1989). Growth of Greenland ice sheet: Measurement. *Science*, 246(4937), 1587–1589.
- Zwally, H.J., Giovinetto, M.B., Li, J., Cornejo, H.G., Beckley, M.A., Brenner, A.C., et al. (2005). Mass changes of the Greenland and Antarctic ice sheets and shelves and contributions to sea-level rise: 1992–2002. *Journal of Glaciology*, 51(175), 509–527.
- Zwally, H., Jun, L., Brenner, A., Beckley, M., Cornejo, H., Dimarzio, J., et al. (2011). Greenland ice sheet mass balance: Distribution of increased mass loss with climate warming; 2003–07 versus 1992–2002. *Journal of Glaciology*, 57(201), 88–102.

C A Digital Elevation Model of the Greenland Ice Sheet

Digital Elevation Models (DEMs) provide key information for assessing the state of the cryosphere, and are e.g. used in repeat-track analyses, for constraining SAR interferometry for ice velocity mapping, or in glaciological modeling. In the recent years, the Greenland Ice Sheet has been subject to temporally and spatially variable changes in ice thickness, ice velocity, mass balance, etc. (Sasgen et al., 2012; Shepherd et al., 2012; Sørensen et al., 2011). Therefore, an updated DEM is necessary in order to accurately correct recent observations. Such one is developed during this Ph.D. study.

In order to maximize the spatial data coverage and DEM accuracy, contemporary Envisat and CryoSat-2 LRM and SARIn radar data from 2010 are merged with ICESat, ATM, and LVIS laser data agreeing in time and space. Surface penetration of the radar echoes introduce vertical errors, which are corrected with laser data. Slope-induced errors introduce horizontal offsets as the reflecting point location is displaced from nadir to the Point of Closest Approach (POCA). Such errors in SARIn data are corrected by assuming a $2-\pi$ phase ambiguity and relocating the observations up-slope; the conventional radar data (Envisat, LRM) are adjusted by relocating the observations to the POCA. This approach uses a-priori knowledge on the surface topography, in this case obtained from the Greenland Ice Mapping (GIMP) DEM (Howat et al., 2014) regrided to a 2 km resolution. The specific resolution was determined in a study of relocation methods (Appendix D), where, however, additional work after submission of the paper revealed the preferred resolution for CryoSat-2 LRM data to be 2 km rather than 500 m as otherwise stated. The resulting model is referred to as the RL-DEM. It is referenced to the WGS-84 ellipsoid and is posted in two projections: In WGS-84 as a $0.02^\circ\text{lat} \times 0.05^\circ\text{lon}$ equi-angular grid, and a 2×2 km equi-distant Polar Stereographic grid. The model, validation hereof, and comparisons with previous DEMs are all described in the following paper:

Authors : J. F. Levinsen, B. E. Smith, L. S. Sørensen, K. Khvorostovsky, S. B. Simonsen, R. Forsberg
Title : A Digital Elevation Model of the Greenland Ice Sheet based on combined laser and radar altimetry
Journal : Earth and Space Science
Submission date : December 23rd 2014

¹ A Digital Elevation Model of the Greenland Ice ² Sheet based on combined laser and radar altimetry

J. F. Levinsen,^{1,2} Ben E. Smith,² Louise S. Sørensen,¹ Kirill Khvorostovsky,³

Sebastian B. Simonsen,¹ René Forsberg,¹

Corresponding author: J. F. Levinsen, DTU Space, National Space Institute, Technical University of Denmark Elektrovej, Building 327, 2800 Kgs. Lyngby, Denmark. (jfl@space.dtu.dk)

¹DTU Space, National Space Institute,
Technical University of Denmark, Denmark.

²University of Washington, Applied
Physics Lab Polar Science Center, Seattle,
Washington, USA.

³NN, Nansen Environmental and Remote
Sensing Center, Bergen, Norway.

3 **Abstract.** This work merges contemporary laser and radar data to de-
4 velop a Digital Elevation Model of the Greenland Ice Sheet. The reference
5 epoch is 2010 and the DEM is posted in two grids, $0.02^\circ\text{lat} \times 0.05^\circ\text{lon}$ and
6 2×2 km. Radar data are acquired with Envisat and CryoSat-2, and eleva-
7 tion errors due to surface penetration are corrected with observations from
8 the Ice, Cloud, and land Elevation Satellite (ICESat), Airborne Topographic
9 Mapper (ATM), and Land, Vegetation, and Ice Sensor (LVIS). Methods for
10 relocating radar data have been investigated and the optimal method has
11 been applied. Validation of the DEM against 2011 ATM and CryoVEx data
12 yields elevation differences of 0.1 ± 7.9 m above 2200 m altitude and $0.1 \pm$
13 59.9 m below. Thus, a radar-based, laser-adjusted DEM has been developed,
14 which is specific to the year 2010, and which is applicable for e.g. relocation
15 or elevation change detection of radar altimetry data.

1. Introduction

16 Monitoring the ongoing changes in the polar ice sheets is important for understanding
17 the physical processes and their global impacts. This can be done, e.g., by analyzing ice
18 velocities from SAR interferometry [*Joughin et al.*, 2010], through glaciological and cli-
19 matological modeling [*Ettema et al.*, 2009], or through surface elevation change detection
20 from altimetry [*Sørensen et al.*, 2011]. Common to the methods is the application of a
21 Digital Elevation Model (DEM) to constrain the observations. SAR-based ice velocities
22 require a removal of the topographic signal to isolate ice movements [*Joughin et al.*, 1996].
23 High-resolution DEMs input to Greenland climate models show more precipitation near
24 the coast than in the interior. This opposes results with lower-resolution DEMs, how-
25 ever better agrees with automatic weather station data [*Lucas-Picher et al.*, 2012]. In
26 elevation change studies, a DEM can be used to remove topography in-between repeat
27 ground-tracks [*Qi and Braun*, 2013], or to correct for slope-induced errors, which shift the
28 reflecting point up-slope from nadir. For example, Envisat’s Radar Altimeter-2 (RA-2)
29 has a half-power beamwidth of 1.3° . In combination with its altitude of 800 km, signifi-
30 cant measurement relocations of up to 18 km may occur. Footprints from laser altimeters
31 are up to 70 m wide and hence do not suffer from such offsets [*Hurkmans et al.*, 2012].

32
33 Observed surface changes of the Greenland Ice Sheet (GrIS) occur on spatial scales of
34 meters to kilometers, and outlet glaciers such as Jakobshavn Isbræ, Kangerdlugssuaq,
35 and Helheim are subject to significant changes in elevation and mass balance [*Korona*
36 *et al.*, 2009; *Pritchard et al.*, 2009; *Levinsen et al.*, 2013; *Howat et al.*, 2011]. An accu-

37 rate modeling process therefore requires the availability of a contemporary DEM. Current
38 DEMs are based on a variety of data sources and have different reference epochs. One
39 [Howat *et al.*, 2014] combines data from different sensors, accumulated over roughly ten
40 years. Another [DiMarzio, 2007] uses only ICESat observations, limited to two to three
41 35-day acquisition periods per year between 2003 and 2005. A third [Helm *et al.*, 2014]
42 uses 2012 CryoSat-2 data. As for many others, the DEMs suffer from either a reduced
43 spatial coverage or intermediate surface changes during data acquisition and relative to
44 the present day.

45 Pulses from radar altimeters penetrate clouds and are acquired more continuously in time
46 than laser observations, which are sensitive to cloud cover. Radar altimetry is, however,
47 subject to vertical errors due to penetration into the subsurface snow/ firn, volume scatter,
48 and shifted measurement locations [Ridley and Partington, 1988]. Thanks to CryoSat-2's
49 operation mode over rough terrain as well as its smaller footprint compared to Envisat,
50 slope-induced errors in such data are reduced so CryoSat-2 better detects, e.g., ridges
51 and edges of ice caps. On the basis of concurrent observations from airborne and space-
52 borne laser and radar missions, this study focuses on the combination of 2010 Envisat and
53 CryoSat-2 data with colocated laser data to develop a DEM of the GrIS. The laser data
54 are acquired with the NASA Ice, Cloud, and land Elevation Satellite (ICESat), Airborne
55 Topographic Mapper (ATM), and Land, Vegetation, and Ice Sensor (LVIS). The different
56 ground-tracks and flight paths increase the spatial data coverage, and a correction of the
57 radar heights using laser data reduces elevation errors. Thorough tests of slope correction
58 methods yield significantly improved relocations of radar data relative to those in previous
59 studies. The result is an absolute DEM, referenced to a specific epoch in 2010. The model

60 exploits the high elevation accuracy in laser data and the large laser-radar data coverage
61 to resolve both large- and small scale topographic features. This is ideal for analyses of
62 observations acquired in or near 2010.

2. Observations

63 Based on data availability and to reduce effects from intermediate surface changes, the
64 observation period is April – September 2010. CryoSat-2 data were available from July
65 to September, while the Envisat data in the study start in April. This ensures a temporal
66 overlap with the airborne campaigns. Laser data are acquired before the onset of the melt
67 season, and the short observation period minimizes seasonal changes in the radar-laser
68 elevation offsets.

2.1. Radar altimetry

69 Envisat operated from 2002 – 2012. It followed a 35-day repeat cycle until October
70 2010 where an orbit lowering put the satellite into a drifting phase. The RA-2 instrument
71 functioned at a nominal frequency of 13.575 GHz (Ku band). The footprint had a diameter
72 of 18 km while the pulse-limited footprint (PLF) ranged from 2 to 10 km depending on
73 the surface topography [*European Space Agency*, 2011].

74 CryoSat-2 was launched into a 369-day repeat cycle in 2010. It orbits at a mean altitude of
75 730 km. The satellite's main payload is SIRAL (Synthetic Aperture Interferometric Radar
76 Altimeter), which operates in one of three modes depending on the surface: The Low
77 Resolution Mode (LRM) is used over flat interior ice sheets where it acts as a conventional
78 radar altimeter. The nominal PLF is 1.65 km. The SAR mode is used over sea ice, while
79 a combination with interferometry (SARIn) is applied over the sloping ice and coastal

80 margins. Both SAR modes have a PLF of 1.65 km across-track vs. 300 m along-track. In
81 the LRM and SAR modes, return signals are received by one antenna, while two antennae
82 displaced by about 1 m are used in SARIn. Thus, in case of a sloping surface, a return
83 pulse will arrive at the antennae at different times, and the phase difference can be used to
84 derive the true reflecting point location [*European Space Agency*, 2012a; *Wingham et al.*,
85 2006]. CryoSat-2's strength for our purposes lies in its SARIn mode.

86 The observations are downloaded from ESA, and the geodetic datum is the WGS-84
87 ellipsoid. Envisat cycles 88–92 (April to September 2010) are implemented in conjunction
88 with CryoSat-2 Baseline B L2i (Level-2 Intermediate) data from July to September 2010
89 [*University of Leeds*, 2013]. L2i is preferred over L2 as the L2i product contains additional
90 information, which allows for relocating the measurement locations. This allows for a
91 consistent relocation of LRM and Envisat data and for correcting for phase ambiguities in
92 SARIn data [*European Space Agency*, 2012a]. Additional Envisat cycle 77 (March-April
93 2009) data are included for an analysis of radar penetration depths.

2.2. Laser altimetry

94 In February 2003, NASA launched ICESat carrying on-board the Geoscience Laser
95 Altimeter System (GLAS). ICESat operated until October 2009, initially with an 8-day
96 repeat cycle, which was changed to a 91-day orbit after seven months of operation. Each
97 laser pulse illuminated an ellipse approximately 60 m wide on the ground, and the along-
98 track separation distance between footprints was approximately 170 m. Data from the
99 GLAS/ICESat Antarctic and Greenland Ice Sheet Altimetry product (GLA12, release 33)
100 are downloaded from the National Snow and Ice Data Center (NSIDC), and the geodetic
101 datum is changed from TOPEX/Poseidon to WGS-84. The dataset provides geolocated

102 and time-tagged elevation estimates with vertical errors of approximately 15 cm [*Zwally*
103 *et al.*, 2002, 2014; *Schutz et al.*, 2005]. Data rejection criteria and corrections are based
104 on the study by *Sørensen et al.* [2011] and concern e.g. the removal of observations with
105 more than one peak and the saturation correction based on the quality flag. Furthermore,
106 the 2003 – 2009 surface elevation change trend derived from model 3 is added to 2009
107 ICESat heights to adjust them to 2010. The data are acquired in March – April 2009 and
108 cover a period of 34 days.

2.3. Airborne laser-scanning data

109 The ATM and LVIS instruments are carried on board aircrafts and conically scanning
110 the ground below. They are flown during the Operation IceBridge campaign, and GPS
111 and inertial navigation systems allow for re-flying previous ground-tracks with a minimum
112 overlap of 50%. The vertical accuracy is 10 cm.

113 ATM is typically flown at altitudes of 300 – 500 m with an off-nadir scan angle of 15°.
114 This illuminates approximately 250 – 350 m wide swaths consisting of measurements with
115 1 – 3 m footprints. LVIS is a high-altitude instrument, and at an altitude of 10 km the
116 12° scan-angle allows for illuminating a 2 km swath with 10 – 25 m footprints. 2009 –
117 2010 ATM Level 1B Qfit and LVIS Level 2 releases are downloaded from the NSIDC. The
118 observations are acquired in April and May and are referenced to the WGS-84 ellipsoid
119 [*Krabill et al.*, 2002; *Krabill*, 2013; *Brooks et al.*, 2012]. The 2009 – 2010 elevation changes
120 from ATM are estimated along repeat flight-lines to update the 2009 heights to 2010. Due
121 to few repeat LVIS flights, and these often following ICESat ground-tracks, 2009 data are
122 used where the ICESat elevation change trend is zero, i.e. mostly above 2000 m altitude.

3. Previous models

123 Several DEMs of the GrIS have been developed, and the first ones were published
124 more than three decades ago [*Brooks et al.*, 1978; *Zwally and Bindshadler*, 1983]. They
125 were based on radar altimetry data from the Geodynamics Experimental Ocean Satellite
126 (GEOS 3) and SEASAT, respectively. Newer models are developed by *Bamber et al.*
127 [2001]; *Sørensen et al.* [2011]; *Helm et al.* [2014] and *Howat et al.* [2014]. As the latter
128 are compared with the radar-laser model (RL-DEM) developed in this study, a short
129 introduction to each follows below.

130 The *Bamber et al.* [2001] model is built from a combination of radar altimetry and airborne
131 laser-scanner data and is posted at a 1×1 km resolution. Geosat and ERS-1 altimetry from
132 the 1985 – 1986 and 1994/1995 geodetic phases are combined with ERS-1 and -2 tandem
133 phase altimetry from 1995, 1991 – 1993 ATM data, aerial photography, and manually
134 digitized maps from the Danish Geodata Agency (GST; previously the National Survey
135 and Cadastre of Denmark, KMS). The digitized maps are used along large parts of the ice
136 sheet margin and have RMS errors of at least 100 m. As the model is unable to resolve
137 surface features with horizontal scales of less than 10 km, surface slopes are smoothed
138 out or distorted [*Scambos and Haran*, 2002]. Thus, the DEM slopes and elevations do not
139 meet the minimum accuracy required for modeling the GrIS state at present. Another
140 model built from data from multiple sensors is the Greenland Ice Mapping Project (GIMP)
141 DEM by *Howat et al.* [2014]. The GIMP is gridded to a 30 m resolution and is based
142 on a combination of e.g. 2003 – 2009 ICESat data, 2000 – 2010 stereo-photogrammetric
143 ASTER DEMs (Aster Global GDEM, *Slater et al.* [2011]), 1999 – 2002 Landsat-7 and
144 RADARSAT-1 imagery. Validation against ICESat data shows RMS errors of elevation

145 differences of 8.5 m over ice-covered terrain and 18.3 m over ice-free terrain. The *Helm*
146 *et al.* [2014] model is based on a 369-day cycle of CryoSat-2 LRM and SARIn data starting
147 in January 2012. The posting is 1×1 km, and validation against 2012 ATM data shows
148 mean elevation differences of -0.01 ± 45.0 m above 2200 m altitude and 3.95 ± 133.6 m
149 below. Finally, the *Sørensen et al.* (2011 Model 3) produced a mean surface topography in
150 500 m along-track segments, the center of each determined by averaging the observations
151 in 500×500 m boxes along-track.

4. Method

152 The radar data are first relocated to reduce the effect of misallocation due to the surface
153 slope. For LRM and Envisat, this is done with the Point of Closest Approach (POCA;
154 *Gray et al.* [2013]; *Hawley et al.* [2009]), which relocates the observations to the closest,
155 highest point within the footprint via local interpolation of the GIMP. This external
156 DEM is chosen as its high resolution and accuracy allows for more accurately resolving the
157 topography within the footprint than what is possible with, e.g., Envisat alone. The GIMP
158 is re-gridded to 500 m (LRM) and 2 km postings (Envisat), respectively, cf. analyses of
159 slope correction methods (see Discussion). Prior to its use, the GIMP is reprojected from
160 the WGS-84 ellipsoid to the EGM2008 geoid [*Pavlis et al.*, 2012], negative elevations are
161 edited out, and photoclinometry above 82N are replaced by GST photogrammetry to
162 account for errors in this region. The geoid heights are then added back. SARIn data are
163 slope-corrected using information from the CryoSat-2 L2i product. The relocation is based
164 on the location and elevation of the satellite nadir point, as interpolated from the GIMP.
165 If the nadir location is higher than the reported L2i location, the data point is assumed to
166 be subject to a $2\text{-}\pi$ phase ambiguity. In this case, the position and height for the return

167 are recalculated from orbit data in the L2i product, assuming a 2π interferometric phase
168 shift that brings the return position uphill in the direction of nadir.

4.1. DEM conceptual algorithm and validation description

169 The Envisat, LRM, and SARIn profiles are corrected individually by adjusting the radar
170 heights to the surfaces spanned by laser data.

171 1. For radar points with laser observations within a specific radius, apply Inverse Dis-
172 tance Weighting (IDW) to derive a laser height at the radar location. To minimize errors
173 from surface changes within the radius and the steep topography along the margin, the
174 radius is 500 m for radar points below 2000 m altitude and 2 km for points above.

175 2. Estimate the radar-laser elevation offset: $dH = H_{RA} - H_{LA}$.

176 3. Reject dH values greater than two standard deviations (STD), 2σ , of the mean.

177 This reduces errors from the location of laser points relative to radar data.

178 4. Recalculate the mean and σ . Then reject outliers exceeding 3σ .

179 5. Use the geostatistical interpolation tool *collocation* to spatially interpolate the dH
180 values onto a grid [*Dermanis*, 1984]: dH_{intp} (prediction values) and σ_{intp} (errors).

181 6. Correct the radar heights cf. $H = H_{RA} - dH_{intp}$.

182 *Collocation* is a linear, unbiased estimator built upon covariances and the spatial correla-
183 tion between observations relative to their separation distance. Neighboring observations
184 are assumed to be highly correlated and clustered observations are weighted less than
185 single points. This makes the method ideal for transferring irregularly distributed obser-
186 vations onto a grid. Data errors are considered by adding a separate variance/covariance
187 matrix, and if disregarding them, prediction to an observation point returns the measure-

188 ment value with a zero error. Collocation assumes the mean, variance, and covariances to
189 depend only on the separation distance. Through minimizing the errors, a great spatial
190 data distribution allows for accurately reproducing the spatial pattern of input values
191 [*Dermanis, 1984*]. Given that the interpolation values are distributed above and below
192 a given mean, and that laser data are available across the entire GrIS, *collocation* is a
193 favorable tool. In addition, IDW is used to account for the spatial distribution of data,
194 yet not their spatial correlation. All computations are carried out using GRAVSOFT
195 GEOGRID [*Tscherning et al., 2008*].

196 The final DEM surface is derived by following the steps below:

197 7. In order to remove topography, thereby reducing potential interpolation errors, sub-
198 tract the GIMP elevations from laser data and each corrected radar surface.

199 8. Use IDW to merge the residual surfaces into a grid. This yields dH_{comb} .

200 9. Finally, add the GIMP to dH_{comb} : $H_{RL-DEM} = H_{GIMP} + dH_{comb}$.

201 The GEOGRID routine produces equi-angular grids in WGS-84, in this case
202 $0.02^\circ\text{lat} \times 0.05^\circ\text{lon}$, i.e. approximately 2×2 km depending on the latitude. This grid
203 spacing is a good compromise between the spatial resolution of input data, and cf. *Levin-*
204 *sen et al. [2014]* it is sufficient for use in elevation change analyses. A 2×2 km grid
205 in Polar Stereographic projection is also produced; the standard parallel is 70N and the
206 central meridian 45W. Both products refer to the WGS-84 ellipsoid. The RL-DEM errors
207 are estimated by applying Gaussian quadratic summation to the interpolation errors, i.e.
208 $\sigma_{RL-DEM} = \sqrt{(\sigma_{intp}^{EV})^2 + (\sigma_{intp}^{CS})^2}$. This is done because the interpolation errors not only
209 represent the amount and spatial distribution of radar points; they also reflect topographic
210 changes within the laser-radar search radius as this is contained in the dH signal. The

211 respective pattern is analyzed by separating the dH values into 20 km bins and analyzing
212 the spatial STD pattern.

213

214 Validation is carried out with 2011 ATM and ESA CryoVEx airborne laser-scanner data
215 [*Skourup et al.*, 2011]. This year is chosen as no CryoVEx flights were conducted in 2010,
216 and other contemporary laser data are included in the analysis. A 500 m search radius
217 between DEM and laser points is used, and the validation is split up into to points above
218 and below 2200 m altitude, similar to the study by *Helm et al.* [2014].

219

220 A separate study of penetration depths is carried out for contemporary ICESat and En-
221 visat data from March/April 2009, and the analysis is constrained to points above 2000 m
222 altitude. This confines observed elevation differences to reflect penetration effects rather
223 than, e.g., temporal variations in the signal or surface climatology as well as surface melt.

5. Results

224 Fig. 1 shows the dH values and Table 1 the corresponding statistics. For CryoSat-2,
225 SARIn data span ± 8.8 m with a mean of -1.1 m and a STD of 3.4 m. For LRM data, the
226 numbers are ± 4.9 m, -0.5 m, and 2.3 m, respectively. The Envisat values over the SARIn
227 region are ± 6.5 m, -1.5 m, and 2.4 m, respectively, while corresponding values over the
228 LRM region are ± 6.5 m, -1.7 m, and 3.0 m. Overall, dH typically spans $-3 - 0$ m in
229 the interior indicating that the surface height observed with the lasers is higher than that
230 seen by the radars. This reflects penetration effects. Larger elevation offsets are found
231 near the coast, particularly for SARIn where regions of $dH = \pm 8$ m occur.

232 The collocation operation reproduces the spatial pattern of dH values. Having done this

233 separately for the three observation types, the corrected CryoSat-2 surfaces are combined
234 into one and merged with the Envisat heights. Adding laser data, Fig. 2 illustrates the
235 resulting elevation model and Fig. 3 the surface slopes. A clear pattern in the distribution
236 of elevation errors (Fig. 2b) arises due to dH : the high density of observations with sim-
237 ilar radar-elevation offsets yield minimum errors of 0.4 m in the interior, which increase
238 outward to a maximum of 4.0 m. Furthermore, an abrupt boundary between LRM and
239 SARIn data exists due to the larger SARIn dH variability. The RL-DEM reveals the
240 topographic features of the ice sheet, as highlighted by Fig. 3: The ice divide, where the
241 surface slopes are at a minimum, can be seen in the interior. Away from the ice divide,
242 the slopes increase, following ice flow patterns over the bed as well as variations in the bed
243 shear stress [Joughin *et al.*, 2010; Rignot and Mouginot, 2012]. The maximum slopes are
244 found along the coastal margins, indicating steep features caused by mountains, narrow
245 ice streams, and outlet glaciers.

246
247 The validation results are presented in Table 2, which gives the mean and STD of the
248 observed elevation differences ($dH_{valid} = H_{RL-DEM} - H_{valid}$). The largest disagreements
249 occur at lower altitudes, while the agreement is slightly better with ATM than CryoVEx.
250 This may be attributed to the repeat or near-repeat ATM flight lines, CryoVEx flights
251 only covering margin regions, as well as the smaller CryoVEx data sampling in time and
252 space. For this mission, the mean and STD are 0.1 ± 59.9 m below 2200 m, which de-
253 creases to -1.6 ± 13.8 m above. For ATM, the corresponding values are 1.2 ± 30.2 m
254 below 2200 m and 0.1 ± 7.9 m above, respectively.

255

256 Fig. 4 illustrates Envisat penetration depths in March/April 2009. The elevation off-
257 sets have a mean and STD of -1.6 ± 2.2 m, with most penetration depths ranging from
258 1 – 4 m. The signal varies throughout the season and with the surface climatology.
259 Therefore, the observed signal solely represents the specific period and region.

6. Comparison with other models

260 A comparison exercise against the models described in Section 3 is carried out to demon-
261 strate not only how the RL-DEM performs relative to those, but also how the models
262 inter-compare. This will clarify that the RL-DEM, in spite of being built from similar
263 datasets and methodologies as previous models, contributes new knowledge concerning
264 the GrIS surface topography. Each model is re-sampled to the 2×2 km posting, and
265 elevation differences are given as $dH_{comp} = H_{RL-DEM} - H_{DEM}$. The mean and STD of
266 dH_{comp} are provided for observations below/above 2200 m altitude (Tables 3 and 4).

267 For both high and low altitudes, the RL-DEM vs. GIMP agreement is best. This is
268 attributed to the use of the latter for the RL-DEM development so the model inherits the
269 GIMP topography where few or no radar data exist. This mainly occurs along the margin
270 and in the north due to the laser-radar search radii. The elevation offsets result from dif-
271 fering reference epochs and measurements as e.g. laser altimetry and photogrammetry are
272 not subject to surface penetration. Based on the validation, however, confidence is pro-
273 vided in using the GIMP. The largest disagreements are found for inter-comparisons with
274 the *Bamber et al.* [2001] model. Considering the elevation and slope errors and significant
275 elevation changes between the mid-1990's and 2010, large offsets between this and other
276 DEMs are expected. The ICESat surface agrees best with the GIMP due to the DEMs
277 used in the GIMP development being co-registered to ICESat data. Differences between

278 ICESat data and the RL-DEM are attributed to the 2006 ICESat reference epoch, errors
279 due to the large ground-track separation distance and data gaps in time, as well as the
280 smaller footprint relative to the RL-DEM posting. The *Helm et al.* [2014] model compares
281 well with the others, particularly at higher elevations, where a small mean and STD is
282 found. Differences increase with a lowering altitude, due to the 2012 reference epoch and
283 the short observation period. The latter is advantageous as errors from elevation changes
284 during data acquisition are reduced. However, the spatial data coverage is reduced, the
285 impact of which is mostly seen by the margin: The model cannot accurately resolve the
286 surface topography.

287 Thus, it is found that the RL-DEM differs from previous models and thus that it con-
288 tributes with new knowledge of the GrIS topography, referenced to a specific epoch in
289 time.

7. Discussion

290 Several methods for correcting radar data for slope-induced errors have been described
291 in literature, e.g. by *Brenner et al.* [1983]; *Bamber* [1994]; *Hurkmans et al.* [2012]. In
292 order to ensure an accurate correction of the points used in this study, two approaches are
293 tested for Envisat and LRM data. Both are based on the GIMP at various spatial resolu-
294 tions to account for surface topography, and both relocate the measurements horizontally.
295 The methods are the POCA and the model by *Hurkmans et al.* [2012], which calculates
296 the displacement from the satellite altitude and the surface slope and aspect. The tests
297 are carried out over the highly dynamic Jakobshavn Isbræ drainage basin (Envisat) and
298 the interior (LRM), and the results are validated against May 2010 ATM data. Envisat
299 data are contemporary while LRM data are acquired in July 2010. The latter covers the

earliest available time period and are preferred to minimize surface changes relative to
ATM. The GIMP is re-gridded to 500 m, 2 km, 4 km, and 8 km postings for Envisat data,
and 90 m, 500 m, 1 km, and 2 km for LRM, respectively. The different grid postings
result from Envisat data covering margin parts of the ice sheet with a high topographic
variability. Validation shows the optimal methods to be the POCA with the GIMP at
2 km and 500 m postings, respectively. The different postings owe to the different test
regions. The corresponding mean and STD of elevation differences are 1.0 ± 13.7 m and
 0.6 ± 1.4 m. Thus, the 2×2 km RL-DEM makes out a strong tool for relocating conven-
tional radar altimetry such as from Envisat and, in the future, Sentinel-3 over regions of
little or no topographic changes [European Space Agency, 2012b]. An important finding
was that for Envisat based on the 500 m GIMP, both approaches revealed intersecting
relocation vectors rather than the points being shifted to the same location. *Flament and*
Rémy [2012] used the POCA with the 90 m GIMP. According to this study, this indicates
the occurrence of unphysical relocations and raises a question mark by Envisat's ability
to resolve topography at such a high posting. The *Hurkmans et al.* model uses the local
topography and assumes a constant slope within the footprint. It is constrained to regions
with slopes $\leq 1.5^\circ$ as it breaks down over rough topography. However, this is also found
with the higher resolution GIMP and for smaller slopes: points are shifted down-slope.
Another flaw of the model is that it misses small-scale topography. The *Hurkmans et al.*
study relocated Envisat data using a 1×1 km grid and lowered the error in volume
change rates by approximately 10% relative to ICESat/ATM. This study suggests that
a 2 km resolution could have improved the results further, and from the tests concludes
that the radar data in this study have a greater horizontal accuracy than those previously

323 published.

324

325 In the interior ice sheet, the radar vs. laser elevation offsets reflect penetration effects.

326 At lower altitudes, these effects decrease, and the elevations offsets likely result from a

327 combination of the following:

328 a) The spatial distribution of laser data relative to the respective radar point location;

329 b) Errors in the slope correction;

330 c) The different footprint sizes;

331 d) The physical properties of the subsurface snow/firn layer.

332 Element (a) explains the interchanging positive and negative dH signals in neighbor-
333 ing locations and result from the applied method. This is concluded after dividing the

334 elevation offsets into 20 km bins and analyzing the spatial STD pattern: in the interior,

335 $STD \approx 0$ m. The STD increases with the proximity to the margin, as does the variation in

336 the spatial distribution of positive/negative dH signals. The variability can be reduced by

337 decreasing the search radius, which will, however, lower the number of possible locations

338 for dH values. This is found in the northern GIS with the 500 m search radius over a low-

339 altitude region extending far inland. Furthermore, (a) explains the larger range of SARIn

340 dH values due to the observations covering greater parts of the margin than Envisat. In

341 the DEM production, the low number of overlapping radar-laser points is accounted for

342 by merging laser and radar data. Effects from (b) are expected to be greatly reduced.

343 However, as the exact surface seen by the radar is unknown, errors may still occur. (c)

344 means that the topographic signal within the footprint may impact when comparing radar

345 and laser elevations. The combined effect from (b,c) explains the larger mean and STD

346 values from Envisat than CryoSat-2 thereby demonstrating the advantage of CryoSat-2:
347 the smaller SARIn footprint, and the SARIn technology, significantly improve the detec-
348 tion of the reflecting point location.

349 The varying dH signals may also arise from a 2009–2010 elevation change not properly
350 being accounted for. The laser points are mostly from ICESat, and as 2010 was a record
351 melt year [*Tedesco et al.*, 2011], the assumption of a constant elevation change trend
352 fails. However, due to the few ATM and LVIS flight lines, the inclusion of ICESat data
353 is a compromise between increasing the spatial data coverage and DEM accuracy, and
354 introducing errors from physical surface changes. Such a surface change occurred during
355 acquisition of the data used in this study. As discussed in [*Sørensen et al.*, 2014], an
356 increased accumulation rate will increase the elevation measured by ICESat while that
357 seen by the radars might remain more stable if the snow added on top of the reflecting
358 layer has a low density. This increases the penetration depth, and, therefore, dH .

8. Conclusions

359 Here, we present a combination of concurrent CryoSat-2 and Envisat observations with
360 ICESat, ATM, and LVIS data to develop a contemporary DEM of the GrIS (RL-DEM). It
361 is available in two grids referenced to the WGS-84 ellipsoid: 0.02° latitude \times 0.05° longitude
362 (WGS-84) and 2×2 km (Polar Stereographic projection). The RL-DEM is referenced to
363 a specific time epoch, namely 2010.

364 The radar heights are corrected for elevation errors by shifting the points to the surface
365 spanned by laser data using the radar-laser elevation offsets, dH . Laser data are acquired
366 in 2009 and 2010, and 2009 data are adjusted to 2010 by adding the surface elevation
367 changes over overlapping flight lines or satellite paths. This increases the spatial data

368 coverage and decreases RL-DEM errors. The best radar-laser agreement is achieved with
369 CryoSat-2's LRM mode: Here $dH = \pm 4.9$ m, while for SARIn $dH = \pm 8.8$ m, and for
370 Envisat $dH = \pm 6.5$ m. The larger range of SARIn values results from the larger data cov-
371 erage along the margin where topography-induced elevation offsets between neighboring
372 radar and laser points occur. Validation of the RL-DEM against 2011 ATM and CryoVEx
373 data shows a good agreement in the interior ice sheet with larger offsets at lower altitudes:
374 Above 2200 m altitude, ATM reveals means and standard deviations of elevation differ-
375 ences of -0.1 ± 10.1 m and CryoVEx -1.6 ± 13.9 m; below 2200 m the corresponding
376 numbers are 2.0 ± 39.3 m and 0.8 ± 61.0 m, respectively.

377

378 Whereas high-resolution models, such as the GIMP, are applicable for processing of im-
379 agery with a similar resolution, the RL-DEM is ideal for accurately relocating conventional
380 radar altimetry with a previously unachievable accuracy, and for using such data for sur-
381 face elevation changes detection. With an increased CryoSat-2 data availability with time,
382 Sentinel-3's launch in 2015, and that of ICESat-2 in 2017, we can continuously develop
383 updated GrIS DEMs to ensure accurate analyses of the GrIS.

384 **Acknowledgments.** The Envisat and CryoSat-2 data were available through ESA's
385 Earth Online (<https://earth.esa.int/web/guest/data-access>), while ICESat, ATM and
386 LVIS data were downloaded from the NSIDC (<http://nsidc.org/>). The CryoVEx data
387 are available in-house at DTU Space and may be available upon request.

References

- 388 Bamber, J. L. (1994), Ice sheet altimeter processing scheme, *Int. J. Remote Sens.*, *15*(4),
389 925–938, doi:10.1080/01431169408954125.
- 390 Bamber, J. L., S. Ekholm, and W. B. Krabill (2001), A new, high-resolution digital eleva-
391 tion model of Greenland fully validated with airborne laser altimeter data, *J. Geophys.*
392 *Res. - Sol. Ea.*, *106*(B4), 6733–6745, doi:10.1029/2000JB900365.
- 393 Brenner, A. C., R. A. Bindschadler, R. H. Thomas, and H. J. Zwally (1983), Slope-induced
394 errors in radar altimetry over continental ice sheets, *J. Geophys. Res. - Oceans*, *88*(C3),
395 1617–1623, doi:10.1029/JC088iC03p01617.
- 396 Brooks, C., M. Beckley, B. Blair, and M. Hofton (2012), IceBridge LVIS L2 Geolocated
397 Surface Elevation Product, <http://nsidc.org/data/docs/daac/icebridge/ilvis2/>, Boul-
398 der, Colorado, USA: NASA DAAC at the National Snow and Ice Data Center.
- 399 Brooks, R. L., W. J. Campbell, R. O. Ramseier, H. R. Stanley, and H. J. Zwally (1978),
400 Ice sheet topography by satellite altimetry, *Nature*, (274), 539–543.
- 401 Dermanis, A. (1984), Kriging and collocation - A comparison, *Manuscripta geodaetica*, *9*,
402 159–167.
- 403 DiMarzio, J. P. (2007), GLAS/ICESat 1 km Laser Altimetry Digital Elevation Model of
404 Greenland, <http://nsidc.org/data/nsidc0305.html>.
- 405 Ettema, J., M. R. van den Broeke, E. van Meijgaard, W. J. van de Berg, J. L. Bamber,
406 J. E. Box, and R. C. Bales (2009), Higher surface mass balance of the Greenland ice
407 sheet revealed by high-resolution climate modeling, *Geophys. Res. Lett.*, *36*.
- 408 European Space Agency (2011), *ENVISAT ALTIMETRY Level 2 User Manual*.

409 European Space Agency (2012a), *CryoSat Product Handbook*, ESRIN, ESA and Mullard
410 Space Sciences Laboratory, and University College London.

411 European Space Agency (2012b), Sentinel-3 ESAs Global
412 Land and Ocean Mission for GMES Operational Services,
413 https://sentinel.esa.int/documents/247904/351187/S3_SP-1322_3.pdf, number: SP-
414 1322/3.

415 Flament, T., and F. Rémy (2012), Dynamic thinning of antarctic glaciers from along-track
416 repeat radar altimetry, *J. Glaciol.*, 58(211), 830–840.

417 Gray, L., D. Burgess, L. Copland, R. Cullen, N. Galin, R. Hawley, and V. Helm
418 (2013), Interferometric swath processing of Cryosat data for glacial ice topography,
419 *The Cryosphere*, 7(6), 1857–1867, doi:10.5194/tc-7-1857-2013.

420 Hawley, R. L., A. Shepherd, R. Cullen, V. Helm, and D. J. Wingham (2009), Ice-sheet
421 elevations from across-track processing of airborne interferometric radar altimetry, *Geo-*
422 *phys. Res. Lett.*, 36(22), doi:10.1029/2009GL040416.

423 Helm, V., A. Humbert, and H. Miller (2014), Elevation and elevation change of Greenland
424 and Antarctica derived from CryoSat-2, *The Cryosphere Discuss.*, 8(2), 1673–1721, doi:
425 10.5194/tcd-8-1673-2014.

426 Howat, I. M., Y. Ahn, I. Joughin, M. R. van den Broeke, J. T. M. Lenaerts, and B. Smith
427 (2011), Mass balance of Greenland’s three largest outlet glaciers, 2000–2010, *Geophys.*
428 *Res. Lett.*, 38(12), doi:10.1029/2011GL047565.

429 Howat, I. M., A. Negrete, and B. E. Smith (2014), The Greenland Ice Mapping Project
430 (GIMP) land classification and surface elevation datasets, *The Cryosphere*, 8(4), 1509–
431 1518, doi:10.5194/tc-8-1509-2014.

- 432 Hurkmans, R. T. W. L., J. L. Bamber, and J. A. Griggs (2012), Brief communication
433 "Importance of slope-induced error correction in volume change estimates from radar
434 altimetry", *The Cryosphere*, *6*(2), 447–451, doi:10.5194/tc-6-447-2012.
- 435 Joughin, I., R. Kwok, and M. Fahnestock (1996), Estimation of ice-sheet motion using
436 satellite radar interferometry: Method and error analysis with application to Humboldt
437 Glacier, Greenland, *J. Glaciol.*, *42*(142), 564–575.
- 438 Joughin, I., B. E. Smith, I. M. Howat, T. Scambos, and T. Moon (2010), Greenland
439 flow variability from ice-sheet-wide velocity mapping, *J. Glaciol.*, *56*(197), 415–430,
440 doi:doi:10.3189/002214310792447734.
- 441 Korona, J., E. Berthier, M. Bernard, F. Remy, and E. Thouvenot (2009), SPIRIT. SPOT
442 5 stereoscopic survey of Polar Ice: Reference Images and Topographies during the fourth
443 International Polar Year (2007–2009), *ISPRS J. Photogramm.*, *64*(2), 204–212.
- 444 Krabill, W. B. (2013), TM L1B Qfit Elevation and Return Strength,
445 <http://nsidc.org/data/ilatm1b.html>, Boulder, Colorado, USA: NASA DAAC at
446 the National Snow and Ice Data Center.
- 447 Krabill, W. B., W. Abdalati, E. Frederick, S. Manizade, C. Martin, J. Sonntag, R. Swift,
448 R. Thomas, and J. Yungel (2002), Aircraft laser altimetry measurement of elevation
449 changes of the Greenland Ice Sheet: technique and accuracy assessment, *J. Geodyn.*,
450 *34*, 357–376.
- 451 Levinsen, J., I. M. Howat, and C. C. Tscherning (2013), Improving maps of ice-sheet
452 surface elevation change using combined laser altimeter and stereoscopic elevation model
453 data, *J. Glaciol.*, *59*(215), 524–532, doi:10.3189/2013JoG12J114.

- 454 Levinsen, J. F., K. Khvorostovsky, F. Ticconi, A. Shepherd, R. Forsberg, L. S. Sørensen,
455 A. Muir, N. Pie, D. Felikson, T. Flament, R. Hurkmans, G. Moholdt, B. Gunter, R. Lin-
456 denbergh, and M. Kleinherenbrink (2014), ESA Ice Sheets CCI: Derivation of the opti-
457 mal method for surface elevation change detection of the Greenland Ice Sheet - Round
458 Robin results, *Int. J. Remote Sens.*, in print.
- 459 Lucas-Picher, P., M. Wulff-Nielsen, J. H. Christensen, G. Adalgeirsdottir, R. Mottram,
460 and S. B. Simonsen (2012), Very high resolution regional climate model simulations
461 over Greenland: Identifying added value, *J. Geophys. Res. - Atmos.*, *117*(D2), doi:
462 10.1029/2011JD016267.
- 463 Pavlis, N. K., S. A. Holmes, S. C. Kenyon, and J. K. Factor (2012), The development and
464 evaluation of the Earth Gravitational Model 2008 (EGM2008), *J. Geophys. Res. - Sol.*
465 *Ea.*, *117*(B4), doi:10.1029/2011JB008916.
- 466 Pritchard, H. D., R. J. Arthern, D. G. Vaughan, and L. A. Edwards (2009), Extensive
467 dynamic thinning on the margins of the Greenland and Antarctic ice sheets, *Nature*,
468 *461*, 971–975.
- 469 Qi, W., and A. Braun (2013), Accelerated Elevation Change of Greenland’s Jakobshavn
470 Glacier Observed by ICESat and IceBridge, *IEEE Geosci. Remote Sens. Lett.*, *10*(5),
471 1133–1137, doi:10.1109/LGRS.2012.2231954.
- 472 Ridley, J. K., and K. C. Partington (1988), A Model of Satellite Radar Altimeter Return
473 from Ice Sheets, *Int. J. Remote Sens.*, *9*(4), 601–624, doi:10.1080/01431168808954881.
- 474 Rignot, E., and J. Mouginot (2012), Ice flow in Greenland for the International Polar Year
475 2008 – 2009, *Geophys. Res. Lett.*, *39*(11), doi:10.1029/2012GL051634.

- 476 Scambos, T. A., and T. Haran (2002), An image-enhanced DEM of the Greenland ice
477 sheet, *Ann. Glaciol.*, *34*(1), 291–298, doi:10.3189/172756402781817969.
- 478 Schutz, B. E., H. J. Zwally, C. A. Shuman, D. Hancock, and J. P. DiMarzio
479 (2005), Overview of the ICESat mission, *Geophys. Res. Lett.*, *32*, L21S01, doi:
480 10.1029/2005GL024009.
- 481 Skourup, H., V. Barletta, I. Einarsson, R. Forsberg, C. Haas, V. Helm, S. Hendricks, S. M.
482 Hvidegaard, and L. S. Sørensen (2011), *ESA CryoVEx 2011: Airborne field campaign*
483 *with ASIRAS radar, EM induction sounder and laser scanner*, DTU Space, National
484 Space Institute, Technical University of Denmark, 1 ed.
- 485 Slater, J. A., B. Heady, G. Kroenung, W. Curtis, J. Haase, D. Hoegemann, C. Shockley,
486 and K. Tracy (2011), Global Assessment of the New ASTER Global Digital Elevation
487 Model, *Photogramm. Eng. Remote Sens.*, *77*(4), 335–349, doi:10.14358/PERS.77.4.335.
- 488 Sørensen, L. S., S. B. Simonsen, K. Nielsen, P. Lucas-Picher, G. Spada, G. Adalgeirsdottir,
489 R. Forsberg, and C. S. Hvidberg (2011), Mass balance of the Greenland ice sheet (2003
490 – 2008) from ICESat data – the impact of interpolation, sampling and firn density, *The*
491 *Cryosphere*, *5*(1), 173–186, doi:10.5194/tc-5-173-2011.
- 492 Sørensen, L. S., S. B. Simonsen, R. Meister, R. Forsberg, J. F. Levinsen, and T. Flament
493 (2014), Envisat derived elevation changes of the greenland ice sheet, and a comparison
494 to icesat results in the accumulation area, *Remote Sens. Environ.*, in review.
- 495 Tedesco, M., X. Fettweis, M. R. van den Broeke, R. S. W. van de Wal, C. J. P. P.
496 Smeets, W. J. van de Berg, M. C. Serreze, and J. E. Box (2011), The role of albedo
497 and accumulation in the 2010 melting record in Greenland, *Environ. Res. Lett.*, *6*(1),
498 doi:10.1088/1748-9326/6/1/014005.

- 499 Tscherning, C. C., R. Forsberg, and P. Knudsen (2008), An overview manual for the
500 GRAVSOFTE Geodetic Gravity Field Modelling Programs, *Tech. Rep. 2*, University of
501 Copenhagen; DTU Space.
- 502 University of Leeds (2013), CryoSat Performance Monitoring – CryoSat L2 data availabil-
503 ity from Kiruna, <http://cryosat.mssl.ucl.ac.uk/qa/availability.php>.
- 504 Wingham, D., C. Francis, S. Baker, C. Bouzinac, D. Brockley, R. Cullen, P. de Chateau-
505 Thierry, S. Laxon, U. Mallow, C. Mavrocordatos, L. Phalippou, G. Ratier, L. Rey,
506 F. Rostan, P. Viau, and D. Wallis (2006), CryoSat: A mission to determine the fluc-
507 tuations in Earth’s land and marine ice fields, *Adv. Space Res.*, *37*(4), 841–871, doi:
508 10.1016/j.asr.2005.07.027.
- 509 Zwally, H., B. Schutz, W. Abdalati, J. Abshire, C. Bentley, A. Brenner, J. Bufton, J. Dezio,
510 D. Hancock, D. Harding, T. Herring, B. Minster, K. Quinn, S. Palm, J. Spinhirne, and
511 R. Thomas (2002), ICESat’s laser measurements of polar ice, atmosphere, ocean, and
512 land, *J. Geodyn.*, *34*(3–4), 405–445, doi:10.1016/s0264-3707(02)00042-x.
- 513 Zwally, H., R. Schutz, C. Bentley, J. Bufton, T. Herring, J. Minster, J. Spinhirne, and
514 R. Thomas (2014), GLAS/ICESat L2 Antarctic and Greenland ice sheet altimetry data
515 V031, <http://nsidc.org/data/gla12>, Boulder, Colorado, USA.
- 516 Zwally, H. J., and R. A. Bindschadler (1983), Surface Elevation Contours of the Greenland
517 and Antarctic Ice Sheets, *J. Geophys. Res.*, *88*(C3), 1589–1596.

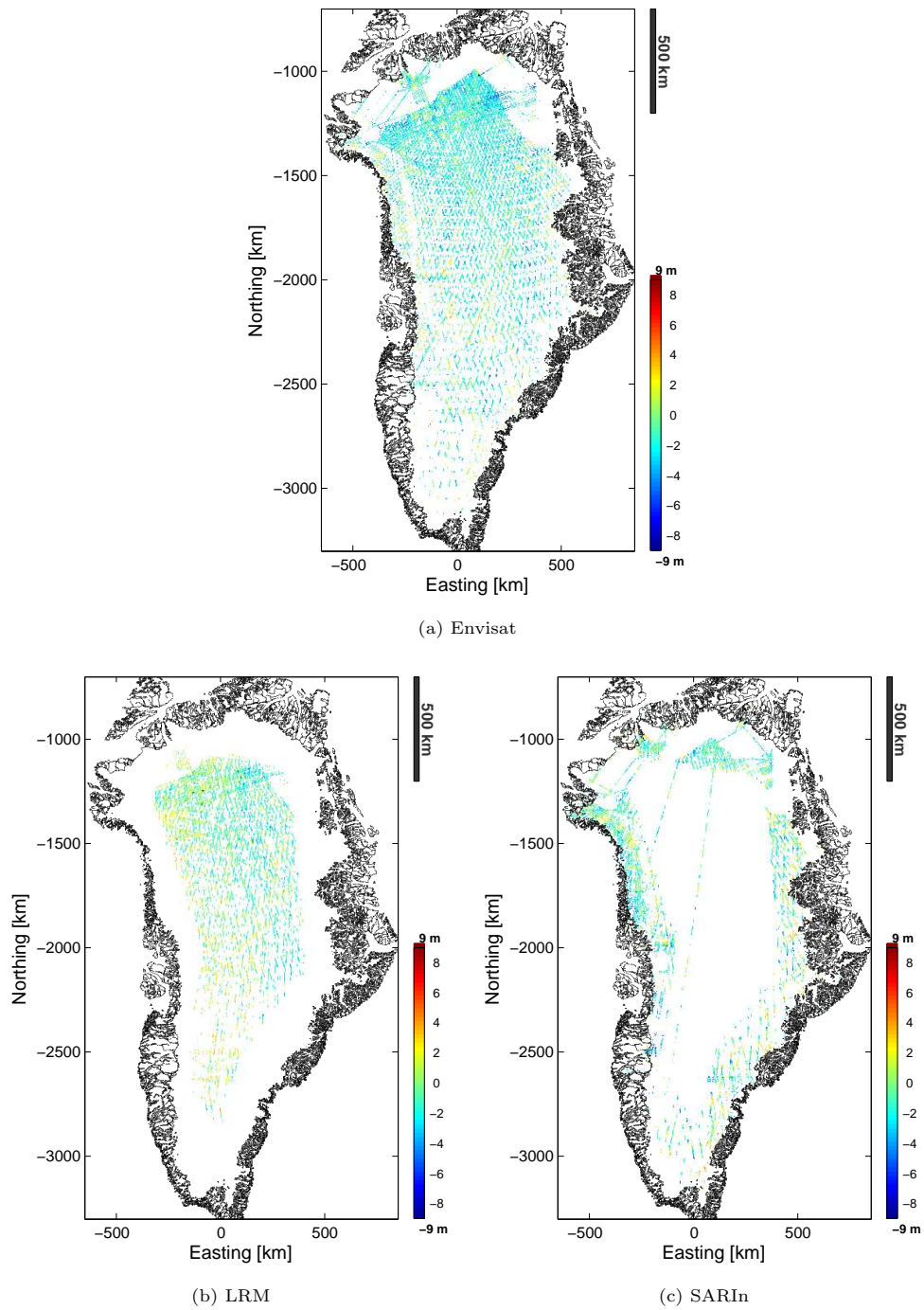


Figure 1. Elevation offsets between radar and laser data cf. $dH = H_{RA} - H_{LA}$, for Envisat (a) and CryoSat-2 LRM (b) and SARIn data (c), respectively.

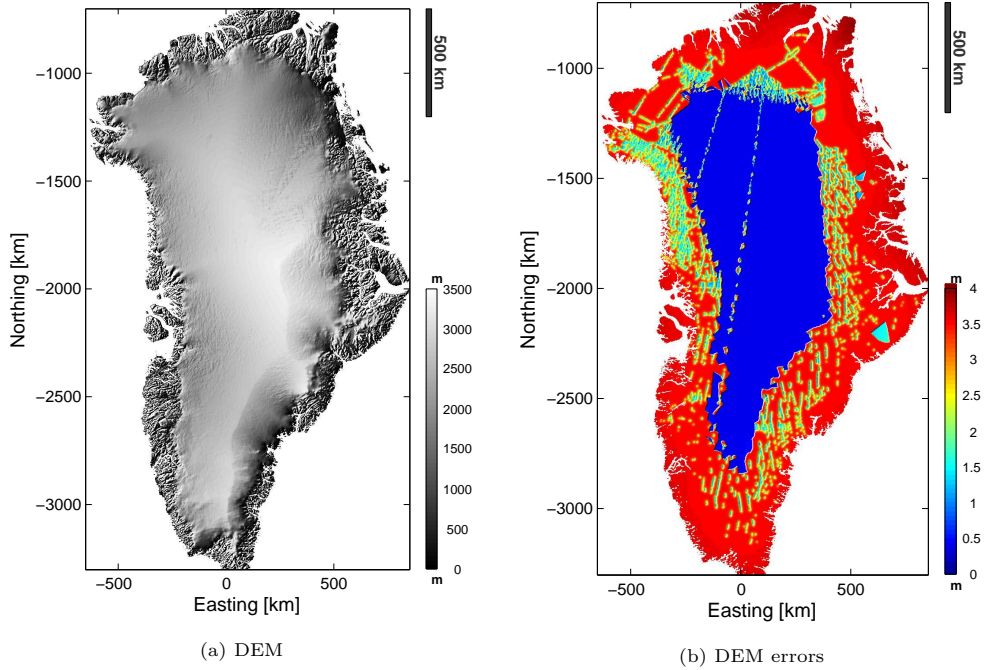


Figure 2. The RL-DEM (a) and error estimates (b). Errors increase with the distance to observation points.

Table 1. Statistics for the radar-laser elevation offsets, dH , visualized in Fig. 1. The Envisat results are split up relative to the location of LRM/SARIn data to enable a comparison of values from the two sensors.

Sensor	# of points	mean [m]	σ [m]	range [m]
CS-2: LRM	88,029	-0.5	2.3	± 4.9
CS-2: SARIn	44,275	-1.1	3.4	± 8.8
EV: RA-2 (LRM)	367,637	-1.5	2.4	± 6.5
EV: RA-2 (SARIn)	122,128	-1.7	3.0	± 6.5

Table 2. Validation of DEM elevations against 2011 ESA CryoVEx and ATM data, respectively. The search radius applied for neighboring observations is 500 m, and the elevation differences are given as $dH_{valid} = H_{RL-DEM} - H_{valid}$.

	Above 2200 m			Below 2200 m		
	# of points	mean [m]	σ [m]	# of points	mean [m]	σ [m]
CryoVEx	195	-1.6	13.8	869	0.1	59.9
ATM	3,860	0.1	7.9	15,094	1.2	30.2

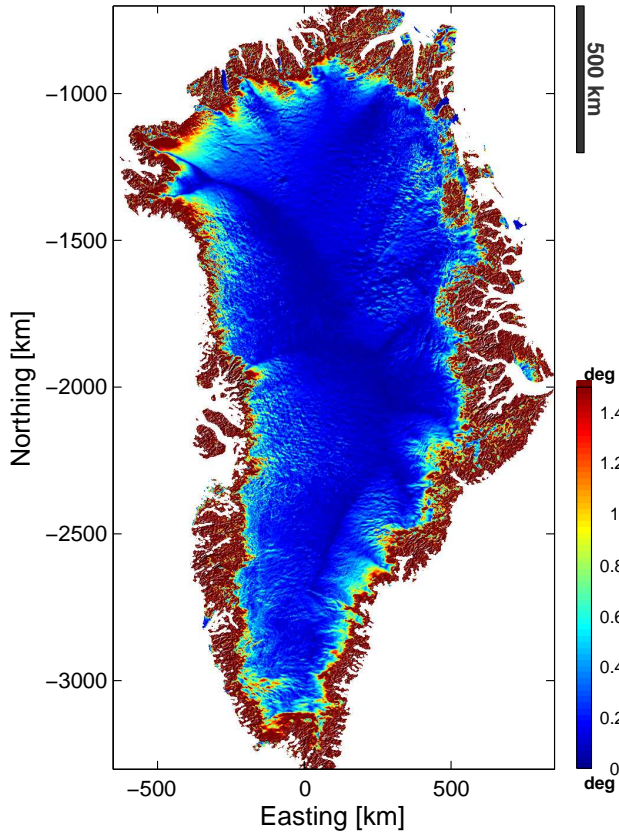


Figure 3. The surface slope. The ice divide and dynamic topography caused by ice flow over the bed topography and variations in the bed shear stress are visible.

Table 3. Inter-comparisons of the RL-DEM and previous models for observations *below* 2200 m altitude: The *Helm et al.* [2014] CryoSat-2 DEM, the *Howat et al.* [2014] GIMP, the *Bamber et al.* [2001] DEM, as well as the 2003 – 2009 mean ICESat heights [*Sørensen et al.*, 2011]. Elevation differences are found as $dH_{comp} = H_{column} - H_{row}$, and the respective mean and STD hereof are given. All units are in m.

	RL-DEM	CryoSat-2	GIMP	Bamber	ICESat
RL-DEM	0	-52.1 ± 228.9	-0.4 ± 15.6	32.1 ± 66.2	-129.1 ± 289.6
CryoSat-2		0	50.6 ± 228.9	83.0 ± 239.3	-76.5 ± 295.2
GIMP			0	32.5 ± 65.1	-128.7 ± 290.4
Bamber				0	-161.2 ± 296.7
ICESat					0

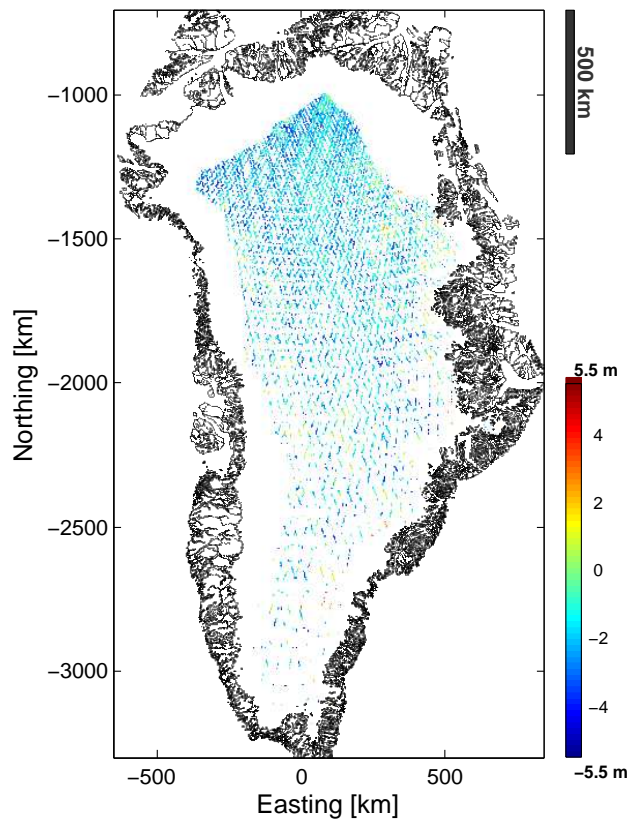


Figure 4. Envisat - ICESat elevation differences illustrating the penetration depth of Envisat echoes into the surface. The observation period is March/April 2009, and observations are constrained to points above 2000 m altitude.

Table 4. Inter-comparisons of the RL-DEM and previous models for observations *above* 2200 m altitude. Elevation differences are found as $dH_{comp} = H_{column} - H_{row}$, and the respective mean and STD hereof are given. All units are in m.

	RL-DEM	CryoSat-2	GIMP	Bamber	ICESat
RL-DEM	0	-1.8 ± 26.5	0.3 ± 7.2	47.0 ± 34.3	3.0 ± 37.9
CryoSat-2		0	2.1 ± 26.9	48.8 ± 34.6	4.8 ± 31.2
GIMP			0	46.7 ± 34.0	2.7 ± 34.6
Bamber				0	-44.0 ± 37.9
ICESat					0

D Relocation of radar altimetry data over ice sheets

As mentioned above, radar altimetry data acquired over ice sheets are subject to slope-induced errors due to a topographic variability within the footprint (Brenner et al., 1983). The outline of this paper is a comparison of two techniques for correcting for such errors. It is applied to Envisat and CryoSat-2 LRM near Jakobshavn Isbræ. The relocation is carried out by horizontally relocating the observations to the POCA to agree with the measured range, given a-priori knowledge on the surface topography.

More specifically, one technique, 'the POCA', uses the satellite altitude, H , and position to relocate the radar echo from nadir to the nearest point within the footprint. The other, which is described by Hurkmans et al. (2012), uses H as well as the surface slope and aspect to estimate the horizontal displacement. A significant difference between the two techniques is that the former allows for a non-uniform slope within the footprint while the latter assumes the slope to be constant. The topography is generated from either Envisat or ATM data or the GIMP DEM (Howat et al., 2014) regridded to a number of spatial resolutions. This prevents errors from the inclusion of external data or reduces those inherent in radar data. It also allows for analyzing the relocation vectors' sensitivity to different methods and DEM resolutions.

Significant differences between the size and orientation of the relocation vectors occur, and validation of the corrected observations against ATM show the preferred approach for both datasets to be the POCA using the GIMP regridded to a 2 km resolution. Therefore, the accuracy of the correction is highly dependent on the technique, which may translate into great errors in the respective analyses of, e.g., surface elevation changes or derived volume or mass changes.

This work is described in the paper below:

Authors : J. F. Levinsen, S. B. Simonsen, L. S. Sørensen, R. Forsberg
Title : Brief communication: Relocation of radar altimetry data over ice sheets
Journal : The Cryosphere Discussions
Submission date : February 26th 2015

Brief communication: Relocation of radar altimetry data over ice sheets

J. F. Levinsen¹, S. B. Simonsen¹, L. Sandberg Sørensen¹, and R. Forsberg¹

¹DTU Space, National Space Institute, Technical University of Denmark, Elektrovej, Building 327, 2800 Kongens Lyngby, Denmark

Correspondence to: J. F. Levinsen (jfl@space.dtu.dk)

Abstract. Beam-limited footprints from conventional satellite radar altimeters have diameters of tens of kilometers. Therefore, topography within the footprint may cause the reflecting point to differ from nadir, and displacements can be up to 18 km. Several techniques exist for correcting for such mispointing errors. Here, two methods are compared using Envisat and CryoSat-2 Low Resolution
5 Mode data near Jakobshavn Isbræ. The correction is proven to be highly dependent on the applied method, and may be associated with significant errors, which lowers the accuracy in analyses of ice sheet changes from radar altimetry.

1 Introduction

At present, more than two decades of continuous satellite radar data are available from European
10 Space Agency (ESA) missions. Several studies have used such observations to map changes in ice sheet elevation, volume, and mass (e.g. Zwally et al. (2005); Li and Davis (2008); Hurkmans et al. (2014); Helm et al. (2014); Sørensen et al. (2015)). Prior to doing so, it is necessary to correct the observations for slope-induced errors resulting from the large footprint: Topography within the illuminated area will relocate the radar echo from nadir to the Point of Closest Approach (POCA).
15 This prevents measurements of surface depressions such as the bottom of narrow outlet glaciers and troughs. As an example, the horizontal displacement for a satellite at an altitude of 800 km, typical for Envisat, and a uniform surface slope of 0.5° will be 7 km, corresponding to a range offset of 30 m. For 1° slopes, the offsets will increase to 14 km and 120 m, respectively (Brenner et al., 1983). Envisat's altitude and 13.575 GHz Ku-band frequency yield beam-limited footprint diameters
20 of 36 km resulting in maximum relocations of 18 km.

A number of methods exist for correcting for slope-induced errors. The 'direct method' corrects the

range to nadir (Brenner et al., 1983) while the 'intermediate method' relocates data from nadir to the POCA to agree with the range (Remy et al., 1989). The 'relocation method' uses the surface slope to find the POCA after which a corrected range estimate is derived (Bamber, 1994). All methods make use of an a-priori surface model, i.e. a Digital Elevation Model (DEM). Furthermore, the first two assume a constant slope within the illuminated area, while the latter allows for a non-uniform slope. We consider two techniques to horizontally displace the observations: The intermediate method, in the following referred to as the 'POCA', and that described by Hurkmans et al. (2012). The observations are acquired with Envisat and CryoSat-2 Low Resolution Mode (LRM). We vary the spatial resolution of the DEM to investigate how different grid sizes impact the relocation. This provides a minimum horizontal scale for topographic features, which the radar can resolve. The results are validated against contemporary laser-scanner data from the Airborne Topographic Mapper (ATM). The main contribution of the study is an important insight into the relocation vectors' sensitivity to different methods and DEM resolutions, which may translate into errors in derived surface elevation changes or interpolated volume and mass changes.

2 Data

Envisat operated from 2002 – 2012. The Radar Altimeter 2 (RA-2) operated at Ku-band and reached latitudes of $\pm 82^\circ$. CryoSat-2 was launched in 2010. Over the interior ice sheet, it operates in LRM mode, which is a conventional Ku-band radar altimeter. It orbits at 730 km, reaching latitudes of $\pm 88^\circ$ (European Space Agency, 2006, 2012). Observations from the two similar sensors are used to illustrate the effect of relocating data over various types of terrain. The ATM is an airborne laser-scanner, conically scanning the ground below the aircraft. At typical flight altitudes of 400 m and with a scan angle of 15° , approximately 140 m wide swaths are illuminated. Footprints typically range from 1 to 3 m (Krabill et al., 2002) making slope effects negligible. The Envisat and ATM data were acquired in May 2010 while CryoSat-2 LRM data were acquired in July 2010, the period closest in time for which observations were available.

3 Methodology

Jakobshavn Isbræ is the largest outlet glacier in Greenland. Envisat data acquired over this region are relocated using the POCA and the method described by Hurkmans et al. (2012). The corrected locations are obtained using a-priori topography generated from Envisat or ATM data or an external Digital Elevation Model (DEM) regridded to various resolutions. Here, we use the Greenland Ice Mapping Project (GIMP) DEM (Howat et al., 2014). Knowing the satellite altitude, H , and position, the POCA relocates the radar echo from nadir to the point within the footprint, which is nearest to the satellite. The method described by Hurkmans et al. (2012) assumes a constant slope and uses this and a displacement factor, $D = H \sin(\alpha) \cos(\alpha)$, to calculate the displacement in the direction opposite

the aspect, β : $dX = D \sin(\beta - \pi)$, $dY = D \cos(\beta - \pi)$. Observations with $\alpha \geq 1.5^\circ$ are discarded, limiting the applicability over rapidly changing areas of the ice sheet where Sørensen et al. (2015) otherwise have demonstrated Envisat data to be applicable for elevation change detection.

More specifically, we test the following techniques:

60 M.1 The method described in Hurkmans et al. (2012) using the GIMP regrided to 500 m, 2 km, 4 km, and 8 km resolutions.

M.2 The POCA using the GIMP regrided to 500 m, 2 km, 4 km, and 8 km resolutions.

M.3 Use Envisat data within an 18 km radius of each radar point to develop a local 1×1 km DEM. Derive α and β , and apply the method described in Hurkmans et al. (2012).

65 M.4 The same as M.3, although ATM data are used in the 500×500 m DEM formation.

M.5 The POCA based on ATM data within an 18 km radius of each radar point.

In M.3 – M.5, Envisat and ATM data are included to eliminate errors from external data or reduce those in radar data. The respective 1 km and 500 m resolutions are a compromise between the size of the footprints and topographic features in the region. The M.1 and M.2 techniques are applied to

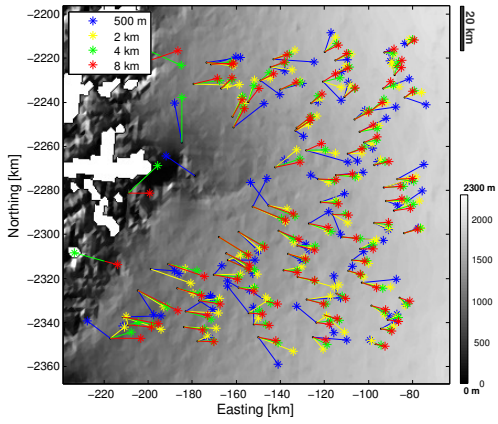
70 CryoSat-2 LRM data near Jakobshavn Isbræ.

4 Results and discussion

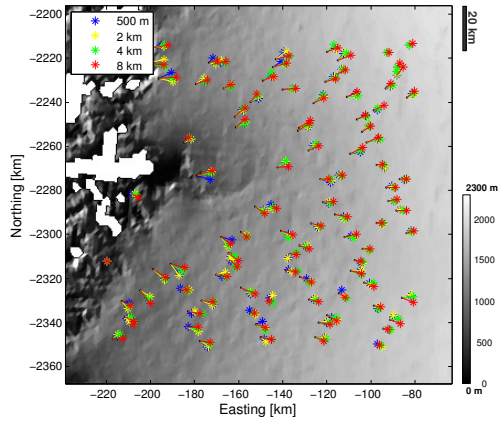
Fig. 1 presents a subset of the relocated Envisat data from M.1 (a), M.2 (b), and M.3 – M.5 (c), which demonstrates the significantly different size and orientation of the displacement vectors. Thus, the relocation is highly dependent on the technique and spatial resolution of a-priori data. M.1 – M.2
75 yield relatively consistent results for low spatial DEM resolutions (> 4 km) while the largest variations are found over lower altitudes with steeper surface gradients.

Fig. 1a shows a number of points being shifted down-slope to locations closer to the glacier margin, or intersecting relocation vectors within the illuminated area. Neither relocations are physically correct. Fig. 1b shows smaller and more consistent relocation vectors, and that points within the
80 drainage basin are shifted up-slope or to the same position. In Fig. 1c, the Hurkmans et al. (2012) method again shifts points down-slope while the POCA more consistently relocates points up-slope. All methods show slope-induced errors to be significant in this region. As CryoSat-2 LRM data are available here (Helm et al., 2014), this study indicates the ideal geographical boundary for the LRM to be located further inland.

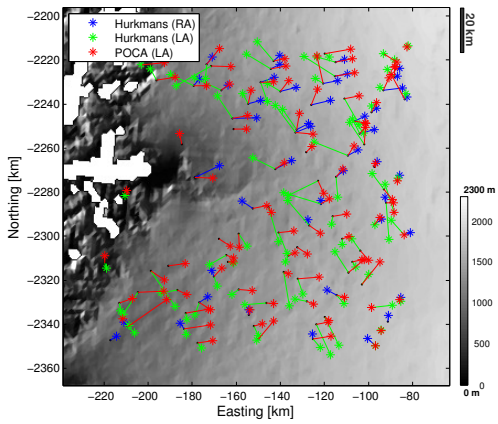
85 The validation is based on the median and standard deviation (STD) of elevation offsets between overlapping ATM and radar points as well as a slope error. The latter is given as the slope of the linear fit between the surface slope in the relocated point and the elevation offset; if the observations have been properly relocated, the slope error should be near-zero indicating that validation and radar



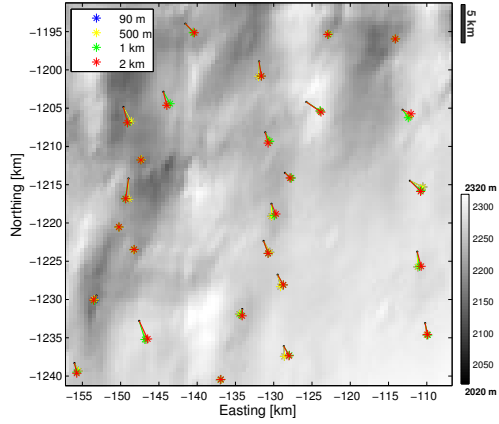
(a) EV: Hurkmans



(b) EV: POCA



(c) EV: Combined Hurkmans and POCA



(d) CS-LRM: POCA

Figure 1: Relocated Envisat ((a) – (c)) and CryoSat-2 LRM data (d) near Jakobshavn Isbræ, respectively, overlain the Levinson et al. (2015) DEM. The relocation is carried out using (a) the method described by Hurkmans et al. (2012), (b),(d) the POCA, and a combination of the two (c). The first two methods use the GIMP DEM to generate surface topography while the latter uses Envisat and ATM data, respectively. Please notice that similar relocation vectors for the 90 m and 500 m GIMP resolutions in (d) complicate visualization of all vectors.

Table 1: Validation of original ('nadir') and relocated Envisat points against ATM data over Jakobshavn Isbræ. The median and STD of elevation offsets are computed along with slope errors. The preferred method is highlighted in red. Numbers in parentheses show the spatial resolution of the external DEM/ dataset used to generate the surface topography.

Method	# points	median(dH) [m]	STD(dH) [m]	Slope error [m deg ⁻¹]
Nadir	550	56.36	55.94	43.06
Hurk (500 m)	336	-0.51	91.42	27.15
Hurk (2 km)	320	-20.40	46.09	11.39
Hurk (4 km)	469	-26.16	49.08	-12.83
Hurk (8 km)	404	-26.03	45.36	6.04
POCA (500 m)	510	13.41	22.99	10.94
POCA (2 km)	508	6.41	22.76	5.89
POCA (4 km)	459	6.54	24.55	6.12
POCA (8 km)	436	7.77	28.02	3.47
Hurk (Envisat)	246	13.25	80.14	22.43
Hurk (ATM)	330	54.96	90.95	26.49
POCA (ATM)	2,536	-0.25	32.43	-5.65

data have measured the same height. Larger values indicate that the correction has not fully reduced
90 the horizontal error. One reason for the near-zero rather than zero slopes is that part of the elevation
offset reflects surface penetration of the radar echoes. It is, however, believed to be constant in space
and time due to the small observation area and the use of contemporary observations. Another reason
is the observations' significantly different footprint diameters. Table 1 provides the validation results.
The POCA reduces elevation offsets to the highest degree possible and mostly for the method using
95 the GIMP at a 2 km posting (M.1). The Hurkmans et al. (2012) approach produces elevation offsets
of tens of meters, possibly due to the assumption of a constant slope within the footprint and a break-
down over regions with steep slopes as the method simplifies local topography. This is found in spite
of the $\alpha > 1.5^\circ$ rejection criteria and explains the generally larger relocation vectors compared to
the POCA results. The inclusion of Envisat or ATM data does not improve the outcome, likely due
100 to biases from the spatial data distribution and error inherent in Envisat data. This demonstrates the
necessity of an iterative approach, as was applied by Helm et al. (2014). In conclusion, none of the
methods reduce horizontal errors sufficiently. The differing positive/negative slope errors reflect the
large fluctuations in positive/negative elevation offsets, as indicated by the large STDs. An additional
key point arises from the poor results with the 500 m GIMP, indicating that the RA-2 simply cannot

Table 2: Validation of original ('nadir') and relocated CryoSat-2 LRM points against ATM data near Jakobshavn Isbræ. The median and STD of elevation offsets are computed along with slope errors. The preferred method is highlighted in red. Numbers in parentheses show the spatial resolution of the external DEM used to generate surface topography.

Method	# points	median(dH) [m]	STD(dH) [m]	Slope error [m deg ⁻¹]
Nadir	363	3.50	2.58	15.68
Hurk (90 m)	337	-5.64	4.81	-8.00
POCA (90 m)	352	0.85	1.41	3.54
POCA (500 m)	353	0.85	1.42	3.53
POCA (1 km)	359	0.70	1.48	4.00
POCA (2 km)	362	0.68	1.47	3.54

105 see small-scale topographic features over regions with steep surface gradients. The POCA takes into
account local topography, and the 2 km resolution shows that the algorithm requires some level of
surface detail to accurately relocate data. The Hurkmans et al. (2012) study applied a 1 km DEM
and reduced errors in volume changes relative to ATM and Ice, Cloud, and land Elevation Satellite
(ICESat) data by 14%. This study shows that a lower resolution and the POCA could further reduce
110 the error.

The M.1 and M.2 experiments are duplicated for CryoSat-2 LRM data based on the GIMP regridded
to 90 m, 500 m, 1 km, and 2 km resolutions. The lower DEM postings reflect the smoother topogra-
phy. A subregion of the observation area is plotted in Fig. 1d. Table 2 contains all validation results
for the preferred approach (found to be M.2) and the optimal solution for the other approach (M.1).

115 It shows that the solution using the GIMP at a 2 km posting again is preferable. Therefore, applying
this resolution over regions with both a steep and smooth topography is sufficient for ensuring a high
accuracy.

5 Conclusions

Relocating radar altimetry data is important to correct for slope-induced errors. This study compares
120 two techniques for horizontally relocating the observations to agree with the measured range. The
methods use an a-priori knowledge on the surface topography. The observations are acquired with
Envisat and CryoSat-2 LRM near Jakobshavn Isbræ. Significant differences between the direction
and distance of displacement occur showing that the correction is highly dependent on the technique.
Validation against airborne laser-scanner data shows the POCA method to be preferable. The highest
125 accuracy for the two datasets is obtained with the Howat et al. (2014) GIMP DEM at a 2 km posting,

indicating this resolution to be sufficient over both the steep ice margin and the flat interior. An additional finding is the poor results when relocating Envisat data using the GIMP DEM at a 500 m posting, suggesting that the radar cannot resolve small-scale surface features over regions with steep topography. The choice of relocation method substantially affects the accuracy of the relocation,
130 which may translate into significant errors in ice sheet elevation, volume-, or mass changes.

References

- Bamber, J. L.: Ice sheet altimeter processing scheme, *Int. J. Remote Sens.*, 15, 925–938, doi:10.1080/01431169408954125, 1994.
- Brenner, A. C., Bindschadler, R. A., Thomas, R. H., and Zwally, H. J.: Slope-induced errors in radar altimetry
135 over continental ice sheets, *J. Geophys. Res. - Oceans*, 88, 1617–1623, doi:10.1029/JC088iC03p01617, 1983.
European Space Agency: ENVISAT RA-2/MWR Level 2 User Manual, 2006.
European Space Agency: CryoSat Product Handbook, ESRIN, ESA and Mullard Space Sciences Laboratory,
and University College London, 2012.
- Helm, V., Humbert, A., and Miller, H.: Elevation and elevation change of Greenland and Antarctica derived
140 from CryoSat-2, *The Cryosphere*, 8, 1539–1559, doi:10.5194/tc-8-1539-2014, <http://www.the-cryosphere.net/8/1539/2014/>, 2014.
- Howat, I. M., Negrete, A., and Smith, B. E.: The Greenland Ice Mapping Project (GIMP) land classification
and surface elevation datasets, *The Cryosphere*, 8, 1509–1518, doi:10.5194/tc-8-1509-2014, <http://www.the-cryosphere.net/8/1509/2014/>, 2014.
- 145 Hurkmans, R. T. W. L., Bamber, J. L., and Griggs, J. A.: Brief communication "Importance of slope-
induced error correction in volume change estimates from radar altimetry", *The Cryosphere*, 6, 447–451,
doi:10.5194/tc-6-447-2012, <http://www.the-cryosphere.net/6/447/2012/>, 2012.
- Hurkmans, R. T. W. L., Bamber, J. L., Davis, C. H., Joughin, I. R., Khvorostovsky, K. S., Smith, B. S., and
Schoen, N.: Time-evolving mass loss of the Greenland Ice Sheet from satellite altimetry, *The Cryosphere*, 8,
150 1725–1740, doi:10.5194/tc-8-1725-2014, <http://www.the-cryosphere.net/8/1725/2014/>, 2014.
- Krabill, W. B., Abdalati, W., Frederick, E., Manizade, S., Martin, C., Sonntag, J., Swift, R., Thomas, R., and
Yungel, J.: Aircraft laser altimetry measurement of elevation changes of the Greenland Ice Sheet: technique
and accuracy assessment, *J. Geodyn.*, 34, 357–376, doi:10.1016/S0264-3707(02)00040-6, 2002.
- Levinsen, J. F., Smith, B. E., Sørensen, L. S., Khvorostovsky, K., Simonsen, S. B., and Forsberg, R.: A Digital
155 Elevation Model of the Greenland Ice Sheet based on combined laser and radar altimetry, *Earth and Space
Science*, in review, 2015.
- Li, Y. and Davis, C.: Decadal Mass Balance of the Greenland and Antarctic Ice Sheets from High Res-
olution Elevation Change Analysis of ERS-2 and Envisat Radar Altimetry Measurements, in: Geo-
science and Remote Sensing Symposium. IGARSS 2008. IEEE International, vol. 4, pp. 339–342,
160 doi:10.1109/IGARSS.2008.4779727, 2008.
- Remy, F., Mazzega, P., Houry, S., Brossier, C., and Minster, J.: Mapping of the Topography of Continental Ice
by Inversion of Satellite-Altitude Data, *J. Glaciol.*, 35, 98–107, doi:10.3189/002214389793701419, 1989.
- Sørensen, L. S., Simonsen, S. B., Meister, R., Forsberg, R., Levinsen, J. F., and Flament, T.: Envisat-derived
elevation changes of the Greenland ice sheet, and a comparison with ICESat results in the accumulation area,
165 *Remote Sens. Environ.*, doi:10.1016/j.rse.2014.12.022, in print, 2015.
- Zwally, H. J., Giovinetto, M. B., Li, J., Cornejo, H. C., Beckley, M. A., Brenner, A. C., Saba, J. L., and Yi, D.:
Mass changes of the Greenland and Antarctic ice sheets and shelves and contributions to sea-level rise: 1992
– 2002, *J. Glaciol.*, 51, 509–527, 2005.

E Posters

E.1 Inter-comparison exercise of surface elevation changes by Jakobshavn Isbræ

Presented at the 2013 EGU meeting in Vienna, Austria.

The poster presents an overview of the Round Robin exercise. This concerns elevation change solutions, validation hereof, and the conclusions leading to the development of the optimal method for an ice sheet-wide elevation change detection over the Greenland Ice Sheet. The Round Robin was conducted over the Jakobshavn Isbræ drainage basin, while the final dataset covers the entire ice sheet. This work led to the publications by [Levinsen et al. \(2015a\)](#) and [Sørensen et al. \(2015\)](#) – see Appendices A and B, respectively.

E.2 A digital elevation model of the Greenland Ice Sheet

Presented at the 2014 EGU meeting in Vienna, Austria.

This provides an overview of the method used for developing a Digital Elevation Model of the Greenland Ice Sheet as well as the preliminary results. The model is based on Envisat and CryoSat-2 radar altimetry data from 2010. Vertical errors in radar data have been corrected using contemporary laser data from ICESat, ATM, and LVIS.

E.3 A digital elevation model of the Greenland Ice Sheet

Presented at the 2014 AGU Fall Meeting in San Francisco, USA.

This poster presents the final outcome of the work described above. A major improvement consists in the final Digital Elevation Model being based on the corrected radar data merged with laser data. This exploits the high accuracy of laser data and the high spatial data coverage achieved when combining observations from both airborne and spaceborne, laser and radar missions. This work has led to the publication by [Levinsen et al. \(2015c\)](#) – see Appendix C.

E.4 Improving maps of ice sheet surface elevation changes

Presented at the SVALI Ph.D. course/ workshop "Applications of radar data from ice sheets to understand flow processes" at the Center for Ice and Climate,

University of Copenhagen, in March 2012.

The work was conducted prior to commencing the Ph.D. study. The focus is a co-registration of high-resolution stereographic imagery from SPOT-5 to contemporary ICESat and ATM data. This corrected the SPOT-5 Digital Elevation Models for horizontal and elevation-dependent errors. The result is a more accurate elevation change detection, which is particularly applicable over ice-covered regions with a large topographic variability in time and space. Therefore, examples are presented for the two Greenland outlet glaciers Jakobshavn Isbræ and Kangerdlugssuaq. The method and results are published by [Levinsen et al. \(2013\)](#).



ESA Climate Change Initiative – Ice Sheets



Validation and inter-comparison of surface elevation changes derived from altimetry over the Jakobshavn Isbræ drainage basin, Greenland – Round Robin results from ESA's Ice_Sheets_CCI (ID #EGU2013-6007)

Joanna Fredenslund Levisen (JFL@space.dtu.dk)¹, Kirill Khvorostovsky², Francesca Ticconi³

- 1) DTU Space, Technical University of Denmark, Building 327, Elektrovej, 2800 Kgs. Lyngby, Denmark
- 2) Nansen Environmental and Remote Sensing Center, Thormøhlens gate 47, 5006 Bergen, Norway
- 3) School of Earth and Environment, University of Leeds, Leeds LS2 9JT, United Kingdom

Abstract:

In order to ensure long-term climate records, ESA has launched the Climate Change Initiative (ESA CCI), which puts focus on 13 different Essential Climate Variables, one of them being Ice Sheets. In this program, four selected key parameters will be determined for the Greenland Ice Sheet: Surface elevation changes (SEC), surface velocities, calving front locations, and grounding line locations. This work focuses on SEC, and the goal is to develop the best routine for estimating this by means of radar altimetry. In order to find the most optimal approach we have completed a Round Robin experiment (RR) in which researchers from various European and US institutions have provided SEC estimates derived from either Envisat radar or ICESat laser altimeter data. The test area was Jakobshavn Isbræ drainage basin, and by analyzing, inter-comparing and validating the results, we have found that a combination of repeat-track and cross-over analyses will result in SEC estimates with a high spatial resolution and low error estimates.

Results from Round Robin participants:

- The RR participants are named SEC-1, SEC-2, ..., SEC-10, and their results (Table 1 and Figure 1) show that:
- SEC-1's Envisat results resolve SEC remarkably well demonstrating the possibilities of radar altimetry for such an analysis.
 - Best agreement between ICESat and Envisat repeat-track results found inland. ICESat results best resolve SEC by outlet.
 - Due to scarcity of cross-over points, these cannot be used to resolve SEC by outlet.
- Validation of the SEC trends were performed with airborne lidar data from NASA's IceBridge and ESA's CryoVex campaigns. They showed (Figure 2):
- Generally good repeat-track results, however best inland where slope effects are smallest.
 - Best cross-over results from laser rather than radar altimetry. Believed to result from ICESat's smaller footprint size → can better resolve the actual SEC trend.
 - As slope-induced errors in cross-over points can be ignored using data from ascending and descending tracks → overall lowest errors found for cross-over data.
- The following inter-comparisons of the RR results were carried out in order to find the most optimal way for estimating SEC throughout GIS:
- Radar vs. laser altimetry → Result: Difference only along ice stream due to slope effects.
 - Repeat-track vs. cross-overs → Result: RT has best spatial resolution and XO the lowest errors.
 - Time series vs. direct estimation of dH/dt → Result: No difference.

RR participant	Sensor	Method	Observation period	Output parameters
SEC-1	Envisat	Repeat-track	2002 – 2010	dH/dt , time series
SEC-2	ICESat	Repeat-track	2003 – 2009	dH/dt
SEC-3	ICESat	Repeat-track	2003 – 2009	dH/dt , time series
SEC-4	ICESat	Repeat-track	2003 – 2009	dH/dt
SEC-5	ICESat	Repeat-track	2003 – 2009	dH/dt
SEC-6	ICESat	Cross-overs	2003 – 2009	dH/dt
SEC-7	ICESat	Cross-overs	2003 – 2009	dH/dt , time series
SEC-8	ICESat	Cross-overs	2003 – 2009	dH/dt
SEC-9	Envisat	Cross-overs	2003 – 2009	dH/dt , time series
SEC-10	Envisat	Cross-overs	2002 – 2010	dH/dt , time series

Table 1: Information on the Round Robin participants' analyses and observation periods.

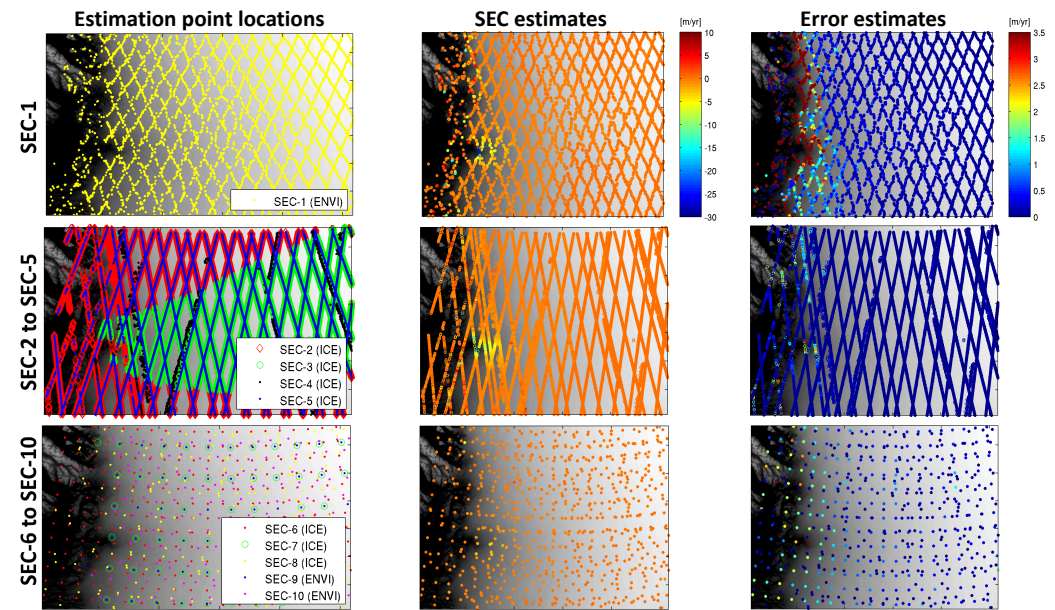


Figure 1: Results of the Round Robin analysis split up depending on the method and choice of altimeter. 'ENVI' refers to the use of Envisat data and 'ICE' to ICESat. See Table 1 for details on the method. Columns: Left: Location of RR participants' estimation points, middle: dH/dt , right: Standard errors. Rows: Top + middle: Repeat-track method; Bottom: Cross-over method. The same colorbar applies for all dH/dt and error plots.

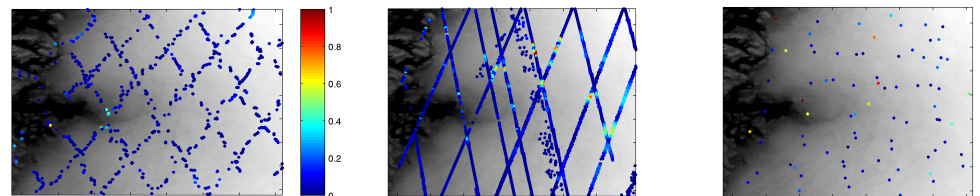


Figure 2: Validation with lidar data, i.e. scaled SEC differences between the lidar and RR dH/dt trends. The lidar trends cover the same time span as the observations, i.e. 2003 – 2009 and 2002 – 2010, respectively: SEC-1 (left), SEC-2 to SEC-5 (middle) and SEC-6 to SEC-10 (right).

Conclusions:

- Generally smaller ICESat than Envisat errors. Probably due to ICESat's smaller footprint size → more realistic resolution of actual SEC trend.
- SEC-1's radar results show large potential for the use of radar altimetry to derive SEC throughout the Greenland Ice Sheet including its margins.
- Most optimal SEC estimates can be obtained by combining repeat-track (high spatial resolution) with cross-overs (low errors in cross-over points). This allows for obtaining reliable values both inland and in areas with a rough surface topography such as by the ice margin.

A digital elevation model of the Greenland Ice Sheet derived from combined laser and radar altimetry data (ID #EGU2014-3063)



Joanna Fredenslund Levinsen (JFL@space.dtu.dk)^{1,2}, Ben Smith², Louise S. Sørensen¹, Sebastian B. Simonsen¹, and René Forsberg¹

1) DTU Space, Technical University of Denmark, Building 327, Elektrovej, 2800 Kgs. Lyngby, Denmark

2) University of Washington, Applied Physics Lab Polar Science Center, 1013 NE 40th Street, Seattle, WA 98105, USA

Introduction:

When using radar altimetry to estimate elevation changes of ice-covered surfaces, correction for slope-induced errors is necessary: In case of topography, the closest point to the satellite may not be at nadir → the reflecting point of the radar pulse is moved up-slope → estimates are returned in the wrong set of coordinates. Slope-induced errors can be corrected for by introducing a Digital Elevation Model (DEM).

Previous DEMs (e.g. Bamber et al., (2001) and Howat et al., (2014)) are based on approximately 10 years of observations. Large surface changes have been observed in that time span, particularly along the ice margin. Hence, updated topographic maps are necessary to continuously derive and correct accurate surface elevation change estimates.

Goal:

To develop a DEM of the Greenland Ice Sheet from a combination of Envisat and Cryosat-2 radar altimetry (RA) data, constrained by laser data (LA) from ICESat, ATM, and LVIS.

This work:

- Reference year: 2010.
- Spatial resolution: 2 x 2 km. This agrees with the ESA Ice Sheets CCI project showing that a 5 x 5 km grid is reasonable for ice sheet-wide change detection (Levinsen et al., 2013).
- Temporally and spatially agreeing LA are used to correct radar elevations for e.g. surface penetration of the signal.
- Separate DEMs will be created for the RA data sets, and spatial interpolation method collocation will be used to merge them. This adjusts for potential inter-satellite biases.

Observations:

CryoSat-2: July + Aug. 2010 L2i LRM + SARin, baseline B,
Envisat RA-2: April – September 2010,
ICESat: April + Oct. 2009; 2003 – 2008 dH/dt trend (Sørensen et al., 2011) to update H_{2009} to 2010,
ATM: April + May 2009, 2010; 2009 – 2010 dH/dt trend to update 2009 surface,
LVIS: April + May 2009, 2010; 2009 – 2010 dH/dt trend to update 2009 surface.

Method:

1. Slope correct radar data: Envisat: Use method described in Hurkmans et al., (2012). Surface slope and aspect found by GIMP model rescaled to Envisat footprint, i.e. 8 km.
LRM: Local interpolation of Bamber et al., (2001) DEM within radar footprint.
SARin: Move points up-slope relative to nadir position.

For each radar surface:

2. Find elevation difference, dH , between RA and LA using LA within 2 km of each RA point: $dH = H_{RA} - H_{LA}$.
3. Use collocation to spatially interpolate dH to observation area to get dH_{intpr} , σ_{dH} .
4. Use interpolation values to correct RA surfaces: $H = H_{RA} - dH_{intpr}$.

Merging into final DEM:

6. Subtract the Bamber et al., (2001) DEM from the corrected RA surfaces.
7. Grid resulting residual surfaces together using Inverse Distance Weighting. This yields dH_{comb} .
8. Obtain final, merged DEM:

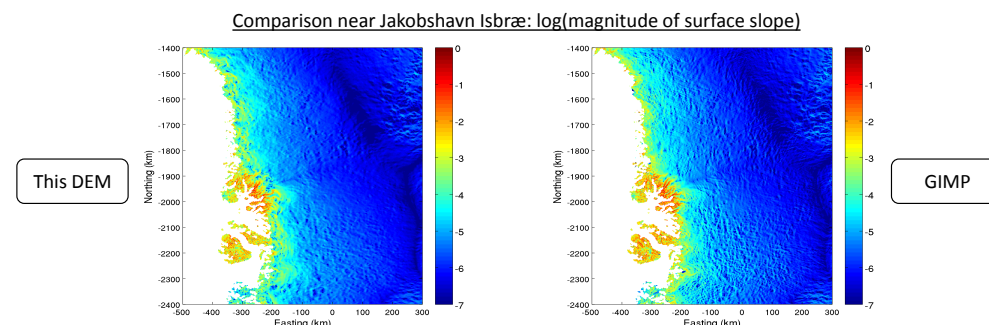
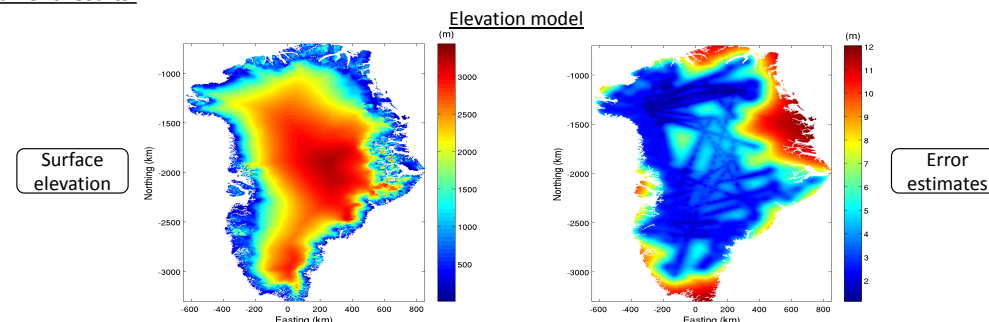
$$H_{DEM} = H_{Bamber} + dH_{comb}$$

References:

- J. L. Bamber, Ekholm, S., and Krabill, W. B.: A new, high-resolution digital elevation model of Greenland fully validated with airborne laser altimeter data, *Journal of Geophysical Research: Solid Earth*, 106(B4), 2001.
- I. M. Howat, Negrete, A. and Smith, B. E.: The Greenland Ice Mapping Project (GIMP) land classification and surface elevation datasets, *The Cryosphere Discuss.*, 8(1):453–478, 2014. doi: 10.5194/tcd-8-453-2014.
- R. T. W. L. Hurkmans, Bamber, J. L., Davis, C. H., Joughin, I. R., Khvorostovsky, K. S., Smith, B. S., and N. Schoen, N.: Time-evolving mass loss of the Greenland ice sheet from satellite altimetry, *The Cryosphere Discuss.*, 8(1):1057–1093, 2014. doi: 10.5194/tcd-8-1057-2014.
- J. F. Levinsen, Khvorostovsky, K., Ticconi, F., Shepherd, A., Forsberg, R., Sørensen, L. S., Muir, A., Pie, N., Felikson, D., Flament, T., Hurkmans, R., Moholdt, G., Gunter, B., Lindenbergh, R. C., and Kleinerbrink, M.: ESA's Ice Sheets CCI: validation and inter-comparison of surface elevation changes derived from laser and radar altimetry over Jakobshavn Isbræ, Greenland – Round Robin results, *The Cryosphere Discuss.*, 7, 5433–5460, 2013.
- L. S. Sørensen, Simonsen, S. B., Nielsen, K., Lucas-Picher, P., Spada, G., Adalgeirsdottir, G., Forsberg, R., and Hvidberg, C. S.: Mass balance of the Greenland ice sheet (2003 – 2008) from ICESat data – the impact of interpolation, sampling and firn density, *The Cryosphere*, 5(1):173–186, 2011. doi: 10.5194/tc-5-173-2011.



Current results:



Outlook and Conclusions:

- The availability of CryoSat-2 data, particularly SARin, have greatly improved our capabilities for DEM development and, hence, change detection using radar altimetry. This is seen through an increased spatial data coverage and accuracy, especially along the ice margin where previous altimeters (Envisat, ERS) are more affected by topography.
- Thus, radar altimetry can be used to develop a Digital Elevation Model of the Greenland Ice Sheet.
- The model is sensitive to the location of laser data as well as to local topography.

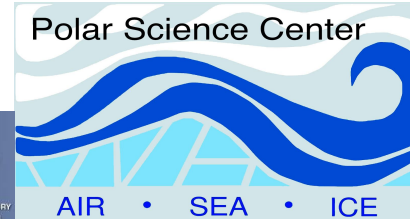
Future work:

- Validation with 2011 CryoVex data.
- Check inter-satellite bias adjustment through comparison of corrected Envisat and Cryosat-2 surfaces where $dH/dt = 0$ m/yr.

A Digital Elevation Model of the Greenland Ice Sheet based on merged radar and laser altimetry (C21B-0318)

Joanna Fredenslund Levinsen (JFL@space.dtu.dk)^{1,2}, Ben E. Smith², Louise S. Sørensen¹, Kirill Khvorostovsky³, Sebastian B. Simonsen¹, and René Forsberg¹

- 1) DTU Space, Technical University of Denmark, Building 327 + 328, Elektrovej, 2800 Kgs. Lyngby, Denmark
- 2) University of Washington, Applied Physics Lab Polar Science Center, 1013 NE 40th Street, Seattle, WA 98105, USA
- 3) NN, Nansen Environmental and Remote Sensing Center, Thormøhlens Gate 47, 5006 Bergen, Norway



Introduction

As the state of the cryosphere is constantly changing, it is highly important to continuously monitor the changes to understand the physical processes and their global impacts. Digital Elevation Models (DEMs) serve multiple purposes in such studies, e.g. for correcting radar altimetry data for slope-induced errors, or for adjusting for surface topography in along-track elevation change studies.

A contemporary DEM is required for ensuring a high accuracy in present-day cryospheric studies. Previous models of the Greenland Ice Sheet (GrIS) are based on observations from multiple sensors covering different time periods (e.g. Bamber et al. (2001); Howat et al. (2014)) or one year of data from one sensor (Helm et al., 2014). They are therefore affected by errors due to intermediate elevation changes or a limited spatial data sampling.

Goal

This work focuses on the development of a DEM of the GrIS based on merged radar and laser altimetry. 2010 ESA Envisat and CryoSat-2 data are relocated using the Howat et al., (2014) GIMP DEM, and elevation errors are corrected using contemporary laser data from NASA's ATM (Airborne Topographic Mapper), LVIS (Land, Vegetation, and Ice Sensor), and ICESat (Ice, Cloud, and land Elevation Satellite), respectively.

Merging the corrected radar data with laser data yields a DEM referenced to a specific time epoch and with a high horizontal and vertical accuracy.

The model

Observations:

- CryoSat-2 = July – September 2010 LRM (Low Resolution Mode), SARIn (SAR Interferometry)
- Envisat RA-2 = April – September 2010
- ICESat = March – April 2009 + 2003–2009 elevation change trend (Sørensen et al., 2011)
- LVIS = April & May 2009, 2010
- ATM Qfit = April & May 2009, 2010

Strategy:

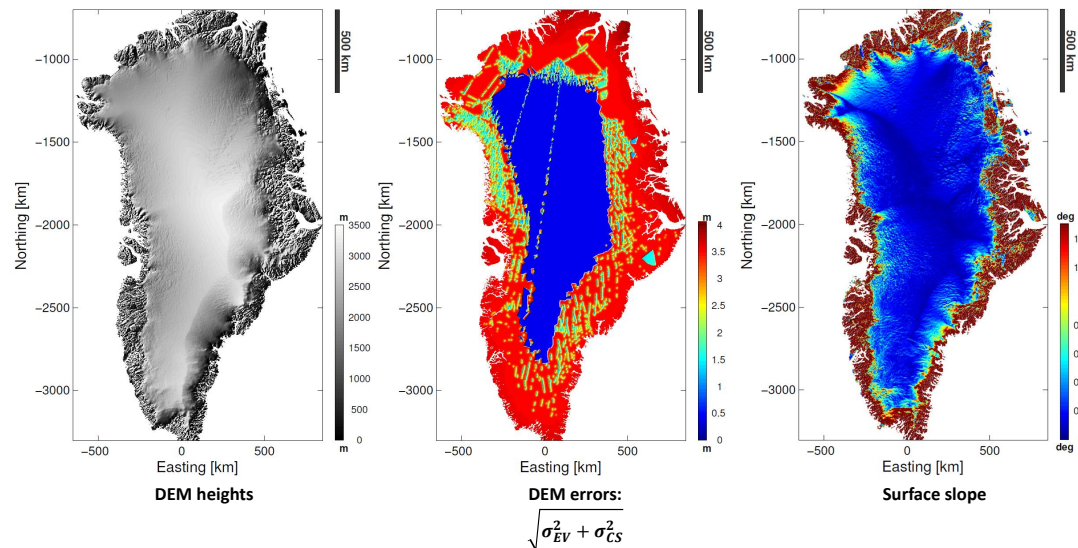
1. Perform in-depth analysis of relocation methods based on the GIMP gridded to different postings.
2. Use the optimal method for relocating Envisat and LRM data. SARIn data are relocated based on the 2π phase ambiguity.
3. Find elevation difference in overlapping observation points: $dH = H_{RA} - H_{LA}$.
4. Spatially interpolate dH to observation area using collocation: dH_{intp}, σ_{mode} .
5. Correct radar heights using radar-laser elevation offsets: $H = H_{RA} - dH_{intp}$.
6. Subtract GIMP DEM from laser data and corrected radar data.
7. Merge resulting residual surfaces using Inverse Distance Weighting: dH_{comp} .
8. Obtain final, merged DEM: $H_{DEM} = H_{GIMP} + dH_{comp}$, and errors by applying Gaussian quadratic summation to the interpolation errors, σ_{intp} .
9. Validate DEM against 2011 ATM and ESA CryoVEx (Cryosat Validation Experiment) data.

Characteristics:

- Reference epoch: 2010
- Geodetic datum: WGS-84 ellipsoid
- Spatial resolution: 2×2 km (Polar Stereographic)
 $0.02^\circ \text{lat} \times 0.05^\circ \text{lon}$ (WGS-84)

References:

- J. L. Bamber, Ekholm, S., and Krabill, W. B.: A new, high-resolution digital elevation model of Greenland fully validated with airborne laser altimeter data, *Journal of Geophysical Research: Solid Earth*, 106(B4), 2001.
- V. Helm, Humbert, A., and Miller, H.: Elevation and elevation change of Greenland and Antarctica derived from CryoSat-2, *The Cryosphere*, 8:1539–1559, doi:10.5194/tc-8-1539-2014, 2014.
- I. M. Howat, Negrete, A. and Smith, B. E.: The Greenland Ice Mapping Project (GIMP) land classification and surface elevation datasets, *The Cryosphere*, 8:1509–1518, doi:10.5194/tc-8-1509-2014, 2014.
- L. S. Sørensen, Simonsen, S. B., Nielsen, K., Lucas-Picher, P., Spada, G., Adalgeirsdottir, G., Forsberg, R., and Hvidberg, C. S.: Mass balance of the Greenland ice sheet (2003–2008) from ICESat data – the impact of interpolation, sampling and firn density, *The Cryosphere*, 5:173–186, doi: 10.5194/tc-5-173-2011, 2011.



Validation

Validation against 2011 CryoVEx and ATM data: Mean and standard deviation (STD) of elevation differences, $dH_{valid} = H_{DEM} - H_{valid}$. The validation is split up relative to observations above/below 2200 m altitude, similarly to Helm et al. (2014), who found -0.01 ± 45 m and 3.95 ± 133.6 m, respectively, using 2012 ATM data.

	# of points	Above 2200 m mean [m]	STD [m]	# of points	Below 2200 m mean [m]	STD [m]
CryoVEx	195	-1.6	13.9	869	0.8	61.0
ATM	3,860	-0.1	10.1	15,093	2.0	39.3

Outlook and Conclusions

- An absolute DEM of the Greenland Ice Sheet has been developed, which is referenced to a specific epoch in time: 2010.
- Elevation errors in Envisat and CryoSat-2 data have been corrected using contemporary, colocated ICESat, ATM, and LVIS laser data.
- Analyses of relocation methods have greatly improved the horizontal accuracy of radar data relative to previous studies.
- Combined with CryoSat-2's smaller footprint and SARIn mode, the range of applications of radar altimetry for analyses of the ice sheet topography have significantly improved.
- The best validation results are found over higher altitudes, consistent with smaller surface changes in time and space.
- Best agreement with ATM due to DEM being based on 2009, 2010 ATM data and the near-repeat flight lines.

Mapping Surface Elevation Changes of Outlet Glaciers Using Combined Laser Altimeter and Digital Elevation Model Data

Joanna Fredenslund Levinsen^{1,2} (Joanna@nbi.ku.dk), Ian M. Howat², Carl Christian Tscherning¹

1) University of Copenhagen, Niels Bohr Institute, Juliane Maries Vej 30, 2100 Copenhagen, Denmark; 2) Ohio State University, School of Earth Sciences, Columbus, Ohio 43210, USA

Abstract:

Ice surface elevation measurements from satellite and airborne laser altimeters have relatively low errors, but are spatially limited to satellite orbits and flight paths. Photogrammetric Digital Elevation Models (DEMs) have larger errors, but provide continuous surface elevations. We combine the complementary capabilities of these datasets to construct high-resolution (~100 m) maps of surface elevation and elevation change over rapidly changing outlet glaciers. Such a high resolution is needed to resolve the spatial variability of change over narrow ice streams and shear margins.

The basic principle of our method is to constrain the DEM surfaces to the altimeter flight lines where they overlap in space and time. This reduces the registration error in the DEM and fills the gaps between altimeter paths. We use laser altimeter data from ICESat and NASA ATM as well as DEMs from the SPOT 5 satellite. The observation areas are the Greenland outlet glaciers Jakobshavn Isbrae and Kangerdlugssuaq, and the elevation changes are estimated during the period 2007 – 2008.

Objective:

- To determine surface elevation changes by the Greenland outlet glaciers Jakobshavn Isbrae and Kangerdlugssuaq during period from 2007 – 2008.
- To combine satellite altimetry data (ICESat GLA12, ATM) with photogrammetrically derived DEMs (SPOT 5), which agree in time and space.

Method:

- Obtain data from observation areas. These are all acquired during spring/ summer of 2007 and 2008. Fig. 1 – 2 provide examples of input elevations, while Fig. 3 illustrates the 2007 and 2008 elevation changes when differencing the input DEMs. All data are from Jakobshavn Isbrae.
- Register the DEMs to altimeter points using planimetric and elevation dependent corrections in order to correct the DEMs. This yields Z_{corr} .
- Apply linear, unbiased geostatistical interpolation method to residuals between corrected DEM and altimeter surfaces: Optimal linear estimation (OLE). This yields interpolated values for the entire DEM surface, dZ_{est} , and variances of estimates, dZ_{err}^2 .
- Derive maps of surface elevation changes and errors cf. the relation: $Z_{new} = Z_{corr} - (dZ_{est} + dZ_{err})$. Fig. 4 shows Z_{new} from Jakobshavn.
- Difference Z_{new} for 2007 and 2008, respectively, to get the elevation changes, dH/dt . Fig. 5 shows the estimates for Jakobshavn and Fig. 6 those for Kangerdlugssuaq. Table 1 gives the results in numbers.

Results	dH/dt (terminus) [m/yr]	dH/dt (flow channel) [m/yr]	dH/dt (remaining surface) [m/yr]	Elevation change error [m/yr]
Jakobshavn Isbrae	-35 to -30	-20 to -10	0	0.3 – 5.2
Kangerdlugssuaq	-20 to -7	-15	+10	0.3 – 5.4

Table 1: Results from the two glaciers, i.e. approximate elevation changes and corresponding error estimates – the latter being based on dZ_{err}^2 .

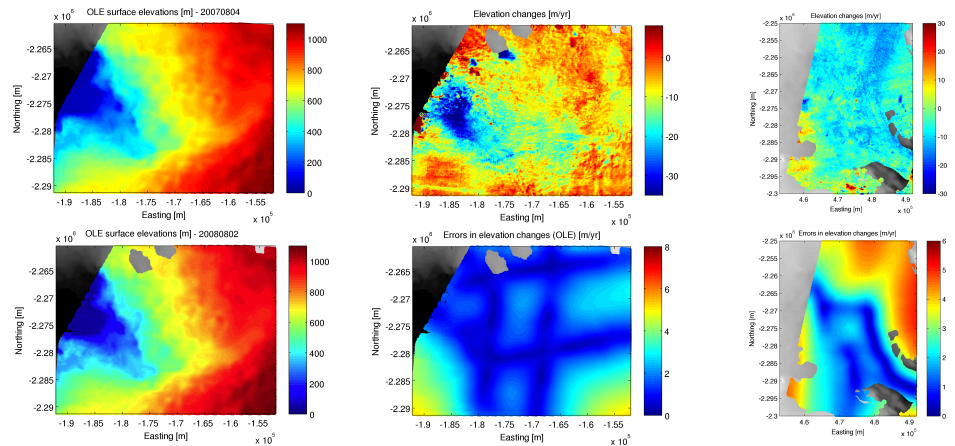


Fig. 4: Maps of Z_{new} from Jakobshavn Isbrae for the 2007 and 2008 data.

Fig. 5: Maps of dH/dt as well as estimation errors for Jakobshavn Isbrae.

Fig. 6: Maps of dH/dt as well as estimation errors for Kangerdlugssuaq.

Conclusions:

- The method is useful for using laser altimetry and photogrammetry to produce high-resolution maps of elevation changes with low errors.
- This method for unbiased minimum error prediction, i.e. OLE, is particularly applicable in areas of rapid surface changes.
- The magnitude of the errors largely depends on the altimeter data coverage: For tracks approximately 2 km apart, the error is 2 m/yr. If the distance halves, the error approximately halves accordingly. Therefore, error maps can be used to improve airborne altimeter flight planning by minimizing the spatial density of the flights.

References:

•Kortum et al. (2009), "SPRIT: SPOT 5 stereoscopic survey of Polar Ice: Reference Images and Topographies during the fourth International Polar Year (2007-2009)", ISPRS Journal of Photogrammetry and Remote Sensing, Vol. 64, pp. 204 – 212
 •Krabill et al. (2002), "Aircraft laser altimetry measurement of elevation changes of the Greenland ice sheet: technique and accuracy assessment", Journal of Geodynamics, Vol. 32, pp. 357 – 376
 •NASA (2011), "The Geosciences Laser Altimeter System", <http://icesat.gsfc.nasa.gov/icesat/>
 •Forsberg and Tscherning (2008), "An overview manual for the GRAVSOFT Geoidetic Gravity Field Modelling Program", 2nd edition

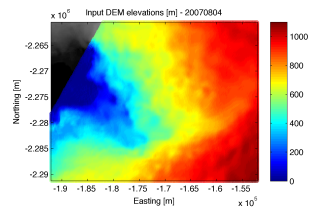


Fig. 1: Input DEM elevations from Jakobshavn Isbrae (August 4th 2007).

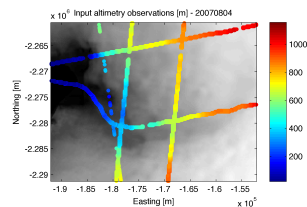


Fig. 2: Input altimeter elevations from Jakobshavn Isbrae (May 2007).

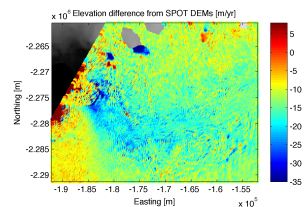


Fig. 3: Original elevation changes when differencing the 2007 and 2008 DEMs.

F Written contributions

Below is provided a complete overview of all written scientific contributions composed during the Ph.D. study. This regards peer-reviewed journal papers, technical reports, and conference proceedings.

Journal papers

J. F. Levinsen, S. B. Simonsen, L. S. Sørensen, and R. Forsberg. Brief communication: Relocation of radar altimetry data over ice sheets. *The Cryosphere Discussions*, 2015b. Submitted.

Contribution: Performed analyses, wrote paper, and produced all figures. Organized discussions with co-authors regarding data interpretation, and structured the work.

L. S. Sørensen, S. B. Simonsen, R. Meister, R. Forsberg, J. F. Levinsen, and T. Flament. Envisat-derived elevation changes of the Greenland ice sheet, and a comparison with ICESat results in the accumulation area. *Remote Sens. Environ.*, 160:56–62, 2015. doi: 10.1016/j.rse.2014.12.022.

Contribution: Participated in development of routine, discussions of how to fully understand the Envisat data, and in editing the paper.

J. F. Levinsen, K. Khvorostovsky, F. Ticconi, A. Shepherd, R. Forsberg, L.S. Sørensen, A. Muir, N. Pie, D. Felikson, T. Flament, R. Hurkmans, G. Moholdt, B. Gunter, R.C. Lindenbergh, and M. Kleinherenbrink. ESA ice sheet CCI: derivation of the optimal method for surface elevation change detection of the Greenland ice sheet – round robin results. *Int. J. Remote Sens.*, 36(2):551–573, 2015a. doi:10.1080/01431161.2014.999385.

Contribution: Performed analyses, wrote paper, and produced all figures. Organized discussions with co-authors regarding interpretation, and structured the work.

J. F. Levinsen, B. E. Smith, L. S. Sørensen, K. Khvorostovsky, S. B. Simonsen, and R. Forsberg. A Digital Elevation Model of the Greenland Ice Sheet based on combined laser and radar altimetry. *Earth and Space Science*, 2015c. In review.

Contribution: Performed analyses, wrote paper, and produced all figures. Organized discussions with co-authors regarding data interpretation, and structured the work.

M. Herceg, C. C. Tscherning, and J. F. Levinsen. Sensitivity of GOCE gradients on Greenland mass variation and changes in ice topography. *Journal of Geodetic Science*, (4):8–18, 2014. doi:10.2478/jogs-2014-0001.

Contribution: Provided corrected Digital Elevation Models and an elevation change map over Jakobshavn Isbræ derived in the study by Levinsen et al. (2013). Participated in discussions on interpretation of the change signal.

J. F. Levinsen, I. M. Howat, and C. C. Tscherning. Improving maps of ice sheet surface elevation change using combined laser altimeter and stereoscopic elevation model data. *Journal of Glaciology*, 59(215), 2013. doi:10.3189/2013JoG12J114.

Contribution: Performed analyses, wrote paper, and produced all figures. Organized discussions with co-authors regarding data interpretation, and structured the work.

Technical reports

K. Scharrer et al. Input/Output Definition Document for the Ice_Sheets_cci project of ESA's Climate Change Initiative. Version 1.2, April 2014. Available from: <http://www.esa-icesheets-cci.org/>.

Contribution: Co-wrote and edited Section 2 related to surface elevation change analyses.

K. Scharrer et al. Detailed Processing Model for the Ice_Sheets_cci project of ESA's Climate Change Initiative. Version 1.1, December 2013. Available from: <http://www.esa-icesheets-cci.org/>.

Contribution: Composed Sections 2.3 and 2.4 related to repeat-track analyses and merging of such data with cross-over solutions. Co-wrote and edited Sections 2.1 and 2.2 related to cross-over analyses and providing a system overview.

K. Scharrer, J. F. Levinsen, and F. Ticconi et al. Product Validation and Algorithm Selection Report for the Ice_Sheets_cci project of ESA's Climate Change Initiative. Version 1.2, April 2013. Available from: <http://www.esa-icesheets-cci.org/>.

Contribution: Composed Section 2 related to the Round Robin exercise.

Conference proceedings

J. F. Levinsen, K. Khvorostovsky, R. Meister, L. S. Sørensen, F. Ticconi, R. Forsberg, and A. Shepherd. Surface elevation changes of the Greenland Ice Sheet - Results from ESA's Ice Sheet CCI. In Proceedings of ESA Living Planet Symposium, number SP-722. ESA Communications, September 2013. ISBN: 978-92-9221-286-5.

Contribution: Performed analyses, wrote proceedings paper, and produced all figures. Organized discussions with co-authors regarding data interpretation, and structured the work.

F. Ticconi, J. F. Levinsen, K. Khvorostovsky, R. Forsberg, and A. Shepherd. Preliminary results of the ice_sheet_CCI Round Robin activity on the estimation of surface elevation changes. In *Proceedings of Geoscience and Remote Sensing Symposium (IGARSS)*, 2013 IEEE International, pages 244–247, July 2013.

Contribution: Performed analyses, organized discussions with co-authors regarding data interpretation, and structured the work. Edited proceedings paper.

R. Forsberg, L. S. Sørensen, J. F. Levinsen, and J. Nilsson. Mass loss of Greenland from GRACE, ICESat and CryoSat. In *Proceedings of CryoSat Third User Workshop*, number SP-717. ESA Communications, March 2013. ISBN: 978-92-9221-281-0.

Contribution: Provided elevation differences estimated from CryoSat-2 (2012 – 2013) and ATM (2011) data, and CryoSat-2 and mean ICESat (2003 – 2009) data, respectively, to detect errors in observations from CryoSat-2. These were mostly pronounced over sloping regions of the Greenland Ice Sheet.

G Least-squares collocation

The spatial distribution of space- and airborne observations is far from regular. Not only can e.g. a drift of a satellite orbit prevent ground-tracks from being exactly repeated, but so can slope-induced errors in RA data, which can displace measurement locations by several km (Hurkmans et al., 2012). Observations from airborne laser-scanners, on the other hand, are constrained to flight lines, which in turn are limited by logistics and costs.

One way of accounting for the spatial data distribution is by applying a geostatistical interpolation tool such as collocation. It is a linear, unbiased estimator, which can be used for interpolating sparsely distributed observations onto a predefined grid. The method was originally developed for solving partial differential equations as the anomalous potential outside the Earth, T , satisfies Laplace's differential equation $\Delta T = 0$ (Hofmann-Wellenhof and Moritz, 2005). The solution uses the spatial correlation between the measurements and prediction points, and thus the result depends on the measurement locations rather than the actual data values. The estimation variance is minimized, which explains the method also being known as optimal linear estimation.

A similar interpolation tool is called kriging, which is based on semi-variograms. By assuming that the value of such one depends solely on the separation distance between a set of observations, namely the lag \mathbf{h} , rather than the direction of displacement, the two methods are related by (Fig. G.1(a)):

$$\gamma(\mathbf{h}) = C(\mathbf{0}) - C(\mathbf{h}) \quad (\text{G.1})$$

Here, $\gamma(\mathbf{h})$ is the semi-variogram for points displaced by \mathbf{h} and $C(\mathbf{h})$ the auto-covariance function. $C(\mathbf{0})$ is the variance, i.e. σ^2 . The condition ensuring this relation is referred to as second order stationarity. Several types of kriging exist, all of which contain information on the input dataset. Fig. G.1(b) shows a spherical semi-variogram model and how the observations become decorrelated with an increasing lag. The sill denotes the variance and the range the corresponding lag; for lags greater than this value, observations are no longer correlated. The nugget effect provides the input data error by directly indicating that measurements acquired at the same location ($\mathbf{h} = \mathbf{0}$) differ by a given offset.

The point to be made here is that the semi-variogram can be described using covariances, and that the mathematical system for simple kriging is identical to that for least-squares collocation. Hence, the literature used for describing collocation in the following refers to both approaches. As it is out of the

scope of this study to provide elaborate details on the derivation leading to the solution of the collocation system, the following references are recommended for further information: [Bohling \(2005\)](#); [Dermanis \(1984\)](#); [Hofmann-Wellenhof and Moritz \(2005\)](#); [Nielsen \(2009\)](#). Unless otherwise stated, these references are used for writing this section.

G.1 Implementation

Consider two measurements at points on a plane or in space, and separated by the lag distance, $z(\mathbf{r})$ and $z(\mathbf{r} + \mathbf{h})$. Assuming that

$$\mathbf{z} = [z(\mathbf{r}_1), z(\mathbf{r}_2), \dots, z(\mathbf{r}_N)]^T = [z_1, z_2, \dots, z_n]^T \quad (\text{G.2})$$

at the locations \mathbf{r}_i , then \mathbf{r} is a vector containing the spatial coordinates, while \mathbf{h} is the lag distance between two points, \mathbf{r}_j and \mathbf{r}_k . \mathbf{Z} is a signal vector given similarly to Eq. (G.2):

$$\mathbf{Z} = [Z_1, Z_2, \dots, Z_n]^T$$

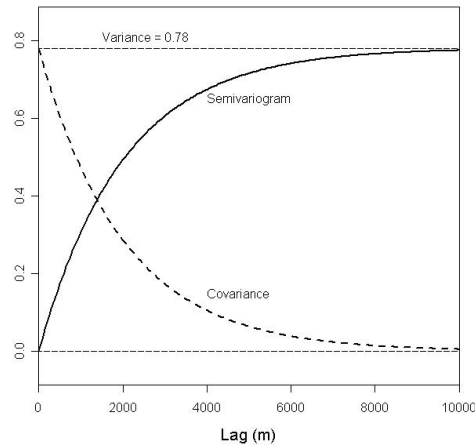
Both have an expected value equal to zero, i.e. the measurements are assumed to be unbiased. Optimal linear estimation is based on linear-least squares, and thus the known measurements, \mathbf{z} , can be used to derive a linear estimate for the unknown \mathbf{Z} as:

$$\hat{\mathbf{Z}} = \mathbf{A}\mathbf{z}$$

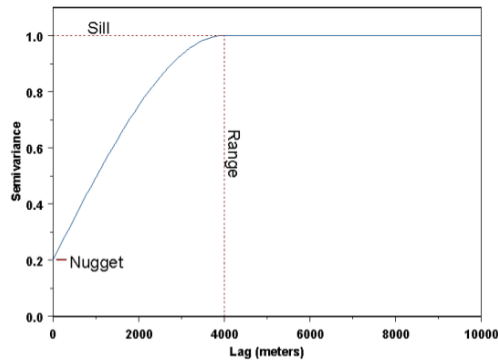
where \mathbf{A} is a matrix containing the auto-covariance function between the measurements and prediction points. Assuming isotropy, i.e. that the auto-covariance function behaves similarly in all directions and hence depends only on \mathbf{h} , and by minimizing estimation errors, i.e. $\epsilon = \hat{\mathbf{Z}} - \mathbf{Z}$, the solution to the collocation system is:

$$\begin{aligned} \hat{\mathbf{Z}} &= \text{Cov}\{Z_0, \mathbf{Z}\}^T \mathbf{C}^{-1} \mathbf{z} \\ &= [C_{01} \quad \dots \quad C_{0N}] \begin{bmatrix} C_{11} & \dots & C_{1N} \\ \vdots & \ddots & \vdots \\ C_{N1} & \dots & C_{NN} \end{bmatrix}^{-1} \begin{bmatrix} z_1 \\ \vdots \\ z_N \end{bmatrix} \end{aligned} \quad (\text{G.3})$$

Here, C_{0k} , $k = 1, \dots, N$ describes the auto-correlation between a given prediction point and the k th measurement, while C_{ij} , $i, j = 1, \dots, N$ denotes the



(a) Covariances and semi-variogram



(b) Semi-variogram model

Figure G.1 (a) Semi-variogram and covariances. The inverse relationship in Eq. (G.1) is evident as the correlation between a given set of observations decreases when their separation distance, the lag, increases. The variance is referred to as the 'sill' for semi-variograms. (b) A spherical semi-variogram model illustrating the information about the observations contained herein: The sill, range, and nugget effect (Bohling, 2005).

auto-correlation between measurements i, j .

The error on \mathbf{Z} is described by the variance/covariance matrix $\sigma_{\mathbf{Z}}^2$:

$$\begin{aligned} \sigma_{\mathbf{Z}}^2 &= \sigma^2 - \text{Cov}\{Z_0, \mathbf{Z}\}^T \mathbf{C}^{-1} \text{Cov}\{Z_0, \mathbf{Z}\} \\ &= C(0) - \begin{bmatrix} C_{01} & \dots & C_{0N} \end{bmatrix} \begin{bmatrix} C_{11} & \dots & C_{1N} \\ \vdots & \ddots & \vdots \\ C_{N1} & \dots & C_{NN} \end{bmatrix}^{-1} \begin{bmatrix} C_{01} \\ \vdots \\ C_{0N} \end{bmatrix} \end{aligned} \quad (\text{G.4})$$

The above solutions correspond to the scenario where no data errors exist. If wanting to account for such, the measurements, \mathbf{z} , are expressed as $\mathbf{z} = \mathbf{s} + \mathbf{n}$, where \mathbf{s} is the measured signal and \mathbf{n} the noise herein. Thus, a separate variance/co-variance function for the noise is added in the estimation process, so $\mathbf{C} = \mathbf{C}_s + \mathbf{C}_n$ rather than, as now, $\mathbf{C} = \mathbf{C}_s$.

Different covariance models exist, and the one used here is the 2^{nd} order Markov covariance model implemented in the GRAVSOFTE GEOGRID routine (Forsberg and Tscherning, 2008). It is given as:

$$C(\mathbf{r}) = C(0) \left(1 - \frac{\mathbf{r}}{\alpha}\right) e^{\left(\frac{\mathbf{r}}{\alpha}\right)}$$

where r is the distance from the measurement to the estimation point, and α is a constant determined from the correlation length of the measurements. The correlation length is given as the lag distance at which half the variance is reached, i.e. $\mathbf{h}_{1/2} = \mathbf{h}(C(\mathbf{0})/2)$. Thus, the corresponding covariance is referred to as that of 50% correlation.

G.2 Advantages

Several advantages follow when using least-squares collocation to spatially interpolate a set of inhomogeneously distributed observations, namely:

1. The method outputs both interpolation values and errors.
2. It takes the spatial distribution of the observations into account by weighing single observations higher than those in a cluster, and by weighing points closer to the prediction point higher than those further away. Thus, the interpolation error increases with the distance to observations.
3. The method is based on covariances, which, unlike some semi-variograms, always are positive definite. This is always the case when working with physical scenarios.

4. Measurement noise can be added.
5. The collocation system uses information on:
 - Errors in the input data, for semi-variograms termed the nugget effect.
 - The correlation length.
6. Assuming no data errors, prediction to an observation point will return the observation value with a zero error.

**DTU Space
National Space Institute
Technical University of Denmark**

Elektrovej 327
DK-2800 Kgs. Lyngby

Tel +45 4525 9500
Fax +45 4525 9575

<http://www.space.dtu.dk>